This is to certify that the

dissertation entitled

Effect of Ion-Sputtered Thermoelastic NiTi Coatings on Fatigue Crack Initiation in Copper

presented by

Seungho Nam

has been accepted towards fulfillment
of the requirements for

Ph.D. degree in Materials Science

D. S. Grummon
Major professor

Date August 1, 1995

EFFECT OF ION-SPUTTERED THERMOELASTIC NiTi COATINGS ON FATIGUE CRACK INITIATION IN COPPER

By

Seungho Nam

A DISSERTATION

Submitted to
Michigan State University
in partial fulfillment of the requirements
for the degree of

DOCTOR OF PHILOSOPHY

Department of Materials Science and Mechanics

1995

ABSTRACT

EFFECT OF ION-SPUTTERED THERMOELASTIC NiTi COATINGS ON FATIGUE CRACK INITIATION IN COPPER

By

Seungho Nam

Surface effects are particularly important in fatigue, since the surface is often the preferred site for fatigue crack initiation, and the fatigue life of materials may often be dominated by the crack initiation stage. NiTi thin films, which give rise to shape memory and superelasticity effects were used as a new surface coating approach to improve fatigue lifetime. The objective of the present work was to study the effect of NiTi surface coatings on fatigue crack initiation in polycrystalline copper, chosen as a model fcc metal. NiTi thin films were deposited on copper fatigue specimens by ion beam sputtering from a NiTi alloy target. By a crystallization annealing process, superelasticity properties were provided to the NiTi films. Fatigue specimens were subjected to carefully controlled fatigue cycling at constant plastic strain amplitude at various temperatures with respect to the transformation temperature of the films. The development of fatigue cracks on specimens was studied by optical microscopy and scanning electron microscopy. The crystal structure changes on surface films were investigated by X-ray diffractometery.

Adhesion between the film and an ion sputter cleaned substrate was very strong. X-ray diffraction study demonstrated that stress induced martensites were produced in NiTi thin films on a plastically deforming metallic substrate. The hardening rate and the saturation stresses were not affected by NiTi thin film surface modification. Amorphous NiTi films demonstrated their brittleness and the fatigue crack initiation life of amorphous film coated specimens was shorter than the unmodified copper specimens. On the other hand, all crystalline film coated specimens demonstrated improved fatigue crack initiation

lives compared to bare copper control specimens. The greatest increase in fatigue crack initiation life was obtained from $Ni_{49.6}Ti_{50.4}$ film coated specimens, which showed around 100 % improvement over bare copper specimens. These films had austenite finish temperatures approximately 35 °C above the test temperature, a condition associated with a minimum in the residual superelastic strain.

The characteristics of notch-peak topography resulting from plastic strain localization and incidence of cracks produced by cyclic strain were delayed by the presence of thermoelastic surface coatings. In addition, the austenite phase of NiTi coatings, which has higher yield strength and elastic compliance than the copper substrate, blocked the egress dislocations and inhibited penetration of slip bands. Thus, the ability of crystalline NiTi films to block (suppress) PSB extrusion from the substrate is attributed not only to superelastic deformation of the film, but also to its strength, ductility, and high elastic compliance.

To my wonderful parents and family:

for their endless love, encouragement and patience.

ACKNOWLEDGMENT

I am deeply indebted to Dr. David S. Grummon, my major professor, for his guidance, interest and continuous support throughout my Ph.D effort. Additionally, sincere appreciation is extended to my guidance committee members: Prof. Martin A. Crimp, Prof. Thomas R. Bieler, and Prof. William P. Pratt Jr.

Special thanks go to all my colleagues for their support and good friendship: Richard Schallek, Zhiwei Cai, Zhibo Zhao, Li Hou, Heyun Yin, Kevin Durning, and Bejeir Brooks. Thanks are given to Mr. Peter Scheuer for proof-reading drafts of my thesis. I would also like to thank the entire MSM Dept. staff for their kindness during the whole of my life in the U.S.A. as a student, especially Mr. Kurt Niemeyer for his help in making the specimens for my research.

My sincere appreciation is also expressed to the National Science Foundation for providing financial support of this research under Grant #MSS8821755.

Finally, I would like to express my appreciation to my wife, Jean-Young, and my lovely daughter, Angie (Youn-Joo), for their never-ending love and patience throughout my school life.

TABLE OF CONTENTS

LIST OF TABLES

LIST OF FIGURES

1. INTRODUCTION

Fatigue is the phenomenon of failure of materials under cyclic loading, and it is strongly influenced by both microstructure and environment. It is known that failure can occur under cyclic loading at stress levels much lower than those which cause fracture under monotonic loading. The fatigue life of materials is determined by the sum of the number of cycles required to initiate a crack and the number required to propagate the cracks to a critical length for fracture. Although the propagation process is of crucial importance in the engineering of many alloy systems, it is well known that the initiation stage of fatigue may often dominate the total fatigue life of materials. Surface effects in fatigue are particularly important, since in most cases the surface is the preferred site for fatigue crack initiation. In face centered cubic (fcc) metals, it is widely accepted that fatigue crack initiation is a result of cyclic strain localization in persistent slip bands (PSBs), which behave as if they are softer than the matrix, causing all cyclic plastic strain to become concentrated in the bands. As a consequence, local plastic strains associated with PSBs are very high (~ 1 %). These PSBs produce extrusions and intrusions at the free surfaces, leading to stress concentrations at the notch roots and finally fatigue crack nucleation. The important role of the surface on fatigue properties was dramatically demonstrated by Basinski *et al.* in copper (1983). When a copper specimen was fatigued to a large fraction of its fatigue life, and its surface then removed by electropolishing, the specimen exhibited a fatigue life as long as that of a virgin specimen.

Several techniques have been developed to prolong fatigue crack initiation life by modification of stress state, microstructure, and topography of the surface or near-surface region. Since surface tensile stresses have a deleterious influence on fatigue life, it is a

generally useful practice to create residual compressive stresses at the surface by mechanical operations such as surface rolling or shot peening (Almen and Black, 1963). Also, surface hardening by nitriding and carburizing strengthens the surface by inhibiting dislocation movement (Chen and Starke, 1976). Plated coatings using different materials to give a surface strengthening effect, which resulted in lowering the stacking fault energy at the surface, have also been studied as possible methods for improving fatigue life of materials (Greenfield and Purohit, 1980). Although plating often degrades fatigue life, ion implantation and ion beam mixing techniques have been investigated as a means of improving the fatigue life by shallow surface modification with controlled thickness, composition and structure of the modified region (Morrison *et al.*, 1989; Grummon *et al.*, 1988). Unfortunately, no surface modification is able to significantly modify the chief driving force for crack initiation, namely the localization of bulk plastic strain, which results from either grain boundary incompatibility, or from dislocation dynamics which lead to the formation of some form of persistent slip band structure.

If the bulk plastic shear strains were perfectly homogeneous, a strengthened surface layer might remain intact indefinitely during fatigue. Since, however, plastic strain in the bulk rapidly concentrates into PSBs (with characteristic plastic shears of ~1%), a strong film will be subjected to intense localized cyclic straining (Meyers and Grummon, 1990) and can be expected to eventually rupture, and/or suffer slip band penetration, forming a potent crack nucleus. Thus, the problem of crack initiation in the presence of surface films is a problem of fatigue of the surface film itself, in localized regions overlying subsurface PSBs.

In the present work, a new surface coating approach proposed by Grummon (1990), which is significantly different from previous surface modification techniques, is evaluated with respect to its ability to improve fatigue crack initiation life. This technique is based on unique fatigue properties associated with the thermoelastic martensitic transformations that give rise to shape memory and superelasticity effects

(Melton and Mercier, 1978). In particular, the superelasticity effect results in unique stress-strain behavior in which anelastic shear strains of several percent occur when a martensite phase is induced by applied stress and reverted back to the original austenite phase by removing that stress. Deformation by this mechanism is able to confer exceptionally high fatigue life under strain controlled conditions. Therefore, surface modification with superelastically deforming materials, which can exhibit large strains without dislocation activity, may resist the concentrated strains which are the result of bulk plastic strain localization during fatigue. Such a modified surface, it is hoped, will inhibit persistent slip band (PSB) emergence to the free surface by blocking dislocation egress, or by promoting slip reversibility through the shielding of slip-steps from environmental interaction, and therefore delay the onset of the kind of severe, localized surface damage that normally leads to fatigue crack initiation in many metals. Essentially, the idea is to impart the high fatigue resistance of superelastic NiTi alloy to other metals by applying the former material as a coating.

Among the many known shape memory alloys, NiTi alloy has high ductility and extraordinarily long fatigue life under high strain amplitude fatigue. This is associated with the superelasticity effect, which occurs not only in austenite-to-martensite transformations, but also in austenite-to-R-phase transformations (Miyazaki and Otsuka, 1984; 1986). These materials, in the form of thin films, have been produced by d.c. magnetron sputtering (Chang, 1993; Busch *et al.*, 1990) or r.f. magnetron sputtering (Ishda *et al.*, 1993), and the optimum conditions for superelasticity and shape memory effects have been investigated. Recently, NiTi alloys in the form of thin films produced by d.c. magnetron sputtering have been shown to posses full transformational superelasticity (Hou, 1995). The stress for inducing martensite obeyed the Clausius-Clapeyron relation[1], as with a bulk NiTi alloy, and the fully superelastic phenomenon

1. This relation explains the realtionships between variation of temperature and stress which are necessary for the maintenance of equilibrium between two phases. For the formation of thermoelastic martensite, there is an equivalence between temperature and stress: a decrease in temperature is equivalent to an

was also observed. The superelasticity effect may allow the film to be deformed up to a plastic strain of 5 ~ 10 % without accumulating severe slip damage that enhances the nucleation of fatigue cracks on the surface.

The first objective of the present study was to fabricate NiTi thin films by ion beam sputter deposition which could be shown to undergo the thermoelastic martensitic transformations, and to understand transformation behavior of NiTi thin films. The second objective was to study the effect on fatigue crack initiation of thermoelastic NiTi coatings.

This thesis is organized as follows: in Chapter 2, a detailed review of the literature on fatigue crack initiation in FCC metals is provided, and fatigue life studies on materials with several conventional surface modification types are introduced. In addition, general concepts of transformational superelasticity and mechanical (especially fatigue) properties of near equiatomic NiTi alloys, with respect to their transformational behavior are reviewed, and recent research on NiTi thin films are discussed in this chapter. An overall description of NiTi thin film fabrication by ion beam sputtering, characterization of the deposited films, low cycle fatigue tests, and other experimental details are given in Chapter 3. In Chapter 4, results of the study are presented and discussed. The first part of this chapter presents characteristics of the thin films such as their microstructure, crystallization behavior, and their transformational behavior. The second part describes the stress strain behavior of the thin films with respect to their transformation temperatures, and provides comparisons of fatigue crack initiation life influenced by NiTi thin surface film coatings. Finally, the thesis is summarized in Chapter 5, where conclusions of the present study are drawn and suggestions for future work are provided.

---

increase in stress, both stabilizing martensite. According to this relation, the stress needed to produce stress-induced martensite increases linearly with temperature.

2. REVIEW OF THE LITERATURE

Introduction

The present study was undertaken as part of a project entitled "Surface Superelastic Microalloying for Improved Fatigue Performance in Ni, Ti, Fe, and Cu Based Alloys" supported by National Science Foundation under grant # MSS-8821755. The main objective of this work was investigation of the thermoelastic NiTi surface coating on fatigue properties of polycrystalline copper. In ductile metals, fatigue crack initiation at moderate strain amplitudes involves two principal processes: the localization of plastic strain in the interior of the material, in the form of persistent slip bands (PSBs), and the progressive development of stress concentrating geometries at the surface where these slip bands emerge. The irreversibility of shear displacements along the slip bands in the near-surface region results in a roughening of the surface. This parasurface region can strongly influence the homogeneity and reversibility of cyclic slip, by mediating interactions with the external environment, controlling the egress of mobile dislocations, and altering the operation of nearby dislocation sources. Modification of the chemistry, stress state, or atomic structure of the surface region has therefore been a logical approach to the improvement of fatigue performance in metals.

In the following chapter, mechanisms of fatigue in ductile metals, including cyclic plasticity, strain localization, and crack initiation, will be treated briefly in section 2.1. In section 2.2, different approaches to improve fatigue properties by surface modification will be discussed. In section 2.3 and 2.4, general features of thermoelastic martensitic transformation, including superelasticity, shape memory effect, and stress-induced martensite formation, will be discussed, and the deformation behavior and fatigue

characteristics of superelastic NiTi alloys will be reviewed. In section 2.5, fundamental aspects of ion beam sputter deposition of NiTi thin films, along with the effect of various process parameters that have an effect on the film, will be outlined. Basic studies related to microstructure and thermoelastic transformation characteristics in sputter deposited NiTi film, which were carried out by Chang (1993), will be discussed in this section. Finally, the influence of the crystalline nature of the deposited film in relation to its desired properties will also be discussed in this review.

2.1. Fatigue Behavior in FCC Metals

In face centered cubic (fcc) metals, it is widely accepted that fatigue crack initiation is a result of cyclic strain localization in PSBs, which behave as they are much softer than the matrix (Neumann, 1983). These PSBs produce extrusions and intrusions at the free surfaces where subsequent stress concentrations occur and promote additional slip, and finally, fatigue crack nucleation; as shown schematically in Figure 2-1. The population of fatigue cracks increased linearly with the number of cycles and the applied strain amplitude after the crystals reached saturation (B. -T. Ma and C. Laird, 1989), because the volume fraction of PSBs is proportional to applied strain and with accumulating cycles. Details of the cyclic stress-strain response, PSB formation, and fatigue crack initiation in FCC metals will be described in the following sections.

2.1.1. Cyclic Stress-Strain Response in FCC Metals

Mechanical testing methods for studying cyclic stress strain response may utilize one of essentially three kinds of control modes: (1) constant stress amplitude mode ($\Delta\sigma_T$), (2) constant total strain mode ($\Delta\varepsilon_T$), and (3) constant plastic strain amplitude mode ($\Delta\varepsilon_p$). In these approaches, the fatigue life of a component is defined as the total number of cycles needed to induce fatigue damage and to initiate a dominant fatigue flaw which is propagated to final failure.

Among these control modes, constant stress amplitude-fatigue life approach was first introduced in the 1860s. Out of this work evolved the concept of an 'endurance limit', which characterizes the applied stress amplitude below which the material is expected to have infinite fatigue life. Although this method has found widespread use in fatigue analysis, it does not provide a realistic account of fatigue life when considerable plastic deformation occurs during cyclic loading.

Strain controlled fatigue testing is commonly used as a basis for structural design in components where fatigue crack initiation ahead of stress concentration is of primary concern. Under typical cyclic loading conditions involving low values of imposed strain, the plastic strain (ε_p) is only a fraction of the total strain amplitude (ε_T) and it decreases with cyclic work hardening. Thus, fatigue tests conducted with total strain amplitude control do not provide a clear description of the progression of cyclic deformation. Instead, the most common method of performing strain-controlled tests involves constant plastic strain amplitude cycling.

Annealed fcc metals generally exhibit a rapid increase in yield stress with increasing number of cycles at a constant plastic strain amplitude during the initial period of cyclic deformation. This process is known as cyclic strain hardening. With further increases in the number of cycles, the hardening rate progressively diminishes and the variation of stress with plastic strain reaches a steady-state condition where the stress amplitude reaches a 'saturation' value. Once the saturation state occurs, there are no further changes in the stress-strain hysteresis loop shape and area with increasing number of cycles, until fatigue cracks form.

A plot can be constructed from the peak shear stress (τ_S) at saturation as a function of the plastic strain amplitude (γ_{pl}) used in the test, which is called the cyclic stress-strain curve (CSS curve). A typical CSS curve for a copper single crystal is illustrated in Figure 2-2 (Mughrabi, 1978). Based on the magnitude of the plastic strain amplitude (γ_{pl}), the plot has been divided into three distinct regions. In regions A and C

which represent very low and high plastic strain amplitudes respectively, the saturation stress increases with increasing plastic strain amplitude, but in the intermediate region, B, the CSS curve shows nearly constant saturation stress independent of plastic strain amplitude. The typical shear stress at the plateau, observed for a copper single crystals at room temperature, is approximately 28-30 MPa, and the plastic strain amplitudes associated with the plateau ranges from 6×10^{-5} to 7.7×10^{-3}. [1]

At a very low plastic strain amplitude, range A in Figure 2.2., τ_s increases with increasing γ_{pl}, and the deformation is reasonably homogeneous. Under these conditions, cyclic deformation is essentially reversible and thus formation of PSBs and strain localization does not occur, thereby extending the fatigue life of any given material to infinity. Thus, the upper limit of this region will correspond to the fatigue limit. With increasing plastic strain amplitude, range B, the shear stress amplitude will reach a steady state condition, where the saturation stress (τ_s^*) is independent of the plastic strain amplitude. This region is related to inhomogeneous deformation localized in PSBs. In this region, the volume fraction of PSBs increases linearly from 0 % to 100 % as the plastic strain amplitude is raised, until region C appears. Further increasees in the plastic strain amplitude (i.e. high strain fatigue) results in an increased saturation stress, range C, and homogeneous deformation. As a manifestation of this, new dislocation patterns will be formed and materials will exhibit a different failure mode. Cyclic stress-strain data for various FCC metals and alloys, fatigued at different temperatures, are given in Table 2-1. Saturation stresses depend on the testing temperature. The saturation stress for copper single crystals fatigued at 4.2 K was almost twice as high as one fatigued at 295 K. However, the plastic strain amplitude range (γ_{pl}) are almost independent of the materials.

1. The ratio of saturation stress to shear modulus is remarkably constant for copper, silver, nickel, and α-iron (Mughrabi *et al.*, 1979).

2.1.2. Dislocation Structures in Fatigued FCC Metals

Annealed FCC metals develop dislocation structures over the range of plastic strain amplitude and number of cycles. At a low number of cycles, the dislocation structure of fatigued pure metals consists of dense bundles (veins) of primary edge dislocations in multipole configurations separated by dislocation depleted regions (channels). With increasing the number of cycles, at saturation stress state, the dislocation structure evolves continuously. The matrix structure, which was created during cyclic hardening, breaks down and is converted into the 'wall' or 'ladder' structure of the PSB's which are softer, and in which the strain concentrates subsequently. The PSBs are described as thin lamellae (~ 1μm) which experience high slip activity, lying parallel to the primary slip plane, embedded in a matrix with a significantly different dislocation arrangement (Mughrabi, 1978). The PSB is composed of regularly spaced edge dislocation walls of high dislocation density, while the matrix veins are irregularly arranged. The last stage in the evolution of dislocation structures in fatigue is that of cell formation. Dislocations collect into a cellular arrangement upon further increases in the number of cycles. However, the cell formation may or may not occur and is apparently not necessary for fracture (Kuhlmann-Wilsdorf and Laird, 1977). In the following section, evolution of the dislocation structure during rapid hardening and formation of persistent slip bands (PSBs) in FCC metals will be discussed in detail.

2.1.2.1. Evolution of the Dislocation structure during Cyclic Hardening A typical set of hysteresis loops obtained from the first 10 cycles of fatigue of a copper specimen, and a schematic illustration of a cyclic hardening curve for fcc metals are shown in Figure 2-3. A fatigue hardening curve gives the peak stress as a function of the cumulative strain ($2\Sigma\Delta\varepsilon_p$) or the number of cycles. The rapid hardening range is comparatively short. One description of the dislocation process which may lead to rapid hardening is as follows: In the early stage of cyclic hardening, initial plastic straining

occurs on some favored slip planes. As a result of non-conservative dislocation motion, debris collects on this slip plane, and it hardens. Slip then becomes favored on another plane which, in turn, accumulates dislocation debris and hardens. The glide planes, where slips are in both negative and positive sense, are mostly separated and the glide dislocations trap one another to form dipoles or multipoles with increase in number of cycles. In this process, screw dislocations are mutually annihilated through cross slip while edge dislocations form very stable dipole groupings with preferential orientation of the dipoles perpendicular to the primary slip direction. The process continues until the entire volume of the material has undergone some cyclic slip, by which time the material has hardened to a level approaching the saturation stress. As a result, the dislocation substructure during cyclic hardening of fatigue hardened pure metals consists of parallel veins of metastable edge dislocation dipoles (multipoles) and channels, which are almost dislocation free areas, as shown schematically in Figure 2-4(a). With increasing cumulative plastic strain, deformation begins with the bowing out of edge dislocation from the veins. When this bowing segment encounters an adjacent vein, annihilation of edge segments takes place. Two screw segments of opposite sign are then liberated and my shuttle back and forth with screws of opposite sign. Thus, most dislocations between the veins have predominantly screw character.

2.1.2.2. Formation of Persistent Slip Bands (PSBs) The transition from rapid hardening to the saturation state is associated with PSB formation. Dislocation models regarding PSB formation were developed mainly by two groups: (1) Essmann, Gosele, and Mughrabi and (2) Kuhlmann-Wilsdorf and Laird. Essmann, Gosele, and Mughrabi (1981) proposed a dislocation model based on experimental observations of point defect generation by the annihilation of edge dislocations and the majority of these point defects have vacancy character. According to this model, the saturation state is characterized by the existence of a dynamic equilibrium between

dislocation multiplication and annihilation. Dislocations can multiply when edge segments bow out and cross the channels, increasing both edge and screw dislocation densities, or when screw dislocations glide along channels, laying down edges along the walls, which is shown in Figure 2-4(b). This is balanced by mutual annihilation of dislocations of opposite signs approaching on glide planes less separated by than a critical distance. Screw dislocations annihilate by cross slip if the distance between glide planes is less than ~50 nm, but the corresponding distance for edge dislocations on the glide plane is less than ~1.6 nm apart in the wall of the PSBs (Mughrabi, 1979). Elimination of edge dipoles is envisaged as giving rise to vacancies. Vacancy production by dipole collapse is then balanced by vacancy capture by dislocations passing within critical distance. The sequence of microscopic slip processes, accompanied by dipole annihilation, has the effect of depositing edge dislocations at opposite PSB-matrix interfaces such as that their extra planes are directed into the PSB.

Kuhlmann-Wilsdorf and Laird (1980) proposed a mechanism for continuous refinement and densification of veins, which were formed during rapid cyclic hardening, with increasing stress amplitude. The veins became hard shelled because dipoles at their surfaces were maintained at a small spacing by the arrival and departure of dislocations gliding under stress. The softer interiors contained wider dipoles, which were protected from moving dislocations. The dislocations were arranged in such a way that there were an equal number of parallel edge dislocations of positive and negative orientation (infinite Taylor lattice) in the veins before the onset of PSB formation. As the stress amplitude rises toward the saturation level, secondary glide occurs, and produces relative shifts in the lattice and thus extensive annihilation of edge dislocations, leading to collapse of the veins to form a PSB. The formation of the dipolar walls in the PSBs begins with a local breakdown of a vein as shown in Figure 2-5. They described a series of events in which a flood of glide dislocations move through the matrix channels annihilating their screw components and trapping their edge components into the wall segments. The wall

segments blocked each other's progress and became stacked up in groups which in turn stopped more walls, resulting in the formation of persistent slip band ladder structures.

Neumann (1986) calculated a theoretical stable configuration of vein and considered the finite Taylor lattices[2] as starting configurations. He concluded that the relaxed and tetragonal Taylor lattices were stable and the changes in polarization between positive and negative dislocations were directly connected to the plastic strain. Figure 2-6(a) shows such a relaxed configuration of a diamond-shaped section of a Taylor lattice in which all the dislocations are at their equilibrium positions at zero applied stress. According to his calculations, when the maximum stress appropriate for a given dipole configuration was exceeded, the veins disintegrated into dipole walls of the type observed in PSBs, which is shown in Figure 2-6(b).

2.1.3. Fatigue Crack Initiation in FCC metals

Since the initiation of cracks in fatigued metals is closely connected with the existence of PSBs, many detailed observations on PSBs profiles and crack initiation behavior have been undertaken. Several methods of obtaining accurate cross sections have been introduced to study the fatigue crack initiation in copper single crystals. Hunsche and Neumann (1986) sectioned fatigue crystals without distortion of the edge using a micro milling technique. Basinski and Basinski (1984) used replication and sectioning technique, and Ma and Laird (1989) used the sharp corner polishing technique. Each of these techniques provides high resolution observations of PSB morphology and initial crack formation. Hunsche and Neumann recorded a number of cracks at various depths across a PSB profile and found that the protrusion[3] geometry was important in

---

2. This lattice is composed of a finite regular planar array of positive and negative edge dislocations and the dislocations in the configurations form a face-centered tetragonal lattice. The tetragonality of the lattice ranges from 1.8 for small (36 dislocations) to 2.2 for large (324 dislocations) sections (Neumann, 1983).
3. A protrusion is a surface uplift (a large extrusion), many micrometers in height (about 7 μm), where a macro-PSB, tens of micrometers wide (about 30 μm) and containing tens of matrix and/or PSB lamellae, emerges at the free surface (Ma and Laird, 1989). It is connected eith excess vacancy production within the PSB.

determining where the most damaging cracks were formed. The height of a protrusion was linearly proportional to the width of the PSB. A crack could occur anywhere in a PSB, but PSB-matrix interfaces were the preferred sites for continued crack growth. Recently Ma and Laird (1989) have made a systematic study of crack growth for fatigue of copper crystals using the above technique. They found that PSBs consist of extrusions and intrusions, that all cracks originated at intrusions, and that the preferred crack sites were isolated intrusions at PSB-matrix interfaces.

Unlike a single crystal, polycrystals contain numerous boundaries and grains with relatively different crystallographic orientation. Thus, cracks can nucleate in a particular grain, while adjacent grains appear to suffer no damage. This may be due to the difference in crystal orientations and the constraint effects of surrounding grains. Also, the initiation of cracks in polycrystalline copper revealed a strong dependence on the strain amplitude used in the test (Figueroa and Laird, 1983). At a high level of strain ($\Delta\varepsilon_p$ > 0.2%), the majority of grains were plastically deformed homogeneously, likewise multiple slip conditions developed in most grains. Intergranular crack nuclei were formed at the intersection of the slip bands with grain boundaries, but were not significantly developed at twin boundaries. Similar observations reported that grain boundaries were the preferred site for both crack initiation and propagation in fatigued copper polycrystals under high plastic strain amplitude conditions (Kim and Laird, 1978).

At a low level of strain ($\Delta\varepsilon_p$ < 0.02 %), the distribution of PSBs varied from grain to grain and the density of the bands was non-uniform across the surface of individual grains. At this level of cyclic plastic strain, PSBs were formed in the most favorably oriented grains and the plastic strain was localized in them. Nevertheless, even for cracks nucleated in PSBs, the preferred crack initiation sites were grain boundaries. This crack nucleation tendency has been explained by the PSB impingement mechanism (Mughrabi *et al.*, 1982). In the model, cracks were expected to nucleate along the grain boundaries

due to the stress concentration between PSBs and grain boundaries caused by piling-up of edge dislocations (PSB-GB crack).

Neumann and Tonnessen (1987) reported that the relative frequency of cracks nucleating at twin boundaries increased with decreasing plastic strain amplitude for polycrystalline copper, and that intergranular crack initiation was insignificant. They rationalized the observation of fatigue crack formation at every other twin boundary utilizing a mechanism which relied on the elastic anisotropy of materials containing twins. For example, the shear modulus of copper varies with direction by a factor of 3.2. In order to ensure strain compatibility at twin boundaries in elastically anisotropic materials, internal stresses must be generated in the vicinity of the boundaries. They considered a stack of lamella twins, where the crystallographic orientation of lamellae changes back and forth from that of the matrix to the twin as one traverses across the boundaries. With the change in orientation, there is also a change in the direction of the internal stresses. The internal stresses act in concert with the resolved stresses arising from the applied loads at every twin boundary. When the resultant stress is of sufficiently high magnitude, a PSB is formed near the twin-matrix interface and eventually develops into a crack. However, the PSB-GB type crack was recently encountered even from low to intermediate amplitudes at room temperature (Liu *et al.*, 1992).

Studies of dislocation structures in polycrystalline copper (Ramussen and Pedersen, 1980; Winter *et al.*, 1981) revealed that PSBs crossed subgrain (twin) boundaries only with very local modifications to the wall structure, but large angle grain boundaries were usually impenetrable. The sudden disappearance of a PSB inside the a polycrystal must be accompanied by a rather large compatibility stress, but these seemed to be accommodated at a grain boundary. Those researchers explained that the incompatibilty of deformation across grain boundaries would be elastically accommodated in bulk polycrystals. Polak and his colleagues (1984; 1992) concluded

that most grains exhibited very similar spatial dislocation structures to that of a single crystal. In their successive studies, they observed regular cell and wall structures within the high amplitude regions and vein structures with a high density of PSBs at the low amplitude region. However, they proposed that PSBs could be interlinked, which means that they were nucleated within one grain and propagated into the suitable slip system of a favorably oriented neighboring grain.

In general, fatigue cracks are nucleated only at PSB boundaries in a single crystal, whereas cracks in polycrystalline materials are initiated either at PSB boundaries (transgranular crack) or at the boundary intersecting PSBs and grain boundaries (PSB-GB crack). In polycrystals, however, PSBs formed within interior grains produce slip that is confined to the individual grain. The large transfer of material causing the creation of a rough topography is possible at surface grains, but not at the interior ones, because of constraints from the surrounding matrix. Therefore, the role of the free surface in crack initiation is very important for both single crystals and polycrystals with regard to their fatigue properties.

2.1.4. Secondary Cyclic Hardening in Fatigued FCC Metals

Secondary cyclic hardening was reported for strain amplitudes above 7×10^{-4} (Polak *et al.*, 1992) and was related to a considerable fraction of secondary slip within a majority of grains in polycrystalline copper.[4] The source for the secondary cyclic hardening of copper specimen was attributed to: (1) build up of the dislocation forest density due to the action of a secondary slip (multiple) system within individual grains, or (2) an activation of slip systems with a lower Schmid factor with continuing strain (Polak and Klesnil, 1984).

---

4. According to the study by Wang and Mughrabi (1984), the secondary cyclic hardening was prominent in the range of around $10^{-3} < \Delta\varepsilon_p < 2 \times 10^{-3}$ and became vague with increasing $\Delta\varepsilon_p$. The distinction between primary and secondary hardening was disappeared when $\Delta\varepsilon_p$ was above 5×10^{-3}.

According to the dislocation study relating the secondary cyclic hardening in copper by Wang and Mughrabi (1984), the gradual formation of a misoriented dislocation cell at the PSB-matrix interface, and their lateral expansion, resulted in a local hardening in single crystals. The secondary cyclic hardening in polycrystals was observed at lower plastic strain amplitudes and slightly earlier than in single crystals. It was claimed that this difference resulted from the variety of grain orientations and the constraint stresses enforced multiple slip at lower amplitudes. The relative amount of secondary hardening with respect to the saturation stress increased with an increase in the plastic strain amplitude.

In another study of polycrystalline copper by Mendez *et al.* (1988), secondary hardening was observed to occur more easily in vacuum than in air, when fatigue tests were conducted under the same constant plastic strain amplitude ($\Delta\varepsilon_p = 6 \times 10^{-4}$). The maximum peak stress in vacuum was slightly higher, and the fatigue life was longer than those in air, whereas the saturation stresses were same whether the tests were carried out in vacuum or in air. This occurrence of secondary cyclic hardening in vacuum was associated with a prolonged fatigue life. Thus, it is deduced that the saturation stress depends only on the constant plastic strain amplitude.

2.2. Effect of Surface Modification on Fatigue Life in FCC metals

The surface of the material is exposed directly to the environment, and mechanical properties, chemical stabilities, as well as electrical properties are affected by the surface physics and chemistry. There is considerable evidence to indicate that the mechanical properties and deformation behavior of crystals can be altered by modifying the surface conditions. The influence of solid surface films on the mechanical behavior of crystal substrates is likely to depend on the elastic properties of both the film and the substrate components, the degree of atomic misfit at the interface, and the residual stresses in the film. Various types of surface modification techniques have been studied

in the context of fatigue, including formation of thin oxide layers, deposition of metal films, ion beam surface modification, and shot peening. Generally, these surface treatments result in surface-strengthening, i.e., increase in the critical resolved shear stress. Patterson and Greenfield (1971) investigated surface alloying effects on the plastic deformation behavior in copper single crystals and explained the nature of the surface-strengthening by nickel and gold thin films. They concluded that both nickel and gold films on copper substrates showed a remarkable surface strengthening effect, which was attributed to solid solution hardening, misfit dislocation networks, and image forces.

The surface condition of the material is a very important factor in fatigue since the surface is often the preferred site for fatigue crack initiation. The important role of the surface in fatigue was demonstrated by the observation that when a specimen was fatigued for a large fraction of its life, and its surface then removed by electropolishing, the specimen showed a remaining fatigue life as long as that of a virgin specimen. Fatigue life is also generally higher in a vacuum. In general, the increase in fatigue crack initiation resistance by surface modification is due to homogenization of cyclic plastic deformation, which leads to lower surface damage accumulation rates, or to effective suppression of slip band penetration to the free surface. Thus, a variety of surface modifications have been developed, such as surface rolling or shot peening, to supply a compressive stress on the surface or surface hardening.

Chen and Starke (1976) investigated the effect of stacking fault energy (SFE) of ion plated surface layers on fatigue life. In experiments on copper substrates, nickel was used as the high SFE coating, silver as the low SFE coating. Copper itself was used to investigate the effect of interface imperfections. They concluded that fatigue crack initiation was sensitive to the topography of the slip bands on the surface, which varied depending on differences in the stacking fault energies of the surface layer and bulk material. Nickel layers produced coarser slip steps and reduced fatigue life, whereas the opposite effect was observed in silver films. Copper self-coated specimen did not show

any appreciable change as compared to the uncoated ones. Lowering SFE at the surface, it was argued, reduced the incidence of cross slip and resulted in more homogeneous and reversible slip, causing a slower accumulation of surface damage.

Greenfield and Purohit (1980) studied the influence of both discrete and diffused surface layers on the initiation and movement of dislocations, in fatigue tests performed on copper specimens with nickel, zinc, silver, gold, and aluminum coatings. In this study, they considered the relative shear modulus of the surface with respect to the substrate, along with the stress and strain for yielding at the surface. The regions of initiation of plastic deformation depended on the elastic stiffness of the surface with respect to the substrates and the magnitudes of the stress and strain. This analysis showed that the increased yield strength of the surface layer is more important in enhancing fatigue life than the modulus effect. If the surface film is harder than the substrate, then the substrate deforms plastically while the surface layer behaves still elastically, then the fatigue damage accumulation rate will slow during cyclic deformation.

Grummon *et al.* (1988) studied the effect of surface microalloying by ion beam modification on fatigue crack initiation, using direct ion implantation by krypton or ion beam mixing of aluminum, in polycrystalline nickel. This study pointed out that a surface film which is strong and more elastically compliant than the substrate, might be expected to both block the egress dislocations and inhibit penetration of slip bands, and also resist plastic deformation itself, and therefore suffer a low rate of fatigue damage accumulation. Grummon *et al.* attributed the increased elastic limit of the material in the modified surface layer to solid solution hardening, the high defect population induced by radiation, and extremely fine grain size of the surface modified area.

It has been shown that direct ion implantation and ion beam mixing techniques can be effectively used for improving fatigue life of materials, by shallow surface modification. The approach has the capability to control thickness, composition, and

structure of the modified volume of the material. In studies on fatigue behavior of boron and nitrogen ion implanted into nickel polycrystals (Hohmuth *et al.*, 1985) and copper polycrystals (Mendez *et al.*, 1987), it was found that increasing the implantation dose reduced the density of slip bands at the surface, and increased the fatigue lifetime. Additional experiments, however, demonstrated that the hardening of the surface layer by ion implantation of interstitial species did not improve fatigue resistance. Favorable effects did result, however, from implanting with the low stacking fault energy substitutional species, which promoted better slip reversibility during cyclic loading.

Carbon ion implantation in a nickel chromium alloy improved fatigue life by solid solution strengthening and by the development of high compressive stress due to the presence of the interstitial carbon. However, carbon implantation in copper and stainless steel shortened the fatigue life because of slip line coarsening, which was observed on the surface by SEM, that causes stress concentration and hence decreased fatigue life. But they did not mention any plausible reasons such as a residual stress effect on the surface or stacking fault energy change related to the surface modification (Sleeswyk *et al.*, 1980).

Fatigue properties were improved in polycrystalline nickel with microalloyed Ni-Al surface layer created using ion beam mixing and direct aluminum ion implantation (Grummon *et al.*, 1989). Self-implanted nickel demonstrated that the microcracks were formed along PSBs and that fatigue features were not altered. However, microalloying the surface with aluminum increased surface hardness and inhibited the formation of surface PSB features. The crack initiation mode was changed from transgranular to intergranular, and the change was usually accompanied by suppressing PSB penetration to the surface. Also, surface residual compressive stress, which may be caused by direct implantation with larger atom species, produced longer fatigue crack initiation life. The increased fatigue life may result from lowering of stacking fault energy on the surface, causing finer and planar slip, resulting in a delay of crack initiation.

In summary, surface effects in fatigued materials are very important since, in most cases, fatigue failure originates from fatigue cracks at the surface. These cracks initiate at the sites of surface roughness which has developed a notch-peak geometry as a result of cyclic slip irreversibility. Particularly for fcc case strain localization in PSBs can exceed the surrounding matrix strain value by a factor of 100. Thus, various approaches to surface modifications have been carried out for the purpose of inhibiting or delaying the fatigue crack initiation on their surface regions. According to the finite element study by Meyers and Grummon (1990), however, the surface layer above underlying active PSBs should possess an elastic limit on the order of 1%-1.5% of shear modulus in order to withstand localized strain during cyclic deformation. Therefore, it is believed that PSB shear displacement will force the surface film in its plastic range so that the improvement of fatigue life by such conventional surface films, which were used in various surface modification techniques in this section, are limited.

2.3. Transformational Superelasticity

Considering plastic strain localization during fatigue, a promising surface coating system to withstand such a large strain is superelastic alloys. Superelasticity results in unique stress-strain behavior, which exhibits large anelastic strain associated with a reversible stress-induced martensitic transformation, and thus superelastic alloys may show extraordinarily long fatigue life under high strain amplitude loading. Especially, fatigue life for NiTi alloy can be extrapolated to over 10^8 cycles at strain amplitudes approaching 1% (Melton and Mercier, 1978; 1979), which is the strain associated with PSB shear in fcc metals. Therefore, surface coatings of NiTi alloys, which are able to accommodate large strains without accumulating severe slip damage, are suggested to be an effective way of delaying fatigue crack nucleation in metals.

In the following section, general features of thermoelastic martensitic transformation, including superelasticity, the shape memory effect, and stress-induced

martensite, will be discussed. Following this, phase transformation behavior in NiTi alloys and factors which affect these transformations, will be presented in detail. Physical and mechanical properties of NiTi alloys will also be reviewed.

2.3.1. General Aspect of Martensitic Transformation and Superelasticity

Martensitic transformations are diffusionless phase transformations in which atoms are cooperatively rearranged into a new and more stable crystal structure without changing the composition of the matrix. Since no long-range atomic movement is involved, the progress of the martensitic transformation does not depend on time, but on temperature. On cooling, the high temperature phase (austenite) starts to transform to the low temperature phase (martensite) at a temperature designated as M_s, and finishes at a lower temperature, M_f. On heating, martensite starts to transform to austenite at a temperature designated as A_s and finishes at a higher temperature, A_f. In the temperature range between M_s and M_f on cooling (and between A_s and A_f on heating), austenite and martensite phases coexist. The primary driving force for the transformation is the free energy difference between the two phases. However, a strain energy is accumulated in the lattice during the transformation which resists further progress of the transformation unless a higher driving force is supplied by a subsequent decrease in temperature.

Martensitic transformations can be divided into two categories, thermoelastic and non-thermoelastic transformations. For materials which follow the non-thermoelastic transformation the martensite-parent interfaces are relatively immobile. Therefore, when the martensite is formed once, the interface does not return back to the parent phase after heating and the austenite phase must be renucleated. However, in thermoelastic transformation the interface of the martensite-parent undergoes reversible movement during heating or cooling due to the balance between thermal and elastic effects. Thus, the occurrence of a thermoelastic martensitic transformation has certain requirements: (1) ordered cubic parent phase, (2) small volume change during martensitic transformation,

and (3) most of its deformation occurs by intervariant boundary motion before slip. Such thermoelastic martensitic transformations give rise to the shape memory effect. In NiTi alloys, martensite can be deformed up to 5 to 10%, by reorientation of martensite variants without activating dislocation slip. The plastic strain resulting from the rearrangement of martensite variants at low temperature is recoverable on heating above A_f, because each martensite variant reverts to austenite in the original orientation.

Shape memory alloys can have another unique mechanical property called the superelastic effect (SE). Phenomenologically, within a specific temperature range ($A_s < T < M_d$[5]) in the superelastic effect, material suffering large anelastic strain on loading can revert to its original shape upon unloading. Figure 2-7 describes the relationship of these effects with temperature and stress. Superelastic effect requires a reversible stress-induced martensite transformation. In other words, the application of stress has a similar effect on the transformation as a decrease in temperature (Swalin, 1972). The stress needed to produce stress-induced martensite (SIM) increases linearly with temperature. The relationship between stress and the M_s can be specified as follow. When the state of a material which has been elongated or shortened, is considered, the conventional enthalpy (H) and free energy (G) have to include the mechanical work (i.e. thermodynamical effect of stress). Therefore,

$$H = U + PV - Fl \qquad (2.1)$$

$$G = U + PV - TS - Fl$$

where F is the force applied to the specimen, l is specimen's length, and the other symbols have the usual meanings. If the free energies of the austenite and martensite

5. The temperature at which M_s equals the critical stress for slip in the martensite is designated as M_d.

phases un

ransition

For an ir

following

From Eq

upon rea

where Δ

(A→M

enthalp

temper

cross se

let ΔI

express

phases under stress are G^A and G^M, then when both phases are in equilibrium at the transition temperature, ΔG for the reaction is zero.

$$G^A = G^M \quad \text{or} \quad dG^A = dG^M \tag{2.2}$$

For an infinitesimal change in temperature and force under constant pressure, the following relations can be obtained:

$$dG^A = - S^A dT - l^A dF \tag{2.3}$$
$$dG^M = - S^M dT - l^M dF.$$

From Eq. (2.2)

$$- S^A dT - l^A dF = - S^M dT - l^M dF \tag{2.4}$$

upon rearrangement of the above equation:

$$\frac{dF}{dT} = - \frac{\Delta S^{A \rightarrow M}}{\Delta l^{A \rightarrow M}} \cong - \frac{\Delta H^{A \rightarrow M}}{T_o \Delta l^{A \rightarrow M}} \tag{2.5}$$

where $\Delta S^{A \rightarrow M}$ and $\Delta H^{A \rightarrow M}$ are the entropy and enthalpy changes of the transformation ($A \rightarrow M$) respectively, and it was assumed that the changes in entropy ($\Delta S^{A \rightarrow M}$) and enthalpy ($\Delta H^{A \rightarrow M}$) during the transformation are constant over a fairly wide rage of temperatures. T_o is the transformation temperature without the applied stress. If the cross sectional area of the crystal is A and the volume of the crystal is V, then $F/A = \sigma$; let $\Delta l / l = \varepsilon$ and $T = M_s$. Thus, the linear variation in stress to induce martensite can be expressed by the Clausius-Clapeyron equation, which is written as

$$\frac{dF}{dM_s \cdot A} = -\frac{\Delta H^{A\rightarrow M}}{T_o \Delta l^{A\rightarrow M} \cdot A} = -\frac{\Delta H^{A\rightarrow M} \cdot l}{T_o \Delta l^{A\rightarrow M} \cdot V}$$

$$\therefore \frac{d\sigma}{dM_s} = -\frac{\Delta H^{A\rightarrow M}}{V \cdot T_o \varepsilon^{A\rightarrow M}} \qquad (2.6)$$

where σ is the applied stress and $\varepsilon^{A\rightarrow M}$ is the strain associated with the transformation and $\Delta H^{A\rightarrow M}$ is now the volume-based enthalpy (J/m^3 = Pa). However, superelastic effects cannot be expected if the temperature of the material is above M_d, in which case slip occurs in the austenite before induction of the martensite phase. If the temperature of the material is below A_s, SME, rather than superelasticity, can be expected due to the stabilization of the martensitic phase at that temperature.

2.3.2. Displacive Transformation in NiTi Alloys

2.3.2.1. Transformation Behavior in Near-Equiatomic NiTi Alloys Near-equiatomic NiTi alloys exhibit unique properties, the shape memory and superelasticity effects associated with the thermoelastic martensitic transformation. For NiTi alloys, three kinds of phases can occur during the transformations, the B2 (CsCl structure) parent phase, rhombohedral R-phase, and monoclinic (B19') martensite phase. Fully annealed binary NiTi alloys transform directly from the B2 parent phase to the monoclinic B19' phase. However, thermally cycled or thermo-mechanically treated NiTi alloys transform in two-steps, namely from the B2 to R-phase and then to B19' phase. Upon cooling, the transformation occurs in the following sequence: B2 parent phase → Incommensurate phase at T_r' → Commensurate phase (R) at T_r → monoclinic (B19') martensite phase.

The R-phase transformation was first treated as a precursor phenomenon to the martensitic transformation. Later investigation showed however, that the R-phase transformation does not necessarily occur prior to the martensitic transformation. Hwang *et al.* (1983) interpreted R-phase transformations in $Ni_{50}Ti_{47}Fe_3$ alloy as an

incommensurate-to-commensurate charge density wave transition. They explained that the B2 parent phase first underwent a second order transition to an incommensurate state associated with a rhombohedral distortion that produces 1/3 (110) and (111) reflections. The onset temperature of the B2-to-incommensurate phase transition was designated as T_r'. The extra superlattice reflections in fact were not located in the exact 1/3 positions (thus the phase 'incommensurate'), and their intensities kept increasing on cooling. A subsequent first order transition occurred involving a structural change from a distorted incommensurate B2 phase to a rhombohedral one causing the extra reflections to lock into precise 1/3 positions. The onset temperature of the incommensurate-to-commensurate phase transformation was defined as T_r. The R-phase transforms to the martensite phase at M_s on further cooling. The shape memory effect and superelasticity arise in both B2↔R and R↔B19' transformations (Miyazaki and Otsuka, 1986).

Physical properties, such as electrical resistivity, elastic modulus, damping capacity, and magnetic susceptibility, change during phase transformations in NiTi alloys, and transformation temperatures in this alloy may be determined by measuring any of these characteristics. The change in electrical resistance with temperature and the measurement of the latent heat during phase transformations are widely used to monitor the transition temperatures. Differential scanning calorimetry (DSC) curves for the transformation show the exothermic peaks on cooling and the endothermic peaks on heating during the phase transformations.

The change in resistivity of NiTiCu alloys, which undergo a distinct two step transformations both on cooling and heating, is illustrated in Figure 2-8. On cooling from high temperature where the parent (austenite) phase is stable, the electrical resistance slightly decreases first and then starts to increase, where the R-phase formation occurs from the B2 phase, due to the negative temperature coefficient of electric resistivity in the R-phase. A sharp increase in resistance occurs at T_r' and increases further beyond T_r until M_s is reached. At the M_s temperature, the resistance starts decreasing until M_f is reached,

after which the rate of decrease becomes gradual on further cooling. On heating from a very low temperature, where only the martensite phase exists, the resistance increases gradually up to the A_s temperature where the curve changes its slope and then increases until A_f is reached, where B19'→R transformation will finish. The resistance decreases until the R→B2 transformation occurs, and then slight increases is followed on further heating. Hereinafter B2↔R and R↔B19' transformations are named R-transformation and martensitic transformation respectively.

2.3.2.2. Effect of Composition on Transformation Temperatures The nickel-titanium phase diagram, which is illustrated in Figure 2-9, shows stoichiometric β-NiTi phase at high temperature with a steep solvus line on Ti-rich side. An eutectoid decomposition from β-NiTi phase to Ti_2Ni + Ni_3Ti at 903 K has been proposed. However, Wasilewski *et al.* (1971) proposed that the β-NiTi phase remained a stable phase down to room temperature, with a very narrow stoichiometric range. On the Ni-rich side, Nishida *et al.* (1986) and Kim *et al.* (1986) reported the existence of metastable phases other than Ni_3Ti, such as Ti_2Ni_3 and Ti_3Ni_4. But the equilibrium phase diagram on the Ni-rich side for the low temperature range is not well established and controversy on the composition and structure of those phases exists. Most researchers accept that the microstructures of NiTi alloys are primarily single phase, with small amounts of other phases distributed throughout the matrix. These phases can change the composition of the matrix and thus affect the transformation temperatures in this alloy system.

Transformation temperature changes are extremely sensitive to the alloy composition, especially on the Ni rich side of NiTi alloy systems, which is shown in Figure 2-10. For example, the M_s temperature decreased linearly with increasing Ni concentration, at about 100 K per 1 at.% of Ni, for alloys with composition of 49.6 to 52.0 at % of Ni after annealing between at 773 K and 923 K (Nishida *et al.*, 1984; Shugo *et al.*, 1985). However, the change in M_s temperature was relatively insensitive on the Ti

rich side due to the low solubility of Ti and Ti_2Ni second phase distributed around the B2 grain boundary. The quantity of Ti_2Ni particles did not affect the transformation temperature (Lin and Wu, 1992). The compositional accuracy required for Ni-Ti in fact exceeds uncertainty levels commonly found in routine chemical analysis. Therefore, in most cases for quality control purposes the transformation temperatures themselves are measured, rather than the chemical composition (Melton, 1990).

Besides the dependence of transformation temperatures on Ni concentration, there are other factors which influence the transformation behaviors in NiTi alloy. These will be reviewed briefly in the following sections.

2.3.2.3. Effect of Heat Treatment on Transformation Temperatures As mentioned in the previous section, stable Ti_2Ni and $TiNi_3$ precipitates with metastable phases, such as Ti_2Ni_3 and Ti_3Ni_4, can be formed in NiTi alloys. Formation of these precipitates changes the composition of the matrix resulting in a shift of the transformation temperature.

Recent study by Xie *et al.* (1990) stated that the Ti_3Ni_4 precipitate in aged specimens had good coherence with the matrix and an internal stress field was built around it. Ti_3Ni_4 precipitate formation caused a widening of the R-phase range and a significant decrease of M_s temperature by the effect of the internal stress fields at the coherent boundary between precipitates and parent phases. Such dispersed fine Ti_3Ni_4 precipitates affected the crystallographic direction of the martensite and thus a single (or strongly preferred) variant martensite could be formed in a parent grain. It was also reported that most Ti_2Ni precipitates were segregated at the grain boundaries and fine Ti_3Ni_4 precipitates were distributed within the grains in annealed NiTi thin films (Busch *et al.*, 1990; Chang, 1993; Ishida *et al.*, 1993).

In addition, the dispersed precipitates raise the strength of the austenite phase by precipitation hardening resulting in an increase in the critical stress for slip in NiTi alloys.

It is important to raise the critical stress for slip in order to stabilize the superelasticity characteristics against cyclic deformation.

In NiTi alloys, the transformation temperatures, recovery strain, and yield stress, which are associated with the formation of precipitates, will be affected by heat treatment parameters, such as aging temperature and time, cooling rate, and post annealing after cold working. Details of these effects will be reviewed briefly.

(1) Aging effect: Dependence of the transformation temperature on the aging temperatures was studied by Miyazaki *et al.* (1982) and extensively by Nishida and his coworkers (1984, 1988). In these studies, all Ti-51.0 at.% Ni alloys were solution treated at 1273 K and aged at various temperatures for different times and then quenched into ice water. The highest transformation temperatures were obtained from the alloys aged between 673 K and 773 K for 1 hour, and transformation temperatures were lowered with increasing aging temperatures. The effect of aging time on transformation was compared between 1 hour and 50 hours for aged alloys with aging temperatures of 673 K and 773 K. The longer aging time displayed a slightly higher transformation temperatures for each aging temperature. Both the 1 hour-773 K and 50 hour-673 K specimens revealed similar behavior due to the similarity in dispersion density and size of the precipitates. Thus, the transformation temperatures are severely affected by precipitate formation which are related to aging time and temperature.

(2) Cooling rate: NiTi alloys used for transformation temperature studies by Nishida *et al.* (1986) were solution treated at high temperatures (1273 K) and aged at various temperatures before finally quenching to a low temperature. Systematic work was done for Ti-50 at.% Ni and Ti-52 at.% Ni. The M_s temperatures was 327 K for quenched Ti-50 at.% Ni and below liquid nitrogen temperature for quenched Ti-52 at.% Ni. Time-Temperature-Transformation (TTT) curves were constructed for Ti-52 at.% Ni from specimens that experienced different cooling rates: as-quenched, which was fast, and furnace-cooled, which was slow. The precipitation sequence for various aging

processes was investigated. $TiNi_3$ and Ti_2Ni_3 precipitates formed in slow cooled Ti-52at.% Ni alloy but, unfortunately, this work did not treat the influence on transformation temperatures. They also concluded that neither eutectoid nor peritectoid reactions took place in non-stoichiometric Ti-52 at.% Ni. The precipitation sequence in Ti-52at.% Ni alloy was expressed as TiNi → Ti_3Ni_4[6] + TiNi → Ti_2Ni_3 + TiNi → $TiNi_3$ + TiNi, where Ti_3Ni_4 and Ti_2Ni_3 are metastable phases. The formation of such precipitates causes compositional changes in the matrix. For example, higher Ti concentration can be expected due to preferential Ni consumption.

(3) Post annealing effect after cold working: The mechanical and shape memory properties critically vary with heat treatment after cold working. One prominent effect of cold working combined with heat treatment is the separation of the R-phase transformation and martensitic transformation in near equiatomic NiTi alloys. Depending on the post annealing temperature and the amount of cold working, the transformation temperatures can change as a consequence of the dislocation or precipitate structure which might strongly impede the movement of martensite interfaces and, therefore, depress the M_s temperature significantly. The effect of the amount of cold work on the transformation temperatures without subsequent annealing was studied by Lin *et al.* (1991) using several methods such as internal friction, shear modulus measurement, hardness, and TEM observation. The B2→B19' transformation temperature on cooling was decreased but reverse transformation (B19'→B2) temperature on heating was increased with increasing cold work. They concluded that martensite phase stabilization at room temperature could be provided by cold working. With higher amount of cold working the martensite phase became more effectively stabilized. The deformed martensite structure, containing induced dislocations was considered to be responsible for the martensite stabilization. Legresy *et al.* (1991) provided more detailed information for

---

6. Ti_3Ni_4 precipitate phase was expressed as $Ti_{11}Ni_{14}$ in several other reports but based on the crystal structure Ti_3Ni_4 is more approprate and this phase denotation was used in later report by Nishida.

ransformat

M_s decreas

2.3

s great int

element,

substitute

particularl

most case

increased

the interr

temperatu

T_t temper

be done

character

Accordir

was as fo

substitut

transform

by Nam

at.% Cu

These r

tempera

tempera

wider w

[7] It has
temperatu
(Funakubo

transformation behavior, and showed that A_f temperature increased, whereas A_s, M_f, and M_s decreased with increasing cold work.

2.3.2.4. Effect of Third Element Additions and Impurities There is great interest in the phase transformation behavior of NiTi alloys when a third metallic element, especially a 3-d transition metal, such as Co, Fe, Cu or Cr, is partially substituted for nickel. These substitutions affect the transformation temperatures, particularly M_s temperature, by different degrees depending on the substituted species. In most cases of such substitution with Co, Fe, or Cr, the intermediate phase[7] region is increased by suppressing M_s temperature more rapidly than the starting temperature of the intermediate phase. For example, Fe substitution for Ni shifted both M_s and T_r temperatures lower; but the drop of M_s temperature was three times greater than that of T_r temperature (Hwang *et al.*, 1983). However, up to 30 at% Cu substitution for Ni could be done without changing the M_s temperature. In addition, the shape memory characteristics were still exhibited in NiTiCu ternary alloys (Melton and Mercier, 1978). According to their investigation, the transformation sequence for $Ti_{50}(Ni_{40}Cu_{10})$ alloy was as follows: cubic B2 → orthorhombic B19 → monoclinic B19'. However, if the substituted Cu for Ni exceeded about 10 at.% , the alloy showed only one stage transformation: cubic B2 → orthorhombic B19. Recently, more studies were undertaken by Nam and his colleagues (1990) of Cu substitution in NiTiCu alloys, especially for 10 at.% Cu, were compared with binary NiTi alloys under constant thermal cycling test. These researchers observed that B2→ orthorhombic B19 transformation starting temperature increased slightly, whereas B19→ monoclinic B19' transformation starting temperature decreased. Thus, the temperature region where B19 was stable became wider with increasing Cu content. But, for NiTiCu alloy in which Cu concentration was

7. It has been reported that the transformations were clearly produced by the two-stage processes: high temperature phase → intermediate phase → low temperature phase due to the substitution of Co, Fe, and Cr (Funakubo, 1984)

above 12.5

transformat

The

content. O

approxima

above 700

was

M_s

where X_o

relative in

the preser

brittlenes

introduce

M_s tempe

during pr

transform

by hydro

the shap

al., 199

occurs w

the shap

phase. E

8 Hydro

caused hig

after remo

above 12.5 at.%, only the B2→B19 transformation was favorable while the B19→B19' transformation was suppressed.

The transformation temperatures in NiTi alloys are also sensitive to impurity content. Oxygen causes a decrease in M_s temperature, which changes monotonically by approximately 100 K/at.% with increasing oxygen concentration from an alloy annealed above 700 K (Shugo *et al.*, 1985). The experimental equation reported from that study was:

$$M_S/K = (351.4 \pm 0.5) - (92.63 \pm 0.93) \times (X_O / \text{at.}\%) \qquad (2.7)$$

where X_O = 0.13 - 1.06 at.%. Most oxygen was bound in Ti_4Ni_2O, and resulted in a relative increase in nickel concentration. In addition, the Ti_2Ni phase was stabilized by the presence of oxygen in this alloy system, and the contamination by oxygen increased brittleness (Nevitt, 1960). Other interstitial impurities, such as carbon, which is easily introduced during melting from a graphite crucible, and nitrogen, have a similar effect on M_s temperature, but to a lesser degree, due to the preferential consumption of titanium during precipitation of TiC, Ti_2Ni, and Ti_4Ni_2N. However, hydrogen has little effect on transformation temperatures[8] or mechanical properties in NiTi alloy even though hydride by hydrogen absorption may form (Shorshorov *et al.*, 1985; Asaoko *et al.*, 1992). Also, the shape recovery was decreased with presence of small amount of hydrogen (Wade *et al.*, 1990).

2.3.2.5. Self-Accommodation and Surface Relief Shape change occurs when one martensite plate is formed within a single crystal of the parent phase and the shape change is manifested directly as changes in the external shape of the parent phase. Even though the parent phase consists of a single crystal, a number of martensites

8. Hydrogen-induced shape memory effect, which was believed to be the result of surface hardening, caused higher tranformation temperatures by hydrogen charging on NiTi alloy but the change disappeared after removing the surface layer (Wade *et al.*, 1990).

with diffe

are called

displacer

crystals t

strain en

accompa

variants.

Miyazak

a typica

formed

strain m

the shap

such a

resultin

accomm

factor u

studied

fundam

variant

there w

axes ca

one an

diffusi

is an e

free su

with different habit plane indices. These martensites with different habit plane indices are called 'variant'. During a martensitic transformation, each martensite plate causes a displacement resulting in an increase in the total strain energy. However, martensite crystals in thermoelastic alloys, since martensite variants are created to minimize the total strain energy through a twinning process, mutually reduce the transformation strain accompanying a multi-variant combination during the formation of the martensite variants. This effect is called 'self-accommodation'. According to the observation by Miyizaki *et al.* (1989), the martensitic transformation in NiTi alloys occurred by forming a typical triangular morphology consisting of three variants and these three variants formed plate groups clustered about one of the $\{100\}_{B2}$ poles. The calculated shape-strain matrix for the overall triangular morphology showed that the shear components of the shape-strain were very small. They found that there were 16 groupings which formed such a triangular self-accommodation morphology about each of the $\{100\}_{B2}$ poles, resulting in 48 possible combinations in all to form such triangles. The ability of self-accommodated martensite to be deformed by means of detwinning is a fundamental factor underlying shape memory properties.

Self-accommodation mechanisms of the R-phase in NiTi alloys have been studied by optical and electron microscope observations (Fukuda *et al.*, 1992). The fundamental unit of the self-accommodation in R-phase of NiTi alloys consisted of four variants. The four variants self-accommodated around one of the $<001>_{B2}$ axes, and there were 6 groupings self-accommodation morphology around each of the $<001>_{B2}$ axes canceling their shape deformation each other. These variants were twin related to one another and there were two types of twin relations.

A martensitic transformation is accompanied by various characteristics like diffusionless character, surface relief, and the presence of many lattice imperfections. It is an evident feature of a martensitic microstructure that a surface relief is produced on a free surface of bulk materials. The surface relief is not irregular, and the angle of incline

in the uphe

et al., 197

transforma

between v

formation

a small tri

phase was

al., 1992)

features of

2.4. Phys

2.4.1. Def

Al

those of

transform

that of m

believed

high mob

can be de

dislocatio

2.

behavior

test temp

A_s and A

2-12. If

martensi

in the upheaval has a definite value which depends on the crystal orientation (Nishiyama *et al.*, 1978). Optical micrographic observations have been performed to observe the transformation morphology and to determine the habit planes and junction planes between variants in self-accommodating morphology. The surface relief due to the formation of B19' martensite has been described as a dominance of three variants forming a small triangular grouping consisting of three variants (Miyazaki *et al.*, 1989) and the R-phase was characterized by saw-tooth like and long straight band morphology (Fukuda *et al.*, 1992) in bulk NiTi alloys, which is illustrated in Figure 2-11. These are typical features of self-accommodation of B19' martensite and R-phase in NiTi alloys.

2.4. Physical and Mechanical Properties of NiTi Alloys

2.4.1. Deformation of NiTi Alloys

Almost all physical properties of austenite, except the density, are different from those of martensite, due to a significant change in crystal structure during the transformation. The yield strength of TiNi austenite is about two to six times higher than that of martensite, and its elastic modulus has the lowest value near M_s temperature. It is believed that the low yield strength of thermoelastic martensite is due to the relatively high mobility of the boundaries between neighboring variants. In NiTi alloys, martensite can be deformed up to 5 to 10% by reorientation of martensite variants without activating dislocation slip.

2.4.1.1 Stress Strain Behavior in NiTi Alloys The stress strain behavior of NiTi alloy can be generally divided into five different types depending on the test temperatures (as normalized to the canonical transformation temperatures: M_s, M_f, A_s, and A_f). The five types of the stress-strain curves for NiTi alloy are shown in Figure 2-12. If the deformation temperature is below M_f (Type I), the alloy is entirely in a martensite phase so that deformation proceeds according to the migration of the

intervariant boundaries within the martensite phase. When the test temperature is increased to above M_f, but is below M_s (Type II), the alloy deforms because of stress-induced growth of martensite phase fraction, and continues with the same mechanism as Type I. In the temperature range between M_s and A_f (Type III), the deformation is only by formation of stress-induced martensite. In Type IV, which temperature range is between A_f and M_d, superelastic characteristics are revealed. Here, the martensite phase forms under stress, and disappears when the stress is released. Above M_d (Type V), the plastic deformation in the austenite phase occurs before stress-induced martensite is formed, because the critical stress for slip in the austenite is lower than the stress to induce martensite.

The stress strain behavior of a NiTi alloy as function of temperature has been extensively studied by Miyazaki *et al.* (1982). In the study of bulk NiTi alloy, superelastic strain recovery (without supplying external heat) was found at test temperature about 15 K above A_f. Recently, the stress strain behavior of NiTi thin film alloy produced by d.c. magnetron sputtering were obtained at various test temperatures by Hou and Grummon (1995). Results are shown in Figure 2-13. Most of characteristics of the thin film were similar to those of bulk NiTi alloys. The results showed that the stress for inducing martensite obeyed Clausius-Clapeyron relations, and the full superelasticity was found at about 30 K above A_f. It is worth noting that the slope of the loading curve before stress induced martensite has formed is higher than that of the unloading curve. The formation of stress-induced martensite results in the differences of Young's modulus ($E_A > E_M$) in the films between the loading and unloading stages. The amount of unrecovered strain, which was designated as ε_u in Figure 2-13, increased when the test temperature deviated from 333 K, which is 28 K above A_f, in both sides: due to occurrence of slip at higher temperature and stabilization of stress induced martensite at lower temperature. This higher temperature for full recovery in the film may be attributed to the internal defects during deposition process.

2.

show an

section 2

a superc

behavior

binary

transfor

1966).

temperc

found t

occurri

rearran

applied

marten

tensile

critica

increas

test te

conclu

exhibi

defor

auste

marte

was a

9. Th
to the

2.4.1.2. Two Stage Yielding in NiTi Alloys NiTi alloys usually show an R-phase transformation prior to the martensitic transformation, as described in section 2.3.2. R-phase transformation is accompanied by rhombohedral distortion so that a superelasticity effect associated with R-phase can be observed. The mechanical behavior related to R-phase formation by an external applied stress was studied for NiTi binary alloy and $Ni_{50}Ti_{47}Fe_3$ ternary alloy which exhibited a well-defined R-transformation and a subsequent martensitic transformation (Miyazaki and Otsuka, 1984; 1986). Miyazaki and Otsuka (1984; 1986) carried out tensile tests over a wide temperature range to study stress-induce transformation associated with the R-phase and found that the first yielding occurred at low stress (~50 MPa), with subsequent yielding occurring at higher stress (above 200 MPa). The first yielding was attributed to the rearrangement of R-phase variant (or variants), which was more favorable under the applied stress, whereas the second yielding was attributed to the stress induced martensitic transformation. The first stage yielding was confirmed by well-controlled tensile tests, where the stress was sufficiently low to avoid the second stage yielding. The critical stress to form R-phase was minimal at T_r temperature and increased with increasing temperature above T_r temperature. The stress-strain curves associated with the test temperature for the alloy were classified as shown Figure 2-14. These researchers concluded that both the R-phase transformation and the martensitic transformation exhibited the shape memory effect and the transformational superelasticity.[9]

2.4.1.3. Plastic Deformation of NiTi Alloys Recent study of plastic deformation of NiTi alloys (Miyazaki *et al.*, 1991) showed that the stress for slip in austenite phase was almost independent of the temperature, whereas the stress in martensite phase decreased with increasing temperature. The elongation of the martensite was always larger than that of austenite phase. Thus, one can combine the relation of the

9. These phenomena were more clearly observed in NiTi binary alloys than in NiTi Fe ternary alloys due to the high critical stress for slip in binary alloys (Miyazaki and Otsuka, 1986).

stresses for

phases with

2.4.

grain size

1984). Su

the polycr

important

decreased

superelas

fine grain

sequentia

martensi

size decr

grain bo

have sh

substrat

fine gra

0.02 - 0

nearly c

2.4.2. F

E

exceptio

martensit

could be

several N

stresses for slip in martensite and austenite phases and for inducing martensite and R-phases with elongation as a function of temperature, which is illustrated in Figure 2- 15.

2.4.1.5. Grain Size Effect on Superelasticity in NiTi Alloys The grain size of NiTi alloy affects the superelasticity effect in NiTi alloys (Saburi *et al.*, 1984). Single crystal NiTi alloys did not display superelasticity at any temperature but the polycrystalline alloys exhibited complete superelasticity behavior above A_f. It is important to note that the superelasticity becomes more pronounced as the grain size is decreased, indicating that the reduction of the grain size is very effective in improving superelasticity, which is shown in Figure 2-16. In a later work (Motohashi *et al.*, 1991), fine grained NiTi alloy was produced by thermomechanical treatment which involved sequential stages of annealing and cold rolling. Motohashi *et al.* found that the martensitic transformation temperatures, particularly M_s temperature, increased as grain size decreased. This shift in M_s temperature to higher temperature was attributed to the grain boundaries as nucleation sites for the martensitic transformation. Recent studies have shown that when depositing NiTi with d.c. magnetron sputtering, heating the substrate to temperature between 598 K and 723 K produced a deposit with extremely fine grain size (Hou and Grummon, 1995). They have observed grain size on the order of 0.02 - 0.05 μm and the films have shown classical transformational superelasticity, and nearly complete strain recovery at temperatures above A_f.

2.4.2. Fatigue Properties of Near-Equiatomic NiTi Alloy

Early studies of the fatigue of NiTi alloys by Melton and Mercier (1979) showed exceptionally large accumulated strains to failure when the alloy was tested either in the martensitic condition, or in the austenitic condition at temperatures where martensite could be stress induced during low cycle fatigue measurement. After investigating several NiTi alloys which had different M_s temperatures, fatigue life was found to

increase with decreasing M_s temperature. A significant finding in this work was that superelastic deformation lead to high fatigue life for NiTi alloys in both the austenitic and fully martensitic conditions. When fatigue life was plotted against the strain amplitude for different alloys, the longest fatigue life was obtained at about 15 °C above M_s temperature, but the fatigue life decreased at higher temperatures, as shown in Figure 2-17.

In a later work by Miyazaki *et al.* (1989), instead of the tension-compression cycling used by Melton and Mercier, loading-unloading (tension-tension) cycling at various temperature was adopted. The critical stress for inducing martensite increased with the test temperature and the fatigue life of the alloys was improved with increasing test temperature, which is shown in Figure 2-18. Here, all test temperatures were above A_f and below M_d, which was presumed to be 130 K above A_f. In another study (Miyazaki *et al.*, 1986), it was found that the critical stress for inducing martensite gradually decreased, the superelastic strain hysteresis loops became smaller, and residual strain increased with increasing cycles during cyclic loading-unloading of NiTi alloys. But all these values became insensitive to cycling with increasing cycle number and maintained a steady state with respect to superelasticity characteristics. Superelasticity characteristics can also be influenced by heat treatment (different aging temperature, time, and annealing histories) and mechanical treatment (cold working), all of which can raise the critical stress for slip in NiTi alloy (Tadaki and Wayman, 1980). The combined effects of precipitation hardening and hardening due to high density of dislocations can be effective in stabilizing superelasticity characteristics against cyclic deformation.

In summary, NiTi alloys have been found to possess exceptionally long fatigue life under conditions of high strain amplitude fatigue. The phenomenal performance of these alloys is attributable to their ability to undergo stress-induced, reversible, martensitic transformations (up to 5 - 10% of strain) and reversible twinning and detwinning reactions in the martensite phase.

2.5. Thin Film Processing

2.5.1. General Features of Thin Film Processing

Thin films can be fabricated broadly by either physical or chemical deposition. The former includes vacuum evaporation and sputtering, and the latter consists of chemical vapor deposition (CVD), thermal oxidation, and electroplating. Thin film properties are strongly dependent on the method of deposition, the substrate materials, substrate temperature, and the rate of deposition. For instance, CVD is a process whereby a solid material is deposited from vapor by a chemical reaction occurring on or in the vicinity of the heated substrates. Although the CVD technique is able to produce coatings with uniform thickness and low porosity, even on substrates of complicated shape, the properties of CVD materials are affected by the interacting processes associated with chemical reaction near or on a heated substrate surface. To date, no reports have appeared which use CVD process for NiTi films.

Electroplating, which is the process of depositing a substance by the passage of electric current through an electrolyte, has been used in both decorative and engineering application as an economical technology. However, the process is problematic in the case of titanium, and will not be discussed further.

In the vacuum evaporation process, vapors are produced from a material located in a source which is heated by direct resistance, radiation, eddy current, electron beam, or an arc discharge. Deposition rates are relatively high compared to sputter deposition, especially with the electron beam evaporation technique. However, it is difficult to produce alloy films in the stringent stoichiometry limits needed for thermoelastic NiTi films. Also, this technique is limited if conformable coverage and strong adhesion to the substrate are needed, since there is a relatively low kinetic energy in the evaporant atoms.

On the other hand, sputter deposition permits a wide selection of film materials and a good control of deposit thickness. It also produces films with high purity and better controlled composition, while providing films with good adhesion and homogeneity. The

transformation behavior of NiTi alloys is highly dependent on the composition. Therefore, sputter deposition is the most promising method for the surface coating by NiTi alloys where careful composition adjustment is needed to provide desired surface film properties, such as superelasticity. In this section, general aspects of thin film structure produced by sputter deposition and ion beam sputter deposition will be described and, in particular, the characteristics of NiTi thin films produced by sputtering will be discussed.

2.5.2. Thin Film Processing by Sputter Deposition

Sputtering is described as the removal of atoms from a surface or near surface of a solid by energetic particle bombardment. This phenomenon has many applications, ranging from surface cleaning and etching, to thin film deposition. The sputtering yield, Y, is defined as the average number of ejected atoms per incident ion, and is a function of many parameters, including the energy, the mass, and the incident angle of the projectile (bombarding energetic particle), as well as the mass and the surface binding energy of the ejected atom. The dependence on sputtering yields for the ion and ion energy for nickel and titanium are shown in Figure 2-19. Within the energy range of practical interest in sputtering processes (50 to 5000 eV), the sputtering yield increases with ion energy, but the variation of the sputtering rate in the low energy region is more sensitive. The sputtering yield data and threshold energies for various pure metals are listed in Table 2-2. The incident angle of the projectile also influences the sputtering yields, usually the maximum yield is obtained near 65 °- 75 °.[10] Figure 2-20 shows the variation of sputtering yield with incident angle for Ar^+ on different targets. Also, the emission angle (θ) of the sputtered particle affects the yield and the angular distribution, from the target surface-normal, of the sputtered atom roughly follows a $(\cos\theta)^{-1}$ relation.

---

10. The maximum sputtering yield for light ion sputtering was obtained from a higher incident angle than the heavy ion sputtering. The maximum was not reached before 80 ° by H^+ for Ni, Mo, and Mo target (Anderson and Ray, 1981).

Among the several sputtering processes, ion beam sputtering, which has been used in the present study, and magnetron sputtering will be discussed briefly. In ion beam sputter deposition, an inert ion beam generated at an ion source is extracted into a high vacuum chamber and directed to a target of the desired material, which is sputtered and deposited onto a nearby substrate (George, 1992). Ion beam sputtering permits independent control over the energy and current density of the bombarding ions. Low background pressures ($\leq$ 0.1 mTorr) are used, resulting in minimized gas inclusions and reduced scattering of the sputtered particles during transit. Also, the directionality of the beam allows the investigator to vary the angle of incidence of the beam against the targets as well as the angle of deposition on the substrate. Adhesion of the ion beam sputtered films is superior to evaporated films, the improvement is attributed to the higher energy of arrival of the sputtered particles. The arriving particle energy helps to clean the substrate by sputtering away absorbed gases, it gives greater mobility to the condensing atoms, and it provides implantation into the substrate, enhancing chemical bonding and localized rearrangement.

On the other hand, in magnetron sputtering deposition, ions are extracted from the plasma and accelerated to strike the target, resulting in the sputtering of the target material. Most magnetron sources operate in the pressure range from 1 to 20 mTorr and a cathode potential of 300-700V. In this process, the magnetic field does not directly affect the ion motion; however, because of electrostatic attraction the ions move with the electrons, keeping the plasma neutral. In a conventional magnetron, most of the discharge is confined near the cathode surface and, therefore, bombardment of the growing film by electrons and ions is minimized.

Thin films can be formed on the desired substrates by sputter deposition. The nucleation of the film on the substrate can be described in several steps. Several modes of thin film growth have been observed depending on the film-substrate interactions: (1) island (Volmer-Webber) mode (2) layer (Frank-van der Merwe) mode, and (3) Stranski-

Krastanov mode (Oring, 1992). These film growth modes depend on the film-substrate interaction, producing island growth when the condensing atoms are bound more strongly to each other than to the substrate and layer by layer growth when the interaction with the substrate is stronger. In the latter case, the interaction will monotonically decrease as each layer is added.

The microstructure which results from sputter deposition is sensitive to deposition conditions such as the pressure of working gas, and the substrate temperature. A relationship between microstructure development and processing conditions was proposed by Thornton (1978) in the form of a structure zone diagram, as shown in Figure 2-21. According to his diagram, the microstructure of the sputter-deposited film is affected by the gas pressure and the substrate temperature expressed as a fraction of the absolute melting point (T/T_m). At low film temperatures, shadowing effects (a simple geometric interaction between the roughness of the growing surface and the incident angle of the arriving atoms) result in poor-quality films with open boundaries, which is called Zone 1 structure. Increasing ambient pressure extends the Zone 1 structure to the higher temperature region. At very high homologous temperatures ($T/T_m \geq 0.5$), bulk diffusion enhances the crystallization process, which produces large columnar or equiaxed grains (Zone 3 structure). Zone 3 structures are recognized by dense grain and twin boundaries, and by grain shapes that do not coincide with the substrate and coating surface topologies. Thus simple metals deposited in high T/T_m regions are similar to fully annealed bulk materials. With limited atom mobility to overcome the shadowing effect, dense fibrous structures (Zone T) and columnar structures (Zone 2) are formed at intermediate temperatures ($0.3 < T/T_m < 0.5$).

2.5.3. Sputtering of Alloys

When a virgin multicomponent alloy target is subjected to energetic particle bombardment, the elemental composition of the sputtered flux is usually different from

that of the target surface. This phenomenon is called preferential sputtering (Betz and Wehner, 1983). The preferential removal of one component from the sputter-target surface leads to the formation of the so-called 'altered-layer', which is a near-surface region with a composition different from the bulk. At sufficiently low target temperatures, where thermal diffusion of the constituents is negligible, the thickness of the altered-layer is limited to the depth in which the collision cascade occurs. Steady-state conditions can be attained in which case the sputtered flux and the bulk alloy are constrained to have the same composition. When steady-state has been achieved, the film composition will depend on the interaction of the sputtered flux with the working gas, and by differential sticking coefficients and preferential re-sputtering of film component atoms.

It has been reported that both ion incident and emission angles can affect the composition of deposited thin film in ion beam sputtering deposition (Theirich and Engemann, 1991). In their study, WTi thin films were produced from a single WTi alloy target. For a normal incidence beam the composition change with emission angle was not prominent, but for an oblique incidence angle the titanium content decreased with increasing emission angle. The concentration of titanium in the film was always lower than that of target. Such lower contents of titanium in the deposited film was attributed to the low sticking coefficient of titanium on the growing film. The sticking coefficient for sputter particles in most cases can be expected to be 1. But, recent studies have indicated that the sticking coefficient may be less than 1 for a low atomic weight element, while the sticking coefficient may be equal to 1 for a high atomic weight element (Emmoth and Bergsaker, 1988). This seems to be due to reflections of the light sputtered atoms from heavier atoms of the substrate. In their studies, the targets were bombarded by a 10 keV Ar beam with a current density of 10-20 $\mu m/cm^2$ for the production of sputtered metal atoms and relative sticking probabilities for sputtered atoms on various substrates were investigated. For nickel, stainless steel and vanadium the calculated relative sticking

probabilities on lighter materials, such as beryllium, graphite and silicon, differed by only 1-2%. However, the sticking coefficient of sputtered vanadium (M = 50.94) on silver (M = 107.87) substrates has been determined to be around 0.82.

Concerning the angular distribution of sputtered atoms for the normal incidence, it is known that the distribution is occasionally "under cosine" for heavy ions whereas the angular distribution is "over cosine" for light ions, which is illustrated in Figure 2-22. In addition, the angular distribution gradually changes to a more symmetrical one as the ion beam energy increases (Okutani *et al.*, 1980). However, it appears very difficult to predict what the angular distribution of the components will be for alloys. The studies for Cu/Ni and Fe/Ni alloys by Olson *et al.* (1979) showed ambiguous results for Ar ion bombardment under 1 keV. In their work, even though Fe and Cu were located on the opposite side of nickel in the periodic table, i.e. M_{Fe} (55.84) < M_{Ni} < M_{Cu} (63.55), nickel was enriched in the normal direction to the surface in both cases. Therefore, the atomic weight effect is not enough to interpret the enrichment of nickel in the direction normal to the surface. No logical explanation for preferential emission for these alloy systems was offered. However, the binding energy of each element was set equal to its heat of sublimation, and there the energies for Fe and Cu are 4.28 eV and 3.49 eV respectively. The result indicated that the binding energy effect for an Fe/Ni alloy and the atomic weight effect for a Cu/Ni alloy were dominant.

In addition, the directionality of the beam during ion beam sputter deposition will give rise to a deviation from the cosine distribution of sputtered atoms. There is usually a small lobe opposite the incident ion beam, which results from the enhanced sputtering due to glancing collisions of ions. Under bombardment conditions, where random collision cascade theory[11] applies, both experiment and linear transport theory give cosine

---

11. The impact of energetic ions with a solid produces a varity of effects. The incoming ion loses energy by inelastic collisions which produce electronic excitations and by elastic collisions which displace atoms from their lattice positions. The displaced atoms produce additional collisions in a short period of time and the series of events is called collision cascade. For the collision cascades started by the primary knockon atoms, these are classified into three different regimes: (1) the single-knockon regime, (2) the linear cascade

distributions. The angular distributions are independent of the incident angle of the beam in the regime of cascade sputtering. The ejection distribution is rotationally symmetric with respect to the surface normal, whatever the angle of incidence. However, in the low energy regime of sputtering, the emission distribution depends on the incidence angle and deviates from the symmetry. Very little information is available on angular distribution in the regime of nonlinear cascades. The angular distribution of sputtered Si atoms was studied by Okutani *et al.* (1980) at angle of incidence of 60° by Ar^+ for 3 keV and 10 keV. It has been also reported that the angular distribution of sputtered polycrystalline W was measured at an angle of incidence of 60° by Kr^+ from 5 keV to 19 keV by Oechsner (1975). Both results revealed similar trends in the angular distribution by an oblique incident beam in this regime. With decreasing bombarding energy the direction of preferential emission was continuously shifted from the target normal into the region of specular reflection of the incoming ions for moderate bombarding angles.

2.5.4. Stress in Thin Films

There may be either intrinsic and extrinsic stresses in thin films. Intrinsic stresses come from defects such as dislocations and precipitates in the film and extrinsic stresses from the differences of the thermal expansion between the film and the substrate. Thin films deposited by physical vapor deposition, such as sputtering and evaporation, possess a residual stress which can result in film buckling, cracking, or delamination. Generally, sputter deposited films prepared at high pressures have tensile stresses, but at low pressure, energetic particle bombardment of the growing film may give rise to high compressive stresses due to the recoil implantation of the surface atoms, in what is called the atomic peening effect (Mattox 1994).

Most importantly, the existence of residual stresses in NiTi films can shift the transformation temperatures, according to the Clausius-Clapeyron equation described in

---

regime, and (3) the spike regime (Sigmund, 1981). The detailed characteristics of each regime will be provided in the reference.

section 2.3.1. Residual stresses in both as-deposited and annealed (873 K, 15 min.) NiTi thin films on silicon wafers bombarded by Ar^+ during deposition were studied by Walles (1993). Films deposited by ion sputtering without assist beam bombardment showed tensile residual stresses of about 50 MPa. After annealing, the tensile residual stress increased to about 380 MPa due to large differences of thermal expansion coefficients between silicon and NiTi thin film.

2.5.5. NiTi Thin Film by Sputter Deposition

2.5.5.1 Crystallization of NiTi Thin Films NiTi alloys in the form of thin films have been produced by d.c. magnetron (Busch, 1990; Kim 1986; Chang, 1993) or r.f. magnetron sputtering (Ishida, 1993; Rai and Bhattacharya, 1987), and the crystal structures and shape memory effects in the films have also been investigated. As-sputtered thin films of NiTi alloys deposited at substrate temperature below 598 K were amorphous in structure (Hou, 1995), with no phase change or shape memory effect. The stability of the amorphous phase was attributed to the small free energy gap between the amorphous and crystalline phases, the sluggish diffusion of titanium, and a large negative enthalpy of mixing (Chang, 1993). Although such as-deposited amorphous film can be used as corrosion resistant and wear resistant coating, the films exhibit shape memory effects only in the crystalline structure, and hence it is necessary to crystallize them.

The crystallization temperature has been reported to be about from 753 K to 853 K (Busch, 1990; Ishida, 1993; Kim, 1986) and the transformation is exothermic. But, Moberly *et al.* (1992) reported the crystallization temperature changes depending on the thickness of the films. It was concluded that the complete crystallization of thicker film occurs at lower temperature than the thinner ones, but that nucleation occurs homogeneously and results in random orientations. No nucleation occurred until the temperature was greater than 853 K for a less than 100 nm thick film. It was also reported that the crystallization progressed much faster in thicker films (Johnson, 1991).

The crystallization temperature increased monotonically from 748 K to 778 K with decreasing Ti contents from 51.0 at.% to 47.4 at.%. An increase in the heating rate raised the crystallization temperature, but depressed the associated enthalpy (Chang, 1993).

According to *in-situ* TEM observations by Moberly *et al.* (1992), the crystallization of the amorphous NiTi thin films occurred homogeneously and the grains were grown spherically until they were impeded by the grain boundaries. The grain size of the annealed thin NiTi film was almost the same or greater than the local film thickness. Thus, the regions which possessed more than one grain through the film's thickness were rare (Moberly *et al.*, 1992; Chang, 1993). Such large grain formation was attributed to the difficulty of the nucleation due to strain build up in the amorphous matrix which hindered further nucleation after the beginning of two dimensional growth (Moberly *et al.*, 1992).

However, sputter deposition of NiTi alloy on hot substrates produces crystalline deposits, and the post-crystallization annealing process is not necessary. Recently, the thin films grown by d.c. magnetron sputter deposition of NiTi alloy on hot substrates, with temperatures between 598 K and 723 K, by Hou and Grummon (1995) revealed ultra-fine grain size (20-50 nm). Furthermore, when the substrate temperature was in the range of 598-673 K the produced film exhibited a strong texture of a (110) $_{B2}$, but this texture was disappeared when the film deposited at higher substrate temperatures (above 673 K).

2.5.5.2. Transformation Behaviors of NiTi Thin Films Transformation behavior of NiTi thin film can be influenced by its chemical composition, impurities in the film, and heat treatment. The influences of heat treatment and precipitation were studied by Busch *et al.* (1992). Film annealed isothermally at 813 K showed a decrease in the transformation temperatures and a more pronouncing R-phase with increasing annealing time. When the films were annealed in the range of 813 K to 1073 K for 30

minutes, the transformation temperatures were decreased and R-phase range was increased with increasing annealing temperature. Busch *et al.* observed two types of precipitates which were formed at the grain boundaries and within the grain interiors. The precipitates inside grains were identified as Ti_2Ni, and those formed along grain boundaries as Ti_3Ni_4. Ti_2Ni precipitates in grain interior were attributed to a decrease of M_s temperature due to the preferential use of titanium in the matrix. Also, they explained that Ti_3Ni_4 precipitate formation caused a widening of the R-phase range and a significant decrease in the M_s temperature by the effect of the internal stress fields at the coherent boundary between precipitates and parent phases. The finely dispersed Ti_3Ni_4 precipitates did not provided the nucleation sites for martensite, however, the coarsened Ti_3Ni_4 precipitates provided the nucleation sites for martensite and constrained it from further development (Xie *et al.*, 1990). This effect might be more dominant than an increase in the relative titanium concentration in the matrix. However, annealing at 813 K for 2 hours did not produce any precipitates at grain boundaries in their studies. Another study showed that the thickness of the crystallized NiTi thin film, which also was deposited by d.c. magnetron sputtering, affected the M_s temperature (Xie *et al.*, 1990; Moberly *et al.*, 1992). The M_s temperature of those films increased with thickness. They observed that the thicker film (> 7 μm) showed a M_s temperature above room temperature, whereas the thinner film (< 1 μm) showeda M_s temperature below room temperature.

In summary, NiTi alloys in the form of thin films, which display the shape memory effect and superelasticity, have been studied recently to aide in the development of the several microdevices, microactuators, microvalves and deformable membrances. For practical engineering applications, the proper control of transformation temperatures in the films is important. The transformation temperatures are influenced by several factors such as grain size, heat treatment, precipitate formation, and chemical composition. Until now, most techniques have used cold substrate deposition by

sputtering. In this case, as-deposited film has an amorphous structure which has no shape memory effect or superelastic properties, and thus crystallization annealing at a certain temperature (~773 K) is required. Recently, however, sputter deposition of NiTi alloy on hot substrates has been introduced, where the post-crystallization annealing process is not necessary. In this case, ultra-fine crystalline NiTi films have been produced, which is effective in improving the superelastic effect.

3. EXPERIMENTAL METHODS

Introduction

The experiments performed in this study are divided into three major parts: (1) NiTi thin film deposition by ion sputtering and film crystallization procedures, (2) the characterization of the films, and (3) the detailed study on fatigue life and surface damage accumulation during and/or after low cycle fatigue. In this chapter, specimen microstructure and detailed sample geometries will be discussed, along with material sources and sample preparation procedures. The section on thin film characterization includes compositional analysis using ZAF correction, the martensitic transformation behavior of crystallized films by electrical resistivity measurement, and crystal structure determination by X-ray diffraction analysis. Since many fundamental fatigue studies of fcc metals have been reported for single crystals and polycrystals of copper, and fatigue phenomena, such as persistent slip band (PSB) formation and fatigue crack initiation, are by now well established for this material. Thus, pure polycrystalline copper was used as a substrate metal in the present work. The fatigue lives of surface film coated specimens, both with amorphous and crystallized films, and bare copper specimens, were investigated by low cycle fatigue tests conducted under constant plastic strain amplitude. Fatigue tests were carried out at various temperatures with respect to the transformation temperatures of coated films, which were martensitic, austenitic, or dual-phase mixtures. In addition, the effect of initial phase[1] of the film on fatigue properties was studied.

1. Since NiTi alloys exhibit a transformational hysteresis, the initial phase of the films at the same test temperature will be different depending on thermal history.

3.1. Fabrication of Fatigue Specimens

The various steps involved in the fabrication of low cycle fatigue specimens are illustrated in Figure 3-1. Dog-bone shaped fatigue specimens of 127 mm length were machined from cylindrical oxygen free high conductivity (OFHC) copper rod. The detail sample geometries are depicted in Figure 3-2. The nominal composition of this material is tabulated in Table 3-1.

Table 3-1
Nominal Composition of OFHC Polycrystalline
Copper Used for Fabrication of Fatigue Specimen [2]

Element	Amount (%)	
Cu	99.99	min.
O	0.0010	max.
Hg	0.0001	max.
Cd	0.0001	max.
Zn	0.0001	max.
S	0.0018	max.
Pb	0.0010	max.
Bi	0.0010	max.
Se	0.0010	max.
Bi	0.0010	max.
P	0.0003	max.
Te	0.0010	max.
Se	40 ppm	max
Bi	40 ppm	max
As	40 ppm	max
Sn	40 ppm	max

Two different kinds of specimens were fabricated depending on the purpose of the study. One had 2 mm flat surface region in the gauge length area, to facilitate direct observation of crack development on the surface, and investigation of changes in crystal

2. The Young's moulus is 120 GPa and the coefficient of thermal expansion is 17×10^{-6}/ °C.

structure by X-ray diffractometry. These specimens were rotated during deposition to allow for coverage of the entire gauge section. Because of the difficulty in deposition and crystallization of the films on the entire surface in the gauge section, a second specimen geometry (for evaluating the fatigue life) was provided with a shallow round notch on one side, to increase local stress and cause crack to initiate at the notch, with films applied carefully to the pre-dertermined crack initiation zone. This specimen was coated without rotation. Both specimens had smooth ends for use with hydraulic collet grips.

After machining, the surfaces of the specimens were mechanically polished (in a specially designed fixture) using silicon carbide papers down to 1200 grit; further polishing was carried out using 600, 5, and 1 μm alumina abrasives. Since the final surface finish was produced by electropolishing after an annealing treatment, a mirror finish was not required at this stage. However, the surfaces were free of deep scratches, which would be difficult to remove during electropolishing.

The specimens were annealed for 1 hour in vacuum at 1173 K and cooled slowly to room temperature to relieve stresses which may have developed during machining. The vacuum was kept below 1×10^{-4} Pa during heating and cooling to minimize surface oxidation[3]. The final grain size after annealing was determined by optical metallography. Samples, cut from the specimens, were mechanically polished with silicon carbide and alumina down to 0.3 μm, and etched in a solution of 10% HNO_3 and 90% H_2O for 10 sec. The microstructure of the annealed copper is shown in Figure 3-3. The average final grain size of these samples was approximately 300 μm (annealing twin boundaries were excluded in this measurement).

The gauge sections of the heat treated specimens were electropolished to provide a smooth surface free of residual stress. The finish also facilitated investigation of surface morphology changes. A masking lacquer was applied to the grip end to shield it from the electrolyte, and the area exposed in the gauge section was kept constant to

3. Even though slight oxidation may occur during the annealing process, the oxide layer was removed during the electropolishing step.

maintain identical electropolishing current density each time. Electropolishing was conducted in a moderately agitated bath of 33% nitric acid and 67% methanol maintained at approximalety 228 K. The applied current density was 2.0 mA/mm^2. The apparatus for electropolishing is shown in Figure 3-4. The specimen was also rotated at 60 rpm to prevent bubble adhesion on the surface, and the total electropolishing time for each specimen was approximately 30 sec.[4] The masking lacquer was removed from the specimen surface and cleaned by acetone, methanol, and deionized water successively in an ultrasonic bath.

3.2. NiTi Film Deposition by Ion Sputtering

3.2.1. Ion Beam Sputter Deposition System

A schematic drawing of the ion sputter deposition system is illustrated in Figure 3-5. The sputtering chamber, a 14-inch diameter metal bell jar, was evacuated by a rotary mechanical pump and by an Alcatel 5400 turbomolecular pump (the pumping speed is 400 liters/sec. of air), and by an APD cryopump-8S, which pumping speed is 1200 liters/sec. of air, in parallel. The chamber was baked for over 12 hours at 353 K. After baking, the chamber was cooled and pumped for 8 to 10 hours. After these operations, the final base pressure was obtained around 7.7×10^{-6} Pa. To monitor the partial pressure of the residual gases in the chamber a Dycor M102 quadrupole mass spectrometer was used.

3.2.2. NiTi Thin Film Deposition by Ion Sputtering

The sputtering target alloy, with composition of $Ni_{50.17}Ti_{49.83}$[5] ,was commercially provided in the form of a 62 mm diameter extruded rod. The alloy was cut

---

4. Because of the presence of oxide layer on the suface of the specimen, the current and voltage increased in the early stage of electropolishing. After removal of the oxide layer, the current and voltage stabilize and this particular stage was believed to be the optimal electorpolishing condition. It took about 15 sec. to electropolish the specimen after achieving the optimal condition.
5. No further information of the trace element contents was available from the company.

and hot rolled at about 1173 K into a thin plate. The final dimensions of the target were approximately 85 mm diameter and 3 mm thick. The target surface was mechanically polished up to 600 grit silicon carbide paper and cleaned in successive bathes of acetone, methanol, and deionized water.

The ion sputter deposition system was equipped with two different ion guns. One was used for sputter-cleaning and the other was used for deposition of NiTi films on specimens. High purity argon gas (99.999% min.) was supplied to both ion guns through a gas purifying cartridge (OxiClear DGP-250 R1) to remove trace oxygen and moisture. A special steel fixture was designed to facilitate successive sputter-cleaning and depositing on four fatigue specimens in one batch (Fig. 3-6). Initially, the specimens were placed in the center of the sputtering chamber, normal to the ion gun which was used for cleaning. Prior to deposition of nickel-titanium films, the specimens were sputter-cleaned by bombarding the substrate surface with 500 eV argon ions for 10 minutes by a Anatech 5-cm cold cathode gun, to remove dirt and the oxide layer. The operating conditions were as follows: a beam current of 9.6 mA, acceleration current of 1.6 mA, and 150 mA of emission current. The working argon gas pressure in the chamber was maintained approximately at 2.9×10^{-2} Pa during sputter-cleaning.

After sputter-cleaning, the specimens were rotated 90° by a linear-rotary feedthrough, to face the target, without breaking the vacuum. Ion-sputter deposition was accomplished by irradiating the NiTi alloy target with 800 eV argon ions generated from a 3-cm Kaufman-type gun (Ion Tech Model 3.0-1500-100), equipped with converging optics. Even though a convergent grid was used for the ion sputter deposition, some amount of the ion beam diverged. Therefore, a titanium aperture was used to reduce beam coverage, and to avoid sputtering undesired elements, such as Fe and Cr, from the chamber wall and other fixtures in the chamber. The incident angle of the ion beam on the target was 45° and the gun was operated with a discharge voltage of 55 V, a beam current of 40-55 mA, and an acceleration current of 1-3 mA, supplied by an MPS-3000

FC power supply. During deposition the working chamber pressure was maintained at 3.9×10^{-3} Pa. To compensate for the preferential resputtering of titanium at the substrate, which was described in section 2.5.3, 0.25 mm diameter titanium wires (99.8 % purity) were placed on the target to control the composition of the films. The average effective composition of the target surface was changed to around $Ni_{47}Ti_{53}$. The distance between target and substrate was 130 mm and the distance from the ion source to the center of the target was 70 mm. Total deposition time to produce the desired 3 μm film thickness was approximately 5 hours.

For direct comparison of crack development between the coated and uncoated surface areas on the fatigued specimens, the specimens were partially masked with copper foil in the gauge area. An additional set of specimens, which were used for evaluating fatigue life, were made with films in a shallow notched area. Simultaneously, films were deposited on slide glass substrates for thickness measurements, resistivity measurement, and composition analysis.

3.2.3. Crystallization of NiTi Thin Films

Crystallization temperatures of as-sputtered films were studied using a DuPont 910 differential scanning caloriometer (DSC). Specimens, which had been deposited on glass, were loaded in sealed aluminum pans and heated at a constant heating rate of 10 K per minute from ambient temperature to 873 K. The crystallization temperature was determined by the peak temperature from the exotherm in the DSC trace.

Crystallization of as-sputtered films on fatigue specimens was performed in vacuum with two 625 watt quartz-halogen lamps at a distance of 25 mm from the surface of the specimens for 10 minute at 873 K with a heating rate of around 20 K per minute. The oxygen partial pressure was kept below 5.0×10^{-7} Pa and the nitrogen partial pressure was maintained near 7.0×10^{-6} Pa during the crystallization procedure. The specimens were cooled at an initial rate of 50 K per min. The time-temperature curve for the

crystallization annealing is shown in Figure 3-7. Crystallization of the films were confirmed by X-ray diffraction analysis on a Scintag 2000 diffractometer.

3.3. Characterization of NiTi Films

3.3.1. Thickness Measurement

Films were deposited simultaneously on microscope slide glass substrates, which were placed next to the fatigue specimens, for thickness measurements. A profile step was produced by masking with an annealed copper foil during deposition. The thickness of the as-deposited film was measured by Dektak II profilometer with a scan rate of 1mm/min. The final thickness of deposited films was in the range of 2.9 to 3.2 μm, and the deposition rate was approximately 100Å per minute.

3.3.2. Composition Analysis

Elemental compositions of the films were determined by energy-dispersive X-ray (EDS) microanalysis by Link analtical AN-1000 with pentafet detector on a Hitachi S-2500 scanning electron microscope (SEM). Standards of pure nickel, pure titanium, and $Ni_{50.1}Ti_{49.9}$, which was provided by a vendor, were chosen to determine the composition of the films. All standard samples were polished using up to a 0.3 μm abrasive alumina powder to obtain a mirror-like surface and then cleaned by acetone and methanol. The films deposited on the glass surveillance substrate were mounted on a graphite stage, together the with standards, and were illuminated by the electron beam with an energy of 20 keV. After stabilization of the SEM LaB_6 filament[6], the spectra from the films were checked for any existence of characteristic Si X-ray peaks from the glass substrate. Absence of these peaks confirmed that no interaction occurred between the electron beam and the glass substrate. All the spectra were collected with a working distance of 15 mm

6. The stablization of the filament (electron source) took approximately 30 min. and could be decided by comparing the dead time percentage and time interval without changing any other conditions with the previous spectrum. If the filament reaches a stable condition, those values become exactly the same as the previous ones.

and magnification of 1,000×, without tilting of the SEM stage. The composition was calculated by using the ZAF-4 program supplied by Link Analytic Inc. to analyze the all spectra.

3.3.3. Transformation Temperature Measurement

3.3.3.1. Eletrical Resistivity Measurements The transformation temperatures of the annealed films were studied by recording electrical resistivity as a fuction of temperature for the surveillance films deposited on glass substrates. The resistivity measurement apparatus is shown in Figure 3-8. Two independent power sources were used for the measurement: one (12 V d.c. battery) for supplying a constant current to the film and the other (HP 6010A d.c. power supply) for controlling the heating rate. Thin-gauge copper wires and a T-type thermocouple were attached by pressing pure indium onto the film. A constant direct current (4 mA) was passed through the circuit, while the voltage drop (ΔV) across a 4 mm long film strip was recorded on an XY-recorder. Both the cooling and heating rates for the resistivity scans were held at approximately 10 K/min.

3.3.3.2. Differential Scanning Caloriometry (DSC) Phase transformation temperatures and enthalpies of the annealed films were determined on a DuPont 910 DSC with heating rate of 10 K/min. The baseline curve of DSC is the continuous change in the heat flow that a material undergoes without transformations. The actual curves are the deviation in the heat flow that a material undegoes with transformations. The transformation start and finish temperatures are determined by superimposing the actual curves upon the baseline curve, and using the points of deviation that the actual curves exhibit from the baseline curve. The transformation start temperature is where the peak begins to deviate form the baseline, while the finish temperature is where the peak return to the baseline.

3.3.4. Crystal Structure Evaluation

A Scintag 2000 diffractometer with copper X-ray tube was used to investigate the crystal structure of the deposited films before and after annealing. A sample holder for the 5 inch dog bone fatigue specimens was designed for mounting on the X-ray sample stage properly. An operating voltage of 40 kV and tube current of 30 mA were chosen, and both step and continuous scanning modes were employed. For step scans, the samples were irradiated by Cu-Kα radiation with a step size of 0.03° and a pretime of 5 sec. For continuous scans, the samples were irradiated with a step size of 0.03° and a scan rate of 3°/min. Structure changes resulting from stress-induced transformations were studied on fatigued specimens after plastic deformation and fatigue cycling.

A Rigaku RU-200B X-ray diffractometer equipped with a Rigaku CN 2351B1 cold stage was used to study the crystal structure of the isothermally annealed NiTi films at various temperature from 348 K to 173 K. An operating voltage of 45 kV and tube current of 100 mA were chosen, and a continuous scanning mode was employed. Samples were irradiated by Cu-Kα radiation, with a step size of 0.03° and a scan rate of 2°/min. from 2-theta angles of 35° to 48°. The whole cold stage resided in a sealed vacuum camber. Sample temperature was controlled by a built-in heater mounted on a cold finger, which was connected to a liquid nitrogen dewar. The temperature fluctuation during scanning was maintained within ± 1 K.

3.4. Low cycling Fatigue Test

All low cyclic fatigue tests were undertaken at a constant plastic strain amplitude using sinusoidal fully reversed uniaxial loading, in a computer-controlled servohydraulic testing machine. The computerized control and data acquisition system for the low cycle fatigue testing program (CPS-405) written in the BASIC language were developed by Dr. Grummon. The schematic block diagram of servohydraulic test and cooling system is

shown in Figure 3-9. Detailed procedures for fatigue testing will be described in the following section.

3.4.1. General Features of the Fatigue Testing System.

The low cycle fatigue testing was conducted in a closed looped servohydraulic system (Instron 2150 series) with a 20,000 pound load cell (Instron 6467-107) and a 10 mm gauge length extensometer of ± 1.0 mm full scale (Instron 2620-530). The gripping system consisted of a set of collet grips (Instron 2742 series) for round specimens and on an electric pump pressurization system.

A cooling system was employed for low temperature fatigue tests. A detailed schematic is illustrated in Figure 3-10. The coolant used was 50 % ethylene glycol with water and was cooled by Neslab refrigerated circulating bath aided by a cryocool immersion cooler (Neslab CC-100II). The lowest temperature obtained in the bath was around 203 K. The specimen was conductively cooled by aluminum cooling blocks through which coolant was made to circulate. The hoses, which carried the coolant, were insulated to minimize thermal losses during circulation and the aluminum blocks were also covered by insulation to prevent heat dissipation to the grips. The specimen and cooling blocks were isolated from the external atmosphere by wrapping the entire assembly with insulating materials. Liquid nitrogen, if needed, was blown to the gauge area to lower the temperature for providing fully martensitic NiTi films.

The gauge section area was calculated according to the formula given below.

$$A = \pi r^2 - \frac{r^2}{2}(\theta - \sin\theta)$$

where (3.1)

$$\theta = Tan^{-1}\left(\frac{\sqrt{r^2 - (t-r)^2}}{(t-r)}\right)$$

where A is the cross section area, r is the radius of the cross section if there is no flat face, and t is the distance between the flat face and the opposite curved part of the cross section. The program, CPS 405, provided a constant plastic strain amplitude control and converted the measured load from the load feedback to stress based on the calculated gauge section area. The measured stress and strain were displayed graphically on the monitor during the test, and the peak stresses for each block were stored continuously. Testing could be terminated or interrupted by various criteria such as a specified amount of the peak stress drop, a predetermined total plastic strain target, or number of cycles.

3.4.2. Specimen Mounting

Since the annealed copper specimens, irrespective of the surface condition (coated or uncoated) were extremely soft, special caution was needed for mounting the specimens. Perfect alignment of the grips had to be maintained to prevent imparting any plastic deformation during this procedure. Initially, the specimen was inserted into the lower grip. The extensometer with the installed gauge length pin was mounted on the specimen by rubber bands. The hydraulic pump and the actuator were turned on under load control mode and then the ram was moved up very slowly. After the specimen was positioned in the upper grip, the upper grip was clamped. Prior to testing, the initial load was maintained at zero when the specimen was clamped, which minimized loading on the specimen before the beginning of the test. While the system was still in load control, the gauge length pin was removed from the extensometer, and both the strain feedback and the strain command were zeroed under zero load. After finishing the above procedures, the testing system was transferred from load control to strain control. All low cycle fatigue tests in these studies were undertaken under strain control mode, with drive amplitudes continuously adjusted by the computer to achieve constant plastic strain amplitude.

3.4.4. Plastic Strain Controlled Low Cycling Fatigue Tests

Figure 3-11 illustrates the cyclic response of a material subjected to repeated loading in the form of a stress-strain hysteresis loop. The total width of the loop is $\Delta\varepsilon_T$ (total strain range) and the total height is $\Delta\sigma$ (total stress range). The total strain is the sum of the elastic and plastic strains as shown below.

$$\Delta\varepsilon_T = \Delta\varepsilon_e + \Delta\varepsilon_p$$

$$\text{so,} \quad \Delta\varepsilon_p = \Delta\varepsilon_T - \Delta\varepsilon_e = \Delta\varepsilon_T - \frac{\Delta P}{A \cdot E} \tag{3.2}$$

where, ΔP is the load amplitude corresponding to elastic region, A is the gauge section area, and E is the Young's modulus of specimen. The plastic strain amplitude can be determined from the hysteresis loop by measuring the distance of the two parallel straight lines corresponding to the elastic responses between the compressive and tensile side. In the present work, the plastic strain amplitude was determined from the strain differences between the two sides at zero stress[7]. This is expressed int he following,

$$\Delta\varepsilon_p = \varepsilon_{\sigma=0^+} - \varepsilon_{\sigma=0^-} \tag{3.3}$$

The plastic strain amplitude of interest of every cycle was compared with the pre-determined plastic strain amplitude and was controlled via computer. Real time stress strain hysteresis loops were displayed during the fatigue test.

To minimize the overshooting or undershooting from a predetermined plastic strain target (e.g. $\Delta\varepsilon_p$ = 0.2 %) in the early stage of the fatigue test the first 10 cycles

7. The actual plastic strain amplitude might be little higher than the target due to Baushinger effect, but the deviation was negligible.

were completed manually. The peak stresses and the cycle numbers were recorded for every cycle. After the first 10 cycles the specimens were fatigued under a plastic strain control at $\Delta\varepsilon_p$ = 0.2 % using a constant frequency of 2 Hz which was controlled by a computer using the 12 bit analog-digital converters. The peak stress was recorded at the end of every block, which consisted of approximately 25 cycles and 1,000 data points, and was compared with that of the previous block. This comparison of the peak stresses was used for the criterion of fatigue crack initiation.

The cyclic hardening curve was constructed from the peak stresses as a function of cycle number. Figure 3-12 illustrates an example of the cyclic hardening curve. The saturation stresses in the present study were determined from the cyclic stress strain data. The fatigue crack initiation life was established as the point where the peak stress dropped by 1%, as shown in Figure 3-13, as detected by the computer controlled system. The accumulated plastic strain (ε_{Acc}) is defined as follows,

$$\varepsilon_{Acc} = 2\sum^{n}\Delta\varepsilon_p \qquad (3.4)$$

The fatigue test was interrupted, if necessary, to monitor surface morphology changes whenever the accumulated plastic strain reached the predetermined value, such as ε_{Acc} = 4, 10, 20, and 40. Damage accumulation at increasing cumulative strains were compared between bare copper and NiTi film coated specimens.

Other sets of the NiTi film coated specimens were removed from the load frame after a specified number of cycles (10,000 cycles). Then, the specimens were annealed by heating rapidly up to 673 K, by quartz lamps, and held for 20 min. in vacuum, and were then fatigued again at 298 K. Effects of post annealing[8] of films which had

8. It is important to raise the critical stress for slip in NiTi alloys in order to stabilize the superelasticity characteristics against cyclic deformation. The post annealing may cause a thermal rearrangement of the dislocations, and precipitation hardening in coated film raising the critical stress for slip.

experienced cyclic deformation less than that needed for fatigue crack initiation were studied.

Stress-strain behavior in NiTi alloy, as described in section 2.4, is different depending on its transformation temperature. Most of the fatigue tests were carried out at 298 K, but the relative temperature with respect to the martensitic transformation temperature of coated films was different. Therefore, the film on fatigue specimens may exhibit fully austenite, R-phase, martensite, or dual phase structures (mixture of austenite and R-phase or mixture of R-phase and martensite). However, since the M_f temperatures of the produced NiTi films were always lower than 298 K, fully martensitic films could be obtained only at low temperatures. In this case, the films were cooled down below the M_f temperature by blowing liquid nitrogen on the gauge section area, while circulating the coolant into the cooling blocks, which is shown in Figure 3-10. Once the desired temperature had been reached, liquid nitrogen cooling was stopped, but the temperature was maintained low enough so as not to transform the film back to austenite by continuously circulating the coolant during the fatigue test.

3.5. Observation of Sputtered Film Structure and Surface Damage Accumulation

Surface characterization was carried out by optical microscopy and scanning electron microscopy (SEM). The cross sectional areas of both as-sputtered and crystallization annealed films grown on glass were observed by SEM (Hitachi S-2500C). The surface morphological differences between the B2 phase and martensite phase on the crystallized thin films having different thermal histories were observed through an optical microscope at 298 K.

Direct comparison of fatigue damage on the surface region in the gauge section was performed between the area covered with the film and the uncoated (masked) copper area with the same cyclic history. The progress of surface damage accumulation was recorded by interrupting the tests, recording surface features, and applying more cyclic

deformation. Macroscopic characteristics such as crack populations and surface rumpling were studied by optical microscopy and SEM. Fatigue crack development on the specimens and the morphological differences between surface film coated specimens and bare copper specimens were also studied at higher magnification. Furthermore, careful observations were carried out on the sputter deposited specimens to understand the crack initiation modes and crack propagation corresponding to the crystal structures of the films and the associated testing temperatures.

4. RESULTS AND DISCUSSION

Introduction

This chapter is composed of two parts: (1) a discussion of NiTi thin films processed by ion beam sputter deposition and their characterization, and (2) a treatment of the effect of the thermoelastic NiTi thin film coatings on surface damage accumulation and fatigue crack initiation in polycrystalline copper. The microstructures of as-sputtered and crystallized NiTi thin films will be described briefly. The transformation behavior of the annealed films, which were used to determine test temperatures, will be reported. The second part will be concerned with the fatigue properties in relation to the transformation temperatures of the films. The fatigue crack initiation life of NiTi film-coated specimens cycled, at various temperatures, will be contrasted to that of a bare copper specimen. Also, a direct comparison of surface damage near the boundary between NiTi thin film coated and uncoated regions of the specimen will be presented and interpreted.

4.1. NiTi Thin Films Fabricated by Ion Beam Sputter Deposition

4.1.1. Composition

The compositions of the thin films fabricated by ion sputter deposition are tabulated in Table 4-1. The chemical compositional data were collected four times from the same vertical and horizontal emission angles for each run and variations were monitored for every run. The composition of all of the films was different from that of the target, whose average effective composition after placing Ti wires on the target surface was $Ni_{47}Ti_{53}$. The titanium content of the deposited films, with a range of 48.1-52.7at. Ti%, was generally lower than that of the composition of the target surface. The

depletion of Ti was attributed to the preferential resputtering of Ti from the growing film (Lee, 1994). In NiTi amorphous thin film studies using ion beam assisted deposition (IBAD) (Chang, 1993), the sputtering yield results showed that $Y_{Ti} > Y_{Ni}$ and the yield ratio of titanium (Y_{Ti} / Y_{Ni}) was increased with decreasing ion energy in amorphous films (Y_{Ti} / Y_{Ni} = 1.75 at 500 eV). In addition, considering the sticking coefficient related to relative atomic weight (M_{Ti} = 47.90 and M_{Ni} = 58.71), which was reviewed in section 2.5.3, the sticking coefficient for titanium will be lower due to the low atomic weight of titanium. Thus, the low sticking coefficient for titanium may lead to lower titanium content in the deposited film compared to that of the target NiTi alloy.

Composition changes depending on vertical and horizontal emission angles were studied. The schematic diagram of the experimental setup used in this study is shown in Figure 4-1. The angle of ion incidence was always 45° to the target normal and the substrates were located at different emission angles, as described in section 3.2. The composition of the films was apparently affected by only the vertical emission angles. No composition changes were observed in the difference of horizontal emission angle. The variations of composition with emission angle are illustrated in Figure 4-2. Ni concentration decreased monotonically with increases in the emission angle in ranges of 25° to 60°. When alloys or compounds are sputtered, the angular distribution of the sputtered atoms can be different for each component. In contrast to other sputter deposition processes, ion beam sputter deposition has the directionality of the beam, so one can change the incident angle of the beam on the target as well as the angle of deposition to the substrate. Therefore, when films are sputter deposited from the multicomponent alloy target, the composition can vary depending with where the target and substrate are positioned. The change of the titanium concentration on emission angle can be explained by differences in atomic weight and surface binding energy (E_{Ti} : 4.85 eV and E_{Ni} : 4.44 eV) between titanium and nickel, which was discussed in section 2.5.3 (Okutani *et al.*, 1980; Oechsner, 1975). Since titanium has a lower atomic weight and

higher binding energy than nickel, the atomic weight effect leads to a preferred emission of nickel from an ion bombarded NiTi alloy in the direction normal to the target. Also, the effect of binding energy on sputtering yield causes same preferred emission of nickel from an ion bombarded NiTi alloy in the direction normal to the target.

EDS study of the films showed a small amount of residual argon in both as-sputtered and annealed films , as shown in Figure 4-3. No change in the intensity of the characteristic peak for argon was observed after the annealing process. The effect of trapped argon gas in the film is not yet understood.

4.1.2. Microstructure

The cross sections and surface morphologies of both as-sputtered and annealed NiTi films on a glass substrate, as observed by SEM after fracture by bending, are shown in Figure 4-4. The thickness of deposited films was approximately 3 μm. Unlike the r.f. magnetron sputter deposited NiTi film by Ishida *et al.* (1992)[1], there is no evidence to indicate formation of zone structures in the films, which was described in section 2.5.2. This may be attributed to the very low argon gas pressure (3.9×10^{-3} Pa) used during ion beam sputter deposition, compared to typical r.f. or d.c. magnetron sputter deposition. A very low argon working gas pressure increases the sputtered atom mean free path, resulting in less collisional scattering, and thus the smoothness of the coating surface increases (Thornton and Hoffman, 1989). In addition, the low operating pressure results in an increased energetic particle bombardment of the substrate, and leads to increased surface mobilities of adatoms on the surface (Thornton, 1974), and hence the density and smoothness of the growing film increase. Also, the fractured surface of the as-sputtered amorphous film exhibits a more brittle nature than that of the annealed film.

---

1. In their study, Ar working gas pressures were from 0.67 Pa to 13.3 Pa and the resultant films revealed columnar structure with pores.

4.1.3. Crystallization

Since nickel-titanium is an easily amorphized alloy system[2], the thin films formed on cold substrates by ion sputtering deposition were amorphous. The driving force for crystallization is the free energy difference between the amorphous and crystalline phases.

The crystallization behavior of the ion sputter deposited NiTi thin films was studied by differential scanning calorimetry (DSC). In the present work, a heating rate was chosen to quantify a reference annealing crystallization temperature that would ensure full crystallization for the deposited film on copper fatigue specimens. No further study relating to the heating rate has been done as a part of this work. Figure 4-5 shows a DSC scanning trace for an as-sputtered film which was heated from room temperature to 823 K with a heating rate of 10 °K/min. An exothermic peak appeared at around 773 K, which is identified as the crystallization temperature of the film.

Two crystallization peaks were observed in the DSC scans. This is comparable to other observations of the crystallization of NiTi films (Busch *et al.*, 1990) and $Ti_x(NiCu)_{1-x}$ films (Chang, 1993), where a small side peak was observed along with a strong crystallization peak. It was reported that the disordered BCC structure was formed during crystallization (Busch *et al.*, 1989). Such double crystallization peaks have been commonly observed in crystallization of metallic glasses, such as $Ni_{58}Zr_{42}$ and $Fe_{40}Ni_{40}B_{20}$ (Cahn, 1983). It has also been reported that small amounts of dissolved oxygen in Cu-Zr glasses caused a transition from single stage to double stage crystallization (Chevalier *et al.*, 1983). Thus, the role of impurities on the side peak may not be excluded. However, the nature of the second peak has not been clearly identified.

---

2. The stability of the amorphous phase of NITi alloy has been attibuted to the small free energy gap between amorphous and crystalline phases, a large negative heat of mixing (- 30 kJ/mol) in the amorphous phase, and abnormally fast diffusion of nickel in Ti (Zoltzer and Bormann, 1988). Schwarz *et al.* (1985) prepared amorphous NiTi alloy powders by mechanical alloying the elemental powders in the concentration range between 28 and 72 at.% Ti.

X-ray diffraction studies were carried out on as-deposited and post-annealed films to investigate the crystal structure changes. The as-sputtered films exhibited a broad diffraction peak at approximately $2\theta = 42°$ which was located near the strongest peak of $(110)_{B2}$ of NiTi alloy, as shown in Figure 4-6. This broadened peak is in agreement with previous reports for the amorphous phase of NiTi alloy (Kim *et al.*, 1986). The amorphous structure was marked by the absence of long range order and characterized by a diffuse X-ray diffraction peak. X-ray diffraction scans of crystallization annealed NiTi films are given in Figure 4-6(b). The largest peak at approximately $2\theta = 42.5°$ appeared along with two smaller peaks at $2\theta = 62.0°$ and $2\theta = 78.2°$, which correspond to $(110)_{B2}$, $(200)_{B2}$, and $(211)_{B2}$ respectively, in NiTi.[3]

The resistivity measurement of an as-sputtered film in the range of 123 K to 373 K is shown in Figure 4-7. The resistivty curves did not exhibit any transformational characteristics, as described in section 2.3.2.

The grain size and grain morphology of annealed NiTi films are shown in Figure 4-8. This SEM micrograph exhibits artifacts apparently associated with radial growth on both copper and glass substrates, which is believed to result from the growth of pancake-shaped microcrystallites. Therefore, such crystallization occurs homogeneously and proceeds until grain impingement. Similar large grain crystalline structures were reported for CuTi liquid quenched amorphous alloys (Marshall *et al.*, 1984). The application of energy dispersive X-ray (EDS) analysis allowed the measurement of the chemical composition of the center of the grain and the radially grown arms. No differences in chemical composition between the two areas were detected. In addition, X-ray diffraction results also showed only a single phase of B2 structure with the same composition, which indicates the crystallization process is a polymorphic reaction[4].

---

3. Even though Ti_2Ni and Ti_3Ni_4 precipitates were observed in the crytsalline film due to a narrow solid solution region in this alloy system, a supersaturated single phase solid solution can be formed.
4. There is no change in composition during crystallization and the crystal shape depends only on the crystallographic anisotropy of growth rate (Cahn, 1983).

Planar-equiaxed pancake grains, 3 to 5 μm in diameter, were observed both on glass and copper substrates after the crystallization process. The average grain size was larger than the thickness of the films., and was larger than those observed in other studies (Chang, 1993; Busch *et al.* 1991). According to their results, crystals of NiTi were produced from free standing films annealed at 773 K and the average grain sizes were 1-2 μm, which was independent of film thickness. For eutectic or polymorphic crystallization, once a stable nucleus has formed, the crystal growth will be linear with time during isothermal annealing (Koster *et al.*, 1984). Therefore, the large grained structure can be predicted from an Arrhenius dependence of growth rate on time and temperature for polymorphic crystallization. The simple expression of this equation is:

$$u = a_o \nu_o \exp(-\Delta E_a/kT) \tag{4.1}$$

where u is crystal growth rate, a_o is the distance across the crystallization front, ν_o is the atomic jump frequency, and ΔE_a is the activation energy for an atom to leave the amorphous to crystal interface. In the present work, the crystallization temperature was 100 K higher than the previous investigations for free standing films (773 K). Also, the large grains were attributed to slow cooling after the crystallization process, due to a relatively large thermal mass of the substrate. In addition, it has been reported that *in situ* observation of crystallization form the amorphous NiTi thin film involves dramatic grain growth, with some grains growing in excess of 10 μm (Moberly *et al.*, 1992). Moberly *et al.* attributed such rapid grain growth to the difficulty of nucleation, such that the grains could undergo extensive growth in the two dimensional film before impinging other grains.

Other explanations for the origins of the large grained film can be attributed to the defects in the deposited film. The presence of point defects generated during ion beam deposition, which is a well known consequence of the bombardment of the solid with

energetic particles (Smidt, 1990), can lead to abnormally large grains in the film. Since ion beam sputter deposition operates at higher energy conditions than the usual magnetron sputtering deposition, the induced point defect density will be higher. Thus, such a high point defect density can enhance grain growth by facilitating grain boundary mobilities in the film (Thompson, 1990).

4.1.4. *Surface Relief*

Surface relief from the retained martensite could be observed in the $Ni_{48.8}Ti_{51.2}$ film (A_f = 322 K and M_s = 286 K) at room temperature, which is shown in Figure 4-9. The films, deposited on both glass and copper substrates, were quenched in liquid nitrogen and then warmed back to room temperature. This surface relief phenomenon was confirmed by observing the same area of the film on the copper substrate from different thermal conditions, as shown in Figure 4-10. This is the first direct observation of the surface relief effect due to the formation of the martensite phase in the thin film form of the NiTi alloy. The surface upheaval on the film due to the martensite phase formation disappeared when the film was heated above its A_f temperature. Successive observations showed that exactly the same shape of martensite variants reappeared and disappeared repeatedly. The surface features of thin films produced in the present study showed neither the triangular morphology of B19' martensite nor the saw tooth morphology of R-phase reported by others for bulk alloys, as described in section 2.3.2. Instead, the martensite developed in random directions on the thin film. These random martensite variants might be the result of thin film constraint effects and residual stresses, which would form during cooling due to the difference in thermal expansion coefficient between the film and substrate. These combined effects will influence the formation of favorable martensite variants locally on the film, but the overall distribution of the martensite variants seems to be random.

4.1.5. Residual Stress

The existence of large intrinsic and extrinsic stresses in thin films have been the subject of numerous investigations because of their importance in the application of thin films. Unlike thermally evaporated metal films, which are often in a state of tension, thin films grown by ion beam sputter deposition tend to possess high compressive intrinsic stresses due to the atomic peening effect. In other words, these compressive intrinsic stresses can be introduced by the bombardment of energetic reflected neutrals which cause forward sputtering and recoil damage to the growing film. Thus, the residual stress of an as-sputtered, unannealed, film in the present study is expected to be compressive.[5]

In the as-sputtered condition, the films had negligible extrinsic thermal stresses because of a relatively low substrate temperature used during the sputter deposition process. For crystallized films, the intrinsic stresses would be relaxed after crystallization annealing at 873 K, and the extrinsic stresses would form during cooling due to the difference in thermal expansion between the film and substrate. For a thin film with a thickness less than 10^{-4} times the substrate thickness, plastic flow in the substrate can generally be neglected (Thornton and Hoffman, 1989) and the thermal stress induced in the film by the substrate is given in a one dimensional approximation (neglecting the Poisson ratio) by:

$$\sigma_{th} = E_f (\alpha_f - \alpha_s) (T_a - T_m) \qquad (4.2)$$

where E_f is the Young's modulus for the film, α_f and α_s are the average coefficients of thermal expansion for the film and the substrate. T_a and T_m represent the annealing temperature and the measuring temperature (room temperature) respectively. In the present work, the crystallization annealing temperature of the films was 873 K. The

5. The residual stress calculations were not carried out in the present study, but it was reported that compressive stress (approximately -60 MPa) was developed in as-sputtered NiTi film produced by ion beam sputtering deposition (Walles, 1993). In this study, the deposition conditions was same as the present work and 0.35μm thick film deposited on Si single crystal was used.

thermal expansion coefficient of bulk copper is 17×10^{-6}/K (Metals Handbook, 1979). The thermal expansion coefficients of austenite NiTi is 11×10^{-6}/K, and that of martensite NiTi is 6.6×10^{-6}/K (Jackson *et al.*, 1972). The Young's moduli of the austenite and martensite phase in NiTi thin film alloys were measured to be 42.5 GPa and 22.5 GPa respectively (Hou, 1995). From the calculation using Eq. 4.3, if the annealed film possesses only B2 austenite or only B19' martensite phasees, the residual stresses will be approximately -147 MPa and -78 MPa respectively at room temperature (298 K). Therefore, the residual stress resulting from the annealing process leads to compressive stresses on the surface film (B2 or B19' phase). However, the actual residual compressive stress was expected to be slightly lower than this due to stress relaxation during cooling.

4.1.6. *Transformation Behavior*

Transformation temperatures varied with the compositions of the films. Figure 4-11 provides the idea of transformation sequences relating to composition of the films. The $Ni_{50.9}Ti_{49.1}$ film showed only R-phase transformation. The martensitic transformation showed an increase in titanium concentration. The highest M_s and M_f temperature values were observed for $Ni_{48.8}Ti_{51.2}$ film. These transformation temperatures decreased when the compositional deviation from 51 at.% Ti was increased, and similar results were obtained from continued runs. This behavior is different from bulk materials, where near-stoichiometric NiTi alloys showed the highest transition temperatures. In addition, the transformation temperatures of thin films were generally much lower than those expected of bulk alloys with similar composition. It is believed that oxygen contamination during film deposition may have affected the transformation behavior significantly. Most oxygen is bound in Ti_4Ni_2O, which was reviewed in section 2.3.2, and results in a decrease in the Ti concentration of the film matrix.

Transformation temperatures for various films used for surface modification of fatigue specimens are presented in Table 4-2 through 4-8. All data in this table were obtained from contemporaneously deposited surveillance specimens having identical deposition and vacuum annealing conditions given to the actual fatigue specimen.

Diffusion between the films and copper substrates was investigated, since transformation temperatures of NiTi alloys are sensitive to composition variation. Figure 4-12 shows the concentration profiles of nickel, titanium, and copper at the interface between $Ni_{48.1}Ti_{51.9}$ thin films and copper substrate before and after annealing. For as-sputtered film on a copper substrate, the concentration profile across the interface was very sharp, indicating that no interdiffusion occurred during deposition. For annealed films on copper substrates, the concentration profiles for each element became smoother at the interface. However, the diffusion layers of both the copper substrate and NiTi films were so limited that the effect of composition change on the transformation behavior of the overall surface film due to diffusion is negligible.

In summary, composition analysis indicated that titanium was depleted in the sputter-deposited films. This was produced primarily by preferential resputtering of Ti from the growing film and a low sticking coefficient of Ti. The deposited films showed a dense structure, which was attributed to a very low working gas pressure. As-deposited films were amorphous in structure and the crystallization process which followed provided their thermoelastic transformation properties. Diffusion between the films and copper substrates, during crystallization, was negligible. Most crystallized films underwent two well separated austenite ↔ R-phase ↔ monoclinic martensite transformations, and surface relief was observed due to the formation of martensite on the films.

4.2. Fatigue Experiments

4.2.1. Specimen Characteristics

As was indicated in Chapter 3, two different kinds of fatigue specimens were fabricated. Specimens with a flat surface on the gauge section were used for direct observation of crack development on the surface, and investigation of changes in crystal structure by X-ray diffractometry. Four different kinds of film-coated specimens were made on the flat surface in the gauge area of copper fatigue specimens. The specimens were designated as F1 through F4 depending on their transformation behavior and composition of the coated films. The transformation temperatures and compositions of the films are given in Table 4-2, and the resistivity curves are provided in Appendix.

Shallow notched specimens with various surface coatings and transformation temperatures were studied with respect to fatigue crack initiation life and surface damage accumulation rate. The transformation temperatures of the films were determined by electrical resistivity measurement, which are given in Appendix. The film types are classified into three different categories depending on the characteristics of the coated films. A/R series films revealed only B2 (austenite) ↔ R-phase transformation during thermal cycling between 373 K and liquid nitrogen temperature. In A/TE type films the A_f temperature was lower than 295 K and thus only the austenite phase existed at room temperature (298 K). A/SIM type films represent the film with an A_f temperature was higher 295 K. Both A/TE type film and A/SIM type film exhibited B2 (austenite) ↔ R-phase ↔ B19' (martensite) transformations in resistivity measurements. The number next to the film types indicates their relative A_f temperature, namely, the higher number means a higher A_f for that film type. The fatigue crack initiation life and transformation temperatures for the various films are listed in Table 4-3 through 4-9, including bare copper specimens and amorphous film coated specimens. In the present study, the test temperature (T_d) was generally fixed at 298 K and the A_f temperature of the films determined the expected transformational behavior during fatigue.

4.2.2. Cyclic Stress Strain Hysteresis

No significant difference in the stress strain hysteresis loops between surface modified and the unmodified specimens was observed. Figure 4-13 illustrates a typical example of the hysteresis loops recorded in the first 10 cycles of annealed polycrystalline copper. The yield stress of the specimen in the first cycle was very low (approximately 20 MPa) and increased with further cycles. During cyclic hardening, the stress amplitude and strain amplitude increased continuously. After reaching the saturation condition, the hysteresis loops maintained an essentially constant shape until the secondary cyclic hardening stage occurred. On occurrence of secondary cyclic hardening, the peak stresses and corresponding strain amplitudes slowly increased again up to fatigue failure.

4.2.3. Cyclic Hardening Curve and Saturation Stress

The cyclic hardening curve was obtained from the peak stresses on each cycle and the corresponding accumulated plastic strain. Figure 4-14 shows a typical example of the cyclic hardening of polycrystalline copper[6] under constant plastic strain amplitudes of 0.1 % ($\Delta\varepsilon_p$ = 0.2 %) and 0.15 % ($\Delta\varepsilon_p$ = 0.3 %). These experiments demonstrated that the fatigue life was slightly shorter and the saturation stress was higher at $\Delta\varepsilon_p$ = 0.3 % than at $\Delta\varepsilon_p$ = 0.2 %. Fatigue crack initiation life studies were carried out only for the specimens cycled at $\Delta\varepsilon_p$ = 0.2 % for various surface conditions. Cyclic hardening occurred rapidly in the first few cycles and the rate decreased gradually, then reached the saturation stage. The behavior depicted in these results are characteristics of cyclic hardening curves acquired from both bare copper specimens and NiTi film coated specimens. The saturation condition was obtained after approximately 250 cycles and the saturation stress was approximately 123 MPa regardless of the surface condition of the specimens. No significant differences were observed in the hardening rates and saturation stresses between bare copper and NiTi film coated specimens. These results indicated that the

6. All specimens were annealed at 1173 K for 1 hour.

film coatings, whether amorphous or crystalline, did not significantly affect the saturation stresses or hardening rates.

Cyclic hardening curves for unmodified specimens in the present investigation showed an initial saturation stage followed by a secondary cyclic hardening stage in Figure 4-14. The saturation stage lasted up to approximately 7,000 cycles ($2\Sigma\Delta\varepsilon_p = 28$) and then secondary cyclic hardening occurred. Identical behavior for secondary cyclic hardening was also observed for the surface film coated specimens.

4.3. Stress-Induced Martensitic Transformation in NiTi Film

The superelasticity effect results in unique stress-strain behavior in which anelastic shear strains of several percent occur when a martensite phase is induced by applied stress and reverted back to the original austenite phase by removing that stress. Deformation by this mechanism is able to endow exceptionally high fatigue life under strain controlled conditions. Therefore, surface modification with superelastically deforming materials, which can provide large strains without dislocation activity, may resist the concentrated strains which are the result of bulk plastic strain localization during fatigue. Evidence of formation of stress-induce martensite in the films on cyclically deforming substrate thus is significant in the present work. The finding of stress-induced martensite in the films suggests that the surface coatings, for which A_f is lower than the test temperature, are presumed to be superelastically deformed during cyclic deformation, resulting in delaying the onset of the kind of severe, localized surface damage that normally leads to fatigue crack initiation.

Stress-induced martensitic transformation was observed in $Ni_{50.3}Ti_{49.7}$ thin film alloy on plastically deformed copper specimens. Figure 4-15 illustrates the X-ray diffraction scans, taken at 298 K, of the $Ni_{50.3}Ti_{49.7}$ thin film coated specimen. Diffraction scan (d) showed a broad amorphous peak from the as-deposited film. Diffraction scan (c) was from the same specimen which had been annealed, furnace

cooled to 298 K, then quenched in liquid nitrogen, and allowed to warm back to room temperature. In this scan, the largest peak was from $(110)_{B2}$ but the other three peaks were from (002), $(11\bar{1})$ and (111) of monoclinic martensite respectively. Reheating the specimen for a few minutes to 400 K caused the martensite peaks to disappear, as shown in the scan from (b). Diffraction scan (a) displays diffraction peaks from the stress-induced martensite phase after the specimen was monotonically overloaded[7]. Since the furnace cooled specimen had only austenite peaks before deformation, the peak should be the same as that of the diffraction scan from (b). Therefore, this observation demonstrates the presence of substantial amount of stress-induced martensite in a NiTi thin film on a plastically deforming metallic substrate.

Similar results were obtained from cyclically loaded specimens which were coated with the same film as the specimen discussed above. The specimens were examined before and after cyclic loading to determine whether martensite had been stress-induced by the modest strain levels associated with the low cycle fatigue test. A specimen with an $Ni_{50.3}Ti_{49.7}$ film, fatigued for 11,755 cycles at a plastic strain amplitude of 0.0015 ($\Delta\varepsilon_p = 0.3\%$), showed clearly the presence of (002), $(11\bar{1})$ and (111) monoclinic martensite peaks along with a $(110)_{B2}$ and $(111)_{Cu}$ peaks, as shown in Figure 4-16. The relatively weak peaks compared to the peak from the austenite phase indicates that the martensite formation occurred over only limited areas of the specimen surface. It is possible, then, that it was induced only in regions which were subjected to large local strain excursions caused by underlying PSBs. Thus, it may be concluded that stress-induced martensite can form in NiTi thin films lying atop inhomogeneously deforming metallic substrates and thus can exhibit the superelastic effect during fatigue.

DSC data for a surveillance film[8] is shown in Figure 4-17. The $Ni_{50.3}Ti_{49.7}$ film displays distinct double endothems in the DSC scan on heating. The first endotherm

7. The specimen was smashed accidently and then the gauge section area suffered a high plastic deformation whose precise magintude is not shown.
8. The film was prepared by deposition on annealed copper foils placed near the gauge area of the fatigue specimen.

resulted from the martensitic transformation and the second one from the R-phase transformation. This is consistent with the enthalpy of the R-phase transformation which is very small (about 2-5 J/g) compared to the martensitic transformation (approximately 20 J/g). The austenite start (A_s) and finish temperatures (A_f) were 307 K and 345 K respectively. The martensite start temperature (M_s) was near 273 K and the martensite finish temperatures (M_f) was below 173 K. These were determined by X-ray diffractometry at various temperatures on cooling, and are given in Figure 4-18.

The critical stress for stress-induced martensite at room temperature (298 K) was calculated using Eq. (2.6), Clausius-Clapeyron equation. T_o, which is the equilibrium transformation temperature without an external applied stress, was approximated as $T_o = (M_s + A_s)/2 = 290$ K, and used a material density of 6.5 g/cm^3 and a theoretical transformation strain of 0.1299 (Matsumoto *et al.*, 1987). ΔH for the transformation was estimated to be 25 J/g, where $\Delta H = \Delta H_{M \rightarrow R} + \Delta H_{R \rightarrow A}$. The critical stress for stress-induced martensite of the film will thus be approximately 255 MPa at room temperature. This estimated value is believed to be low enough to form stress induced martensite in coated film in the regions of severe local straining above underlying PSBs[9].

On the other hand, it was reported that the pseudoelasticity effects were observed in both R-phase and martensitic transformations (Miyazaki *et al.*, 1989). R-phase transformation exhibited smaller enthalpy, a narrower hysteresis, and lower critical stress values than the martensitic transformation (Fukuda *et al.*, 1992). In other words, the R-phase can be formed with a small driving force. Therefore, the stress-induced transformation for the R-phase can occur more easily than that for martensite. Since the R-phase appears prior to the martensite, the initial R-phase will be formed in plastically deformed NiTi thin film alloys by applying an external stress at a certain temperature range, which was described in section 2.4.1. For example, if the T_r temperature of the

9. Considering that the localized strain at PSB is approximately 1% and the Young's modulus of austenite NiTi film, which was used in the present study, is 42.5 GPa (Hou, 1995), the stress of NiTi film on a PSB is expected to be slightly higher than 400 MPa.

film is near the test temperature, the shape memory and superelasticity effects of the R-phase can be expected. However, no distinguishable R-phase peak[10] was found in the X-ray diffraction scan of a A/TE1 type film coated specimen, with a T_r = 284 K, after fatigue at 298 K. Even though the stress induced R-phase can be formed in the films on deforming copper substrate at this condition, it is very difficult to distinguish whether the peak, which is near $2\theta = 42.8°$, is from the B2 or R-phase, especially when the $(111)_{Cu}$ peak is from the substrate[11]. Also, since the maximum transformational strain of the R-phase, subjected to an external applied stress, is very small, with the maximum shear strain of less than 0.3 % (Miyazaki and Otsuka, 1986), the stress induced R-phase would transform to martensite again at a higher strain (~1%) during cyclic deformation. Thus, the small peak of the R-phase may not be detected on the X-ray diffraction scan.

4.4. Surface Damage Accumulation

4.4.1. Surface Crack Formation on Flat Surface Gauge Area of Surface Modified Specimens

Four different kinds of film-coated specimens were made with a flat surface in the gauge area of copper fatigue specimens, which are give in Table 4-2. For the F1 specimen, a fully annealed copper foil was attached to the specimen which remained in place for the deposition process, resulting in a boundary between the thin film modified area and the completely uncoated pure copper. The specimen was examined for crack development between the coated and uncoated areas. The other specimens had fully covered gauge areas and were examined for crack density and crack modes. The specimens were cycled in strain control at a constant plastic strain amplitude of 0.015 ($\Delta\varepsilon_p$ = 0.3 %) and the saturation stress was approximately 140 MPa, regardless of the

10. Peak splitting below T_r, associated with R-phase formation from B2 austenite phase, was reported as $(011)_R$ and $(0\text{-}11)_R$ at 42.5° and 43° respectively (Ling and Kaplow, 1981).
11. Reinstallation of the 5 inch long specimen on a X-ray stage after mechanical test also caused a slight change in the height of exposed surface resulting in the peak shift, as shown in Figure 4-19.

surface condition. Tests were terminated when the maximum peak stress dropped by 1 %.

4.4.1.1. Specimen F1 Viewing through an optical micrograph showed no prominent cracks in the film coated area, while cracks and slip bands were developed in the uncoated area, as shown in Figure 4-20. A detailed SEM micrograph of the surface between a film coated and uncoated area of the specimen is shown in Figure 4-21. The strain amplitude and number of cycles in both areas of this specimen are identical. Direct comparison of the fatigue damage accumulation in the surface region was performed in the vicinity between the gauge section covering the film and the uncoated copper area.

It is obvious that the uncoated portion of the specimen behaves much differently than the coated part. In the unmodified region of the specimen (lower half), a significant number of cracks and severely extensive PSB extrusions were formed throughout the entire area, whereas the area coated with the film apparently has suffered no surface damage, as shown in Figure 4-21 (a). With the exception of the area at the edge of the film-copper boundary, the morphologies shown in these micrographs are typical of the behavior of the specimen as a whole. A detailed study of the coated portion of the specimen revealed no detectable signs of PSB extrusion or microcrack formation. As a whole, when the PSBs encountered the coated portion of the specimen, they became fully indistinct. It is noted that in the uncoated portion, the extrusion-intrusion bands in a substrate grain were clearly developed but those bands were totally suppressed when they projected into the coated zone, as shown in Figure 4-21(b). The result of fatigue tests, shown in this figure, are quite different from the results from the surface modifications by ion implantation. Unlike the surface modifications by ion implantation, distinguishable microscopic feature changes, such as the crack initiation mode changes (Morrison *et al.*, 1989) or slip line spatial density changes (Grummon, 1988), were not observed in the

coated area. The surface morphology changes with accumulated strain will be described in section 4.4.2.

Some PSB surface activity was present in the immediate vicinity of the film boundary, but this is considered to be an artifact associated with the masking procedures which slightly shadowed the film in this region, causing it to be much thinner, and also probably contamination of the film near the boundary. Occasionally, cracks were observed at a few areas such as near the film boundary (cracks from unmodified region) and at some delaminated areas of the film especially at the triple points of grain boundaries, which is marked by an arrow in Figure 4-22. But, in general, the film adhered very firmly and no cracking occurred from those locally uncovered areas (or at defected areas which were formed during deposition) as shown in Figure 4-23, where PSBs were developed in the copper substrate. This observation showed that these films strongly adhered to the matrix, suppressed PSB penetration to the free surface, and inhibited fatigue crack initiation.

4.4.1.2. Specimens F2 and F3 As was provided in Table 4-2, the films on specimens F2 and F3 exhibited a higher titanium concentration than stoichiometric NiTi alloy. In addition, the film on specimen F3 did not show transformation behavior in electrical resistivity measurement, as shown in Figure A-2. The crack modes and density of the films of specimens F2 and F3 were compared and analyzed.

An optical micrograph showed several cracks on specimen F2, as shown in Figure 4-24. Detailed crack mode and density on the specimen were studied on the SEM micrographs in Figure 4-25. The average distance between cracks, developed perpendicular to the loading direction, was 0.2 mm and the average crack length was approximately 0.4 mm. Most cracks developed perpendicular to the loading axis, while a few 'wrinkles' were observed parallel to the loading axis.

On the other hand, a high density of cracks was observed by an optical micrograph on specimen F3, as shown in Figure 4-26. A detailed SEM micrograph of the crack shapes is shown in Figure 4-27. The average distance between cracks, which developed perpendicular to the loading direction was approximately 0.06 mm and the average crack length was 0.6 mm. All cracks were produced in the transverse direction of the loading axis, and the films near those cracks were severely wrinkled parallel to the loading axis.

Almost identical features were observed on specimens F2 and F3, with only the crack populations and modes being slightly different. All cracks were developed perpendicular to the loading axis on both specimens F2 and F3. This result indicats that these cracks penetrated into the copper substrate from the surface film and propagated in the same direction as the lateral film cracking. This is in marked contrast to cracks in fatigued bare copper specimens, which evolved along the PSBs or grain boundaries associated with specific crystallographic directions, as was observed in the uncoated area of specimen F1. The high density of cracks on specimens F2 and F3 is believed to be the result of a high Ti concentration on the films, which resulted in the formation of Ti_2Ni precipitates. Ti_2Ni peaks were observed from X-ray diffraction scan of the specimen F3, as shown in Figure 4-28. The Ti_2Ni particles usually precipitated out at grain boundaries in NiTi alloys during the annealing process (Busch *et al.*, 1990; Chang, 1993) and caused deleterious effect on mechanical properties. The difference in crack population between specimen F2 and F3 may be from higher Ti concetration on F3 film, causing an increase in its brittleness. It can be attributed to the balance between the strength of the film and stress on the film. These relations result in more cracks on specimen F3 than on specimen F2, because the reduction in stress caused by cracking occurs only over a finite distance away from the crack plane.

On the other hands, the 'wrinkles' were developed parallel to the loading axis on both specimen F2 and F3. The 'wrinkles' which developed on the specimen F3 were

more frequently observed than on the specimen F2. This result occurred because of the relative distance between the cracks and the crack lengths. For the specimen F3, the distance between cracks was shorter and the average crack length was longer than that of the specimen F2. Careful observations by SEM showed that the 'wrinkles' occurred near the center of each crack; it is believed that the fatigue crack originated there. Since the thickness of the surface film is negligible compared to that of the substrate, the stress distribution in film is taken in two dimensions. A situation of plain stress typically exists in a thin film loaded in the plane of the film where there is no stress normal to the free surface. The 'wrinkles' in the film might be explained by 'compressive cyclic creep' in the films during fatigue testing. Consider alternating compressive and tensile stresses on the surface film along the loading axis due to cyclic deformation. While the tensile stress in the loading axis produces an extension along that axis on the film, it also produces a compressive strain perpendicular to that axis. The transverse strain would be balanced with the applied stress along the loading axis before cracking. However, the balance will be broken after developing cracks on the films, which were perpendicular to the loading axis. Let the loading direction be the x-axis and the transverse direction be the y axis, as shown in Figure 4-29. After cracks formed in the films, the tensile stress along the x-axis would act for crack opening and closing by alternating stresses. As a result, the stress effect in the x-direction might be nullified between cracks and only the stress along the y-axis would be left between them. Thus, it can be assumed that the crack propagated in the y-direction from the origin of the crack, which is believed to be the weakest area, during cyclic deformation. But the effect of the stress along the y-axis increases with decrease in the distance between cracks and it also increases with an increase in the crack length. It was considered that the residual compressive stress in the surface film, which was described in section 4.1.5, intensified the stress effect between the cracks. With an increasing the number of cycles, the crack length will increase, and thus the stress along the y-direction tends to go more to the compressive side continuously, which was named

'compressive cyclic creep' as shown in a schematic stress-strain response in Figure 4-29. The wrinkles are presumed to occur from the weakest area when the compressive stress was high enough to form. In this study, other stress effects, such as stress near crack tips, were ignored.

4.4.1.3. Specimen F4 An optical micrograph did not show any crack formation on the F4 specimen, as shown in Figure 4-30. The crack was found on the opposite side of the flat surface in gauge section area. Only a large crack was observed after faigue crack initiation, shown in Figure 4-31. It is different from the surface coated region of the specimen F1, in which the crack was formed on the uncoated area proir to the crack formed on the coated area. The crack on specimen F4 formed on the coating region.

In summary, the crack population and crack size of each specimen were significantly different depending on the film properties related to its comnposition, and the transformation temperatures with respect to the testing temperature (298 K). The coated area of specimen F1 and specimen F4 did not show any prominent cracks, while specimens F2 and F3 showed a relatively high cracking density. The relationship between the films and crack mode will be dicussed in following section.

4.4.2. Fatigue Damage Accumulation in Shallow Round Notched Surface Modified Specimens

Shallow round notched specimens with NiTi films were also studied after fatigue crack initiation occurred. All specimens were cycled in strain controlled at a constant plastic strain amplitude of $\Delta\varepsilon_p = 0.2$ %. All tests were terminated when the maximum peak stress was dropped by 1%, which was described in section 3.4.

4.4.2.1. Bare Polycrystalline Copper Figure 4-32 shows several extrusions of persistent slip bands in a polycrystalline copper specimen fatigued after 500 cycles ($2\Sigma\Delta\varepsilon_p = 2$). It is quite evident that the slip bands were formed only in specifically favored crystallographically oriented grains dependent upon the loading direction and compatibility with neighbor grains, especially at low cumulative strains during cyclic deformation. This observation showed that the slip lines indicated parallel primary single slips. The spacing of slip bands was almost equal in individual grains, but the intensities and shapes of extrusions were different from grain to grain. It is also apparent that the shape of PSB extrusions and the spacing of slip bands varied with orientation of the grains in a polycrystalline copper. Figure 4-33 illustrates a tongue-shape extrusion emerging at the crystal surface due to PSBs which exhibited a typical width of approximately 1 μm.

Successive observations of the same area of a copper specimen were carried out at various cumulative plastic strains. The specimen was reinserted in the testing frame and fatigued for a predetermined number of cycles and further observations were carried out using SEM. The specimen was observed after five interruptions of the fatigue test ($2\Sigma\Delta\varepsilon_p = 4$, 10, 20, and 40) and after fatigue crack initiation. An example of such observations is presented in Figure 4-34. The area, as a reference, was chosen to be easily identified in continued observations. Unlike the extrusion shown in Figure 4-33 which exhibited generally small and discontinuous tongue-shapes, the spacing of slip lines has become narrower and the extrusions have been altered to a continuous ribbon-shape upon increasing the number of cycles. These observations indicate that the extrusions with tongue-shapes were developed in only a small number of cycles and then grew and coalesced into ribbon-shapes with an increased amount of accumulated plastic strain. Continued observations showed that slip bands were developed in more grains and the extrusions were intensified continuously with increasing the number of cycles. The heights of extrusions and intrusions were larger, but the spacing was not changed any

further continued cycling. However, there was little change of surface morphologies between N = 10,000 ($2\Sigma\Delta\varepsilon_p = 40$) and N_I = ~15,000, where fatigue crack initiation occurred. Secondary slips occurred near the grain boundary in the reference area. The above observations demonstrated that the intrusions made notches where stress concentrations occurred and eventually fatigue cracks would initiate. It was also observed that crack nuclei formed at the intersection of the slip bands and grain boundaries (PSB-GB crack).

Another observation in SEM of fatigued polycrystalline copper after crack initiation was accomplished near grain boundaries, as shown in Figure 4-35. This observation shows the presence of secondary slip traces in the vicinity of grain boundaries. It is believed that such secondary slip systems near the grain boundary are activated to accommodate the strain compatibility between neighboring grains consisting of different crystallographic orientations. This is the major difference between single crystal and polycrystalline copper, where the secondary hardening related to secondary (or multiple) slip occurs due to a wide variety of orientations.

4.4.2.2. Amorphous Film Coated Specimens The surface morphology of the specimens were observed at low magnification after fatigue failure, as shown in Figure 4-36. Several major cracks developed in these specimens, unlike crystalline film coated specimens, which will be described in the following sections. Fatigue cracks propagated in a straight manner perpendicular to the loading-axis and the remaining surface area did not show any distigiushable features. Figure 4-37 (a) shows that amorphous NiTi film coated specimens demonstrated a typical brittle nature, with spalling of the films on the substrate. It is also observed that some part of the film was delaminated from the copper substrate, as shown in Figure 4-37 (b). Detailed examination of the crack shapes and directions on the film and substrate demonstrated

that the cracks penetrated from the surface film to the copper substrate regardless of the crystallographic orientation.

4.4.2.3. A/SIM Film Coated Specimens The surface morphologies, at low magnification, of the specimens A/SIM1 and A/SIM5 displayed a large crack which developed perpendicular to the loading axis after fatigue failure, as shown in Figure 4-38. The cracks developed small wavy morphologies, unlike the amorphous film coated specimens, but the crack displayed more of a straight character in the specimen A/SIM5 than that in the specimen A/SIM1. Observations near the crack tip area and near a large crack on the specimens were carried out at high magnification. It was found that all specimens had developed only one major crack in the high stress region, and the crack tip area of the specimen A/SIM1 is shown in Figure 4-39. However, it was revealed that very fine microcracks formed near the major crack and crack tip area of the specimen A/SIM5, which is shown in Figure 4-39. These microcracks also developed perpendicular to the loading axis and independent of substrate grain orientations, as shown in Figure 4-40.[12] But, these microcracks were not found in other A/SIM type specimens, which exhibited longer fatigue life.

4.4.2.4. A/TE Film Coated Specimens Observation of the surface morphology for the specimen A/TE1 at low magnification, also showed that a crack developed in the specimen. Surface rumples, also, were observed, as shown in Figure 4-41. It was found that the crack propagated in a wavy manner, as was observed crack tip area of the specimen A/TE1, shown in Figure 4-42. All crystalline film coated specimens showed wavy crack propagation, while the amorphous film coated specimens displyed a straight crack propagation. However, the high degree of 'zig-zag' crack

12. In this micrograph, the grain boundaries, including twin boundaries, were revealed underneath of the film as an artifact of electropolishing.

propagation was observed near the crack tip area, which indicated that crack propagation would be slower than in other specimens.

Since the servo-hydraulic grip allowed for specimen removal and reinsertion, it was possible to monitor a specific region of the specimen surface using SEM. It was checked whether the fatigue crack initiation life was affected by several interruptions of the test or not. The resultant fatigue lives for both cases did not show any effect due to the interruption of the test; the data is presented in Table 4-7. In the previous section, it was found that cyclic hardening of specimens occurred only at the very early stage of the fatigue tests and then reached the saturation stage, which was approximately after 250 cycles under present fatigue conditions. Thus, the evolution of surface damage accumulation was not monitored from the cyclic hardening stage but from the saturation stage until the fatigue crack initiated. Successive fatigue damage accumulations of A/TE2-4 and A/TE3-1 specimens were also investigated at various accumulated strains, that is, $2\Sigma\Delta\varepsilon_p$ = 4, 10, 20, and 40, 80 and after fatigue crack initiation, as shown in Figure 4-43 for the A/TE3-1 specimen. The observations of surface damage accumulation in A/TE2-4 and A/TE3-1 specimens disclosed very similar results. No sign of surface cracks was found until $2\Sigma\Delta\varepsilon_p$ = 80. Unlike the unmodified copper specimens in which damage accumulation occurred continuously, as shown in Figure 4-33, the crack formation was substantially delayed in these specimens and then the crack developed abruptly.

4.4.2.5. A/R Film Coated Specimens The observation of surface morphology for specimen A/R did not show any significant difference from other crystalline film coated specimens, which revealed a crack perpendicular to the loading axis. SEM micrograph near crack tip area was given in Figure 4-44.

In summary, for both shallow round notched specimens and flat gauge sectioned specimens, all cracks were produced in the transverse direction against its loading direction whether the surface films were crystalline or amorphous in structure. It is noted that cracks of both amorphous and crystalline film coated specimens initiated from the surface film first and propagated to the substrate. The surface observation results showed that the adhesion between substrate and film was very strong, and thus once a microcrack was formed at the surface this cracking led to failure of the substrate. If the adhesion is not strong enough to transfer the stress, the film will be delaminated from the substrate. Therefore, once cracks are formed on the surface film, it is possible that the fracture of the film generates a notch effect and facilitates the propagation of fatigue crack into the matrix, and also that growth of the crack within the interior is due to the loss of the protective influence of coating, thus markedly impairing fatigue life.

The crack shape was related to fatigue crack intiation life, which was given in Table 4-3 thrrough Table 4-9. Amorphous film coated specimen showed several straight cracks, which revealed the shortest fatigue life, while other film coated specimens revealed a large crack at the shallow notched area. A/TE type film coated specimens demonstrated a high degree of wavy crack propagation, which exhibited the longest fatigue initiation life. A/SIM5 specimen dislplayed very fine 'hairy' cracks, which also were deveolped perpendicular to the loading axis, associated with a large crack.

4.5. Fatigue Crack Initiation Life

Shallow round notched specimens were used for studying fatigue crack initiation life. Fatigue crack initiation lives for the surface-modified specimens were evaluated from cyclic hardening curves defined by a 1 % drop from the peak stress. The results of fatigue crack initiation life for the surface films with various transformation behaviors, including bare copper specimens, are given in Table 4-3 through Table 4-9.

4.5.1. Bare Copper specimens The annealed bare copper specimens were used as a baseline comparing fatigue crack initiation lives for the specimens given in Table 4-3. The average fatigue crack initiation life (N_I) was 15,292 and its standard deviation was approximately 2,448.

4.5.2. Amorphous Film Coated Specimens The fatigue initiation life of amorphous film coated specimens was reduced by approximately 30 % compared to that of unmodified pure copper specimens. Degradation of fatigue properties of copper in amorphous film coated specimen resulted from the brittle nature of the film, which was explained in previous section. It is normal to find that amorphous materials exhibit brittle behavior before a well defined yielding in the stress strain relation and strong inhomogeneous plastic flow (Kimura and Masumoto, 1983). The short fatigue life of amorphous film coated specimens is attributed to these characteristics of amorphous materials. Thus, fatigue failure occurs from the growth of cracks nucleated at defects, and then facilitates crack propagation into the matrix.

4.5.3. A/SIM Film Coated Specimens The A/SIM type film coated specimens, which exhibited relatively high transformation temperatures, showed approximately 50% improvement over the bare copper specimen. Since the A_f temperature of A/SIM type films was slightly higher than the ambient temperature, the stress induced martensite formed during cyclic loading was retained in the sample after being removed from the load frame. The retained stress induced martensite peaks from X-ray diffraction study were observed from A/SIM type film coated specimens after fatigue, which was given in Figure 4-16. The retained martensite is presumably due to the stabilization of the stress-induced martensite formed during cyclic deformation of the film. The results for A/SIM type film ($A_f \geq T_d$) coated specimens showed that the fatigue crack initiation life increased with decreasing A_f temperatures, as shown in Figure

4-45. The A/SIM1 type film coated specimens demonstrated the best fatigue strength among A/SIM type film coated specimens. A/SIM5 type film coated specimen showed an improved fatigue strength, but the least among these type of film coated specimens. Since the test temperature was well below A_s for A/SIM5 type film, once the martensite phase forms at highly localized strain areas in the film on the deforming substrate, the martensite will remain stable throughout the remainder of the fatigue test.

A/SIM4 type film coated specimens were tested at different conditions from other A/SIM type film coated specimens, which were tested at 298 K. A/SIM4 type film coated specimens, with the A_f of 309 K and the A_s of 263 K, were tested at 276 K.[13] The crystal structure of the films prior to the fatigue test was expected to have dual phases of thermally-induced martensite and R-phase mixture under these conditions. A/SIM4 film type coated specimens showed better fatigue crack initiation life than other A/SIM type film coated specimens, whose films were austenitic before the fatigue test. This is probably a consequence of the reversible intervariant boundary motion of pre-existing martensite in the A/SIM4 film. Additionally, the favorably oriented stress-induced martensite variant formed during tension will be different from that formed in compression in other A/SIM type films. In addition, these stress-induced martensites formed during cyclic deformation will remain stable throughout the remainder of the fatigue test, because the A_f temperatures were higher than the test temperature (T_d = 276 K). Thus, the superelasticity effect in those films may less than in A/SIM4 type film. This contradicts the result of Melton and Mercier (1978), where a higher fatigue life was observed for stress-induced martensite compared with thermal matensite. Melton and Mercier claimed that no selection of favorable variants in a thermal martensite might occur with respect to the applied stress. However, it is not clearly understood which mechanism has been dominant in A/SIM4 film during cyclic deformation.

---

13. The specimens were quenched by liquid nitrogen, and then warmed back to 276 K, which temperature was maintained during the fatigue tests.

4.5.4. A/TE Film Coated Specimens The A/TE1 type film coated specimen, whose A_f temperature was lower than the test temperature (T_d = 298 K), showed the greatest improvement in fatigue crack initiation life. This film was believed to have a substantial amount of stress induced martensite formed during cyclic deformation which, however, is presumed to have reverted back to austenite after removal from the load frame. The unrecovered strain[14] depends on the test temperature relative to the A_f temperatures. A minimum in unrecovered strain is usually obtained from at 10 K to 30 K above the A_f, and the unrecovered strain increased at higher or lower temperature (Hou, 1995; Miyazaki *et al.*, 1981). The unrecovered strain was attributed to residual martensite for $T_d > A_f$, which could be recovered after heating, and slip of martensite phase for $T_d < A_f$, which would not be recovered. For A/TE type film coated specimens, the test temperature was approximately 23 K to 35 K higher than A_f for A/TE type films. If all A/TE films are presumed to behave superelastically at present test conditions, the critical stresses for inducing martensite will increase with decreasing A_f, according to the Clausius-Clapeyron relation. Therefore, the films are expected to have a higher critical stress with a full recovery when the slip of austenite is not involved among A/TE type films. A/TE1 type film coated specimens, which exhibited the longest fatigue initiation life, were tested at approximately 35 K above A_f, suggesting that transformational superelasticity in coatings might be applicable to the enhancement of fatigue properties of substrates. It can be connected with the stress-strain studies of NiTi film produce by Hou (1995), where the perfect superelastic behavior was found at approximately 30 K above its A_f. The stress for slip in martensite and austenite phases also may increase due to the internal defects which was formed during film deposition. This result is comparable to the observations by other research groups, where the critical stress for inducing martensite increases with increasing test temperatures and the fatigue

14. The unrecovered strain is defined as the strain, when the stress is relesed to zero, from the origin of stress-atrain curve, which was shown in Figure 2-13.

life of NiTi alloys improves with increasing the test temperature (T_d) above A_f, but below M_d (Miyazaki, 1986).

Fatigue crack intiation life are plotted as a fuction of temperature difference (T_d -A_f) for A/TE and A/SIM type film coated specimens, whose A_f temperatures of the films ranged from 263 K to 322 K, in Figure 4-46. The results indicate that the fatigue crack initiation life increased gradually when the difference between the test temperature and the A_f temperature of the film increased. Some of the martensite induced during cyclic deformation would be stabilized when $T_d \leq A_f$, whereas most of the induced martensite presumed to revert back to austenite when $T_d > A_f$. Even though T_d was slightly higher than A_f, unrecovered martensite was observed in $Ni_{50.8}Ti_{49.2}$ film, which is shown in Figure 2-13. Therefore, the perfect superelasticity of NiTi thin films can be expected when the test temperature is slightly higher than A_f. In other words, the improvement in fatigue life can be achieved by reducing the A_f relative to the test temperature. However, when the specimen is tested well above A_f, that is $T_d >> M_d$, the film may not form stress induced martensite and the amount of unrecovable strain due to slip of austenite will increase[15].

4.5.5. A/R type Film Coated Specimens A/R type film coated specimens, which showed only R-phase transformation, displayed better fatigue properties than average A/SIM type film coated specimens, but worse than average A/TE type film coated specimens. This prolonged fatigue strength of A/R type film coated specimens can be attributed to the high ductility and yield strength of the austenite phase in the film, but not to the superelasticity of R-phase of the film. Even though the R-phase can be stress induced and exhibit pseudoelasticity, the transformational strain may be relatively small. In addition, the transformation strain associated with the rearrangement of the R-phase variant decreases with increasing temperature difference (T_d - T_r)

15. The yield stress of austenite is in ranges of 200 to 800 MPa at 473 K depending on Ni concentration (Miyazaki *et al.*, 1991), and the stress of austenite film lying on PSB is enough to induce slip.

(Miyazaki and Ostuka, 1986) and thus the strain for R-phase is assumed to be diminished or affected little at the present test temperature. Therefore, the austenite phase film might suppress the formation of extrusions and intrusions on the surface, thereby enhancing the fatigue lifetime.

The results of fatigue crack initiation life indicates that all crystallized NiTi film coated specimens demonstrated longer life and amorphous film coated specimens showed shorter fatigue life than the bare copper specimens, as shown in Figure 4-47. The stress-strain behavior for the surface film and substrate during cyclic deformation may occur two ways. If the strain localization does not occur before fatigue crack initiating in a material, the relations between the discrete surface film and the substrate by Greenfield and Purohit (1980) can be applied due to the same axial strain on the film and substrate near the interface. Considering this approach, the stresses on the film and substrate depend only on their Young's modulus and yield strength. Since the Young's modulus is lower for crystallized NiTi film and the yield strength of crystallized NiTi film is higher than those of copper[16], the surface layer will experience less plastic (or only elastic) deformation than the substrate during fatigue. Thus, it is desirable for fatigue that the surface film hold higher compliance and yield strength than the substrate.

However, when the strain is localized into PSBs in a polycrystalline copper with increasing the number of cycles and the plastic shear strain in the PSB is about 1%, regardless of the applied plastic strain amplitude (Hunch and Neumann, 1986). As a result, the strain of the surface film on PSBs and overall bulk are not identical any longer. Thus, once the plastic shear strain is localized in the substrate during cyclic deformation, the surface film above an underlying PSB will encounter a large strain. The computation by finite element model showed if the surface film on a PSB responds only elastically, the extreme tensile (or compressive) stress on the film could well approach 1 GPa

16. The Young' moduli of the austenite and martensite phase in NiTi alloy are 42.5 GPa and 22.5 GPa, and the yield stress is 100 MPa near M_S, where the yield stress is minimum (Hou, 1995). The Young' modulus of copper is 120 GPa and the yiels stress of annealed is ~20 MPa.

(Grummon *et al.*, 1990).[17] But, yielding of the surface film will occur before reaching such a high stress level on the film. Therefore, the stress-strain behavior of the bulk, PSB, and the presumed superelastic film lying atop active slip bands will be different. Schematic stress strain curves by this model are depicted in Figure 4-48. The overall specimen displayed a narrower hysteresis loop than PSB region. The slope of superelasitc film on loading is steeper than unloading due to the formation of stress induced martensite, but the slope for a copper substrate is much steeper ($E_{Cu} > E_{NiTi(A)} > E_{NiTi(M)}$).

Based on the above model, the differences in fatigue crack initiation life for crystalline film modified specimens are thought to be mainly due to two reasons. One is due to the reversibility of film deformation during cyclic loading, which in turn relates to transfromation temperatures of the films and test temperature, i.e., the amount of unrecoverable strain. During cyclic deformation, the thermoelastic martensite in a surface film is presumed to exhibit twinning pseudoelasticity by the reversible motion of martensite twin boundaries at below M_s temperature. The austenite phase is assumed to show superelastic behavior by formation of stress-induced martensite below the M_d temperature. In addition, twinning pseudoelasticity in the austenite phase of NiTi alloys, even well above M_d (Duerig and Zadno, 1990), might improve the fatigue life. However, the unrecovable strain in martensite, if external heat is not supplied, and in austenite, above M_d, are larger than that in superelastically behaved austenite. Thus, it is expected that the surface film, which has superelastic properties, is more effective in resisting large strains induced during fatigue.

The other reason for prolonged fatigue life of NiTi film coated specimens may result from the high ductility and strength of the surface film (Grummon *et al.*, 1988). The Young's modulus of copper is higher than that of NiTi alloy and the yield strength of

---

17. In their study, the shear modulus of the ion beam surface microalloyed film is 66.3 GPa. However, since the shear modulus of NiTi alloy, which was used in present study, is around 27 GPa (Jacson *et al.*, 1972), the stress of NiTi film on a PSB is expected to be slightly higher than 400 MPa.

the austenite phase of NiTi alloy is higher than that of copper. These results mean that the ability of NiTi crystalline film to block PSB extrusion is attributed not only to superelastic deformation of the film, but also to its strength and ductility. It is important to note that the increase in fatigue life is associated with the retardation or near elimination of the formation of PSBs on the surface by NiTi thin film coatings.

4.5.6. Effect of Post Annealing on Fatigue Crack Initiation Life

The effect of post annealing, after cycling to a specified accumulated plastic strain ($2\Sigma\Delta\varepsilon_p = 40$), on fatigue crack initiation was studied. It is important to raise the critical stress for slip in order to stabilize superelasticity characteristics against cyclic deformation (Miyazaki *et al.*, 1986). Work hardening was expected due to the introduction of dislocations in the film lying atop of a large locally strained substrate during fatigue. Thus, the post annealing process might facilitate precipitation hardening and/or the annihilation and rearrangement of dislocations introduced in the film during cyclic deformation. The former process can be expected to increase the critical stress for slip by precipitate hardening, resulting in enhanced superelastic effects and thus possibly increased fatigue life. After cycling up to approximately 10,000 cycles, A/TE3-3 and A/TE3-4 specimens were removed from the load frame, and then annealed for 20 minutes at 673 K in vacuum[18]. After heat treatment, the specimens were cycled until fatigue crack initiation occurred. The fatigue crack initiation life, for heat treated specimens, was slightly longer (approximately 15 %) than that for the untreated ones, as shown Figure 4-49. However, this slight change in fatigue lifetime can be affected by not only annealing the film, but also annealing the copper substrate itself. The result of post annealing the films after cycling was not a very effective way to improve the fatigue life in the present condition. It is believed that the limited post annealing time to prevent the formation of

18. According to precipiattion process in NiTi alloy, the formation of precipitate was insufficient aged temperature below 673 K (Nishida *et al.*, 1986), and thus lowest possible temperature, expected to be formed fine precipitates in the film, was chosen.

precipitates in NiTi film and the diffusion of Cu, Ni, and Ti atoms was not long (high) enough to change the internal structure of the film. The effect of post annealing associated with formation of precipitates and texture and diffusion between film and substrate on fatigue lifetime of NiTi film coated specimen needs more study.

Summary

Amorphous NiTi films demonstrated their brittleness resulting in the development of straight fatigue cracks perpendicular to the loading axis on the surface. The fatigue crack initiation life of amorphous film coated specimens was reduced compared with that of bare copper specimens. However, the fatigue cracks in all crystalline film coated specimens formed wavy morphologies and their fatigue crack initiation lives were longer than that of bare copper specimen. Fatigue cracks, in general, were developed perpendicular to the stress axis in both amorphous and crystalline film coated specimens and propagated from the surface film to the substrate. Fatigue crack initiation life for crystalline NiTi film coated specimens was related to the transformational characteristics of their surface film. The greatest improvement in fatigue crack initiation life was observed from A/TE type film coated specimens, which $A_f > T_d$, and was related to the superelastic effect of surface films. A/R type film coated specimens also showed better fatigue properties than bare copper specimens. The improvement of fatigue life in crystalline NiTi film coated specimens suggests that the ability of NiTi crystalline film to block (or suppress) PSB extrusion from the copper substrate, resulting in the inhibition of fatigue crack initiation, is attributed not only to superelastic deformation of the film, but also to its strength and ductility.

5. CONCLUSIONS

NiTi thin films, which give rise to shape memory and superelastic effects, were evaluated as a new surface coating approach to improve the fatigue lifetime in polycrystalline copper. The films were produced by ion-beam sputter deposition on copper substrates and the thickness of the deposited films on fatigue specimens was maintained approximately 3 μm. All the as-sputtered films were deposited on cold substrates and the resultant films were amorphous in structure. Subsequent crystallization annealing was done, using a heating rate of 10 K/min. and maintained at 873 K for 10 minutes. The average grain size was 3 - 5 μm, which was larger than the thickness of films.

Followings are the detailed conclusions of the present study:

(1) Strong adhesion between the film and substrate was obtained as a consequence of ion-cleaning a substrate and highly energetic atom bombardment during ion-beam sputter deposition.

(2) The concentration of titanium in the deposited films was always lower than that of the effective target surface, $Ni_{47}Ti_{53}$, and increased with increases in vertical emission angles. Depletion of titanium in the film is attributed to the preferential resputtering of titanium from growing films and the lower sticking coefficient of titanium relative to nickel. The directionality of the beam and the working conditions are responsible for variation in concentration in the deposited films.

(3) Annealed films exhibited lower transformation temperatures than near stoichiometric NiTi bulk alloys. Short annealing time and oxygen contamination during

deposition is believed to be the main factors. Oxygen, especially, can be bound in Ti_4Ni_2O resulting in a decrease in a Ti concentration of the films.

(4) Surface relief, due to the formation of thermally induced martensite, was created on the free surface of the films. The martensite developed in random directions on the film, unlike triangular morphology of B19' martensite in bulk alloys, behavior which can be attributed to thin film constraint effects and residual stresses.

(5) Stress-induced martensites were produced in NiTi thin films, whose A_f was higher and M_s were lower than the test temperature (T_d = 298 K), on a plastically deforming copper substrates after cyclic deformation. Once stress-induced martensite was formed from the initial austenite, the martensite could be retained but the area was expected to be limited due to the strain localization during cyclic deformation.

(6) Amorphous NiTi films accelerate fatigue crack initiation, which is a result of their brittle nature, and thus a shortened fatigue life of the copper specimens.

(7) Crystalline films improved the fatigue life by inhibiting PSB extrusions, resulting in the suppression of fatigue crack initiation. This is attributed not only to superelastic deformation of the films, but to their strength and ductility as well. The greatest improvement in fatigue crack initiation life was achieved from A/TE1 type film coated specimens ($Ni_{49.6}Ti_{50.4}$: A_f (263 K) < T_d (298 K)), which showed approximately 100 % ($N_I^{A/TE1\ film} / N_I^{Cu} = 2.02$) improvement over bare copper specimens.

(8) Thermoelastic NiTi coatings increase the fatigue life of a specimen, when the difference between T_d and A_f becomes more positive in value.

(9) All cracks developed perpendicular to the loading axis, transfered from the film to the subsrate, whether the surface films were crystalline or amorphous in structure. However, the fatigue lifetime of coated specimen was related to their crack modes, the longer fatigue initiation life of specimen exhibited the higher degree of wavy crack propagation.

Directions for Future Research

The study presented herein showed the possibility of a new surface alloying system, which exhibits the thermoelastic martensite transformation, to improve the fatigue life of structural metals. However, there are questions remaining and more areas to study related to the transformation behaviors, especially in the thin film form of the NiTi alloy.

First of all, the thin film form of the NiTi alloy produced by sputtering deposition exhibits several behaviors that differ from the bulk material due to the non-equilibrium state of the film. The transformation temperature varies with compositions, inclusions, heat treatment, and the internal stresses induced by defects. Thus, the parameters to decide its transformation temperatures should be adjusted so that the film can be applied practically. In addition, when the films are deposited on metals such as Fe, Ni, and Cr, expected diffusion between film and substrate would occur whether the cold substrate deposition, which required a crystallization process, or the hot substrate deposition was used. The diffusion of each element in film and substrate changes the relative composition of the deposited films, which affects the physical and mechanical properties, especially if the annealing temperature is high and the cooling rate is slow. Therefore, the effects of diffusion, precipitates, and texture formations during deposition and/or annealing processes on fatigue lifetime are left for future.

Even though physical properties of the coated films were normally identical, the fatigue lifetimes may increase or decrease depending on the thickness of the film due to a change of stress distribution. The boundary conditions between the surface film and substrate can be constructed and related to the balance of stress and strain behaviors during cyclic deformation. Detailed study of dislocation substructures near the interface region between the film and the substrate using TEM should be carried out so that surface hardening (softening) or secondary hardening phenomena could be interpreted.

Table 2-1. Cyclic Stress-Strain Characterictics of FCC Crystals. (Suresh, 1991)

Material	$\gamma_{pl,AB}$	$\gamma_{pl,BC}$	τ_s^* (MPa)
Cu (4.2 K)	1.0×10^{-4}	3.0×10^{-3}	73.0
Cu (77.4 K)	—	8.0×10^{-3}	48.0
Cu (295 K)	6.0×10^{-5}	7.5×10^{-3}	27.5
Cu (523 K)	1.0×10^{-4}	1.0×10^{-3}	14.0
Cu-2.0 at% Al (295 K)	1.0×10^{-4}	3.0×10^{-3}	33.0
Cu-5.0 at% Al (295 K)	—	—	32.0
Cu-2.0 at% Co (295 K)	3.0×10^{-4}	5.0×10^{-3}	27.5
Ni (295 K)	1.0×10^{-4}	7.5×10^{-3}	52.0
Ag (295 K)	6.0×10^{-5}	7.5×10^{-3}	17.5
Al-1.6 at% Cu (295 K)	1.5×10^{-4}	1.5×10^{-3}	95.0

$\gamma_{pl,AB}$ is the plastic strain amplitude of starting the plateau stage in CSS curve.

$\gamma_{pl,BC}$ is the plastic strain amplitude of ending the plateau stage in CSS curve.

τ_s^* is the saturation stress in CSS curve.

Table 2-2. Sputtering Yield Data for Various Metals (atoms/ions)

Sputtering Gas Energy (eV)	He 500	Ne 500	Ar 500	Kr 500	Xe 500	Ar 1,000	Ar Threshold Voltage(eV)
Ag	0.20	1.77	3.12	3.27	3.32	3.8	15
Al	0.16	0.73	1.05	0.96	0.82	1.0	13
Au	0.07	1.08	2.40	3.06	3.01	3.6	20
Be	0.24	0.42	0.51	0.48	0.35		15
C	0.07	-	0.12	0.13	0.17		
Co	0.13	0.90	1.22	1.08	1.08		25
Cu	0.24	1.80	2.35	2.35	2.05	2.85	17
Fe	0.15	0.88	1.10	1.07	1.00	1.3	20
Ge	0.08	0.68	1.1	1.12	1.04		25
Mo	0.03	0.48	0.80	0.87	0.87	1.13	24
Ni	0.16	1.10	1.45	1.30	1.22	2.2	21
Pt	0.03	0.63	1.40	1.82	1.93		25
Si	0.13	0.48	0.50	0.50	0.42	0.6	
Ta	0.01	0.28	0.57	0.87	0.88		26
Ti	0.07	0.43	0.51	0.48	0.43		20
W	0.01	0.28	0.57	0.91	1.01		33

Table 4-1. Measured Concentrations of Ni and Ti in Deposited NiTi Thin Film for Different Vertical Emission Angles.

(Ni-Ti at.%)

Angle	1	2	3	4	5	6	7	8	9	10	Average
27.6°	51.6-48.4	53.8-46.2	–	–	–	–	–	–	–	–	52.70-47.30
38.4°	–	–	51.6-48.4	51.7-48.3	51.1-48.9	50.5-49.5	51.3-48.7	50.3-49.7	–	–	51.08-48.92
39.3°	–	–	–	–	–	–	–	–	49.4-50.6	50.7-49.3	50.05-49.95
41.5°	50.7-49.3	51.0-49.0	50.5-49.5	50.7-49.3	49.9-50.1	49.6-50.4	50.5-49.5	49.8-50.2	49.3-50.7	50.1-49.9	50.21-49.79
43.8°	–	–	–	–	–	–	–	–	48.7-51.3	50.0-50.0	49.35-50.65
44.8°	–	–	48.9-51.1	50.0-50.0	48.1-51.9	48.9-51.5	49.5-50.5	48.4-51.6	–	–	48.97-51.03
57.2°	48.5-51.5	47.7-52.2	–	–	–	–	–	–	–	–	48.10-51.90

Table 4-2. Transformation Data, Compositions, and Fatigue Crack Initiation Life for NiTi Thin Films on Flat Gauge Sectioned Copper Fatigue Specimens.

Specimen	Film Composition (Ni-Ti at.%)	M_f	M_s	A_s	A_f	Fatigue Crack Initiation Life (N_I)	Transformation Temp. Measuring Method
F1	50.3-49.7	(<100 K)	273 K	307 K	354 K	11,755	DSC
F2	46.5-53.5	131 K	263 K	238 K	293 K	12,840	ER
F3	44.9-55.1	-	-	-	-	11,185	ER
F4	48.3-51.7	(<100 K)	211 K	244 K	270 K	15,059	ER

* DSC: Differential Scanning Calorimetry, ER: Electrical Resistivity

Table 4-3. Fatigue Tests on Bare Copper Specimens and Amorhpous Film Coated Specimens.

(Test Temperature: 298 K)

Specimen	Film Type	Sat. Stress (MPa)	Max. Peak Stress (MPa)	Fatigue Crack Initiation Life (N_I)
Amor.-1	Amor-	122	126.6	9,792
Amor.-2	phous	123	128.4	11,473
Amor.-3		123	129.1	12,517
Amor.-4		123	127.9	9,942
Ave.		**123**	**128**	**10,931**
Bare Cu-1	N/A	121	129.4	21,453
Bare Cu-2		121	128.9	15,199
Bare Cu-3		123	131.1	15,296
Bare Cu-4		122	129.1	12,117
Bare Cu-5*		125	134.1	14,415
Bare Cu-6		123	130.3	15,372
Bare Cu-7		123	129.1	14,245
Bare Cu-8		124	132.9	16,157
Bare Cu-9		122	128.4	12,384
Bare Cu-10**		123	131.7	17,568
Bare Cu-11**		123	130.3	14,008
Ave.		**122.5**	**130.5**	**15,292**

* Damage Accumulation was monitored (N = 1,011-2,518-5,025-10,032-14,415).

** After cycling up to 10,000 cycles, the surface film of specimens were annealed for 20 min. at 673 K then resumed cyclic deformation until fatigue crack initiation occurred.

Table 4-4. Transformation Temperatures and Composition of A/R Film.

Film Type	Ni-Ti at.%	M_f	M_s	A_s	A_f	T_r	T_r'
A/R	49.1-50.9	-	-	-	-	283 K	297 K

Table 4-5. Fatigue Tests on A/R-type Specimens.

(Test Temperature: 298 K)

Specimen	Film Type	Sat. Stress (MPa)	Max. Peak Stress (MPa)	Fatigue Crack Initiation Life (N_I)	Remark
A/R-1	A/R	122	135.2	28,149	
A/R-2		123	131.2	21,485	
A/R-3		123	133.3	21,965	
A/R-4		123	134.9	28,801	
Ave.		**123**	**133.4**	**25,100**	

Table 4-6. Transformation Temperatures and Compositions of A/TE-type Films.

Film Type	Ni-Ti at.%	M_f	M_s	A_s	A_f	T_r	T_r'
A/TE 1	49.6-50.4	(<100 K)	228 K	210 K	263 K	284 K	290 K
A/TE 2	50.5-49.5	105 K	213 K	252 K	269 K	283 K	294 K
A/TE 3	47.8-52.2	134 K	224 K	254 K	275 K	284 K	299 K

Table 4-7. Fatigue Tests on A/TE-type Specimens.

(Test Temperature: 298 K)

Specimen	Film Type	Sat. Stress (MPa)	Max. Peak Stress (MPa)	Fatigue Crack Initiation Life (N_I)	Remark
A/TE 1-1	A/TE 1	123	136.5	29,372	
A/TE 1-2		124	138.5	31,316	
A/TE 1-3		122	132.2	31,015	
A/TE 1-4		125	137.8	30,001	
Ave.		**123.5**	**136.3**	**30,426**	
A/TE 2-1	A/TE 2	123	134.5	27,317	* Damage Accumulation was monitored (N = 1,016-2,522-5,040-10,029-20,035)
A/TE 2-2		125	132.8	23,297	
A/TE 2-3		123	136.4	29,299	
A/TE 2-4*		124	135.9	26,551	
Ave.		**123.5**	**134.9**	**26,616**	
A/TE 3-1*	A/TE 3	123	133.0	24,861	* Damage Accumulation was monitored (N = 1,010-2,517-5,023-10,034-20,039)
A/TE 3-2		123	133.8	25,480	
Ave.		**123**	**133.4**	**25,170**	
A/TE 3-3**		123	135.5	30,972	
A/TE 3-4**		123	133.1	26,472	
Ave.		**123**	**134.3**	**28,772**	

** After cycling up to 10,000 cycles, the surface film of specimens were annealed for 20 min. at 673 K then resumed cyclic deformation until fatigue crack initiation occurred.

Table 4-8. Transformation Temperatures and Compositions of A/SIM-type Films.

Film Type	Ni-Ti at.%	M_f	M_s	A_s	A_f	T_r	T_r'
A/SIM 1	47.1-52.9	(<100 K)	245 K	277 K	296 K	305 K	326 K
A/SIM 2	48.1-51.9	195 K	263 K	254 K	299 K	317 K	321 K
A/SIM 3	47.3-52.7	174 K	243 K	256 K	300 K	295 K	323 K
A/SIM 4	47.7-52.3	230 K	288 K	263 K	309 K	311 K	316 K
A/SIM 5	48.8-51.2	250 K	286 K	311 K	322 K	316 K	323 K

Table 4-9. Fatigue Tests on A/SIM-type Specimens.

(Test Temperature: 298 K)

Specimen	Film Type	Sat. Stress (MPa)	Max. Peak Stress (MPa)	Fatigue Crack Initiation Life (N_I)
A/SIM 1	A/SIM 1	121	131.5	25,377
A/SIM 2-1	A/SIM 2	125	134.5	20,232
A/SIM 2-2		125	135.5	26,403
A/SIM 2-3		122	132.2	26,164
A/SIM 2-4		123	133.2	21,728
Ave.		**123.7**	**133.8**	**23,631**
A/SIM 3-1	A/SIM 3	125	133.2	22,241
A/SIM 3-2		124	132.4	25,335
A/SIM 3-3		122	130.5	21,064
A/SIM 3-4		123	131.8	25,804
Ave.		**123.5**	**132.0**	**23,611**
A/SIM 4-1*	A/SIM 4	124	134.5	25,952
A/SIM 4-2*		125	133.8	25,646
A/SIM 4-3*		123	134.9	30,018
A/SIM 4-4*		125	135.1	27,102
Ave.		**124.5**	**134.6**	**27,676**
A/SIM 5	A/SIM 5	123	131.7	22,371

* The specimens were tested at 276 K, where the specimens were quenched by liquid nitrogen, and then warmed back to the test temperature.

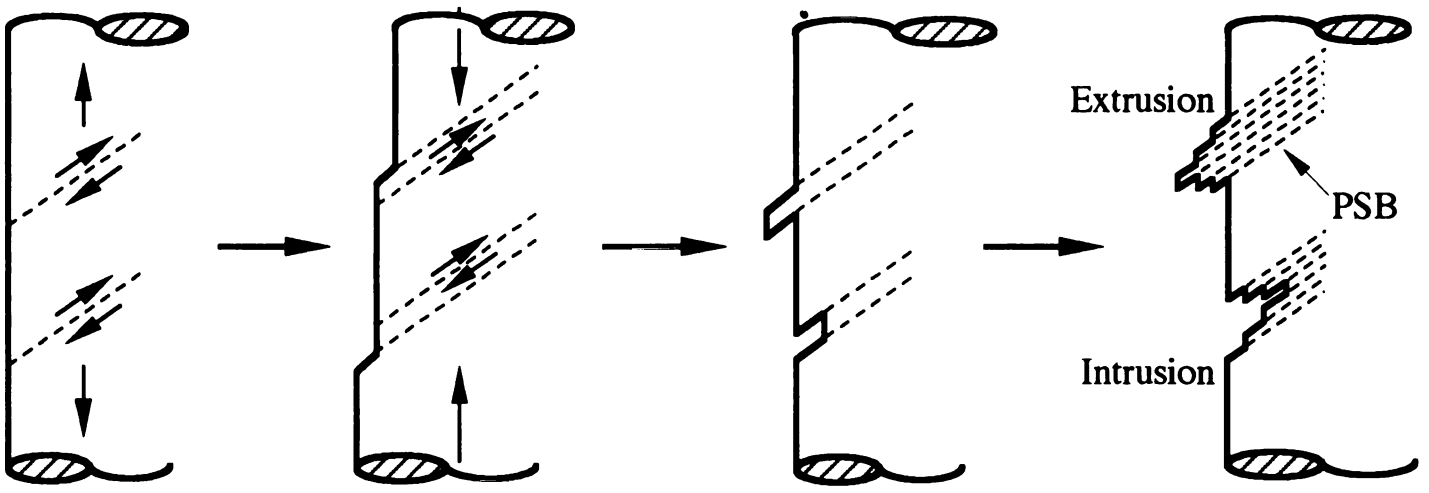

Figure 2-1. Schematic representation of pesistent slip band (PSB) formation during cyclic deformation. PSBs form at sites of original slip planes which are softest. Extrusions and intrusions at the free surface cause the stress concentration resulting in promoting additional slip and fatigue crack nucleation.

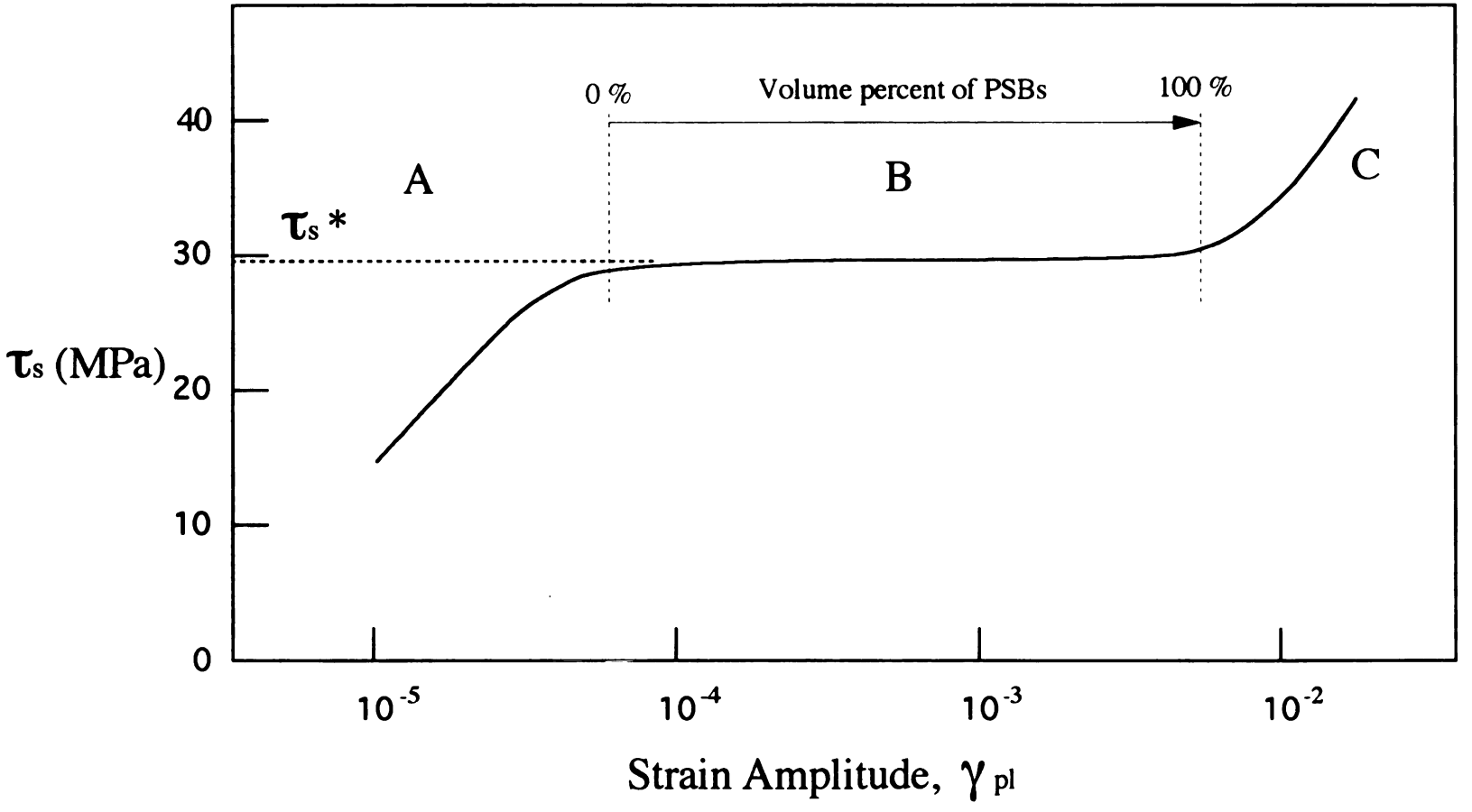

Figure 2-2. Cyclic stress-strain curve for copper single crystal, which is obtained by plotting saturation stress, τ_s, as a fuction of plastic strain amplitude, γ_{pl}. τ_s* stands for the saturation stress. The volume percent of PSBs increases with strain amplitude in region B. (Mughrabi *et al.*, 1978)

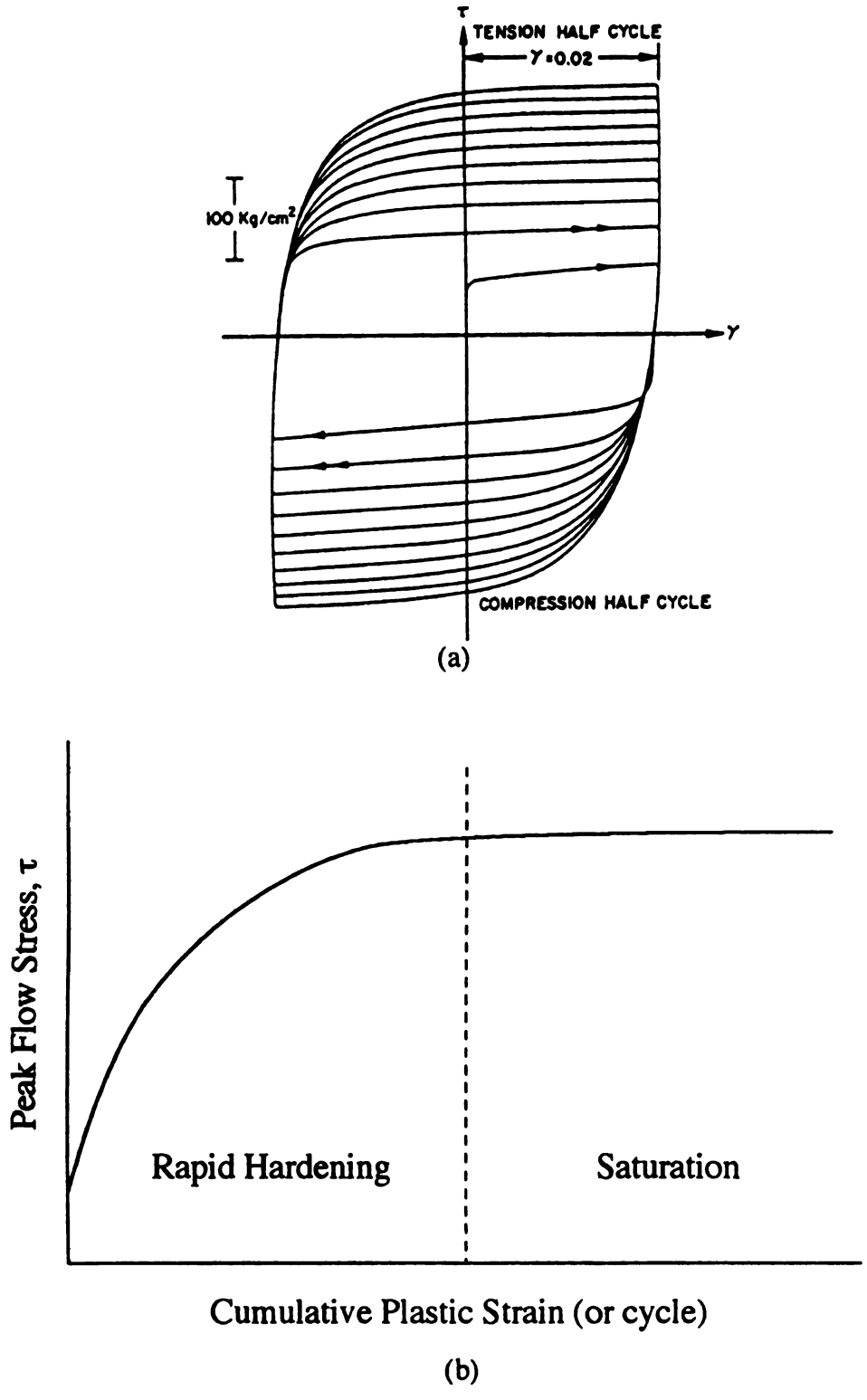

Figure. 2-3. (a) Hysteresis stress-strain loops for the first 10 cycles of a copper crystal subjected to a constant strain amplitude of $\Delta\gamma$ =0.02 at 200 K and (b) a schematic of a cyclic strain hardening curve. (Feltner, 1965)

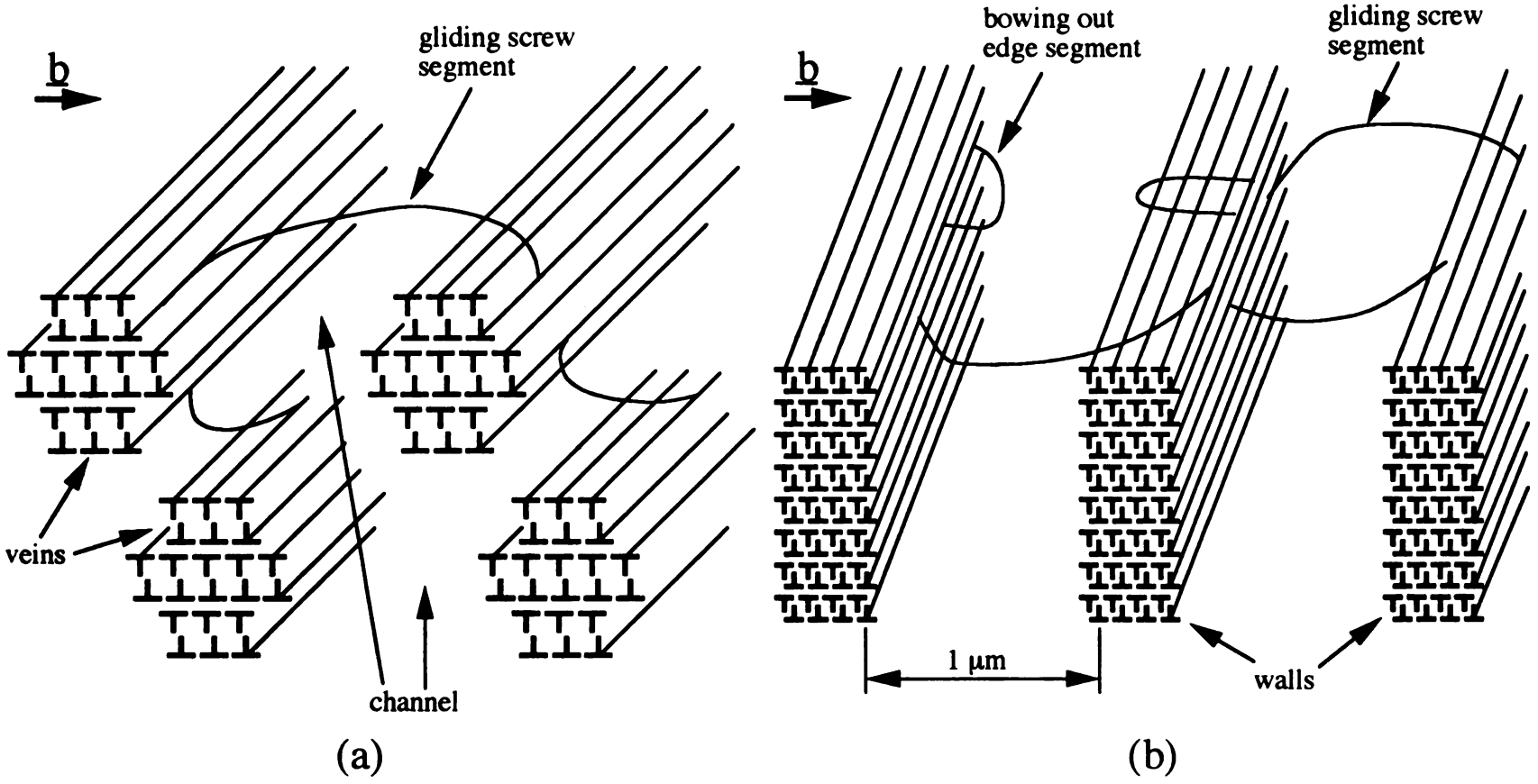

Figure 2-4. Dislocation structure in (a) matrix and (b) persistent slip bands of fcc metals at cyclic saturation. The steady state deformation occurs by a to and fro glide of the same dislocations in the matrix,whereas a dynamic equibrium between multiplication and annihilation exists in the wall structure of persistent slip bands. (Mughrabi, 1979)

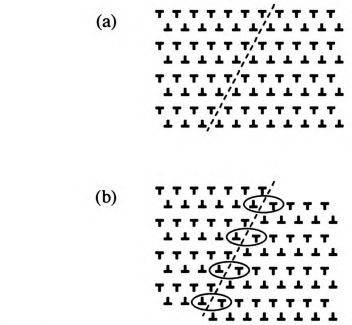

Figure 2-5. Persistent slip band formation by non-promary slip model: (a) the ideal infinite Tylor lattice in veins prior to saturation and (b) when cyclic saturation is reached slip occurs on a secondary slip plane and thus extensive annihilation of opposite edge dislocations can occur. (Kuhlmann-Wilsdorf and Laird, 1980)

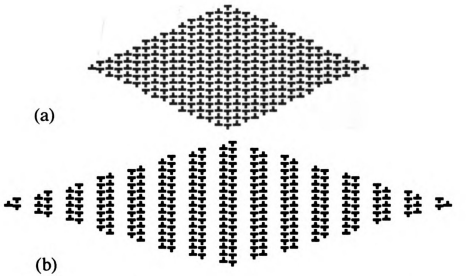

Figure 2-6. (a) the relaxed position at zero applied stress (b) the relaxed position at the possible maximum stress before disintegration into dipole wall. (Neumann, 1986)

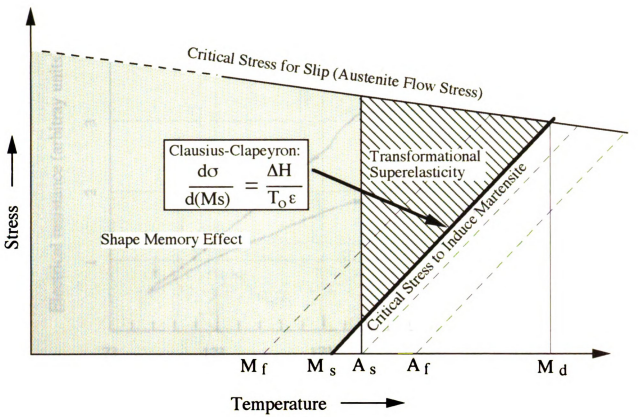

Figure 2-7. Stress-tempreature phase diagram illustrating region of shape memory effect and transformational superelasticity. The required stress to induce martensite shows the linear variation which obeys the Clasius-Clapeyron relationship. (Funakubo, 1987)

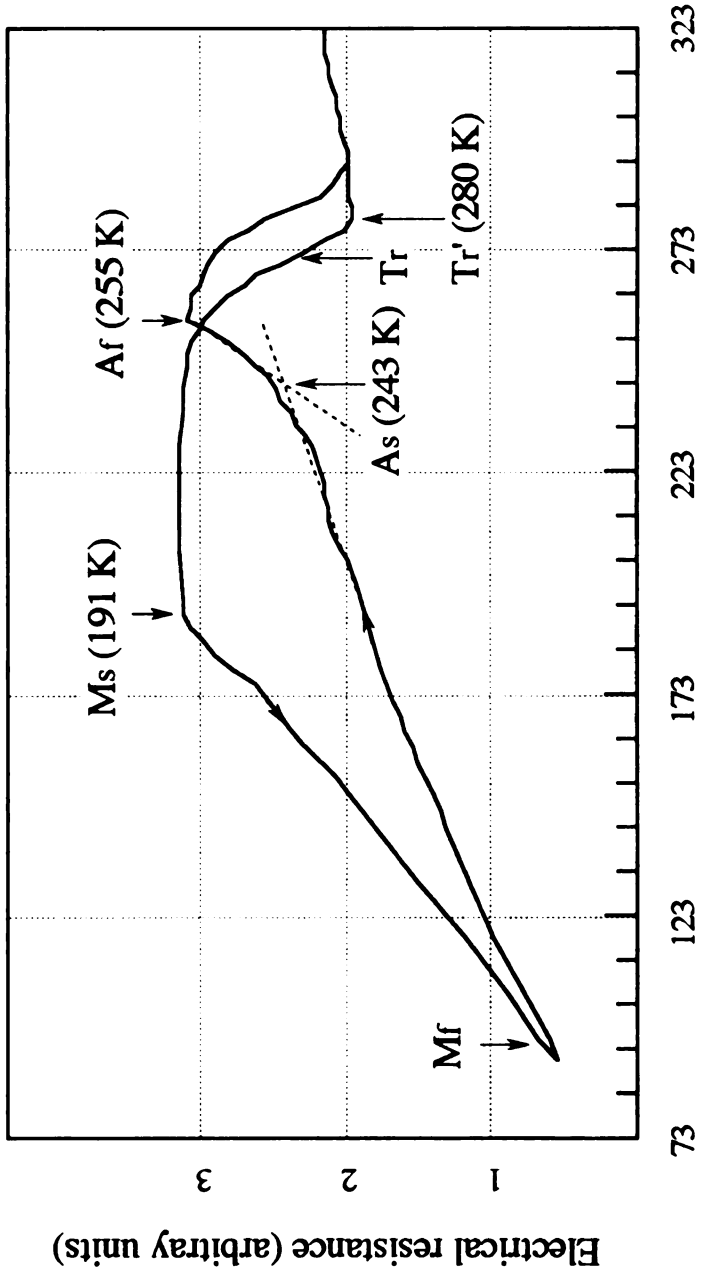

Figure 2-8. Electical resistance vs.temperature curve for a $Ni_{46.5}Ti_{47.5}Cu_6$ alloy film annealed at 923 K for one hour (Chang, 1993).

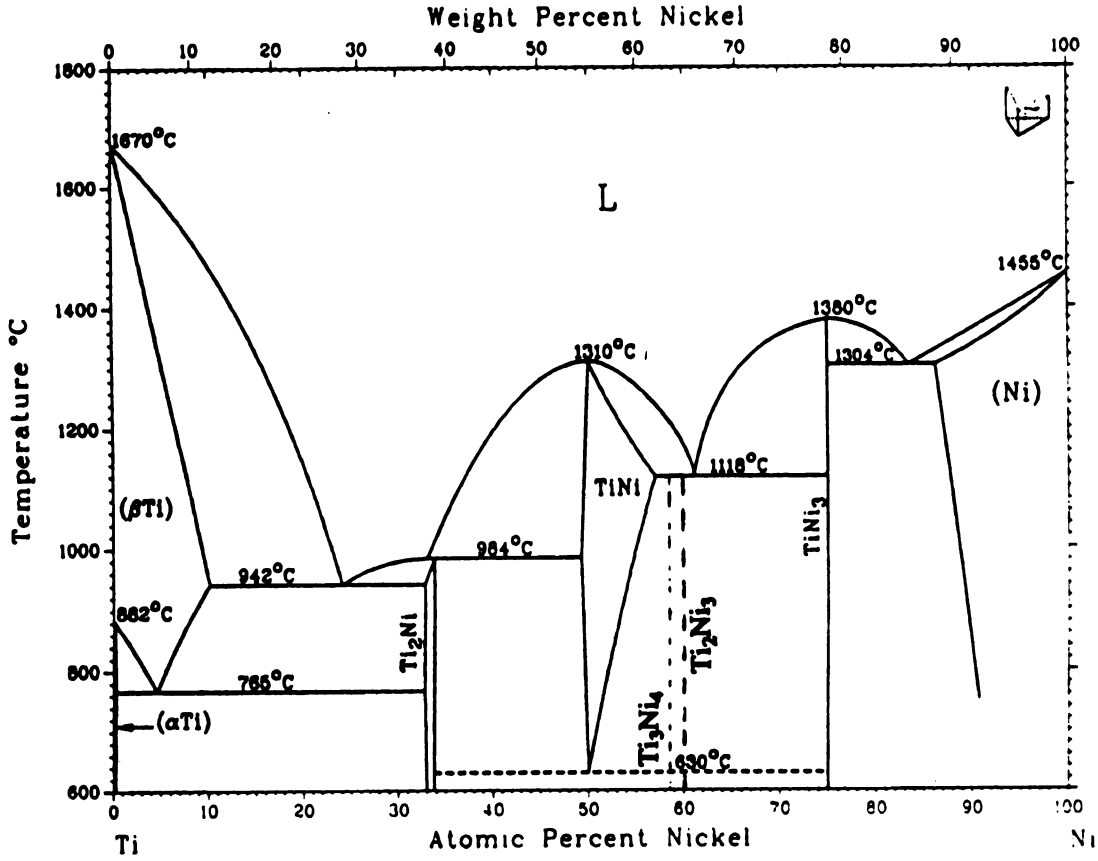

Figure. 2-9. Equilibrium phase diagram for Ni-Ti alloys. (Massalski, 1987)

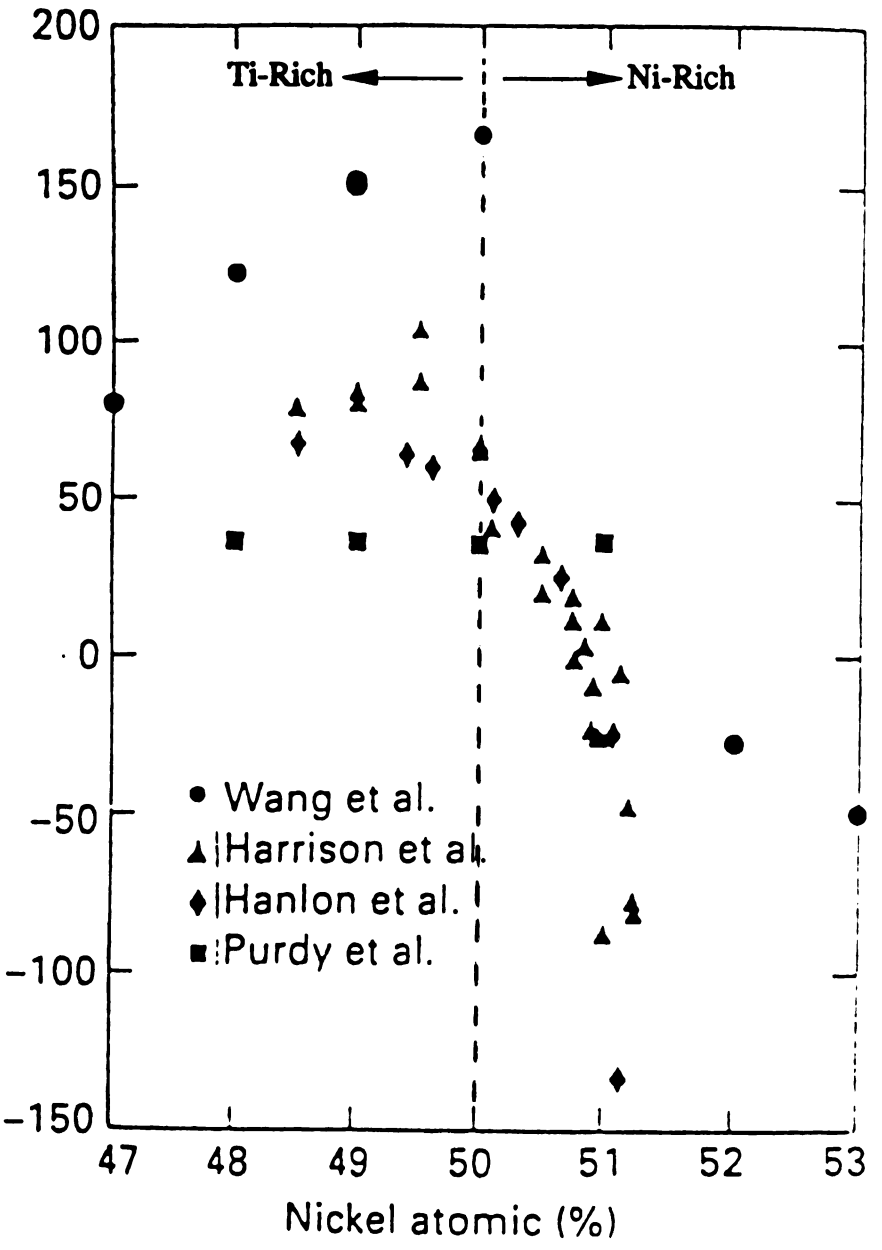

Figure 2-10. The dependence of the transformation temperature (Ms) on nickel conentration in NiTi alloys (Melton, 1990).

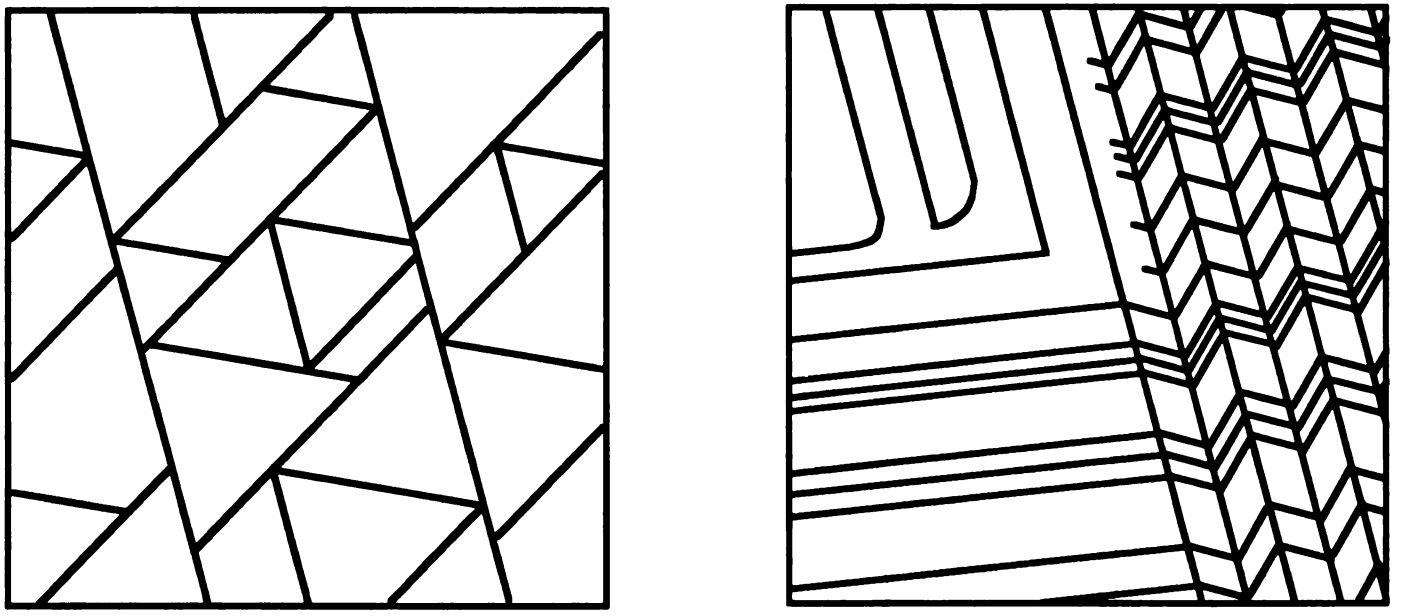

Figure 2-11. A schematic of surface relief morphologies showing the typical (a) triangular self-accomodating morphology of martensite phase and (b) saw-tooth self-accomodating morphology of R-phase in NiTi alloy

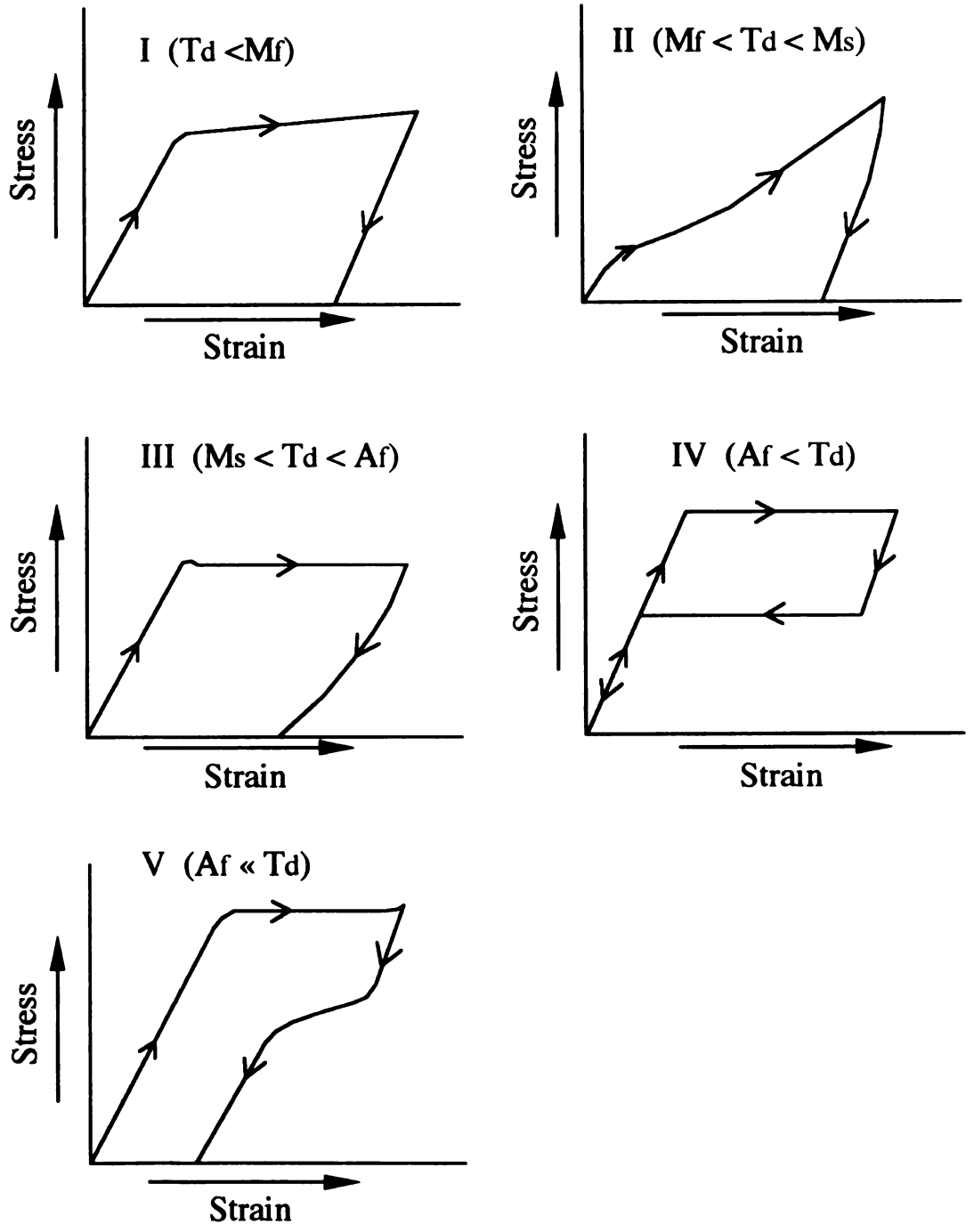

Figure 2-12. Five types of Stress-Strain curves depending on the deformation temperature relative to the transformation temperatures. (Funakubo, 1984)

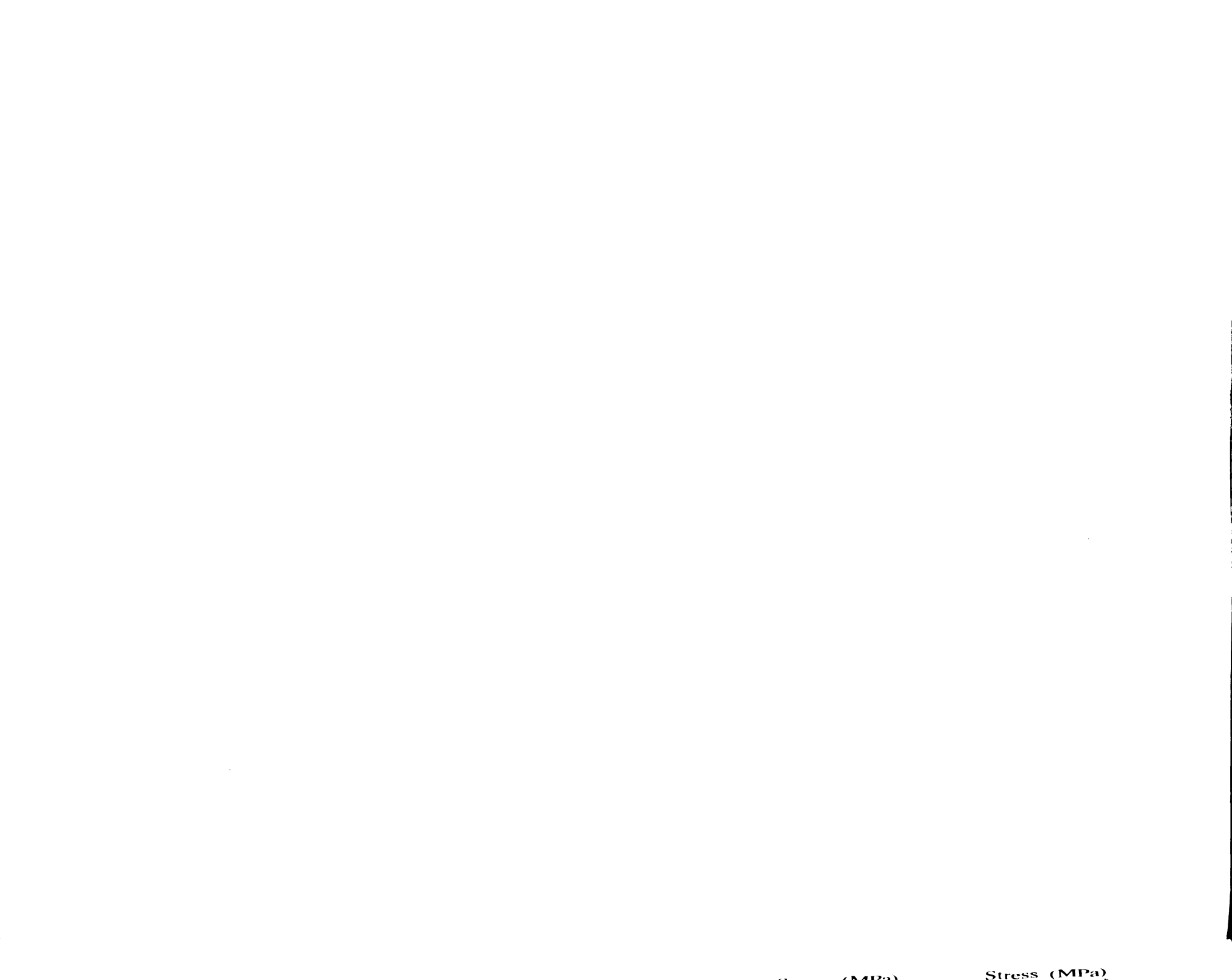
Stress (MPa)

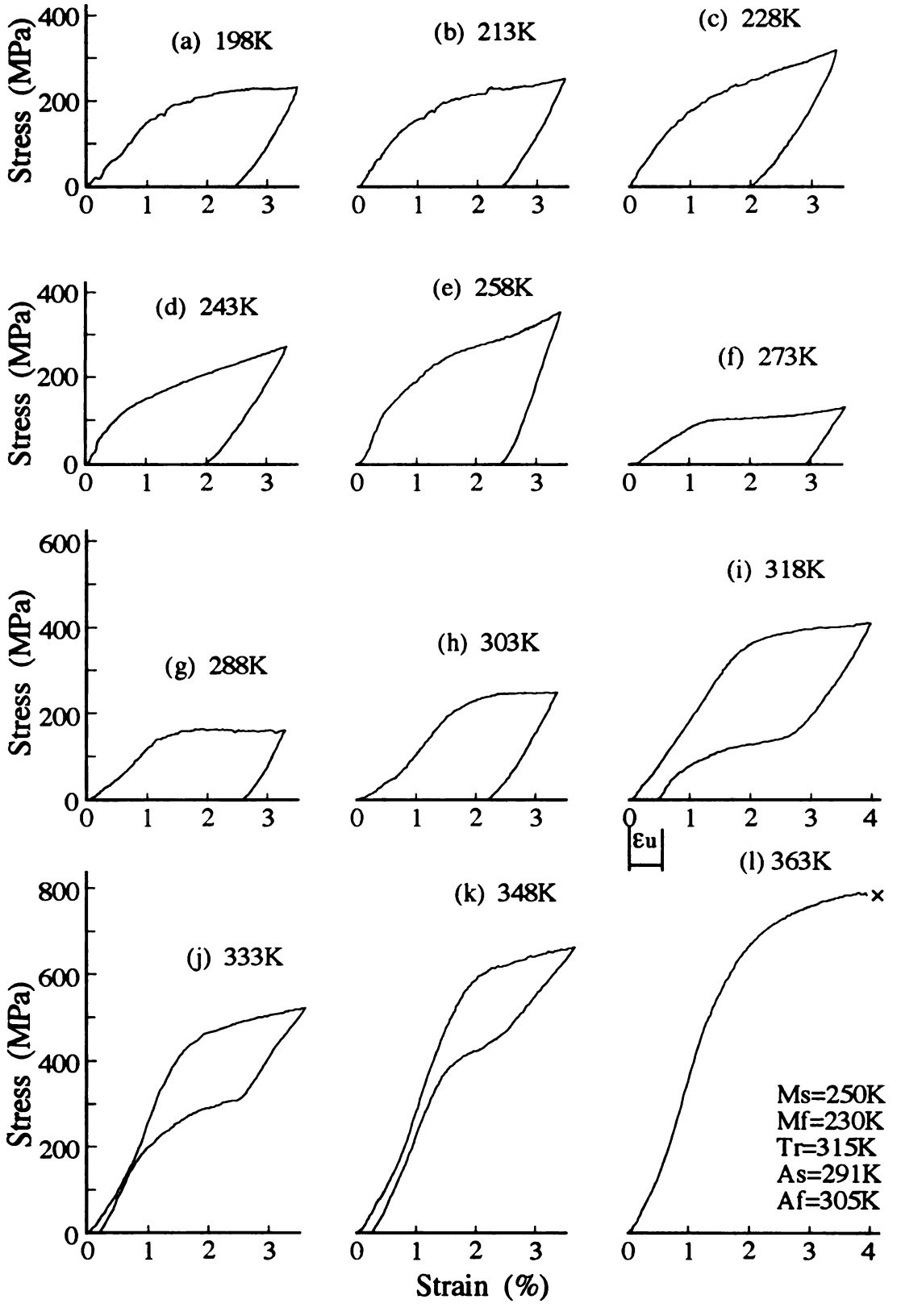

Figure 2-13. Stress-Strain Behavior of NiTi thin film as a Function of Deformation Temperatures (Hou, 1995).

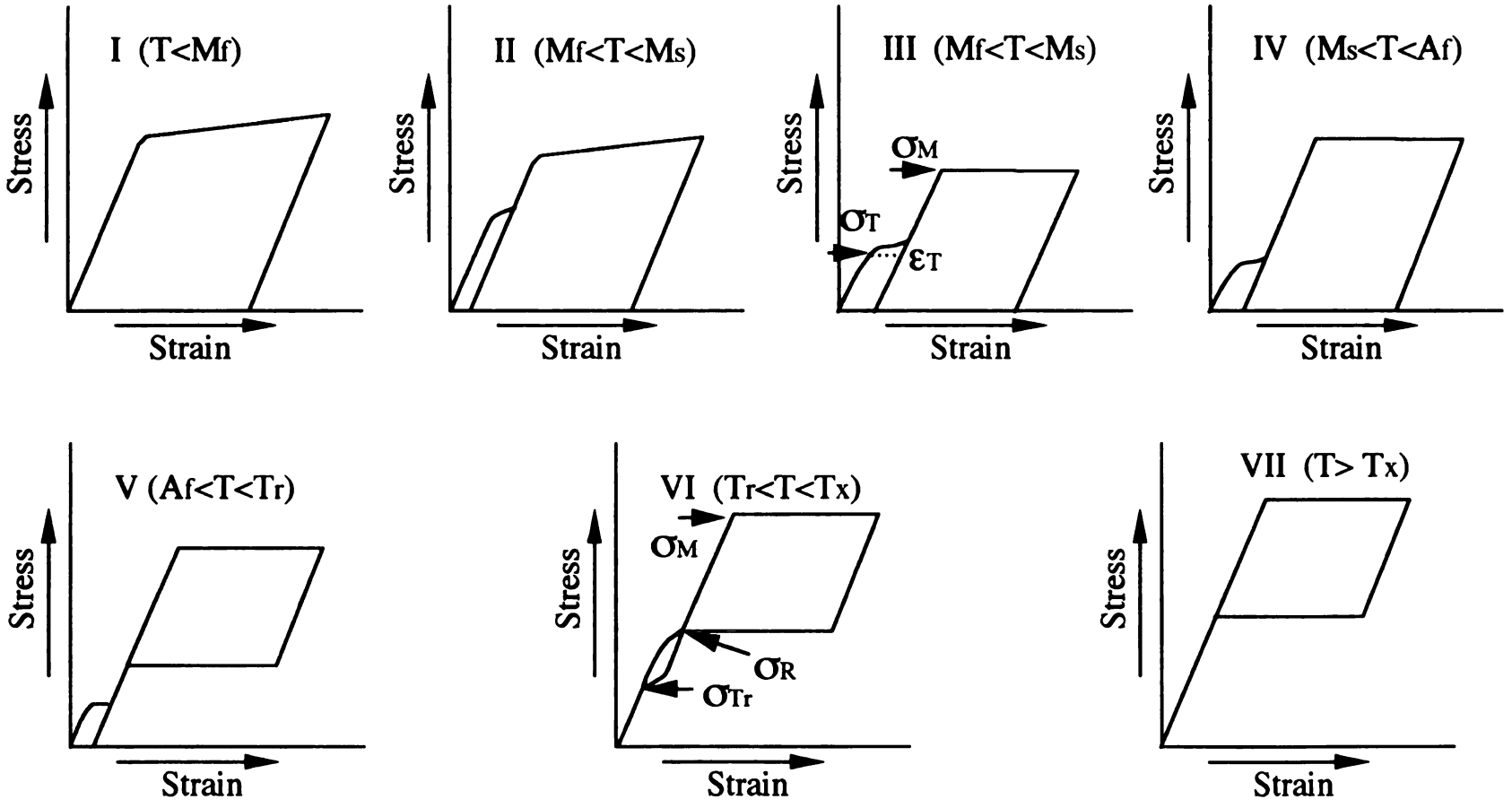

Figure 2-14. Seven types of Stress-Strain curves showing dependence on the deformation temperature relative to the transformation temperatures associated with the R-phase and martensitic transformations. (Miyazaki and Otsuka, 1986)

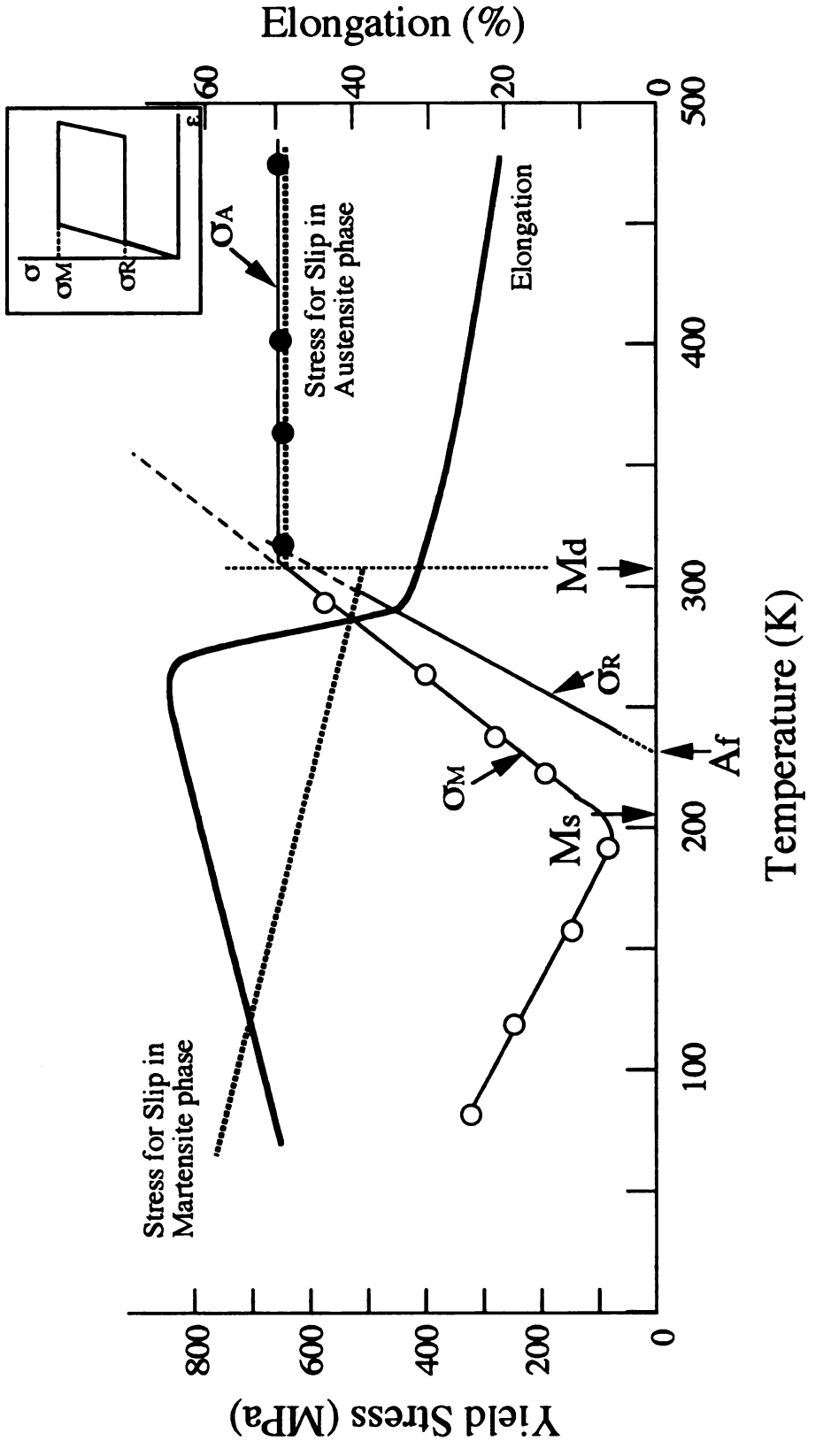

Figure 2-15. Three types of yield stresses, the stresses for slip in martensite and austenite phases, the stress for reverse transformationm (σ_R), and the elongation as a function of test temperature for NiTi alloy; the yield stress represents for twinning deformation below Ms, for inducing martensite between Ms and Md (σ_M), and for slip deformation above Md (σ_A).

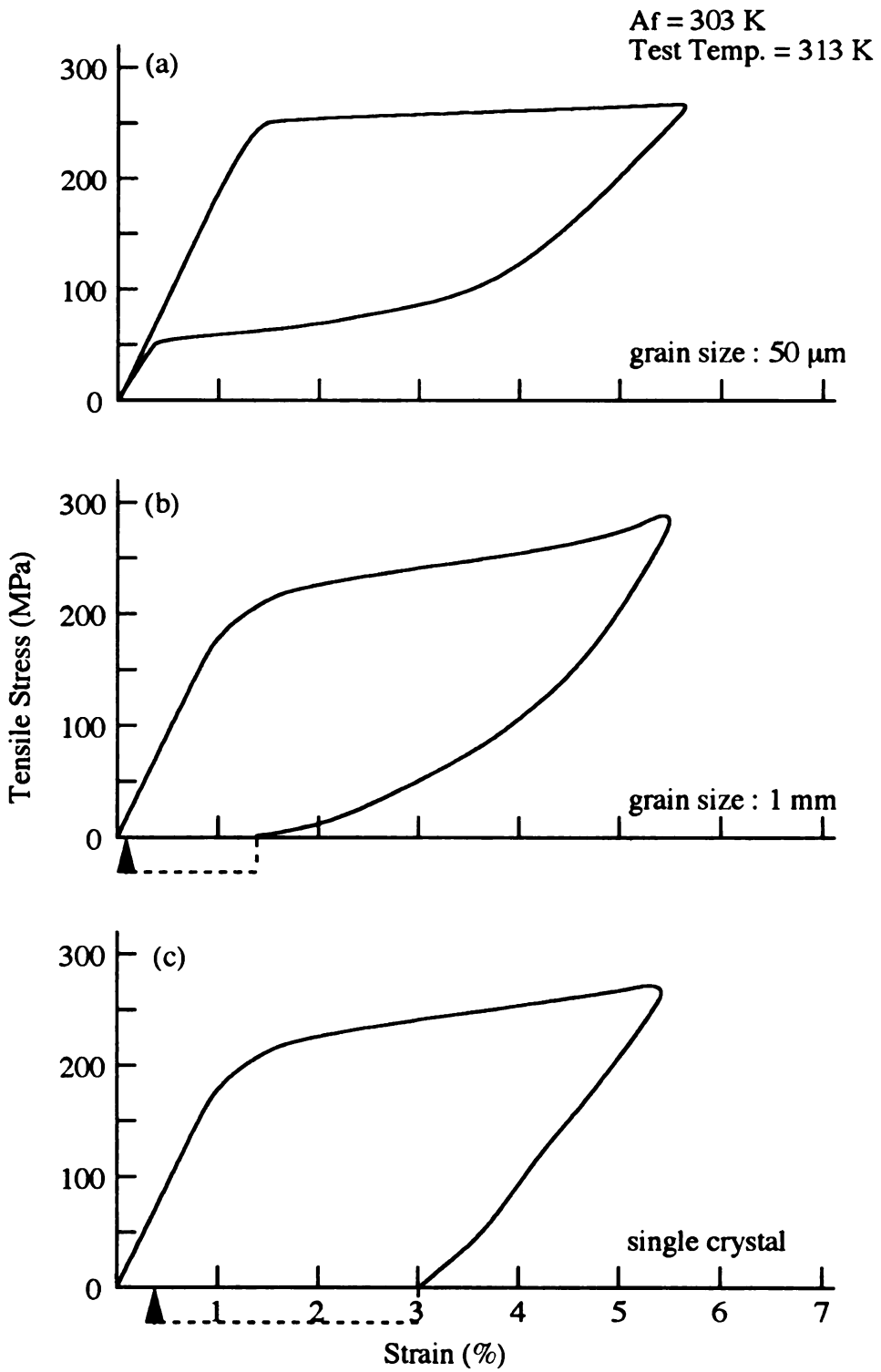

Figure 2-16. Grain size effect on psudoelasticity in NiTi alloy (T. Saburi *et al.*, 1984).

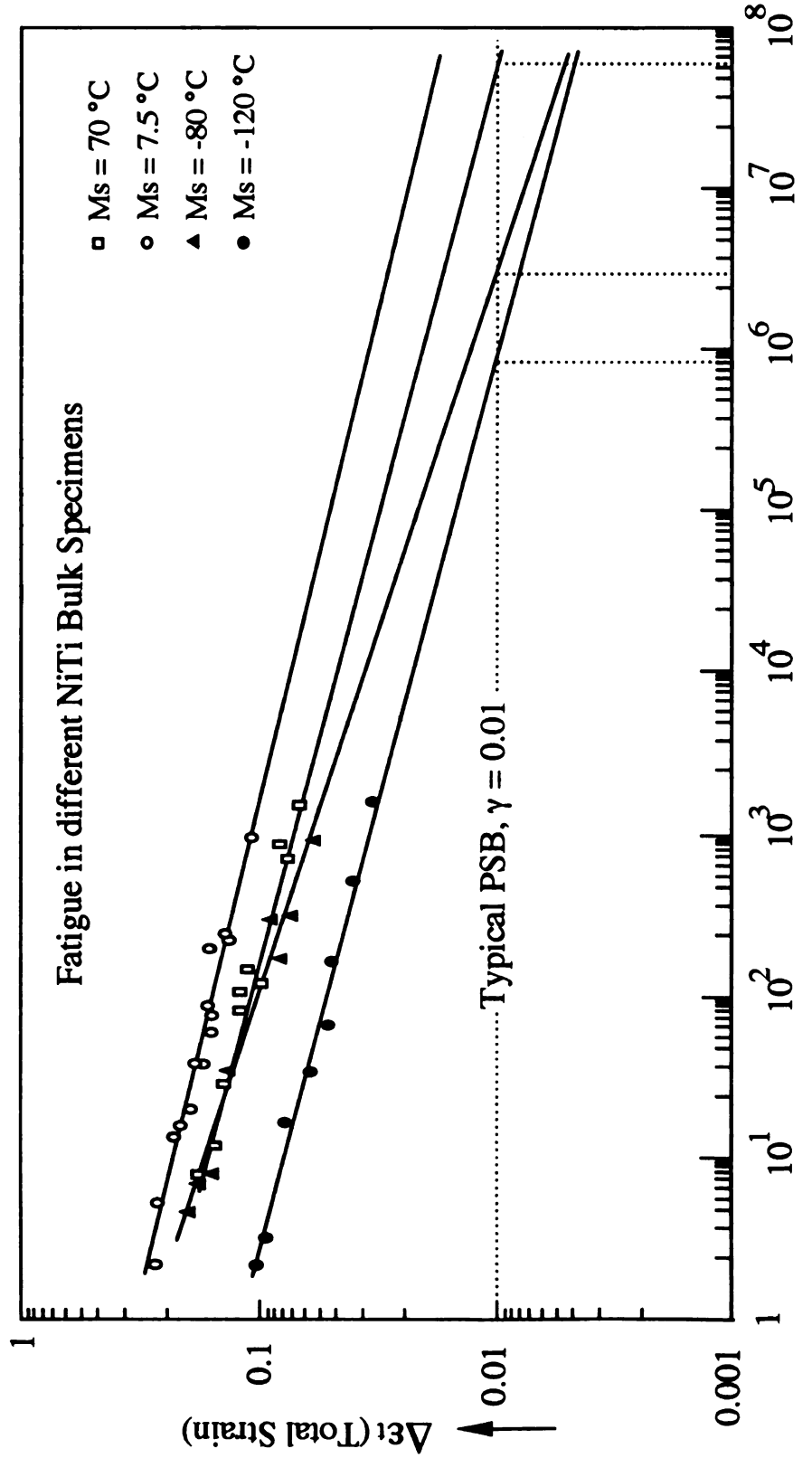

Figure 2-17. The total strain per cycle plotted against number of cylces. The test temperature was performed in air at 20 °C (Melton and Mercier, 1979). The longest life was obtained at about 15 °C above Ms temperature for a total strain of 0.01 which is a typical strain of PSB.

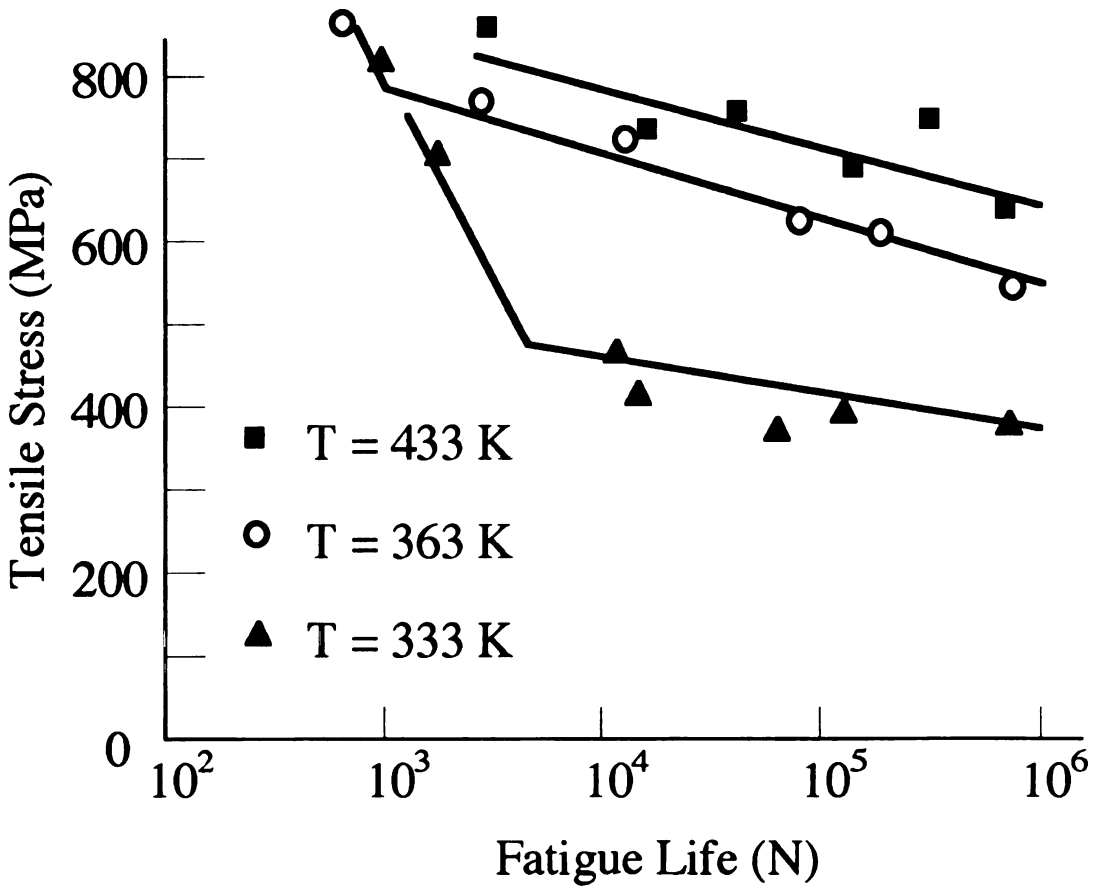

Figure2-18. Effect of test temperature on fatigue life of Ti - 50.8 at% Ni alloy with austenite finish temperature (Af) of 300 K (Miyazaki et al., 1989).

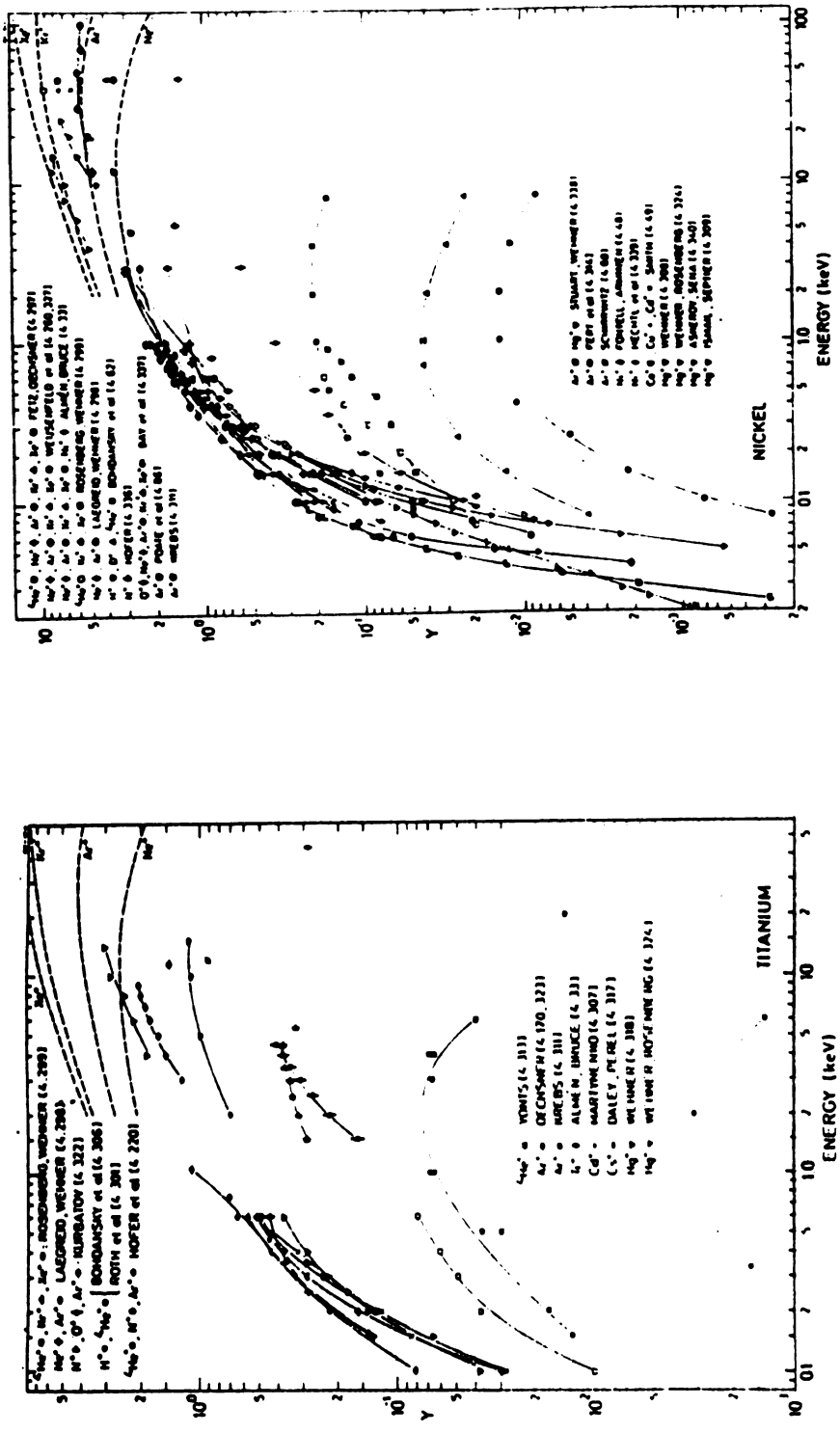

(a) (b)

Figure 2-19. Sputtering yields of (a) nickel and (b) titanium as a fuction of ion energy and ion mass (Anderson and Ray, 1981).

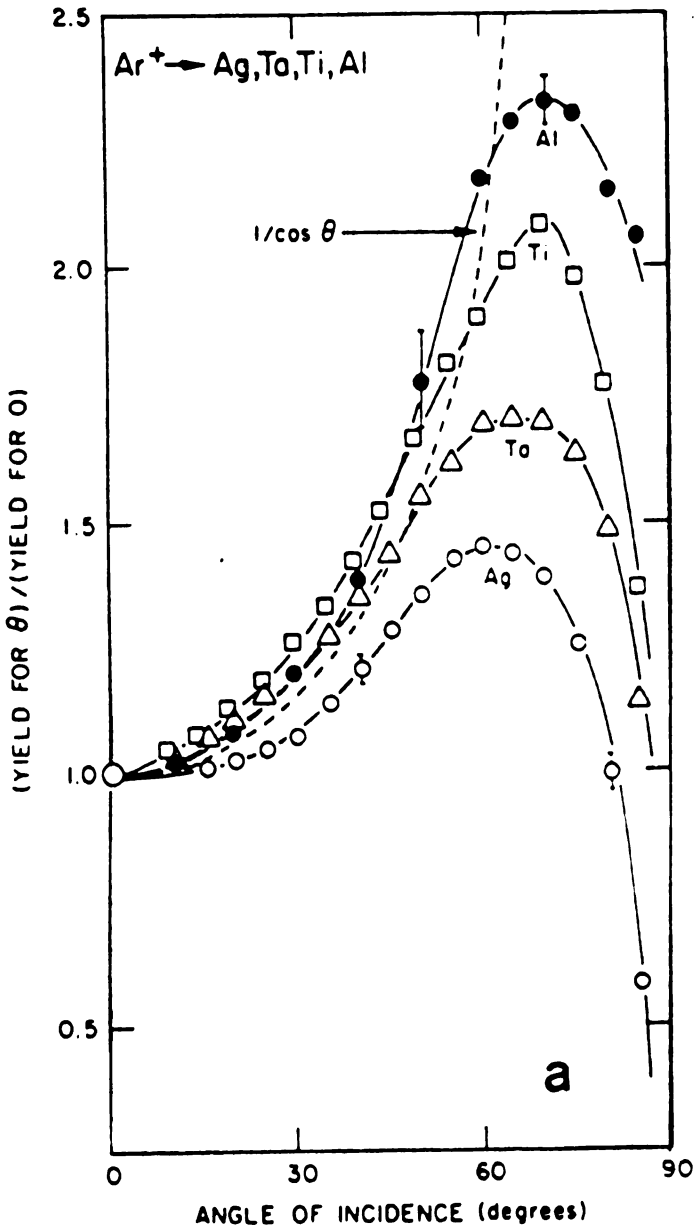

Figure 2-20. Variation of sputtering yield with angle of incidence for 1 keV Ar+ incident on Ag, Ta, Ti, and Al (Kelly, 1984).

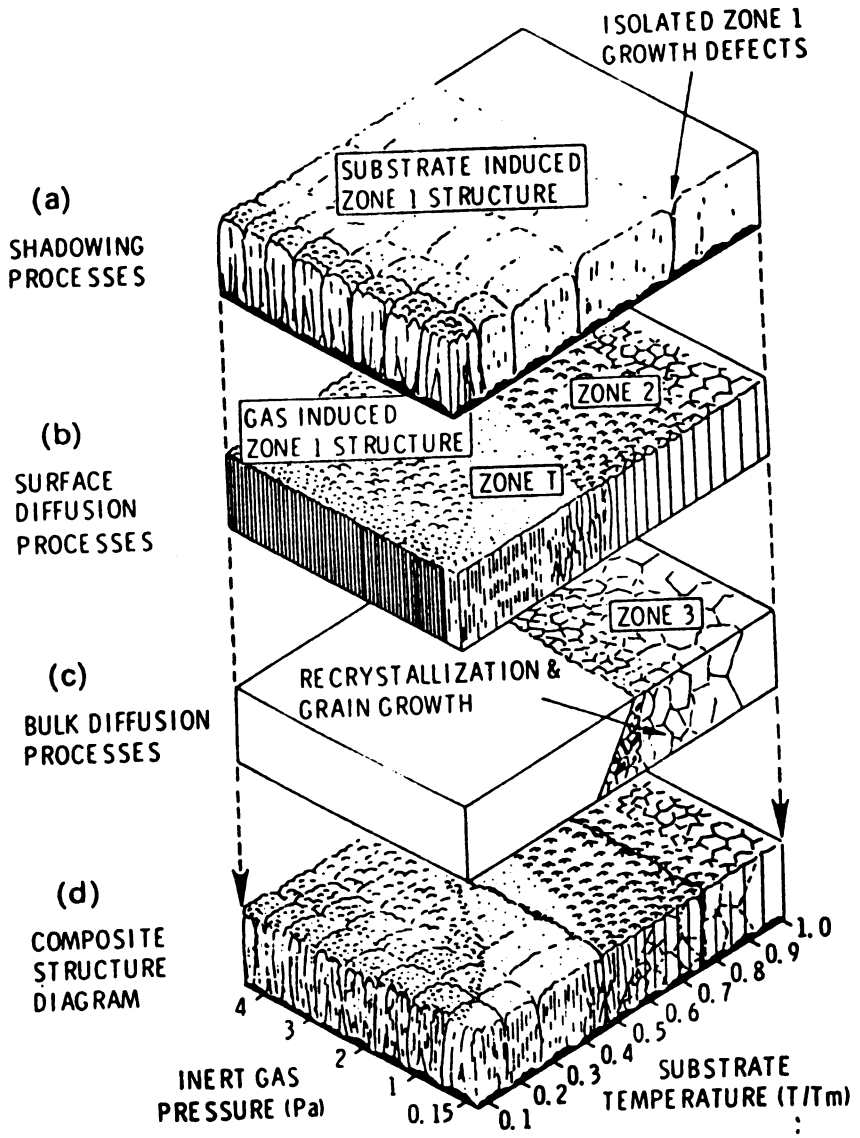

Figure 2-21. Schematic representation showing the superposition of physical processes that established structure zone (Thornton, 1977).

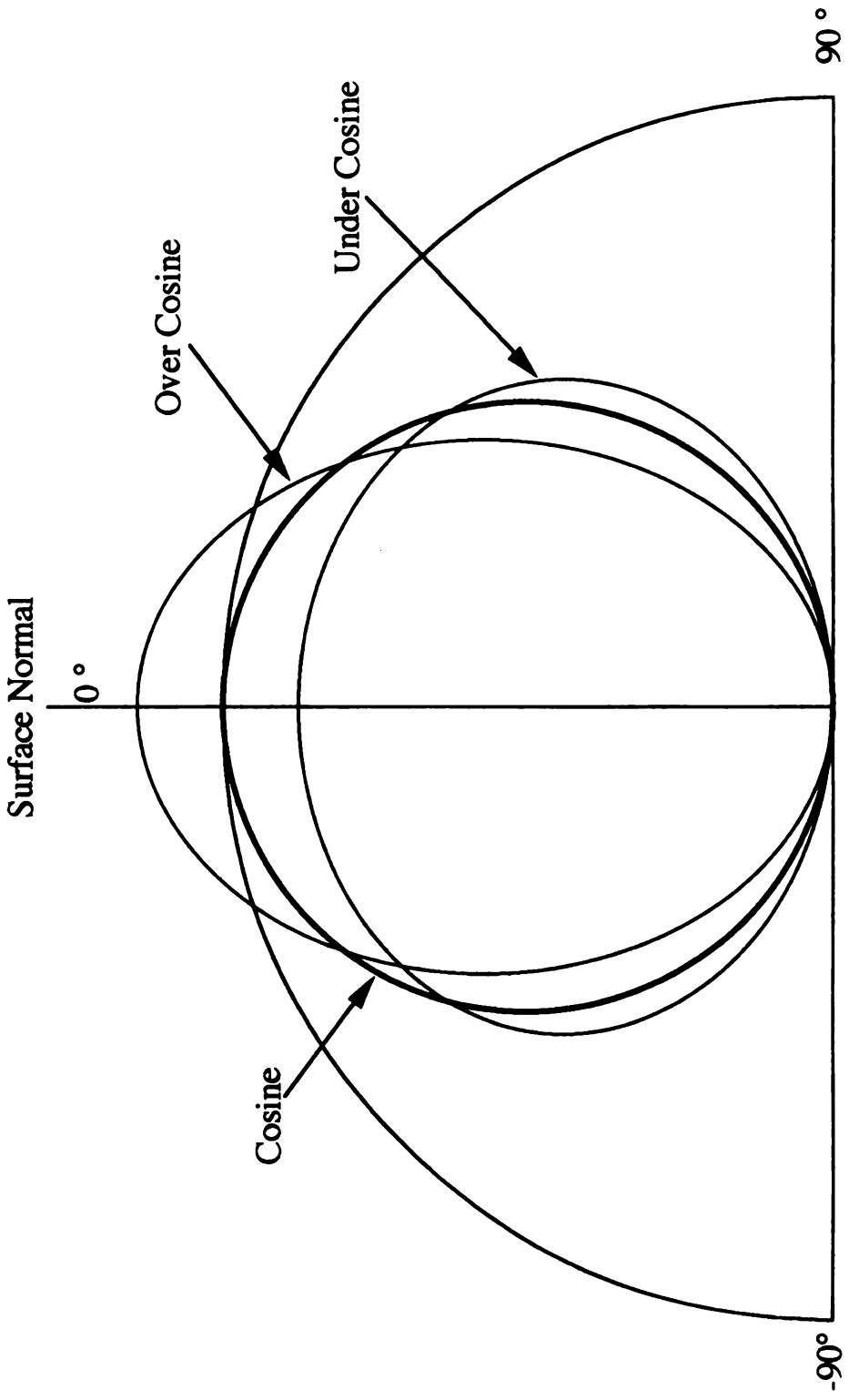

Figure 2-22. Angular Distribution of Sputtered Atoms for Ion Bombardment at Normal Incidence (Kay, 1962).

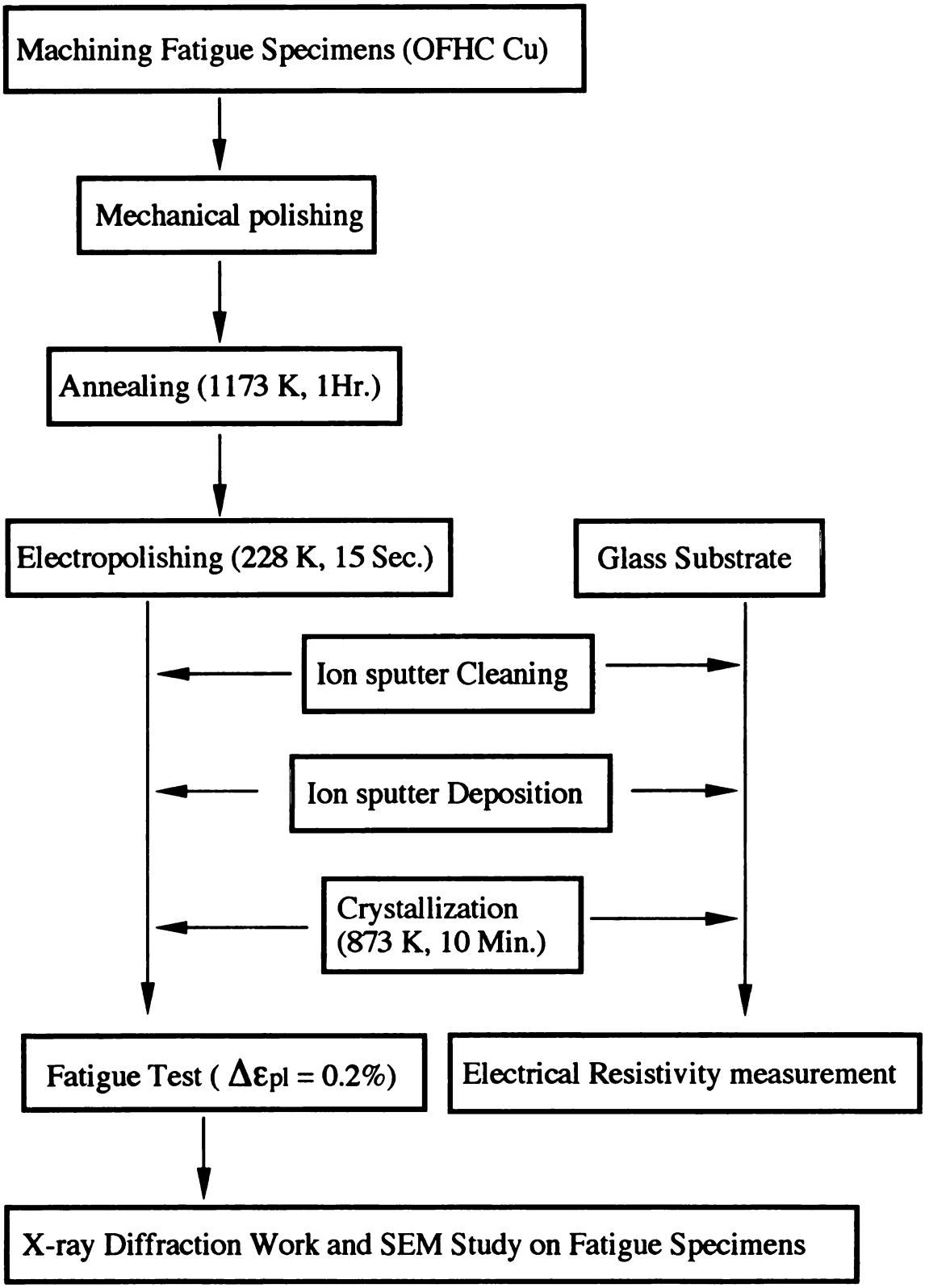

Figure 3-1. Flow Chart of the Experimental Methods.

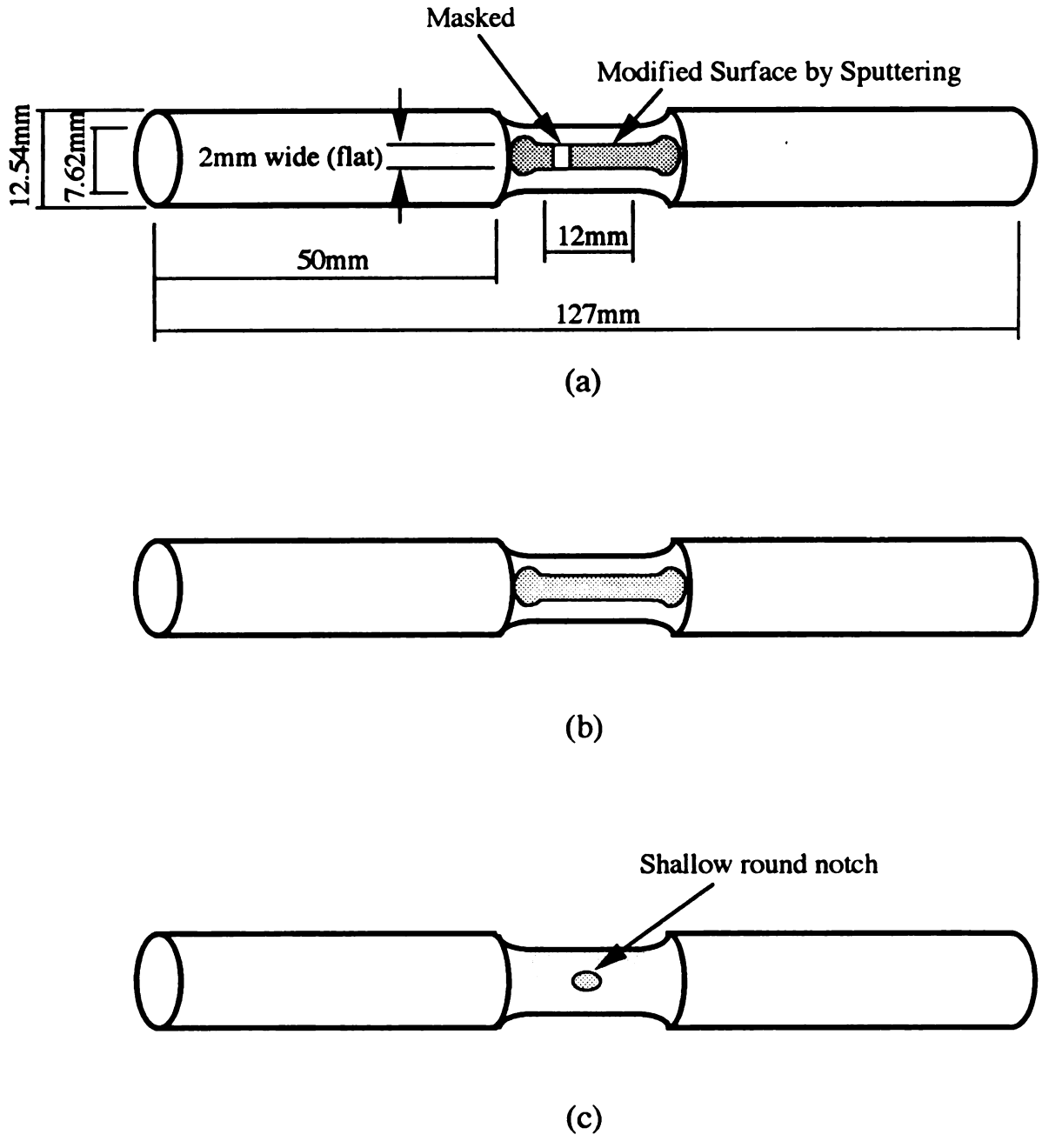

Figure 3-2. Shape of surface modified specimens: (a) films were partially, (b) fully covered in gauge section on flat area to observe surface morphology and crystal structure, and (c) on shallow round notched area to investigate fatigue life.

Figure 3-3. Polycrystalline OFHC copper fatigue specimen microstructure after anneailng at 1173 K for 1 hour. The average grain size is 300 µm. (Electrolyte was used 1 part of HNO_3 and 9 parts of water solution).

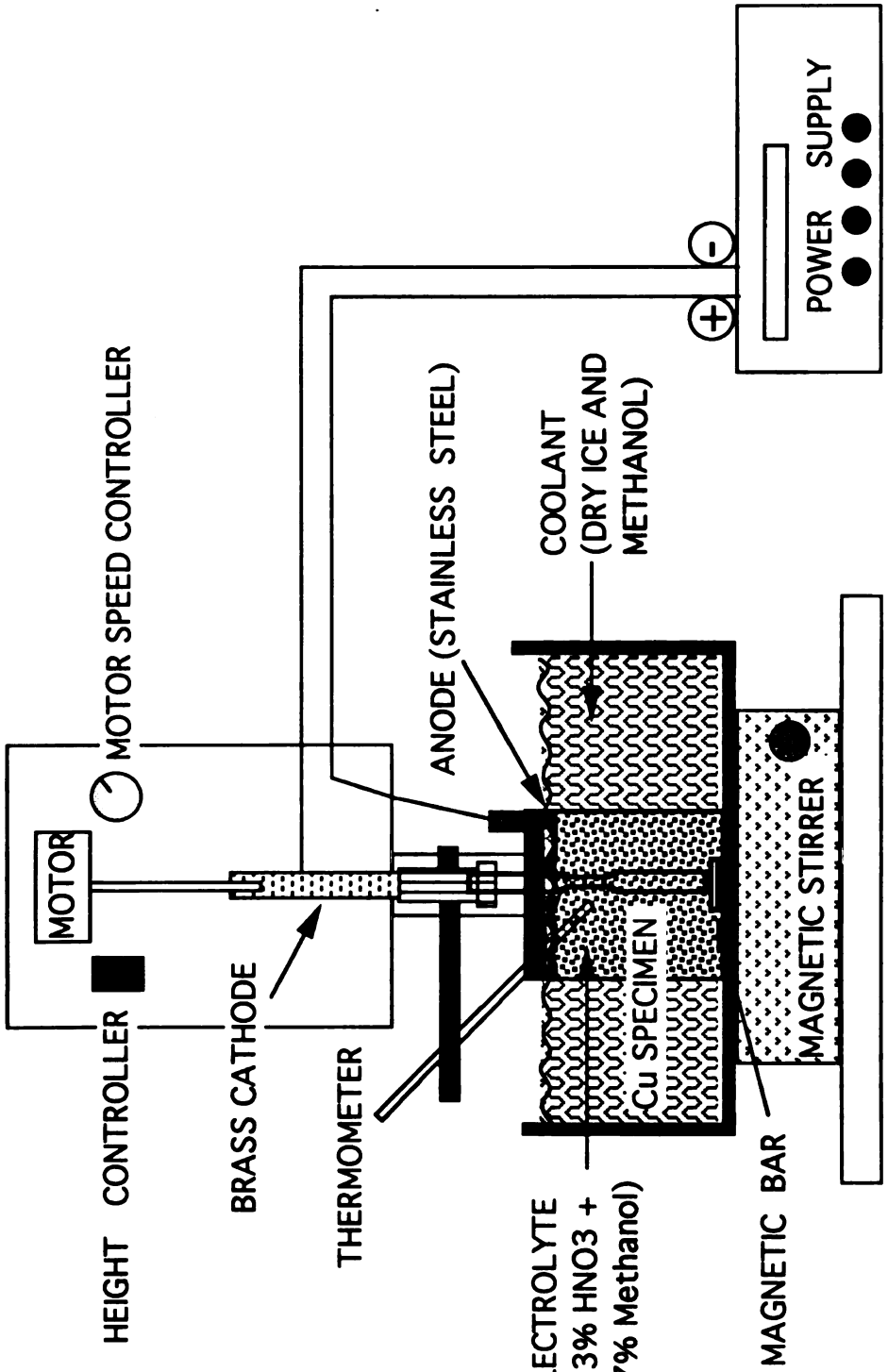

Figure 3-4. Schematic Diagram of Electropolishing Apparatus: Electropolishing was performed in a solution of 33% of nitric acid and 67% of methanol at around 228 K.

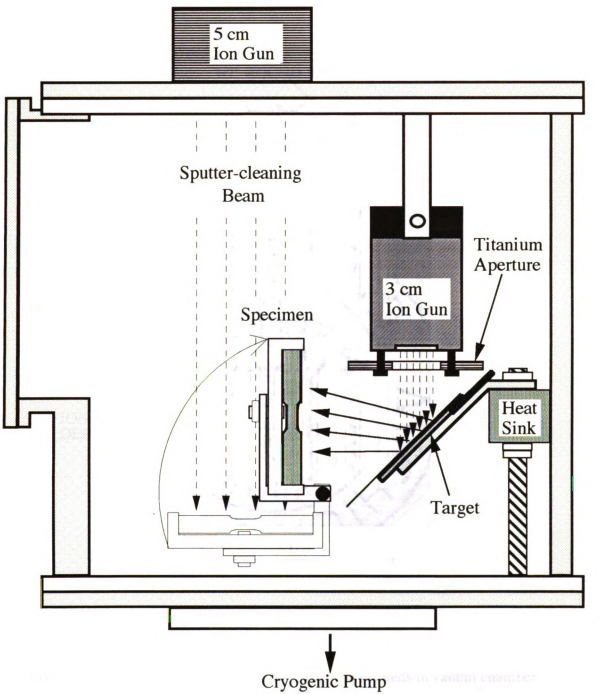

Figure 3-5. Schematic Diagram of Sputtering System: After sputter-cleaning by bombarding to remove dirt and the oxide layer, films were deposited on the specimens (side view).

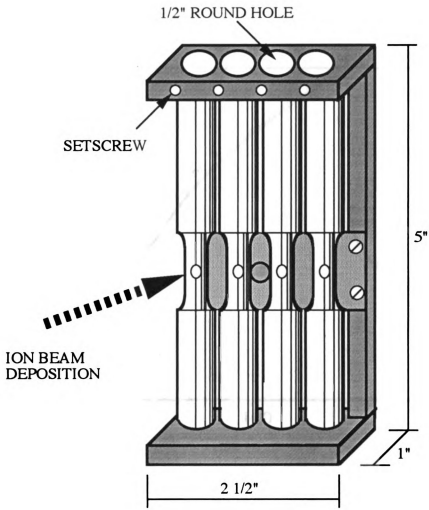

Figure 3-6. Steel fixture used to position fatigue specimens in vauum chamber during sputter-cleaning and ion beam deposition. This is designed to facilitate sputter-cleaning and film deposition on four specimens in one batch.

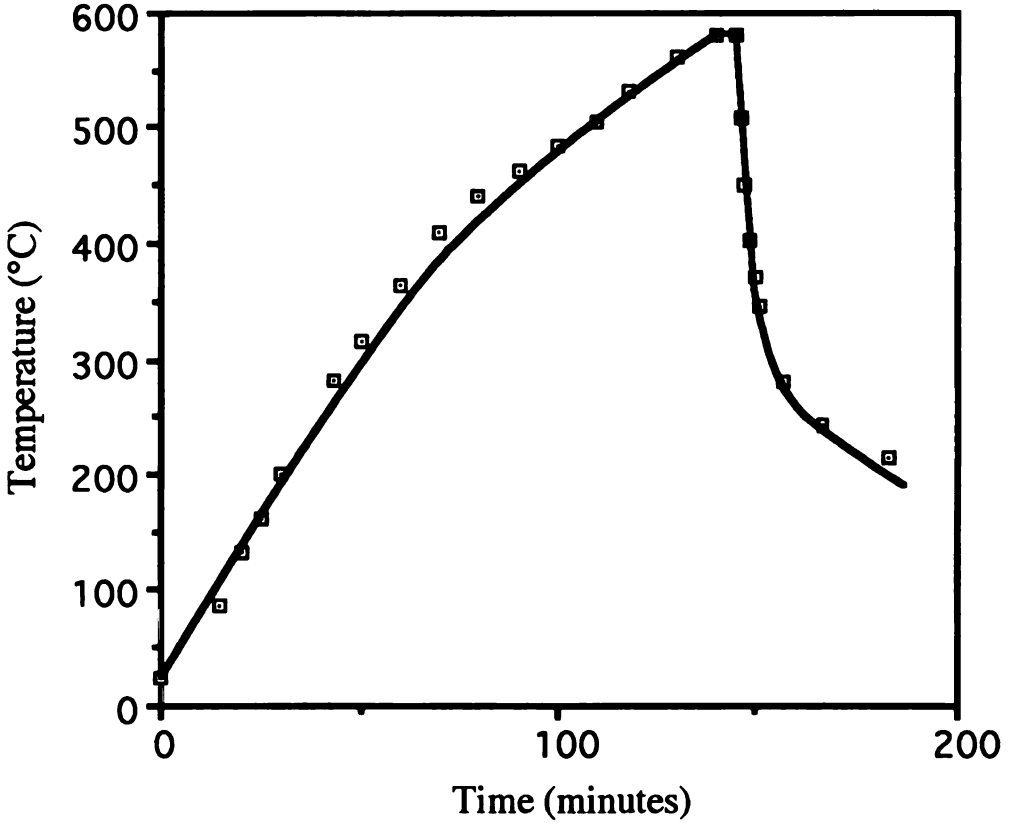

Figure 3-7. Time-temperature plot for the crystallization annealing treatment of as-sputtered NiTi thin films.

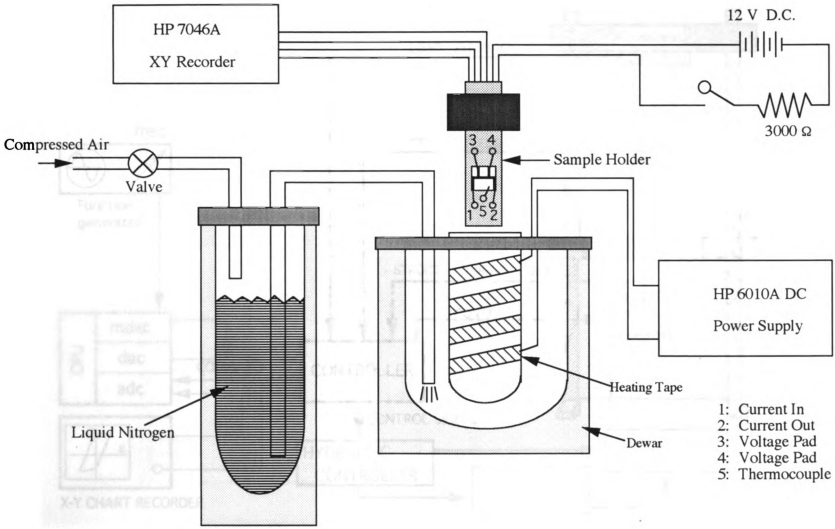

Figure 3-8. Schematic Drawing of The Electrical Resistivity Measurement Apparatus.

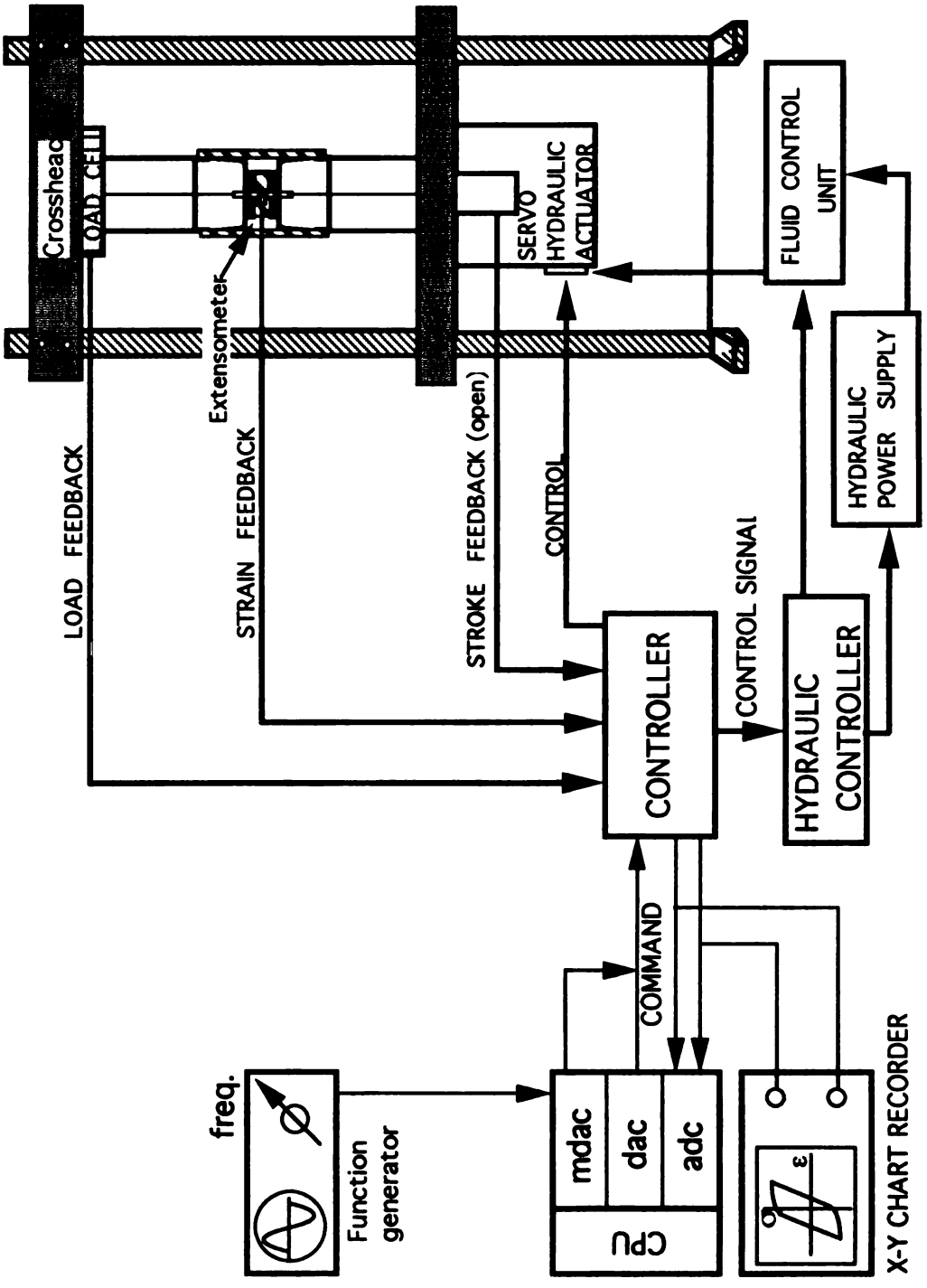

Figure 3-9. Block Diagram of Servohydraulic System.

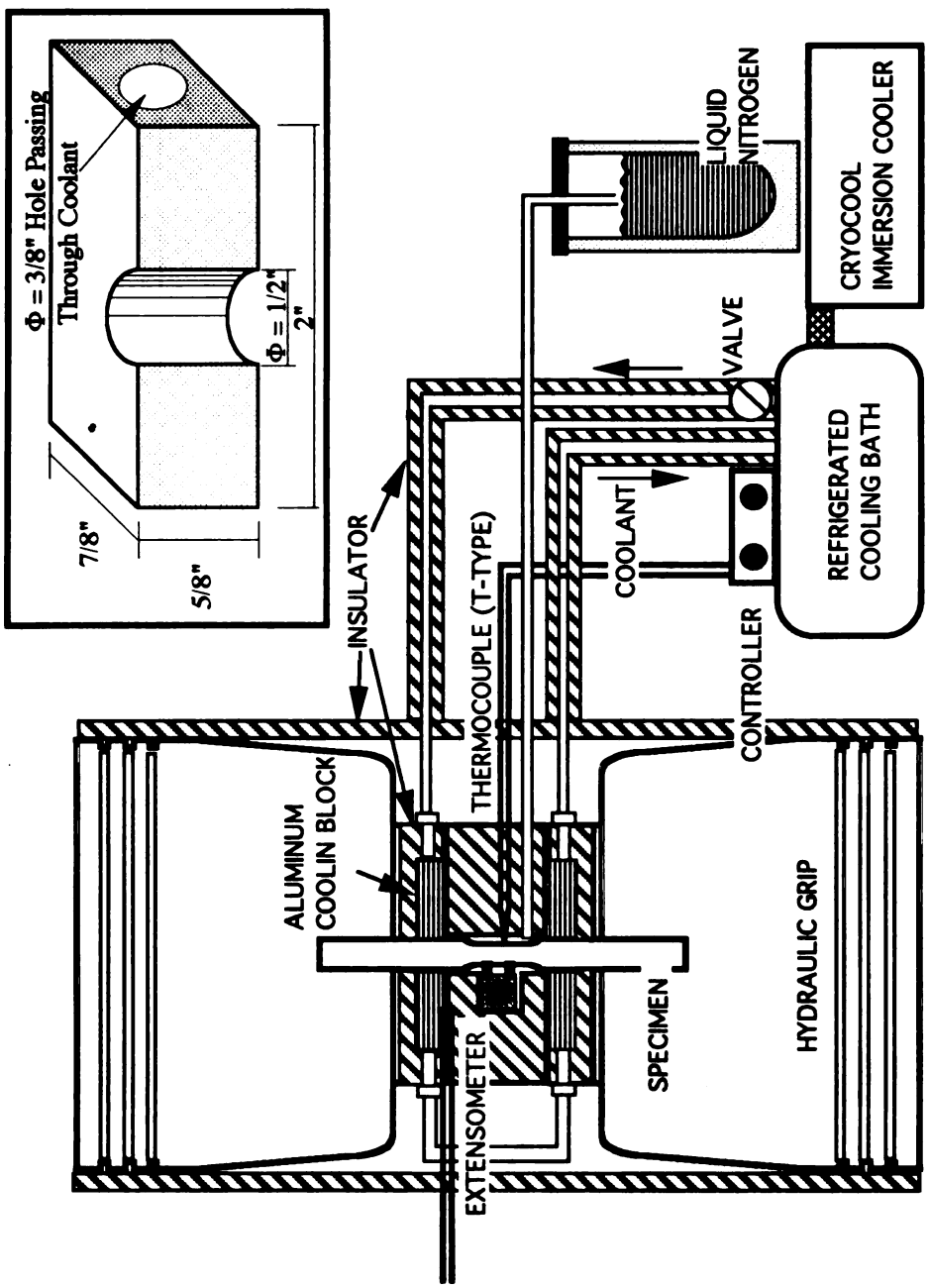

Figure 3-10. A Schematic Diagram of the Cooling System for Low Temperature Fatigue Tests and Details of an Aluminum Cooling Block. The specimen was conductively cooled by aluminum blocks through coolant was made to circulate.

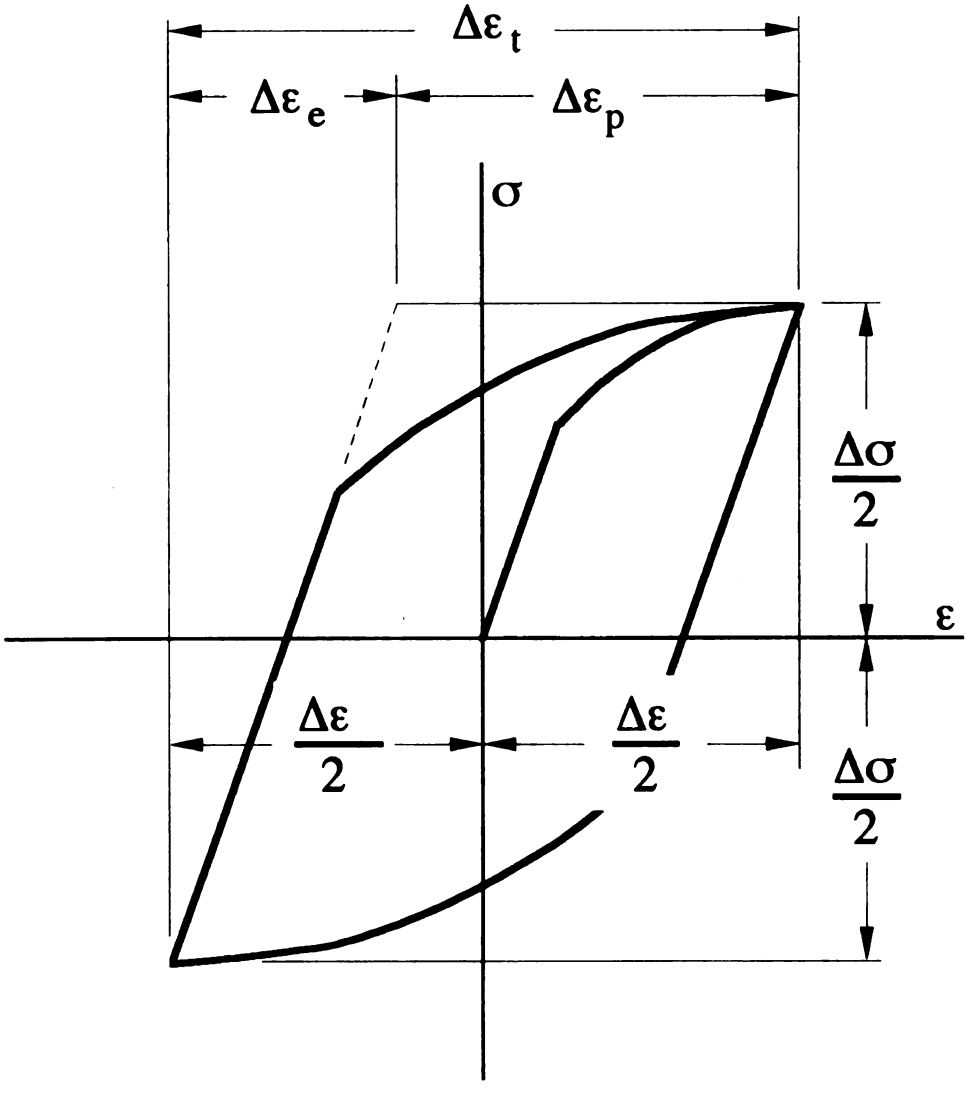

Figure 3-11. Hysteresis stress-strain loop for constant strain cycling. Low cycling fatigue test in present study was carried out at a constant plastic strain amplitude ($\Delta\varepsilon_p$).

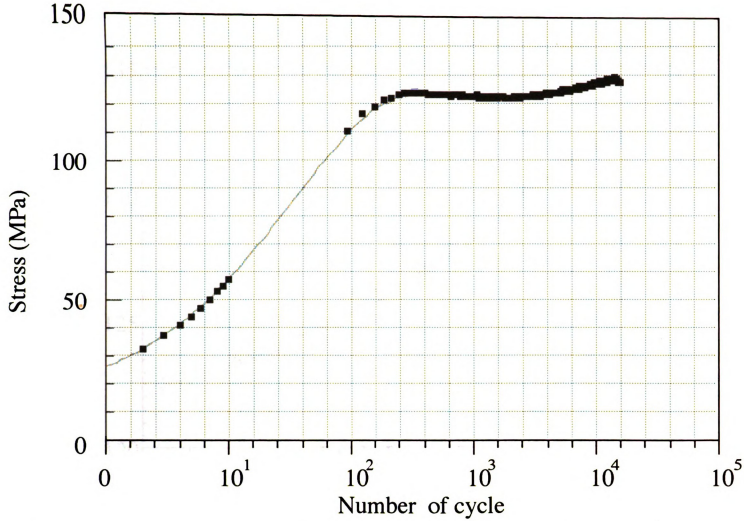

Figure 3-12. Cyclic hardening curve from the annealed polycrystalline copper: Grain size was 300 μm and the plastic strain amplitude was 0.002. The curve was constructed by connecting the peak stresses for each cycle and was terminated 1 % peak stress drop as a criterion for fatigue crack intiation.

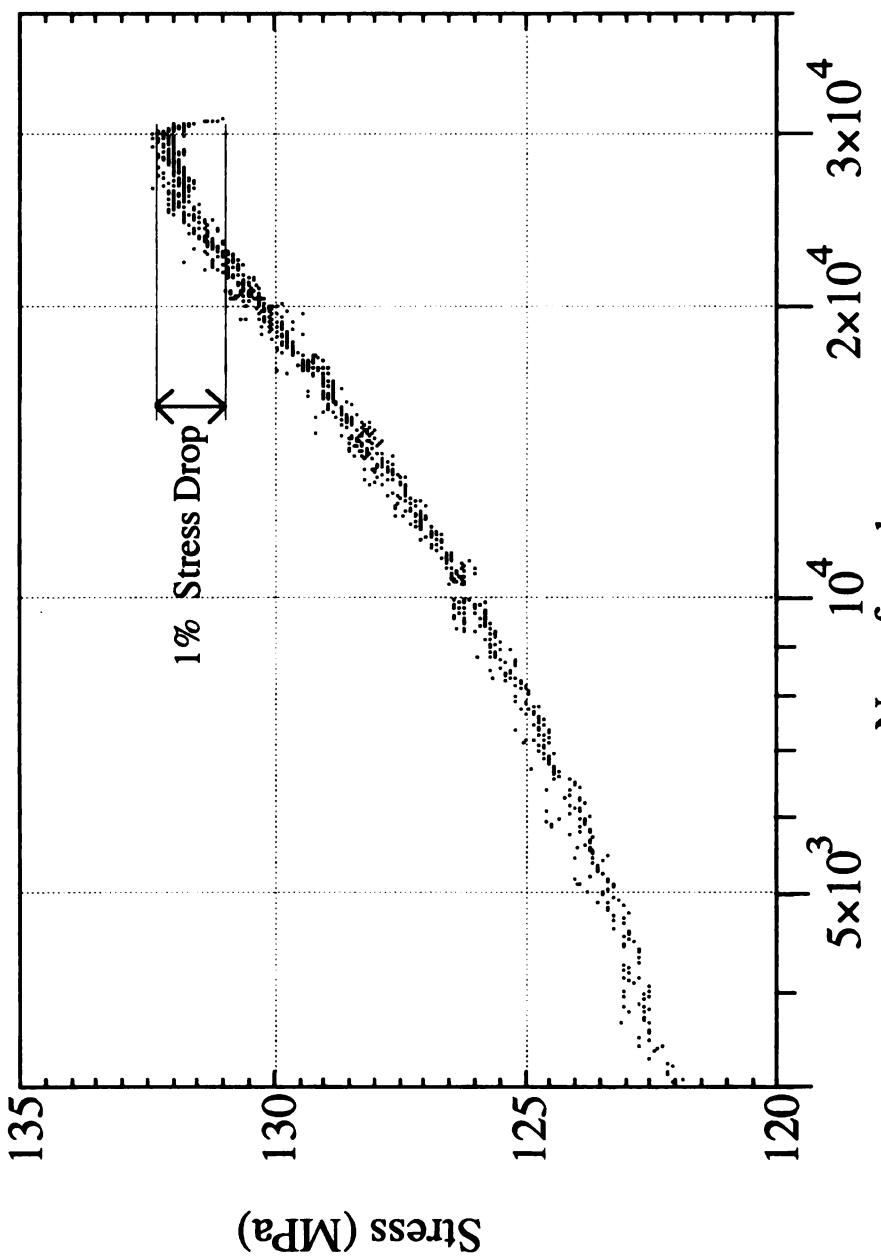

Figure 3-13. Detail of cyclic hardening curve near fatigue crack initiation life (NI) defined by 1% stress-drop.

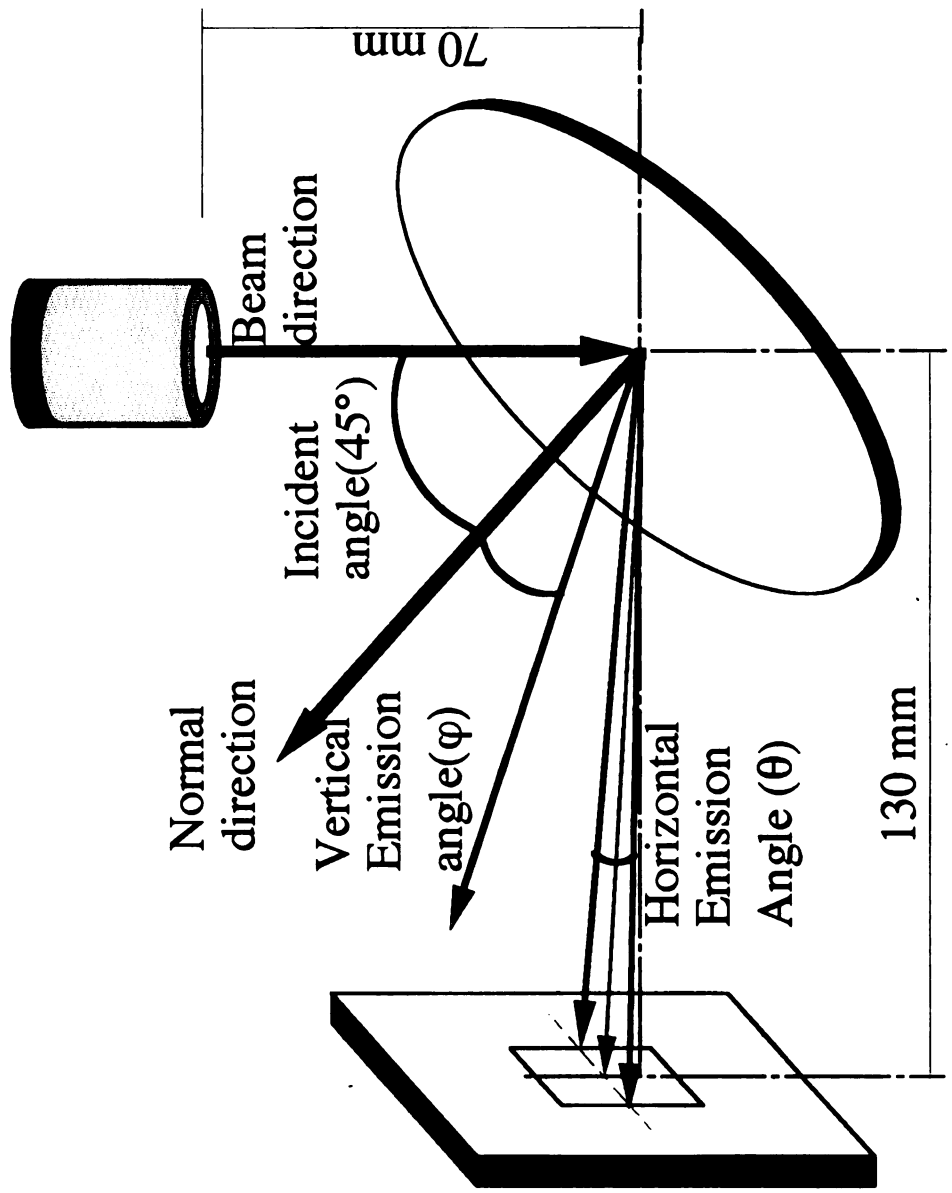

Figure 4-1. Schematic Diagram of Angular Distribution of Ion Beam Sputtering Deposition: The incident angle to taget is 45°against the target plane normal. The vertical emission angle (φ) is defined as an angle from the target plane normal and the horizontal emission angle (θ) is defined as an divergent angle on the same vertical emission angle.

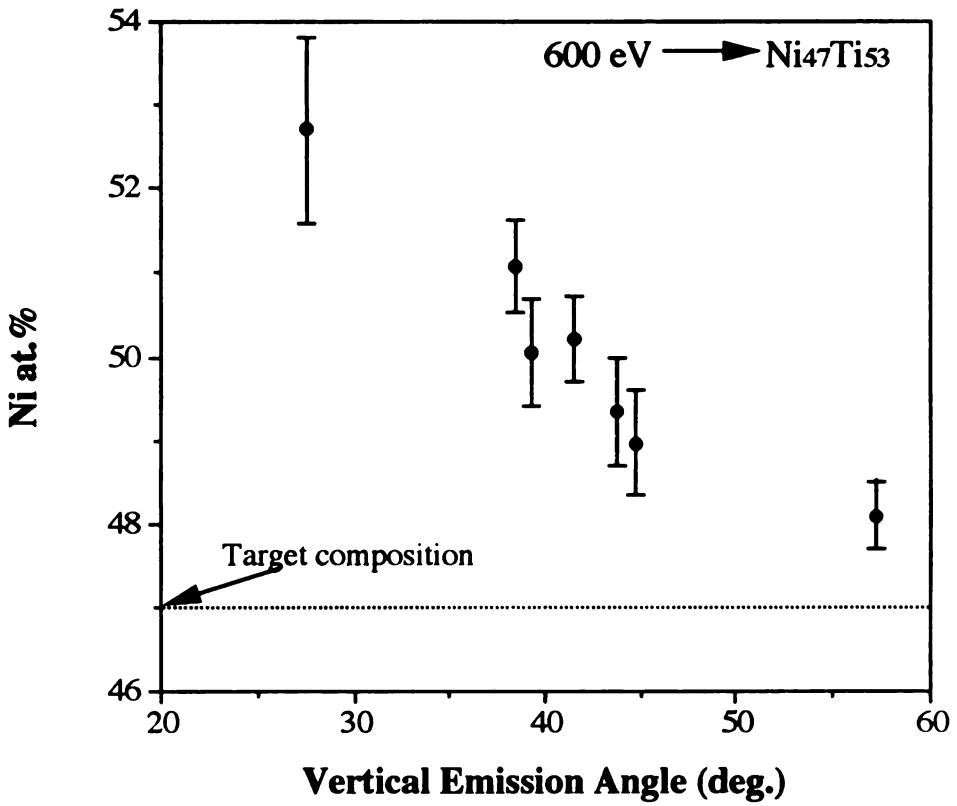

Figure 4-2. Measured concentrations of Ni and Ti in deposited NiTi thin films for various vertical emission angles.

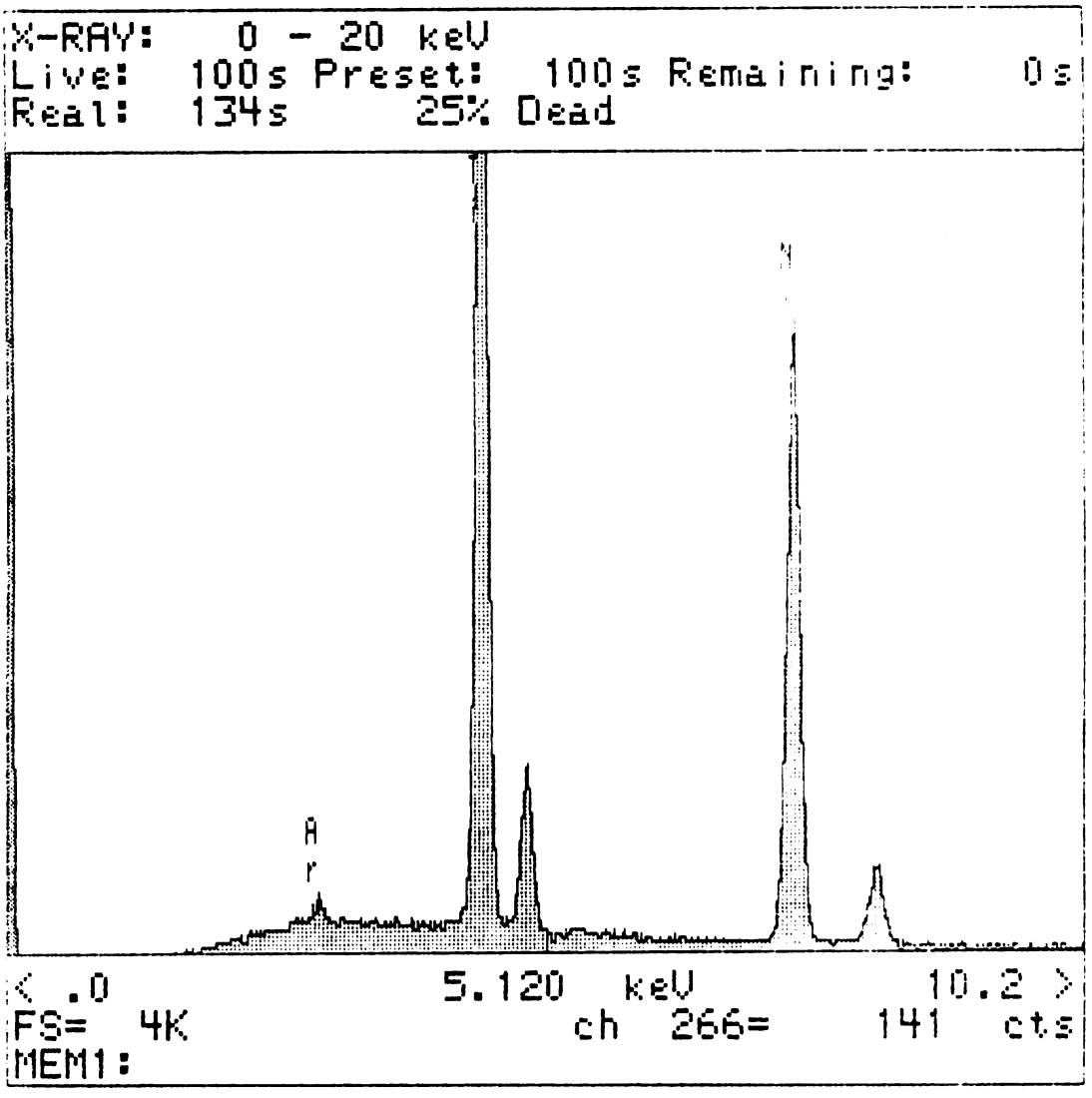

Figure 4-3. EDS spectrum of crystallization annealed NiTi thin film: The argon Kα peak was detected from both as-sputtered and annealed films.

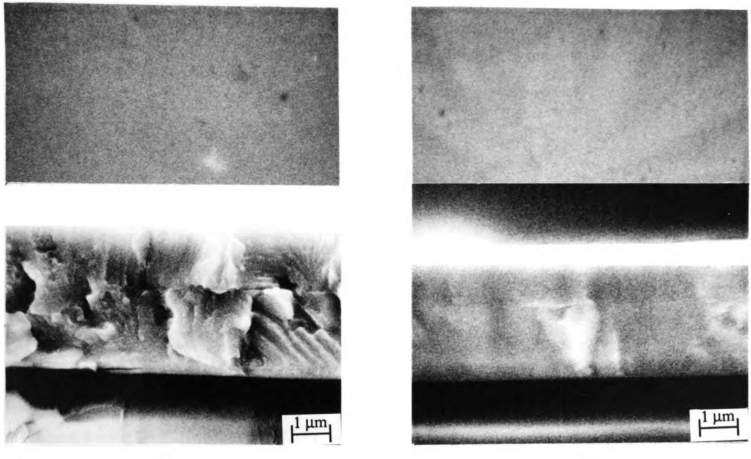

Figure 4-4. Structure of NiTi thin films formed by ion sputter deposition on glass subtrates. Fractured surface (bottom) and surface morphology (top) of (a) the as-sputtered film (amorphous phase) which shows more brittle nature than (b) the crystallization annealed film.

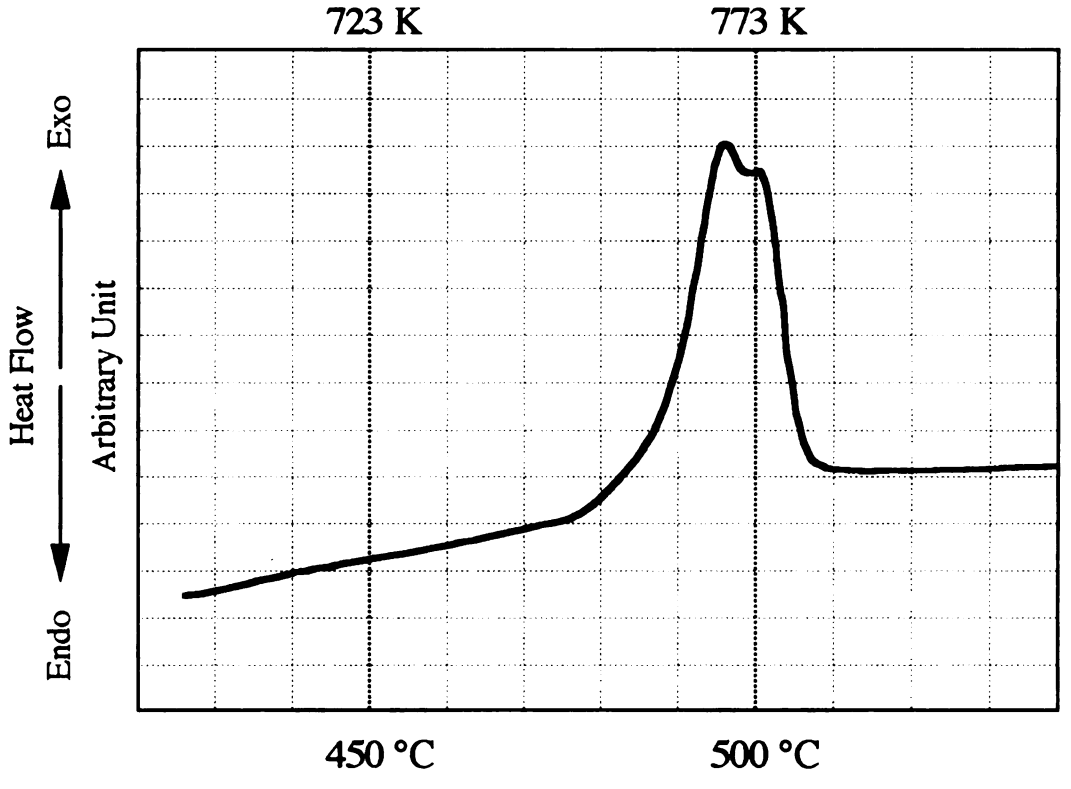

Figure 4-5. DSC trace obtained by heating the 3 μm-thick amorphous NiTi thin film with a heating rate of 10 K/min. The exothermic peak appeared approximately 773 K and was taken to be the crysatliization temperature for the thin film.

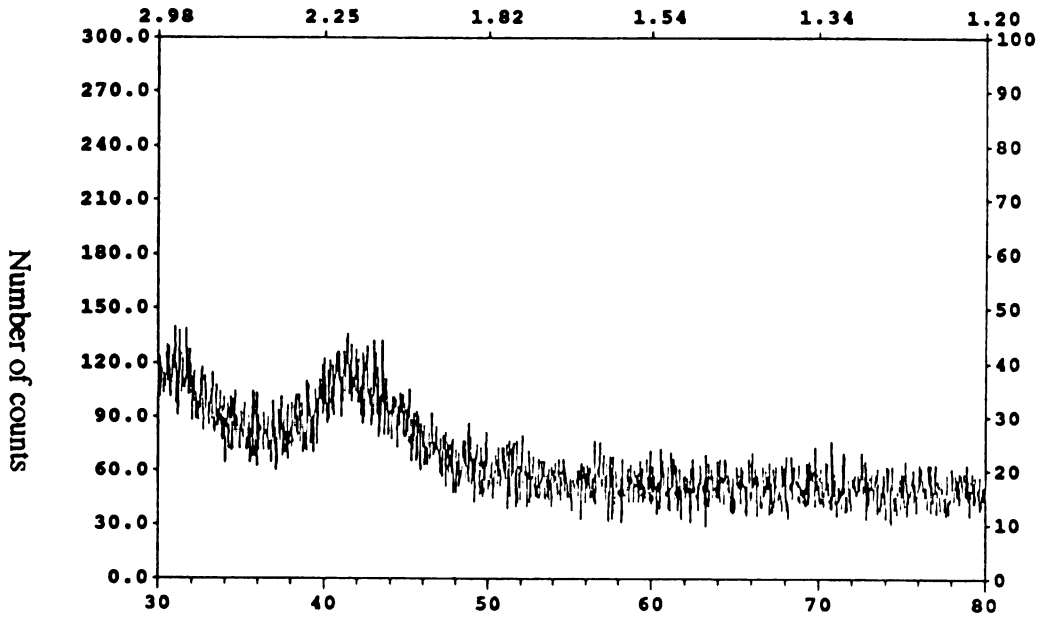

(a)

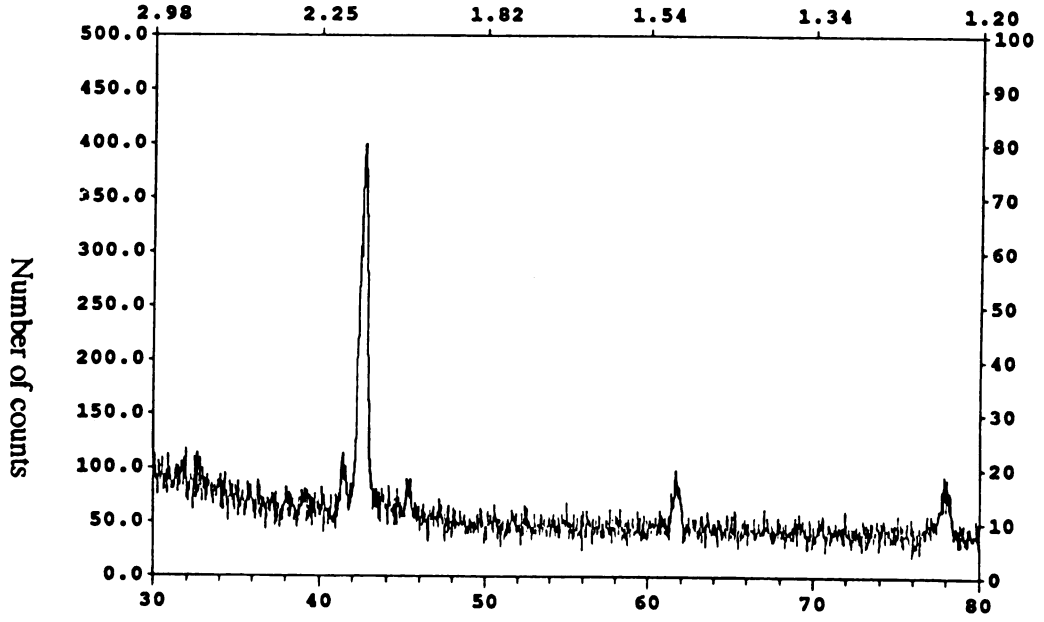

(b)

Figure 4-6. X-ray diffraction scans of (a) as-sputtered and (b) crystallization annealed NiTi thin films.

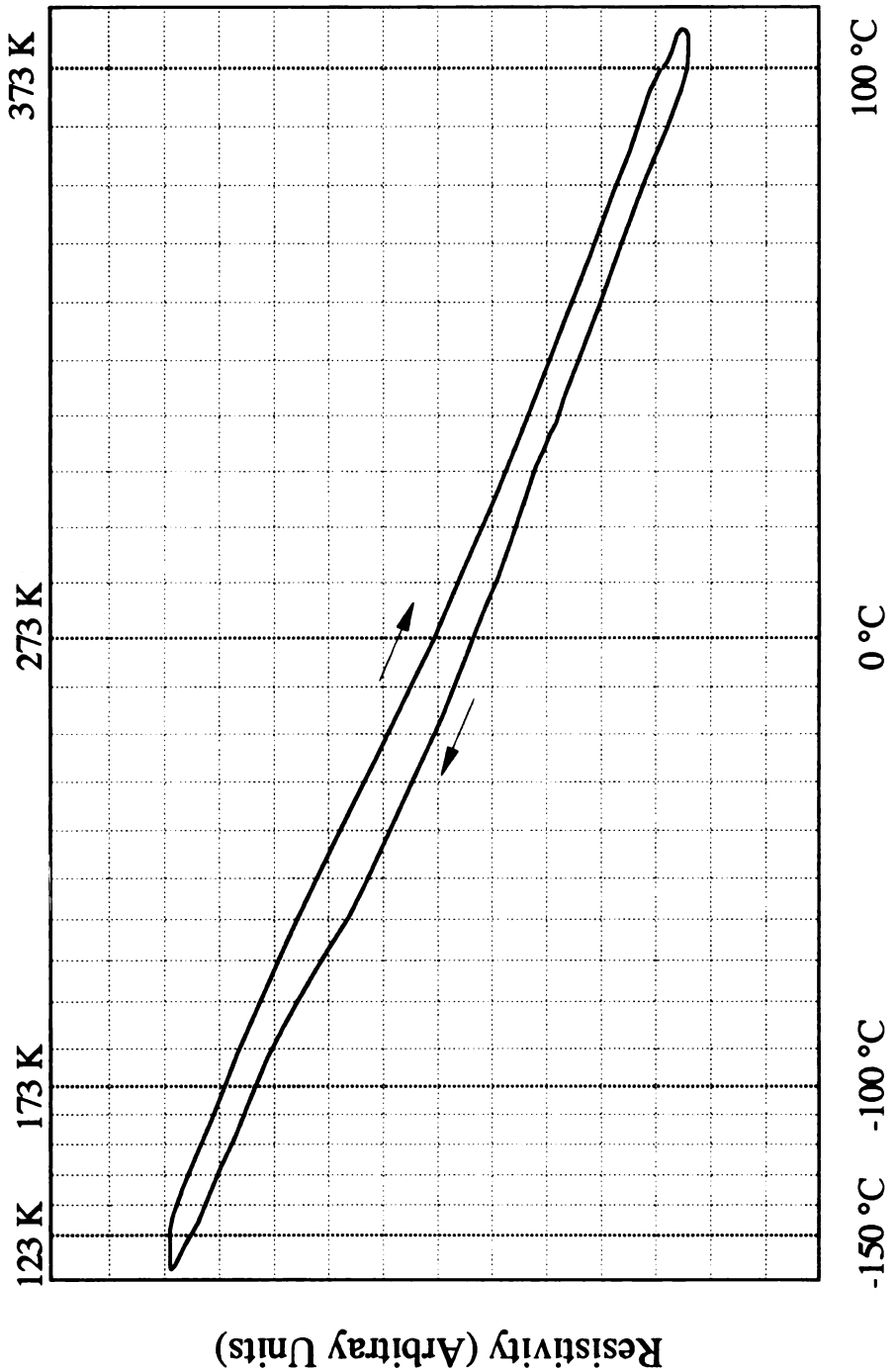

Figure 4-7. Electrical Resistivity as a Function of Temprature for NiTi Amorphous Thin Film.

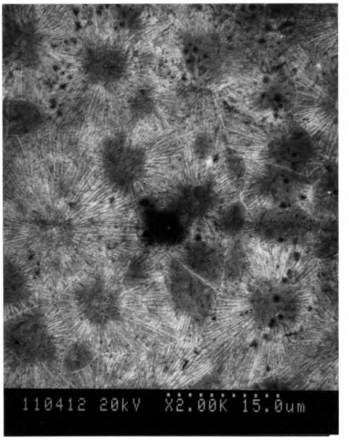

Figure 4-8. SEM micrograph for the NiTi thin film annealed at 873 K for 10 minutes showing grain size and grain morphology.

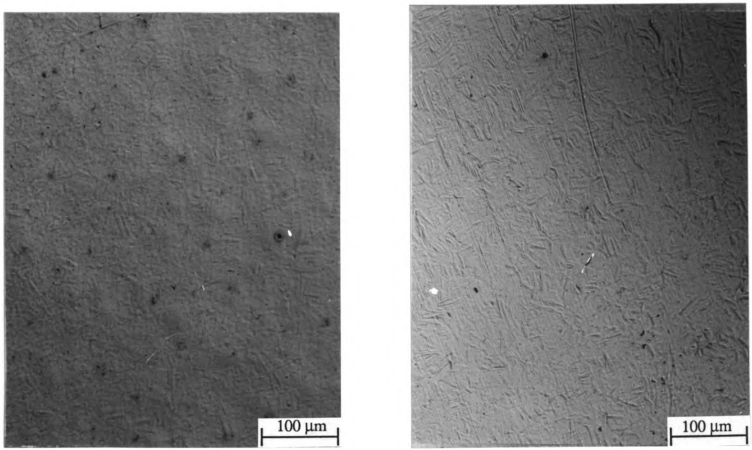

(a) (b)

Figure 4-9. Optical micrographs showing the surface relief morphologies in $Ni_{48.8}Ti_{51.2}$ thin film (A_f = 322 K and M_s = 286 K) deposited on (a) glass and (b) copper substrates at 298 K followed by quenching into liquid nitrogen.

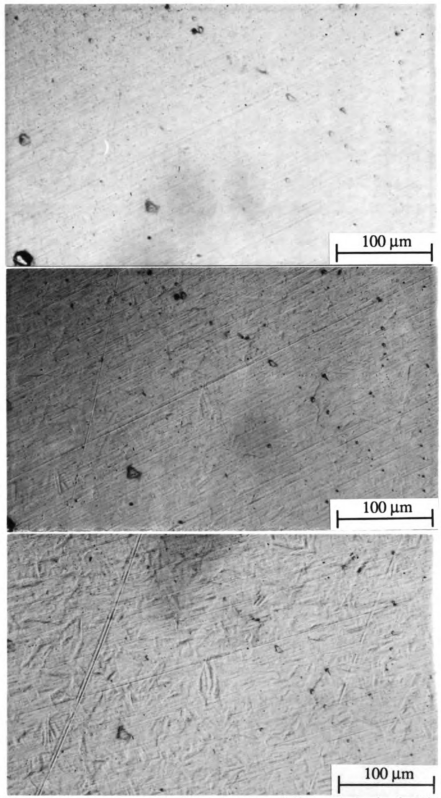

Figure 4-10. Optical micrographs showing the surface relief morphologies in $Ni_{48.8}Ti_{51.2}$ thin film (Af = 322 K and Ms = 286 K) deposited on copper substrates at 298 K (a) cooled from above Af, (b) followed by quenching into ice water and then warmed back to 298 K, and (c) followed by quenching into liquid nitrogen and then warmed back to 298 K.

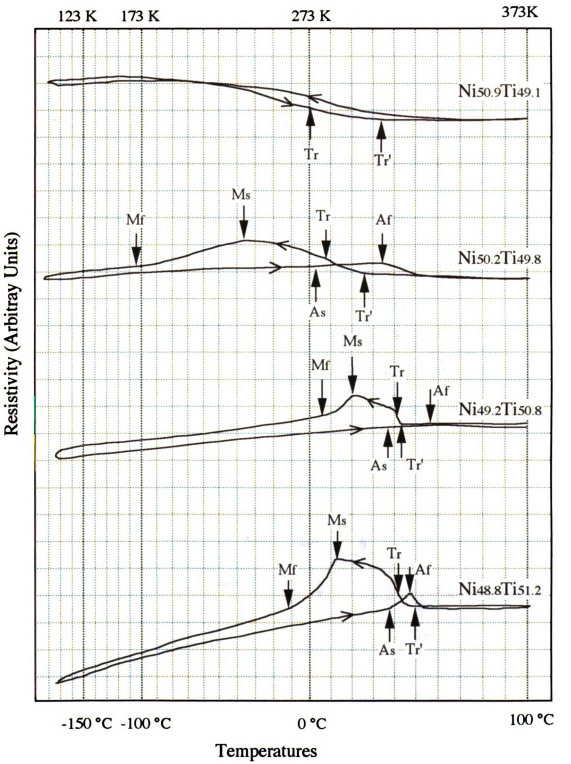

Figure 4-11. Electrical resistivity versus temperature curves for various compositions of NiTi thin film alloys annealed at 873 K for 10 minutes.

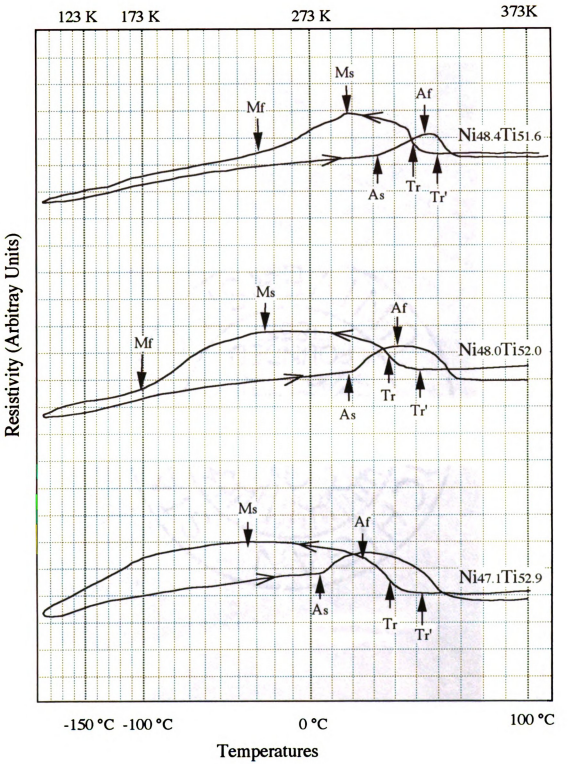
123 K
173 K
273 K
373K
Ms
Mf
Af
Ni48.4Ti51.6
As
Tr
Tr'
Ms
Mf
Af
Ni48.0Ti52.0
As
Tr
Tr'
Ms
Af
Ni47.1Ti52.9
As
Tr
Tr'
Resistivity (Arbitray Units)
-150 °C
-100 °C
0 °C
100 °C
Temperatures

Continued.

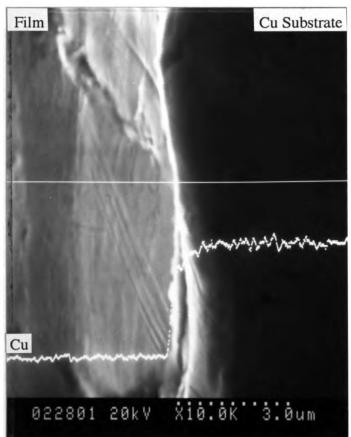

(a)

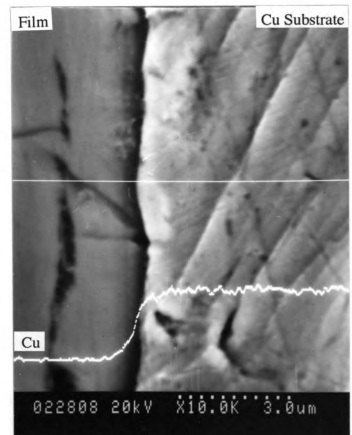

(b)

Figure 4-12. Characteristic X-ray line scanning at the interface between $Ni_{48.8}Ti_{51.2}$ film and substrate showing concentration profiles for (a) Cu before annealing, (b) Cu after annealing, (c) Ni, and (d) Ti after annealing.

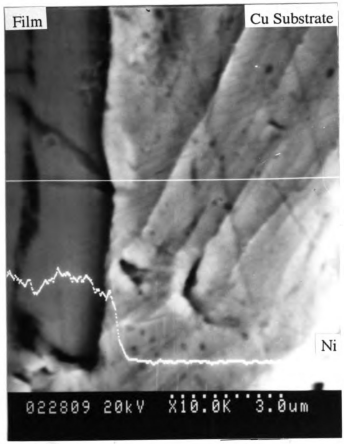

(c)

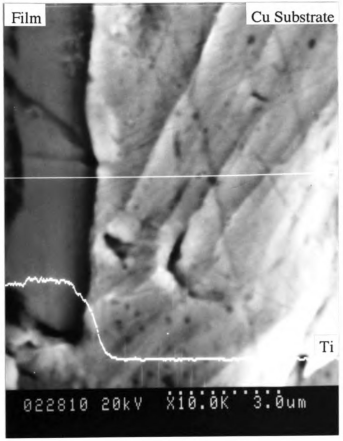

(d)

Continued.

TEST
DATE
FILE

EMC

ARE
TAE

STR

STI

NC
TE
DA
TI
FI
SE
EI
E
S
S
E
E
A
F
T
E
T
E
V
F

TEST: BARE CU(10/7-2/93)
DATE: 10-07-1993
FILE: F1007

EMOD: 120 GPa

AREA: 43.92883 mm^2
TARG: .002

STRS: 41MPa

STRN: 0.001

NCYC: 10005
TEST: BARE CU(10/7-2/93)
DATE: 10-07-1993
TIME: 16:54:48
FILE: F1007
SPEC: F1008
EREM: -1.026154E-03
EPMX: 2.055329E-03
STMX: 124.6745 MPa
SCMX: -129.4277 MPa
EACC: 20.00103
EMOD: 120 GPa
AREA: 43.92883 mm^2
FREQ: 2.202151 Hz
TARG: .002
EPLS: 1.998269E-03
TMAX: 60.01011
BLOK: 324
WRITING
F1008H

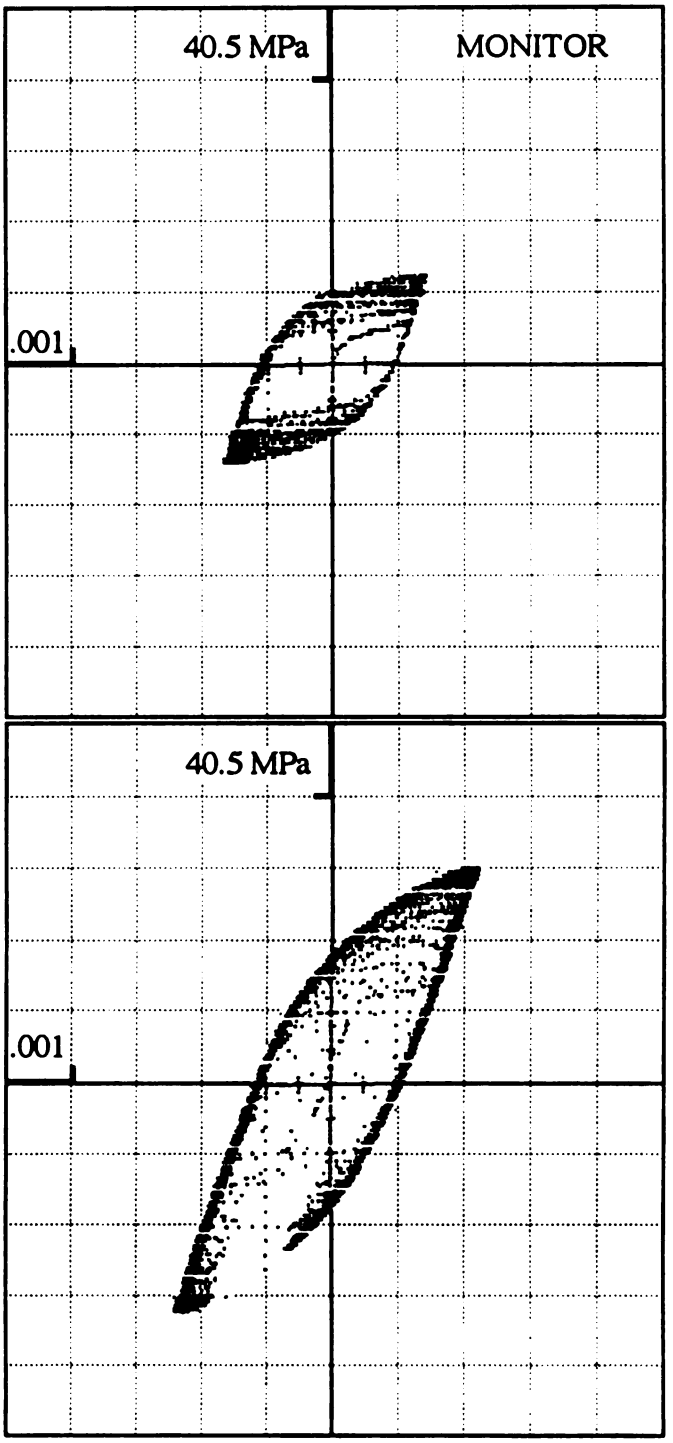

Figure 4-13. The hysteresis loops for the first 10 cycles (top) and after reaching saturation for polystalline copper specimen annealed for 1 hour at 1173 K. ($\Delta\varepsilon_p = 0.2\%$)

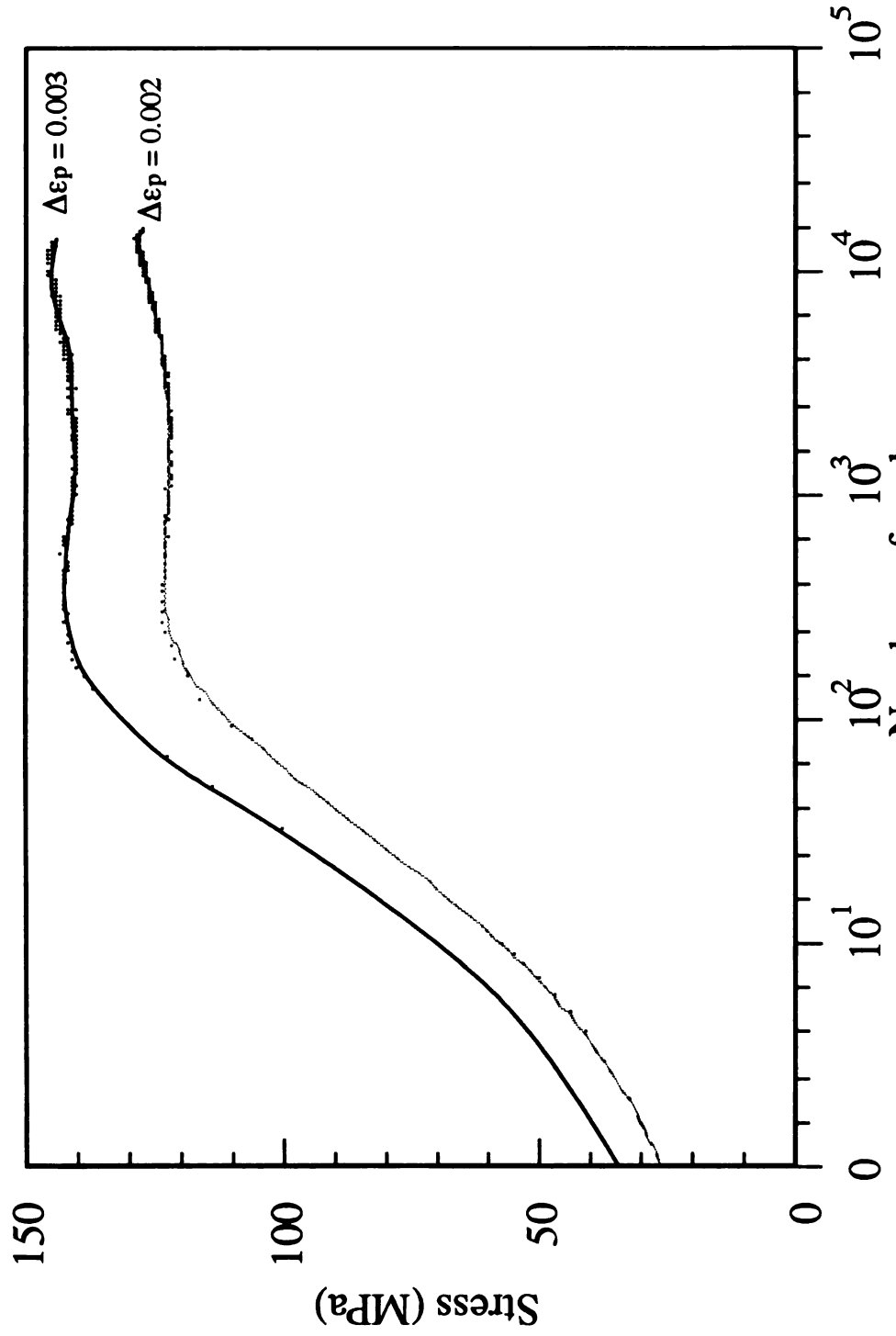

Figure 4-14. Cyclic hardening curve from the polycrystalline copper annealed at 1173 K under plastic strain amplitudes of 0.002 and 0.003. The fatgiue life is shorter and the saturation stress is higher at $\Delta\varepsilon_p = 0.3$ % than at $\Delta\varepsilon_p = 0.2$ %.

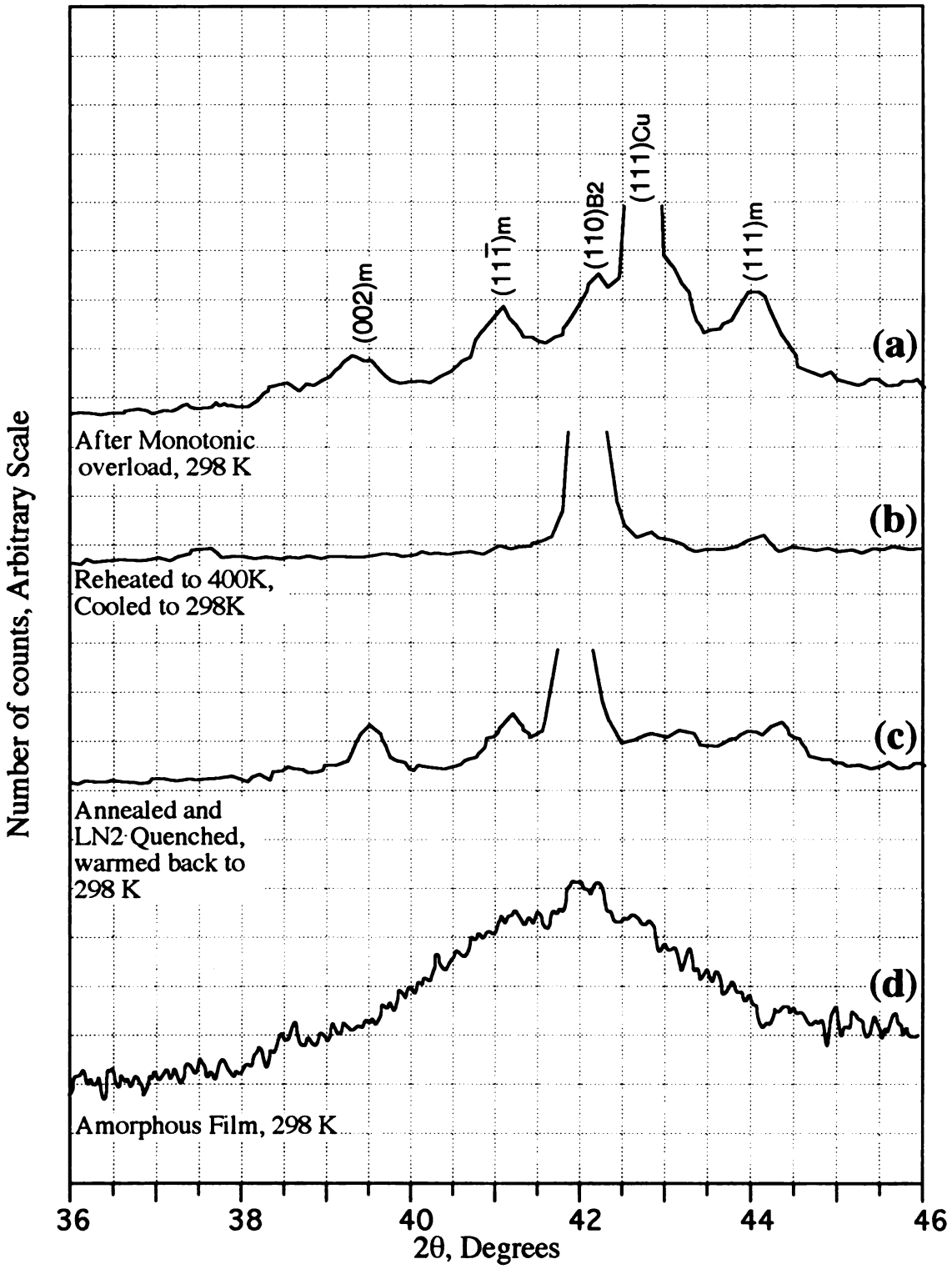

Figure 4-15. Cu-Kα X-ray diffraction scans for $Ni_{50.3}Ti_{49.7}$ film coated specimen at 298 K (Af = 345 K and Ms = 273 K): showing stress-induced martensite peaks on a monotonic loaded (a), crystallization annealed (b), and quenched films followed by warm back to 298 K (c), and as-sputtered films (d).

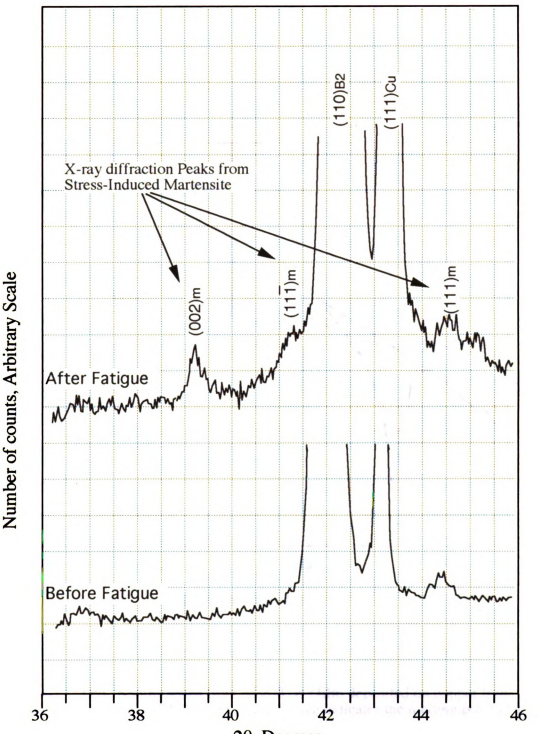

Figure 4-16. X-ray diffraction results from $Ni_{50.3}Ti_{49.7}$ film on fatigue specimen (Af = 345 K and M_s = 273 K). Definite (002), (11-1) and (111) martensite peaks are present after fatigue which are believed to have formed in regions of severe local straining above underlying PSBs.

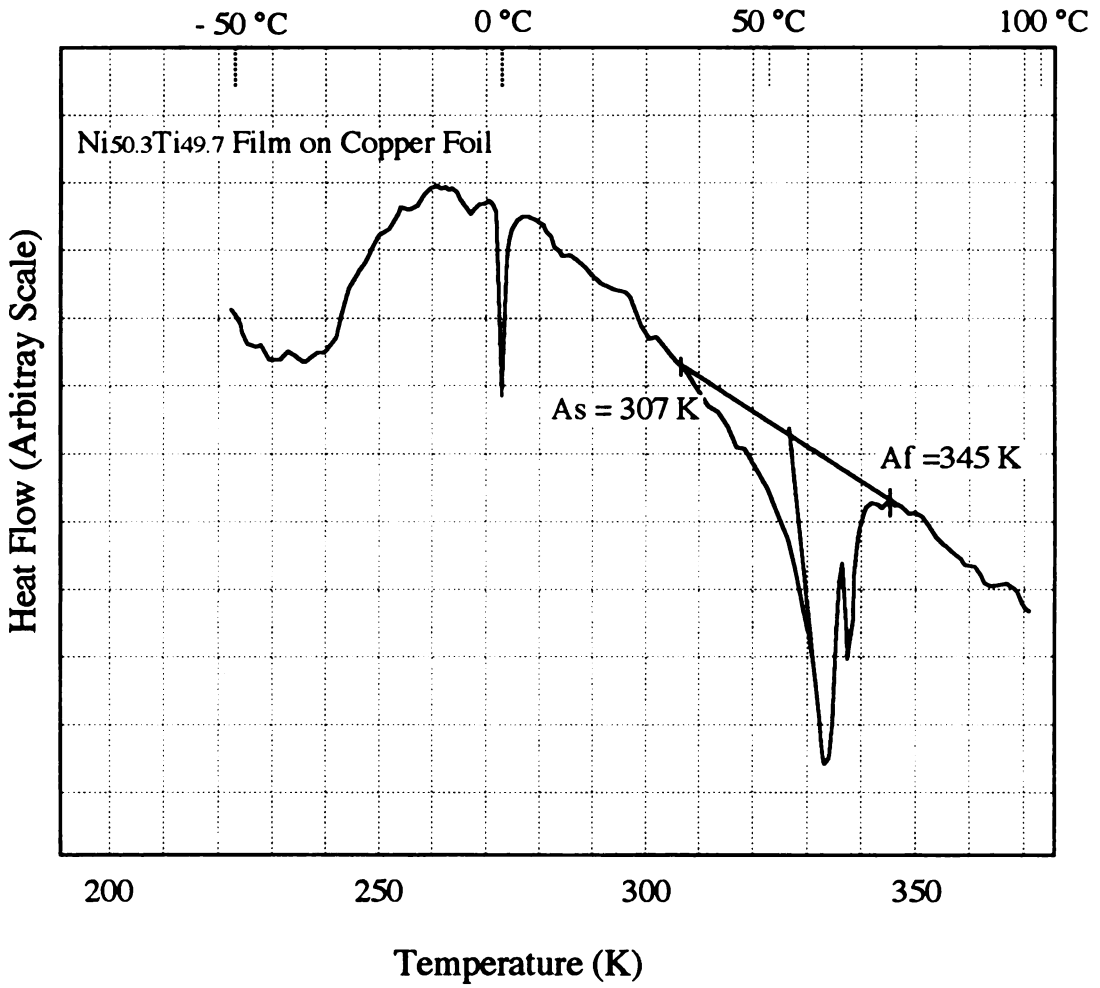

Figure 4-17. DSC heating scans from $Ni_{50.3}Ti_{49.7}$ film deposited on copper foils. The sharp endotherm at 273 K in the scanned trace indicates the melting point of ice.

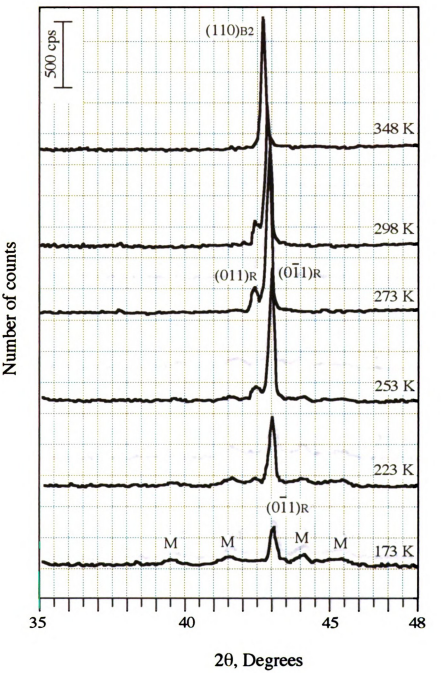

Figure 4-18 (a). X-ray diffraction scans of $Ni_{50.3}Ti_{49.7}$ film on glass substrate on cooling from 348 K to 173 K.

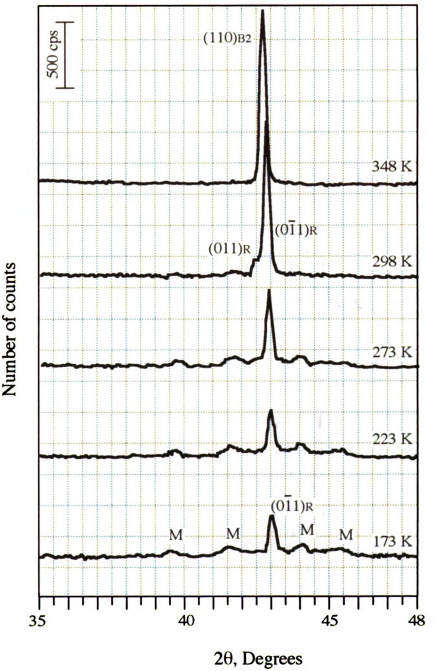

Figure 4-18 (b). X-ray diffraction scans of $Ni_{50.3}Ti_{49.7}$ film on glass substrate on heating from 173 K to 348 K.

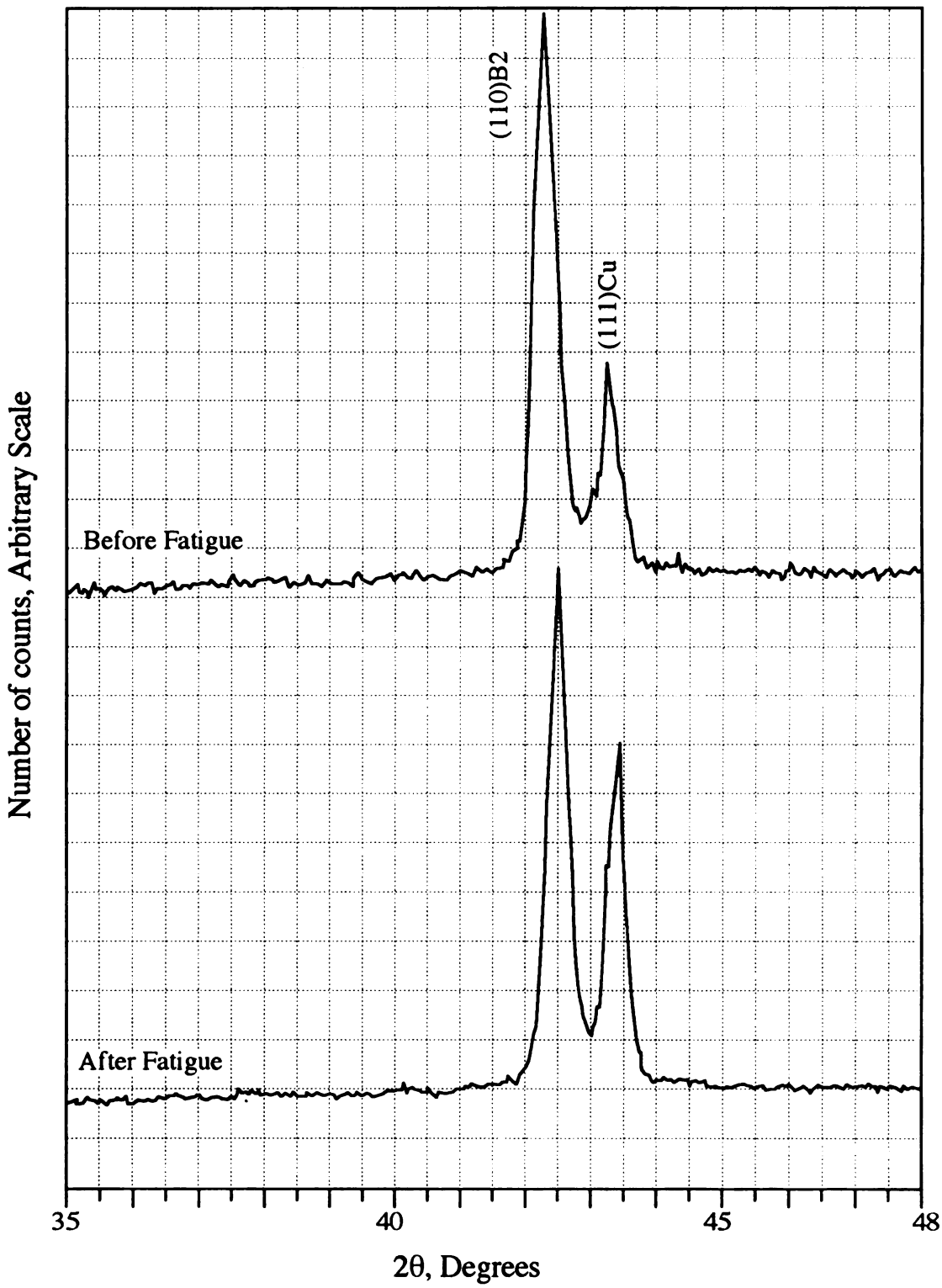

Figure 4-19. Peak shift resulted from a slight change in the height of exposed surface; both (110)$_{B2}$ and (111)$_{Cu}$ peak were shifted to a higher angle at X-ray diffraction scan from fatigued specimen.

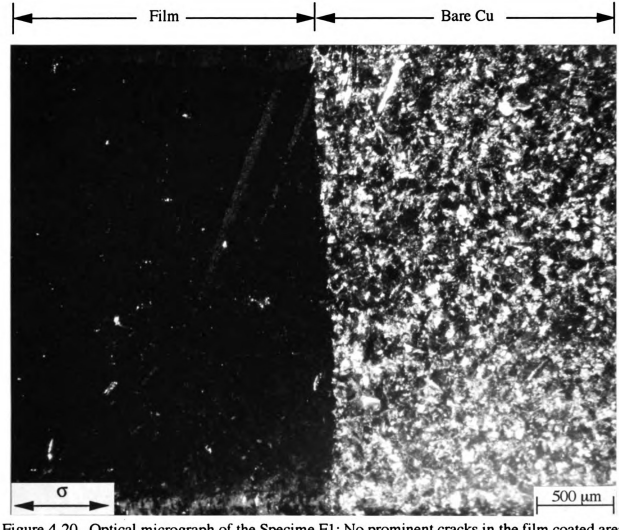

Figure 4-20. Optical micrograph of the Specime F1; No prominent cracks in the film coated area, while severe surface damages were observed in uncoated area ($2\Sigma\Delta\varepsilon_p = 70$).

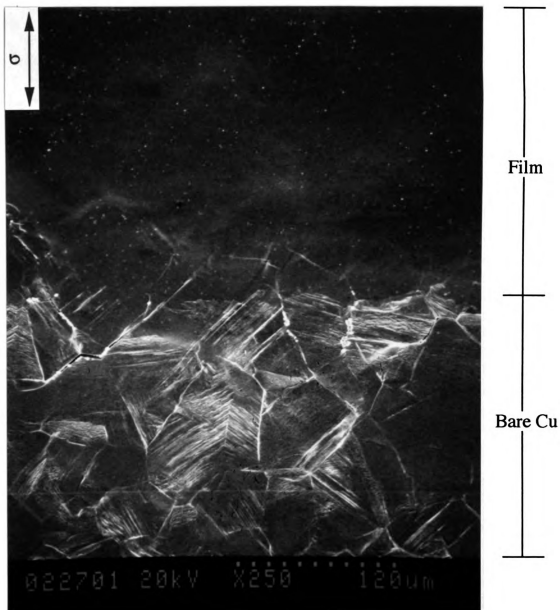

Figure 4-21. (a) SEM micrographs of specimen F1at the boundary between modified (top) and unmodified area (bottom): Significant number of cracks and severe extensive PSB extrusions distributed in unmodified area, whereas no surface damage was observed in the film modified area at a low magnification ($2\Sigma\Delta\varepsilon_p = 70$).

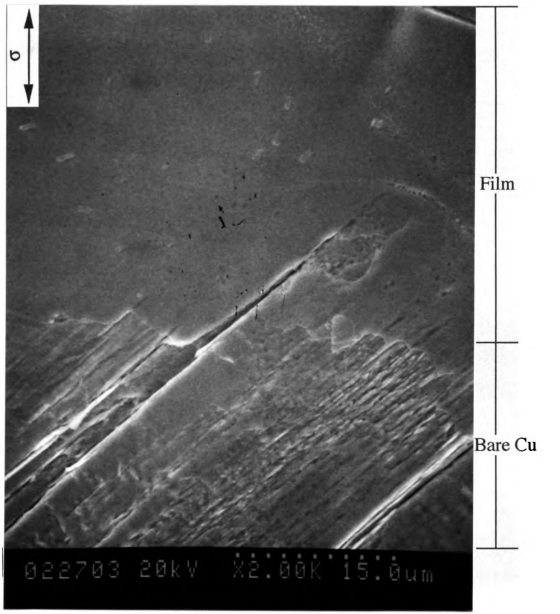

Figure 4-21. (b) SEM micrographs of specimen F1at the boundary between modified (top) and unmodified area (bottom) at a high magnification : The extrusion-intrusion bands in a substrate grain were totally suppressed in tne coated area ($2\Sigma\Delta\varepsilon_p = 70$).

Figure 4-22. SEM micrograph from specimen F1: the film delamination is observed at the triple points of grain boundaries (arrow).

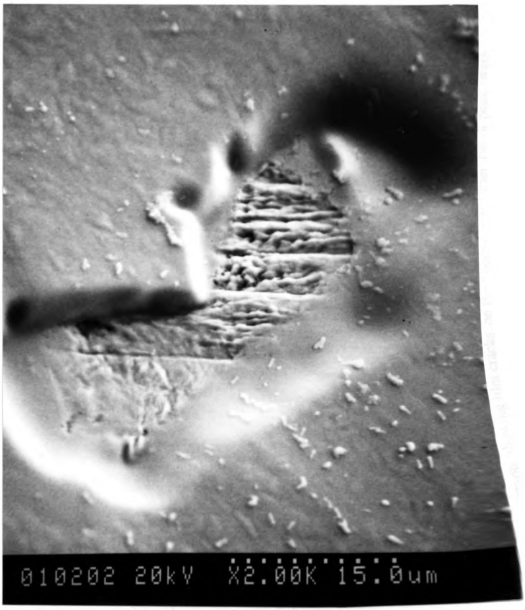

Figure 4-23. SEM micrograph from specimen F1:uncovered local matrix area showed PSBs but film adhered firmly and the slip bands were supressed by the film

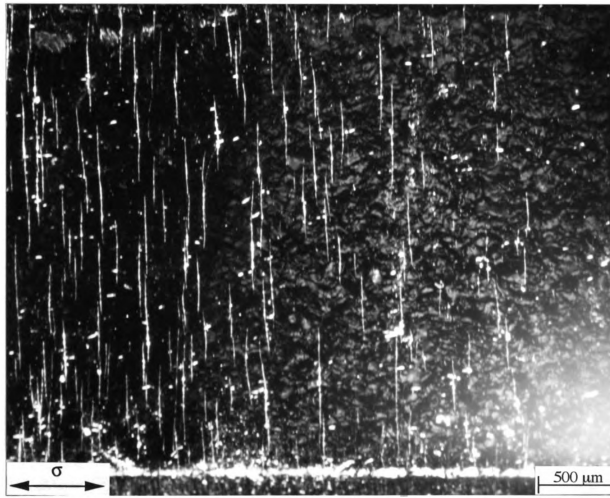

Figure 4-24. Optical micrograph showing film cracks on the Specimen F2 after 1% of peak stress drop ($2\Sigma\Delta\varepsilon_p = 77$).

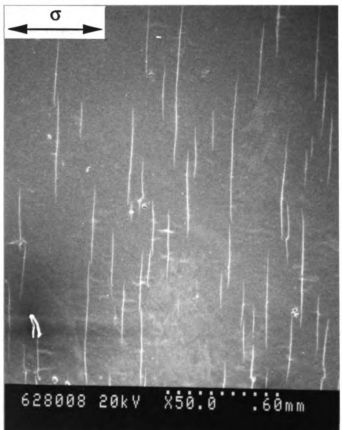

(a)

(b)

Figure 4-25. SEM micrographs from specimen F2: (a) cracks developed perpendicular to the loading direction and (b) few 'wrinkles' were observed at a high magnification.

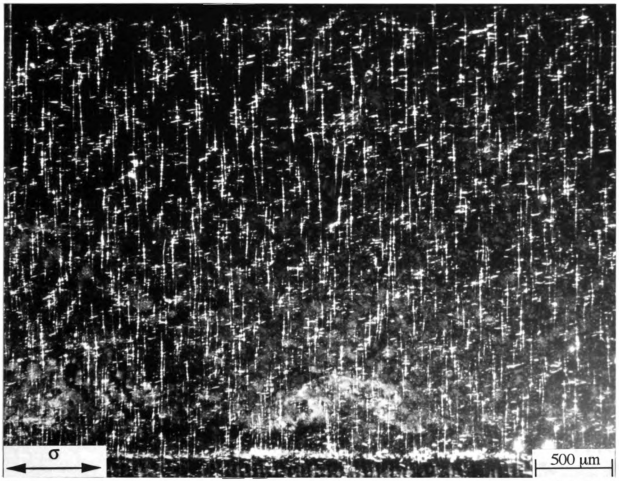

Figure 4-26. Optical micrograph showing film cracks on the Specimen F3 after 1% of peak stress drop ($2\Sigma\Delta\varepsilon_p = 67$).

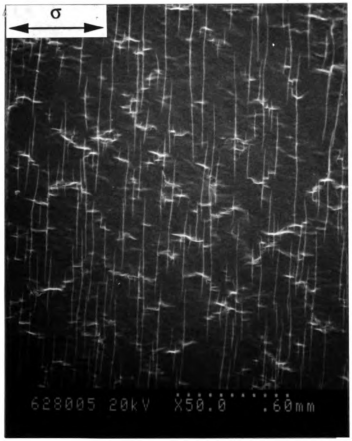

(a)

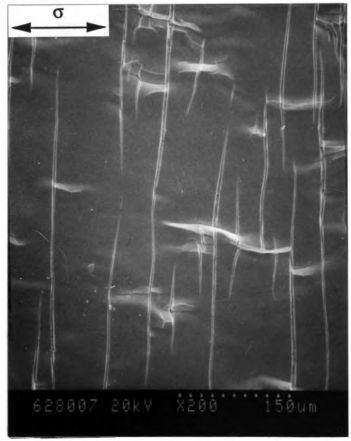

(b)

Figure 4-27. SEM micrographs from specimen F3 showing a high density of cracks developed (a), severe 'wrinkles' were observed (b), and a crack penetrated from the film to the substrate (c).

(c)

Continued.

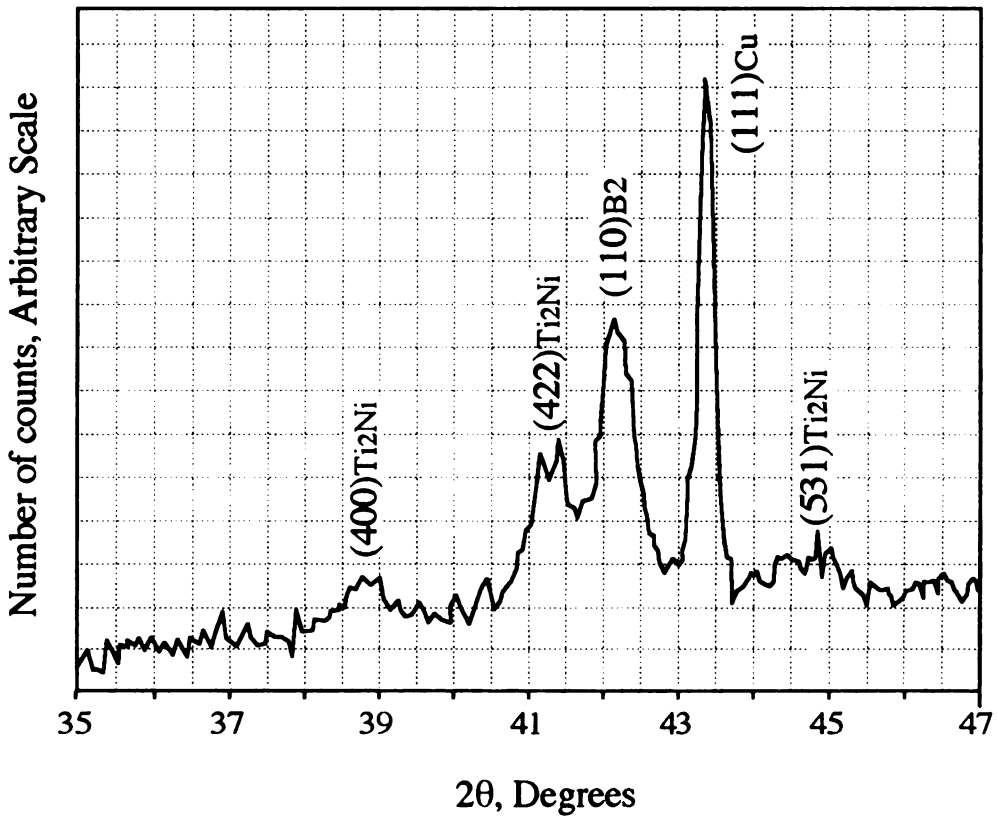

Figure 4-28. Cu K-α X-ray diffraction scans of the specimen F3. Ti2Ni peaks were observed with copper and B2 austenite peaks.

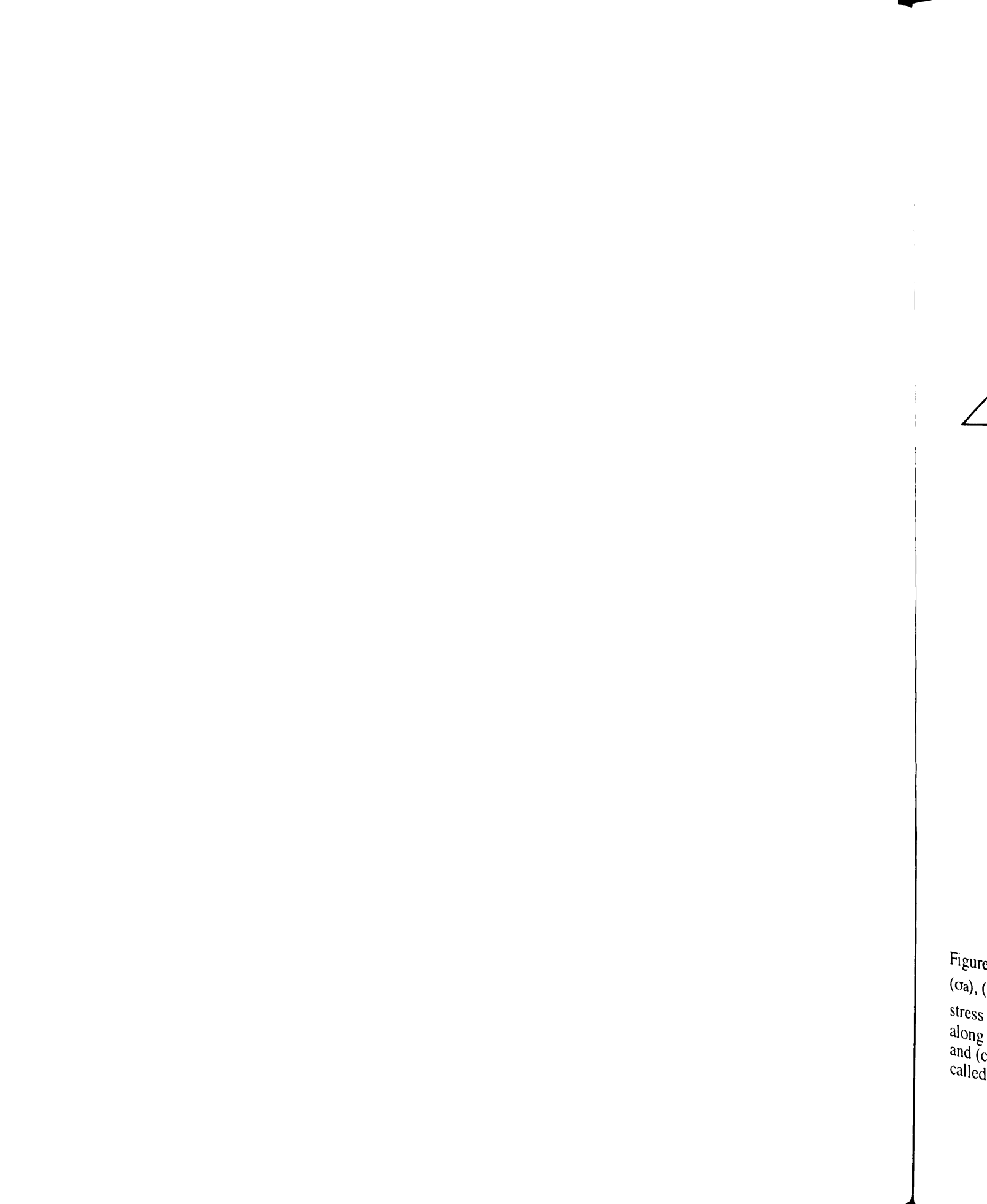

Figure
(σ_a), (
stress
along
and (c
called

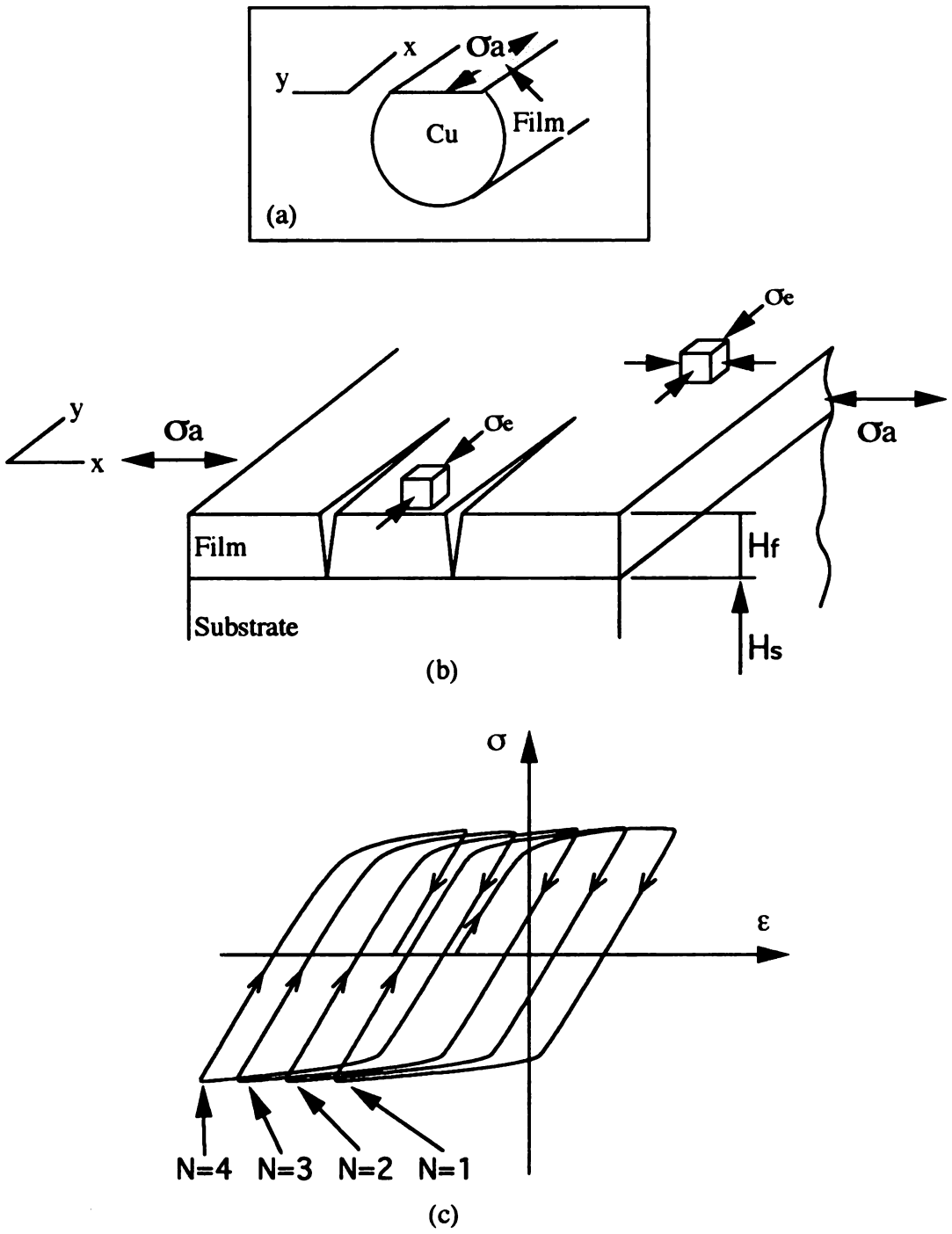

Figure 4-29. (a) A schematic illustration of the gauge area of specimen and applied stress (σa), (b) when parallel cracks developed prependicular to the loading axis on the film, the stress effect in x-direction on the film between the cracks decreases and the stress (σe) along y-direction, will intensify with an aide of residual compressive stress on the film, and (c) the resultant strain along y-direction goes more compressive side continuously called 'cyclic compressive creep'.

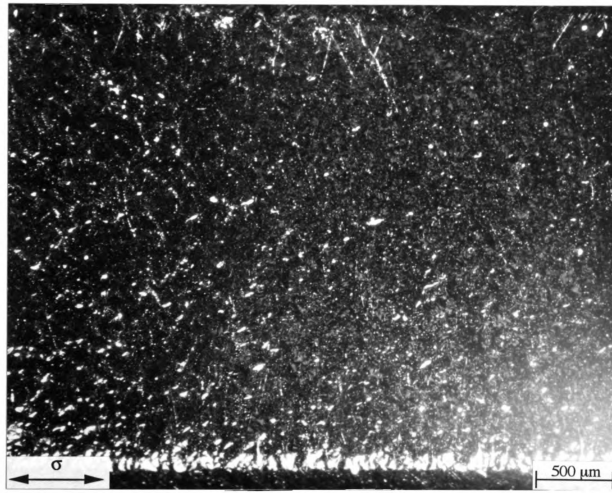

Figure 4-30. Optical micrograph showing no cracks in the flat gauge section area on the Specimen F4 after 1% of peak stress drop ($2\Sigma\Delta\varepsilon_p = 90$).

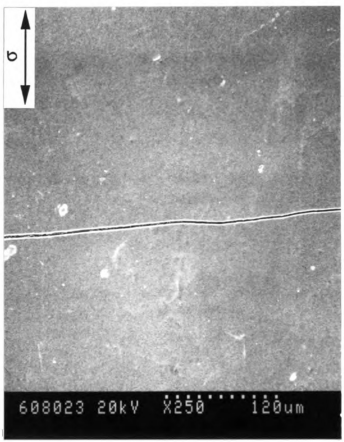

Figure 4-31. SEM micrograph showing a large crack in the opposite side of the flat gauge section area on the Specimen F4 after 1% of peak stress drop ($2\Sigma\Delta\varepsilon_p = 90$).

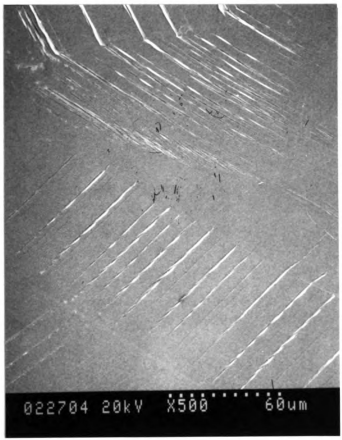

(a)

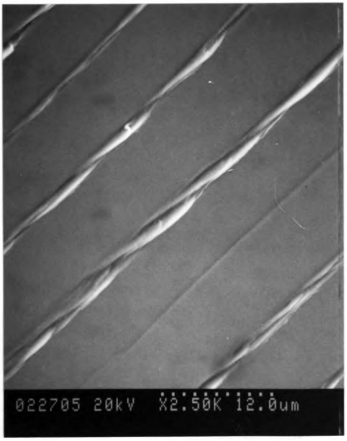

(b)

Figure 4-32. Persistent slip band fromation in unmodified copper after 500 cycles ($2\Sigma\Delta\varepsilon_p = 2$). The slip bands were formed in only favored crystallographic grains (a) and were parellel with same spacing in an individual grain (b).

Figure 4-33. Persistent slip band structure in bare copper after 500 cycles ($2\Sigma\Delta\varepsilon_p = 2$).

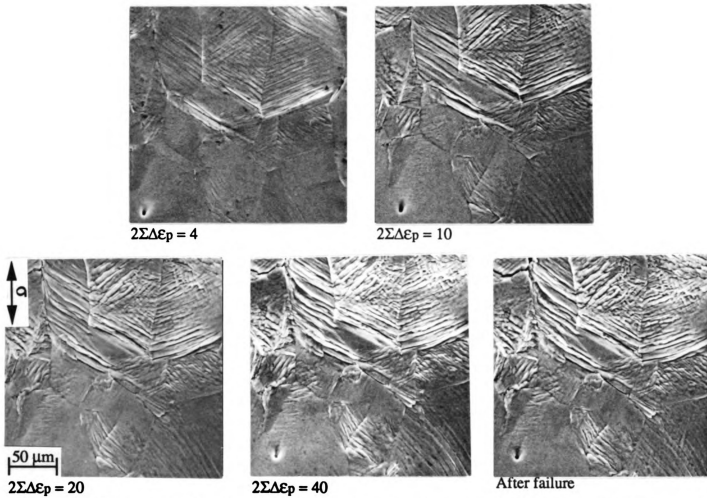

Figure 4-34. SEM photographs of unmodified copper specimen at various cummulated strains ($2\Sigma\Delta\varepsilon_p$ = 4, 10, 20, 40, and after failure) at $\Delta\varepsilon_p$ = 0.2%. The spacing of the slip lines was narrowed and the intencity of the extrusions increased.

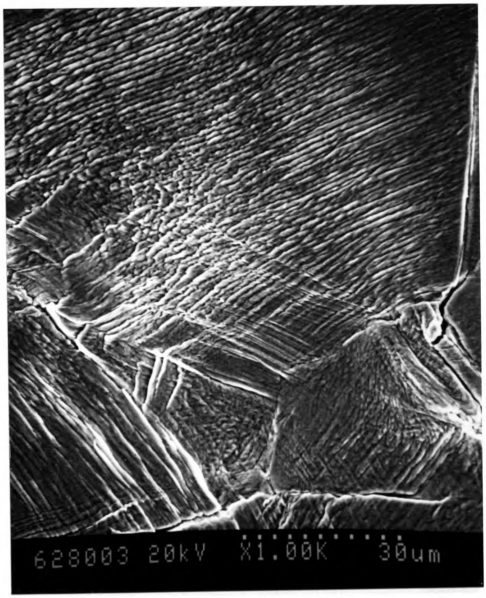

Figure 4-35. SEM micrographs showing the presence of secondary slip trace near grain boundary after fatigue crack initiation occurring ($2\Sigma\Delta\varepsilon_p = 60$).

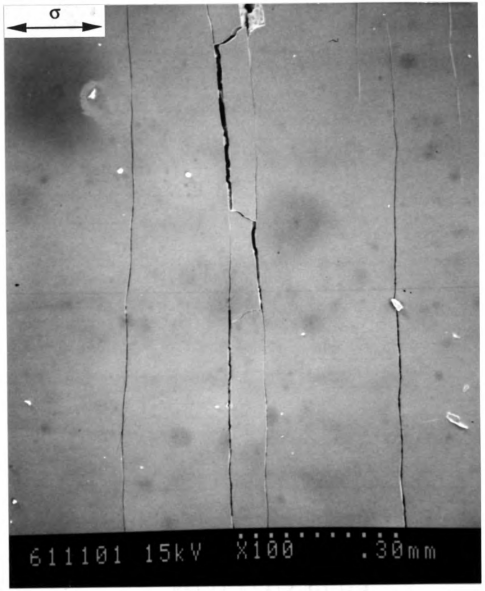

Figure 4-36. SEM micrographs of the specimen Amor.-2 showing fatigue cracks propagated in a straight character ($2\Sigma\Delta\varepsilon_p = 44$).

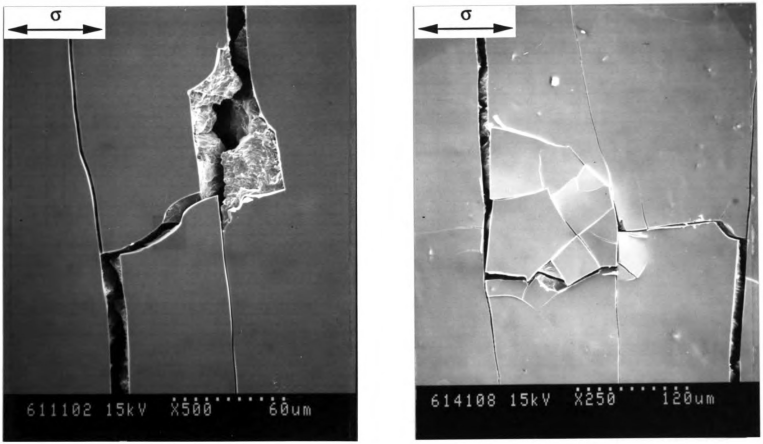

(a) (b)

Figure 4-37. SEM micrographs from amorphous film coated specimen after 1 % peak stress drop (a) cracks were nucleated from amorphous film and (b) the typical brittle nature was observed. ($2\Sigma\Delta\varepsilon_p = 44$)

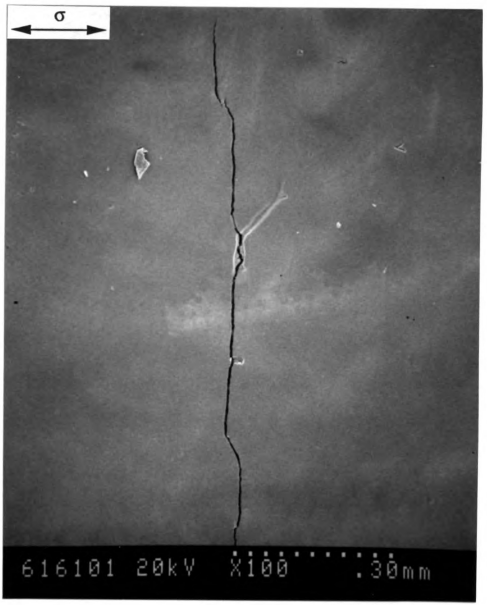

Figure 4-38. SEM micrographs of the specimen A/SIM1 showing a fatigue crack propagated perpendicular to the loaidng axis ($2\Sigma\Delta\varepsilon_p = 100$).

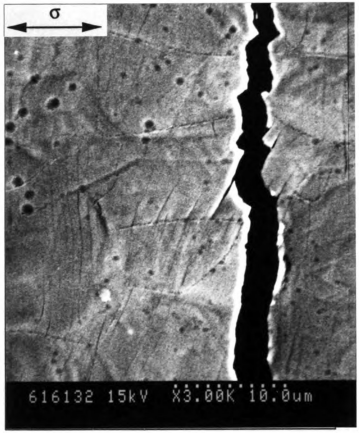

(a)

(b)

Figure 4-39. SEM micrographs of (a) near a large crack and (b) crack tip area of the specimen A/SIM5, and (c) crack tip area of the specimen A/SIM 1.

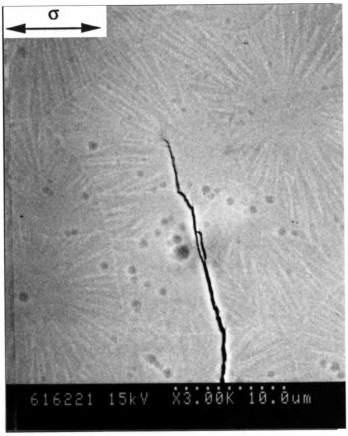

(c)

Continued.

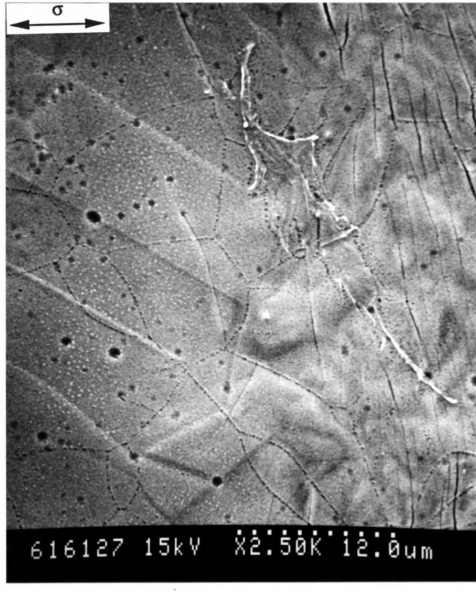

Figure 4-40. SEM micrographs of the specimen A/SIM5 showing a large crack with fine cracks independent of substrate grain orientation ($2\Sigma\Delta\varepsilon_P$ = 90).

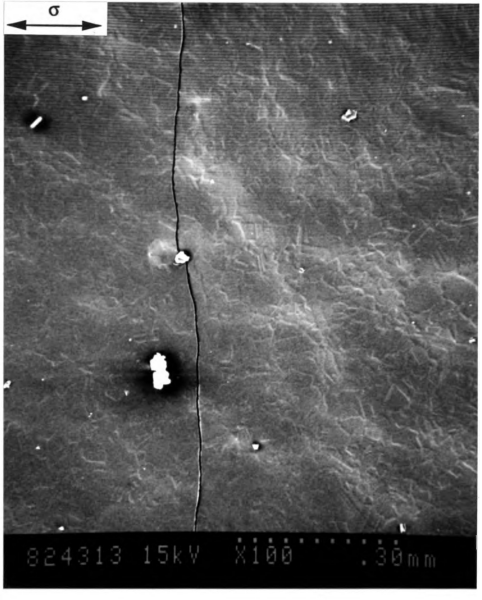

Figure 4-41. SEM micrograph of the specimen A/TE1-1 showing a large wavy crack with surface rumples ($2\Sigma\Delta\varepsilon_p = 120$).

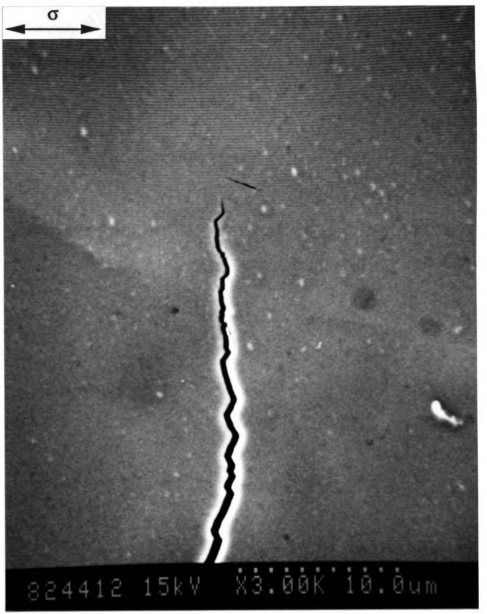

Figure 4-42. SEM micrographs of crack tip area of the specimen A/TE1-1 showing a 'zig-zag' crack propagation ($2\Sigma\Delta\varepsilon_p = 120$).

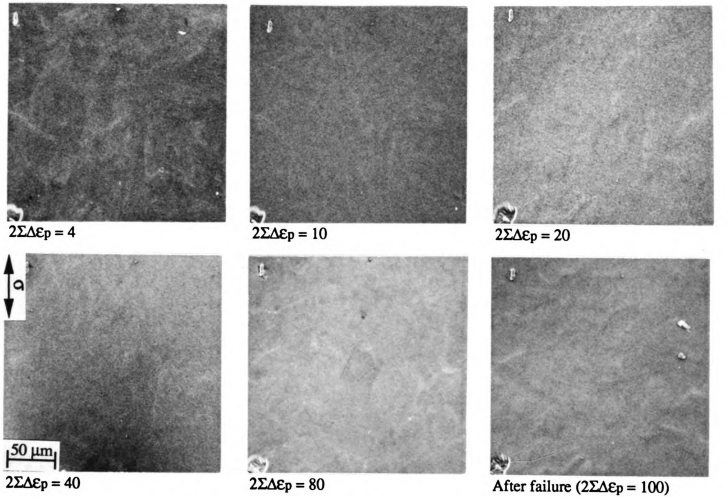

Figure 4-43. SEM photographs of the specimen A/TE3-1 at various cummulated strains ($2\Sigma\Delta\varepsilon_p$ = 4, 10, 20, 40, 80, and after failure).

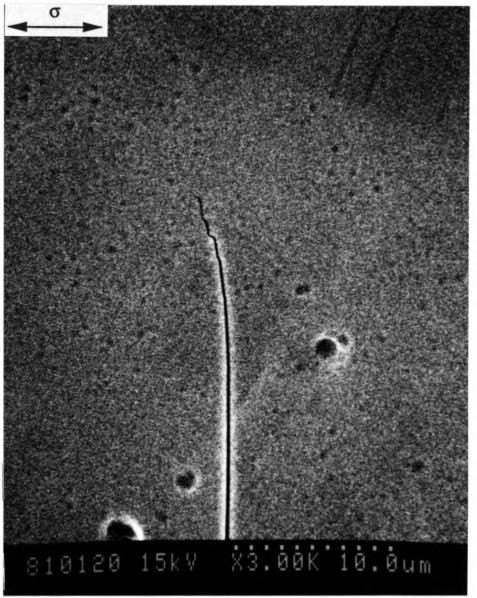

Figure 4-44. SEM micrograph showed the crack tip area of the specimen A/R-3 ($2\Sigma\Delta\varepsilon_p = 88$).

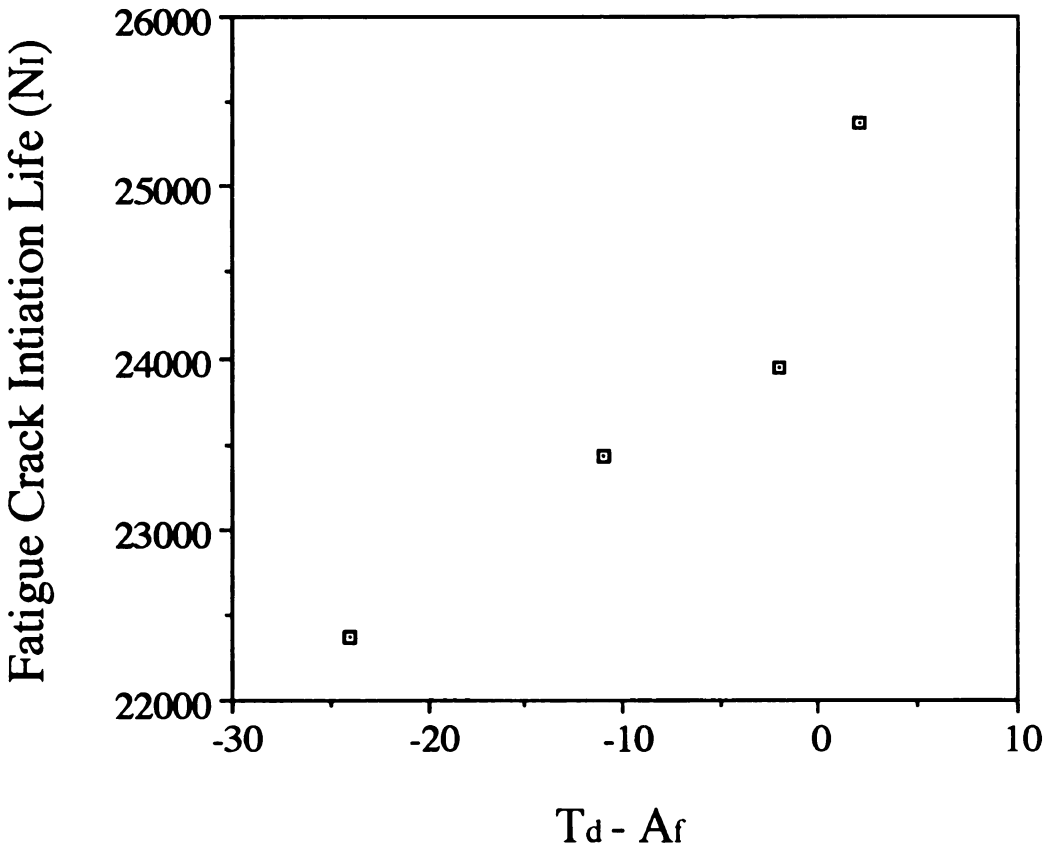

Figure 4-45. Effect of the Difference between Test Temperature (Td) and Af on Fatigue Crack Intiation Life (Ni) of A/SIM-type Film Coated Specimens.

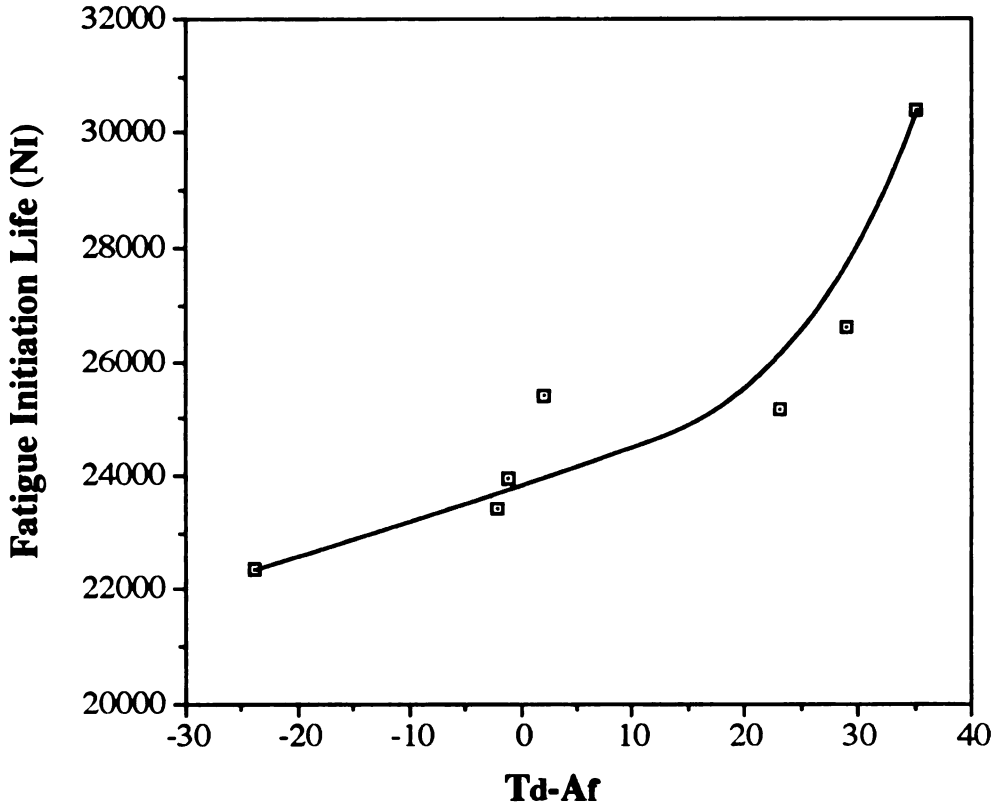

Figure 4-46. Effect of the difference betweenTest Temperature (Td) and Af on Fatigue Crack Initiation life of A/TE andA/SIM-type Film Coated Specimens.

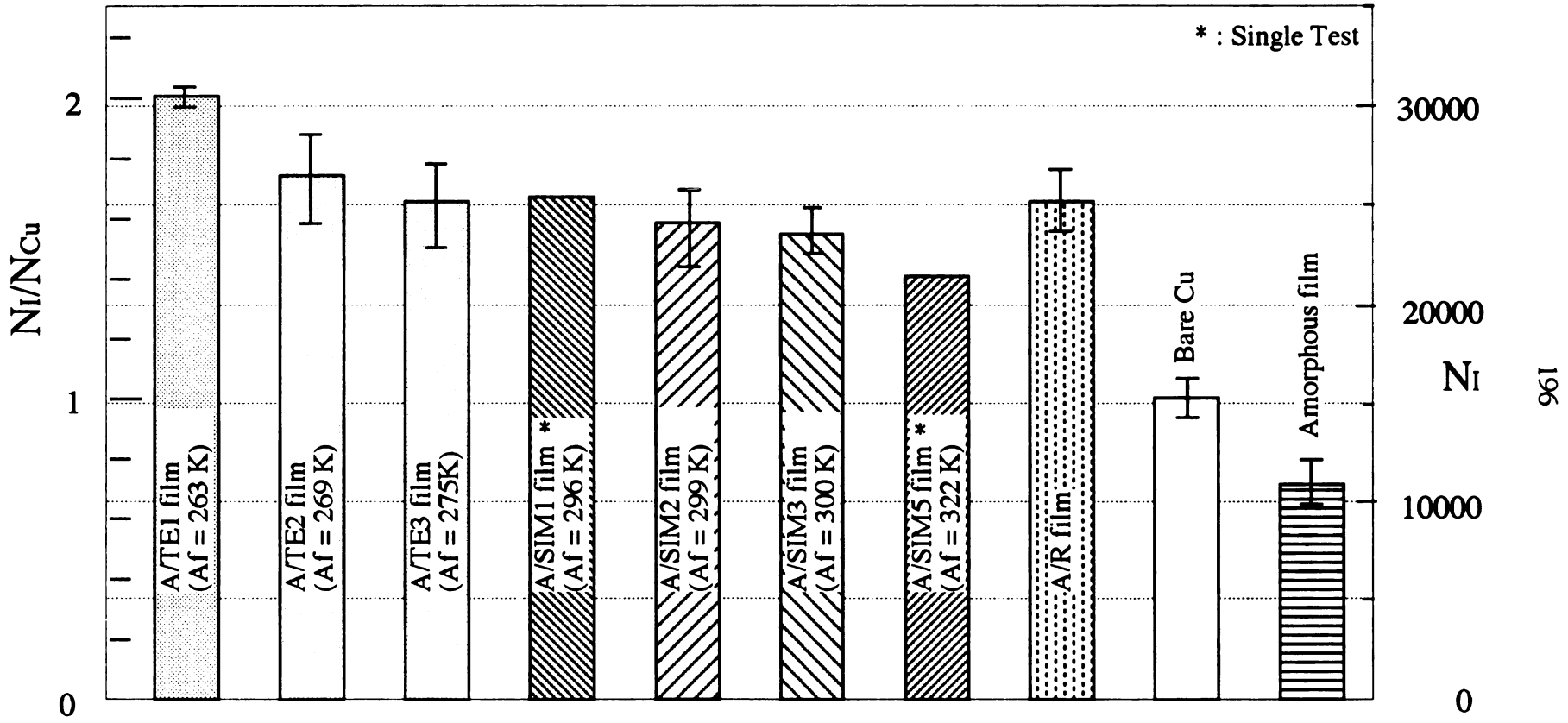

Figure 4-47. Fatigue crack initiation life for various types of film coated specimens. (Test Temperature was 298 K)

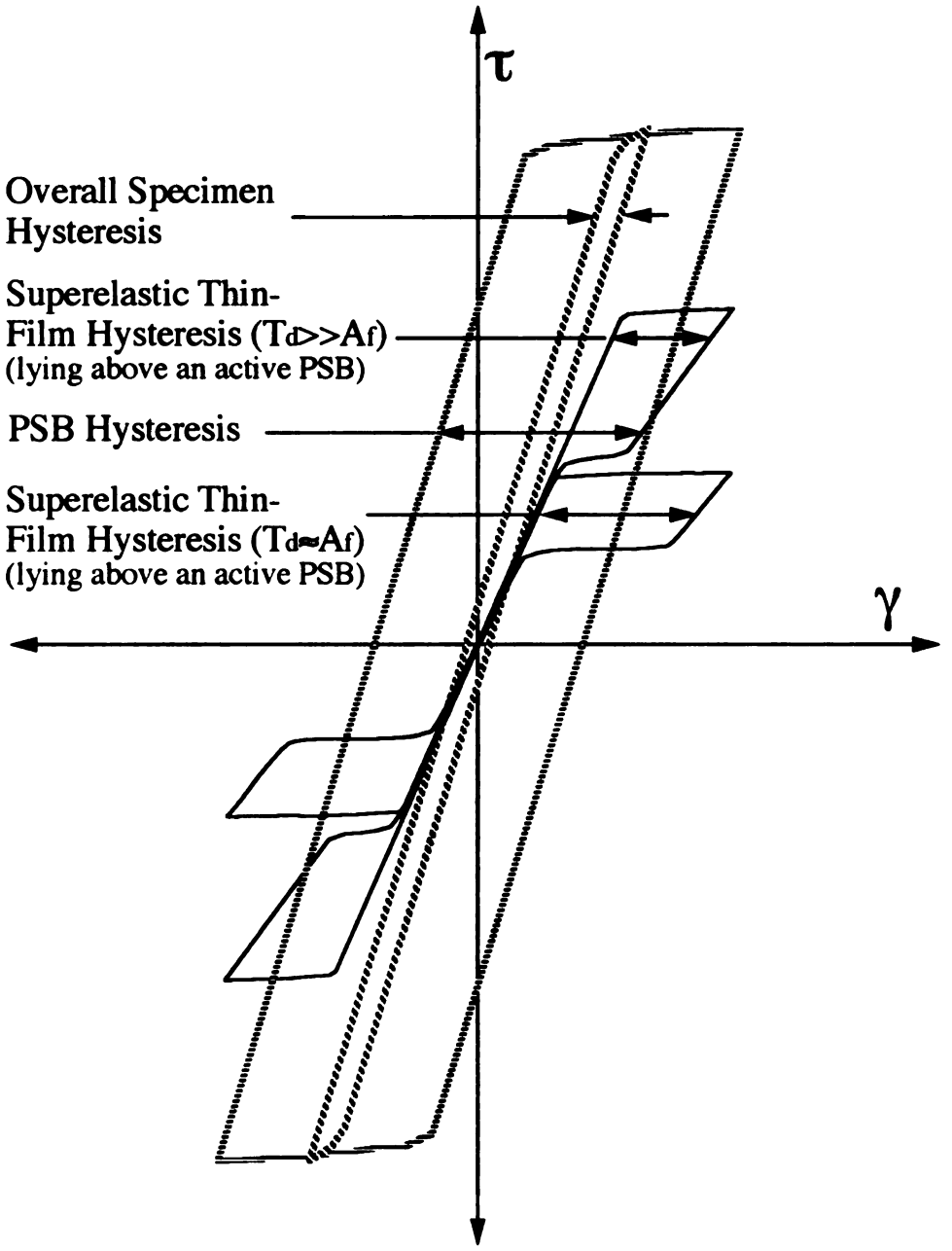

Figure 4-48. Hysteresis loops representing the assumed cyclic stress srtain behavior of the overall (inner, narrow loop), PSB (outer,wide loop) and presumed superelastic film lying above the PSB. The critical stress for the formation of stress-induced martensite is higher at Td>>Af than at Td≈Af.

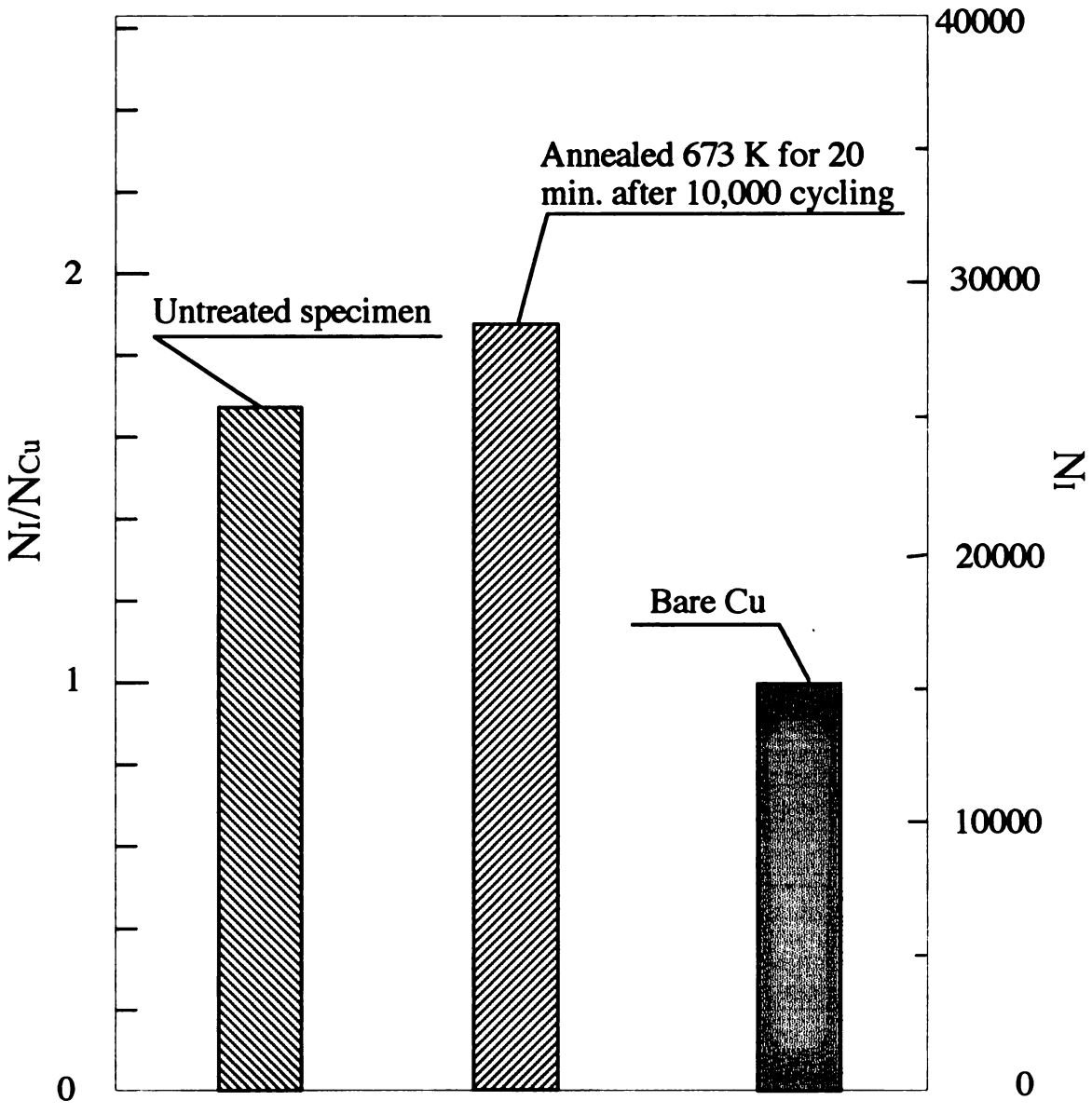

Figure 4-49. Fatigue crack initiation life for A/TE3 type film coated specimens, one kinds specimens fatigued until fatigue crack initiation occurred and the other annealed at 673 K for 20 min. after 10,000 cycles, and resumed the fatigue test until fatigue crack initiation.

APPENDIX

Electrical Resistivity Curves

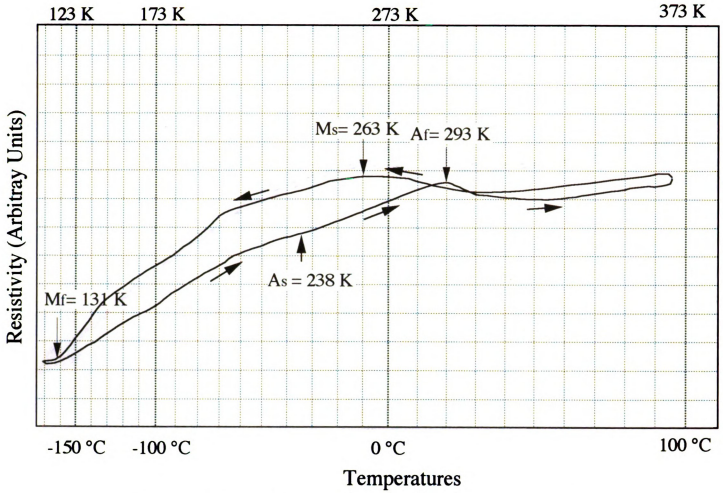

Figure A-1. Electrical Resistivity as a Function of Temperature for F2 Film.

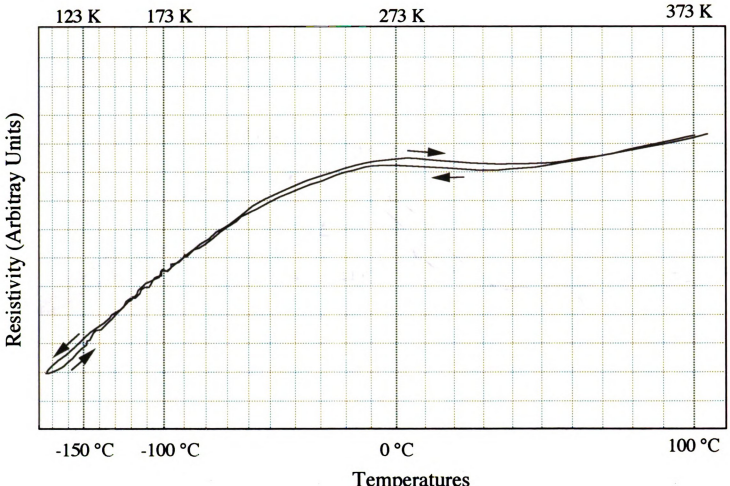

Figure A-2. Electrical Resistivity as a Function of Temperature for F3 Film.

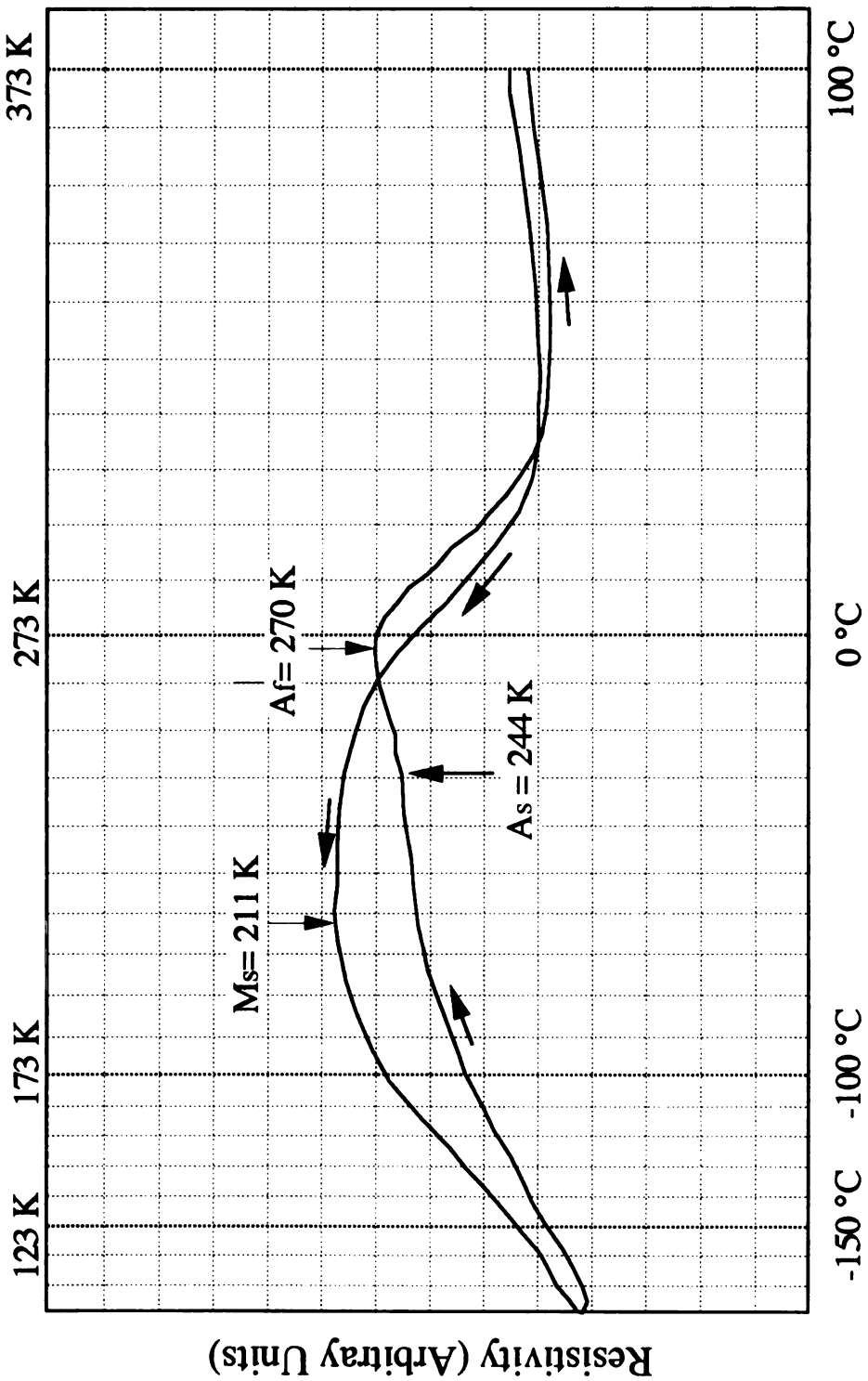

Figure A-3. Electrical Resistivity as a Function of Temperature for F4 Film.

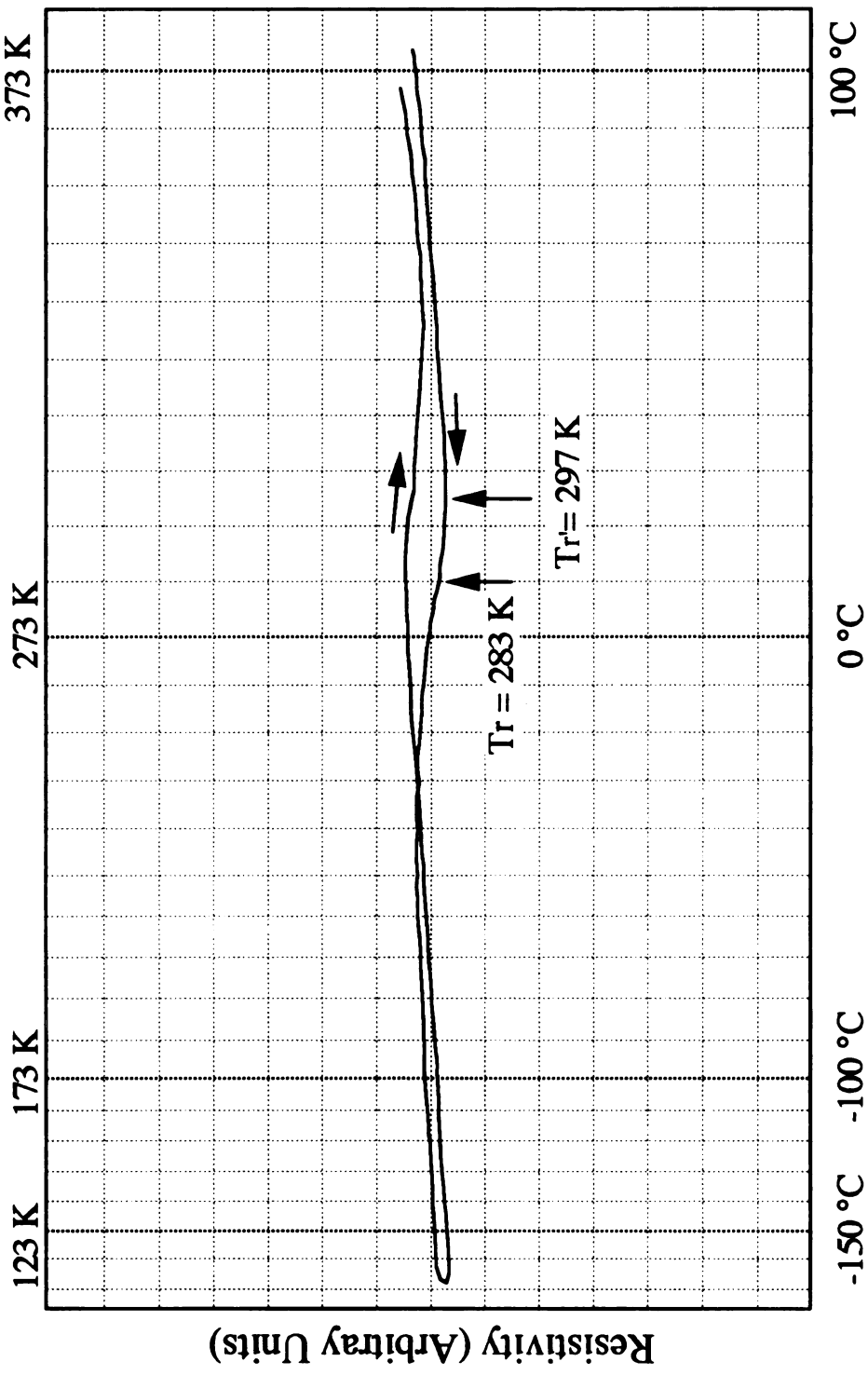

Figure A-4. Electrical Resistivity as a Function of Temperature for A/R tpye Film.

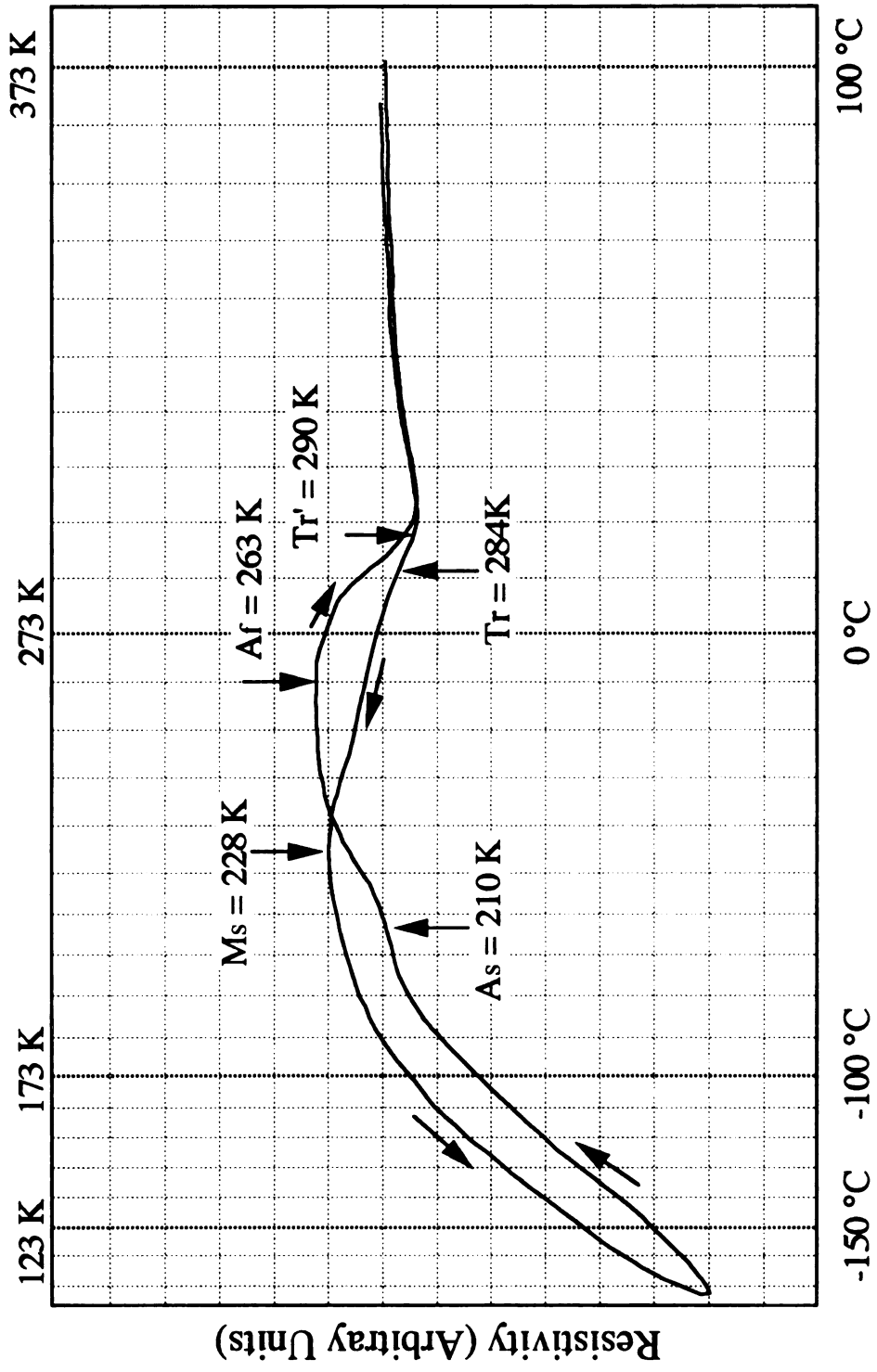

Figure A-5. Electrical Resistivity as a Function of Temperature for A/TE1 tpye Film.

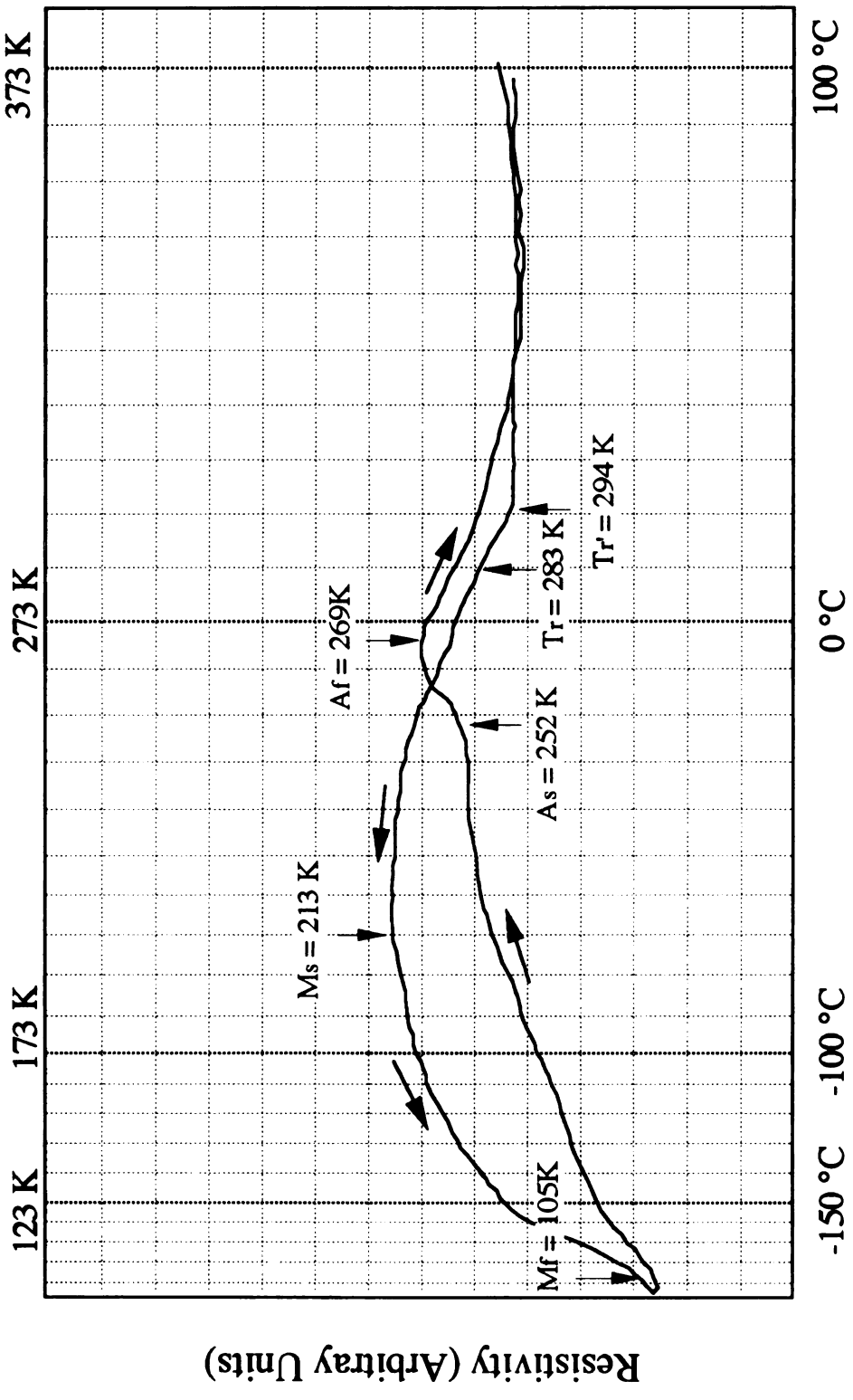

Figure A-6. Electrical Resistivity as a Function of Temperature for A/TE2 tpye Film.

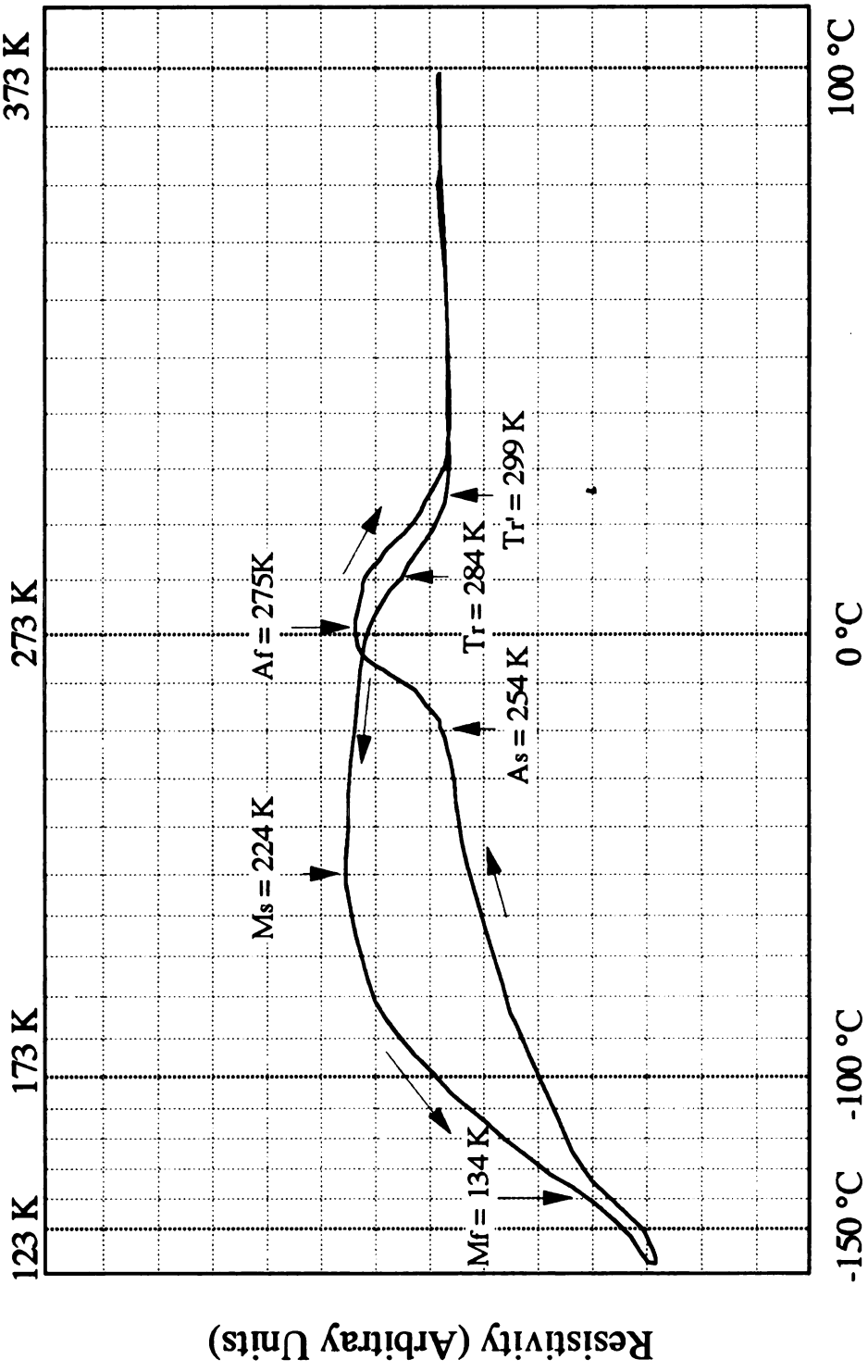

Figure A-7. Electrical Resistivity as a Function of Temperature for A/TE3 tpye Film.

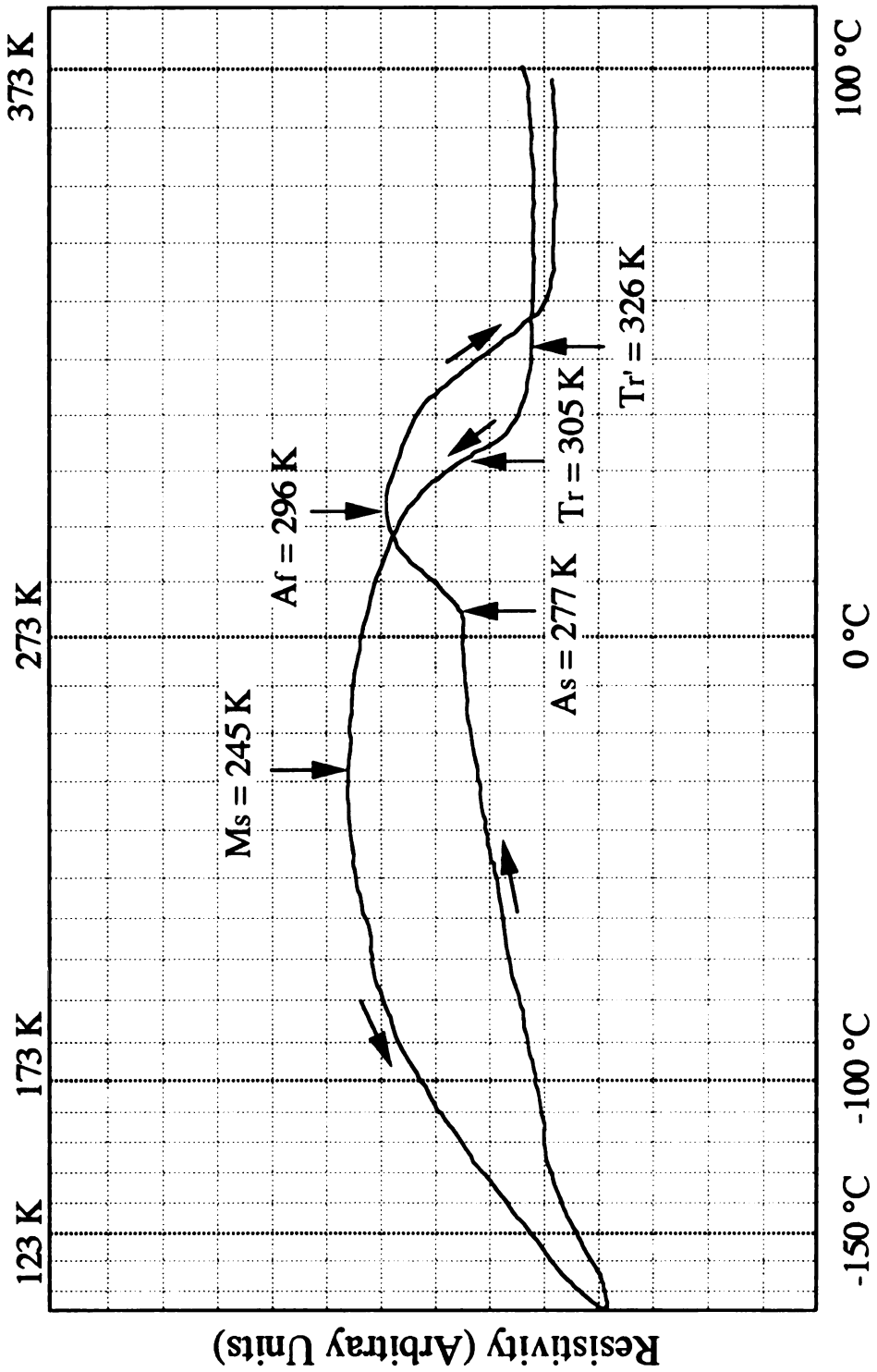

Figure A-8. Electrical Resistivity as a Function of Temperature for A/SIM1 tpye Film.

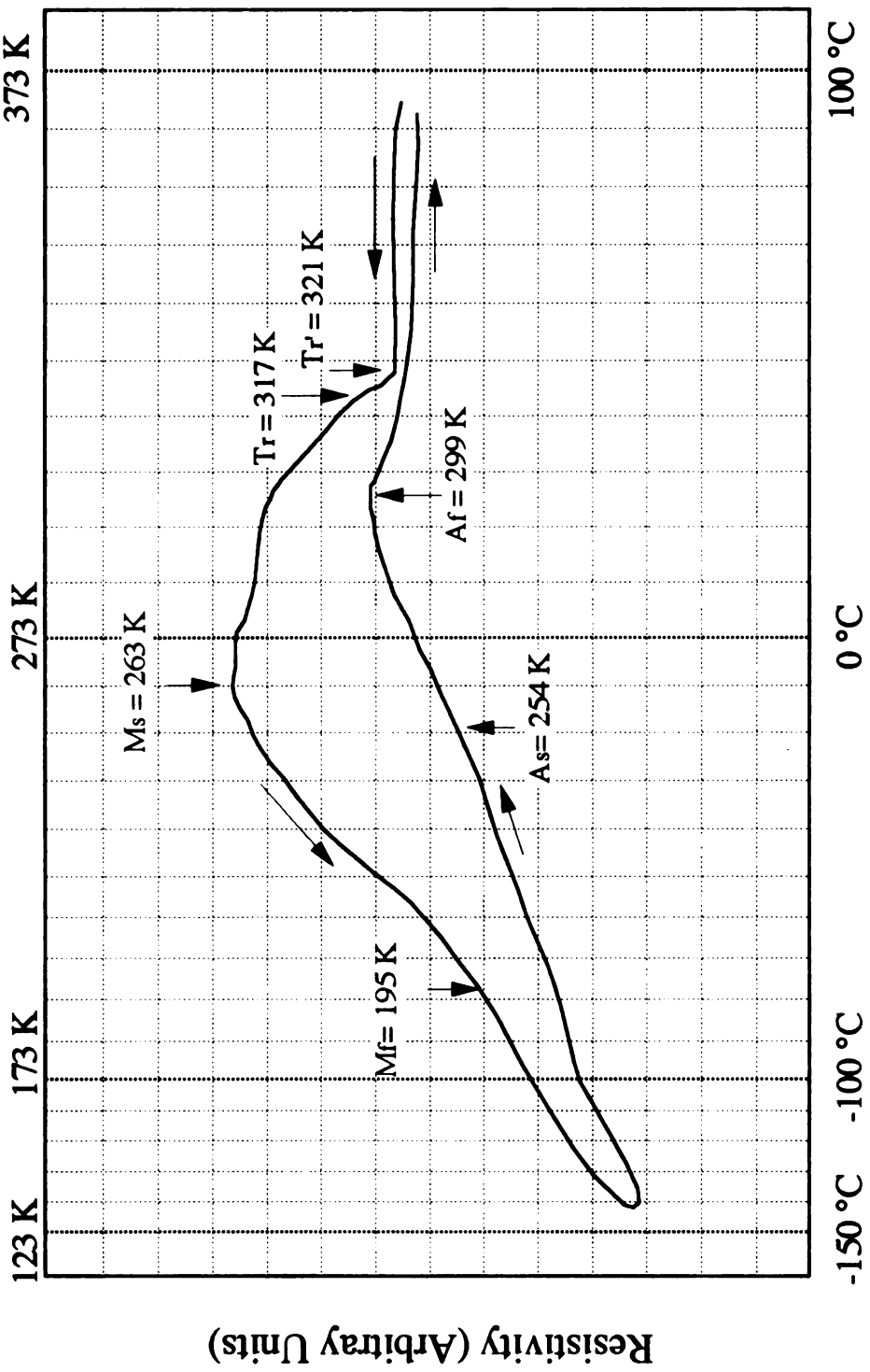

Figure A-9. Electrical Resistivity as a Function of Temperature for A/SIM2 tpye Film.

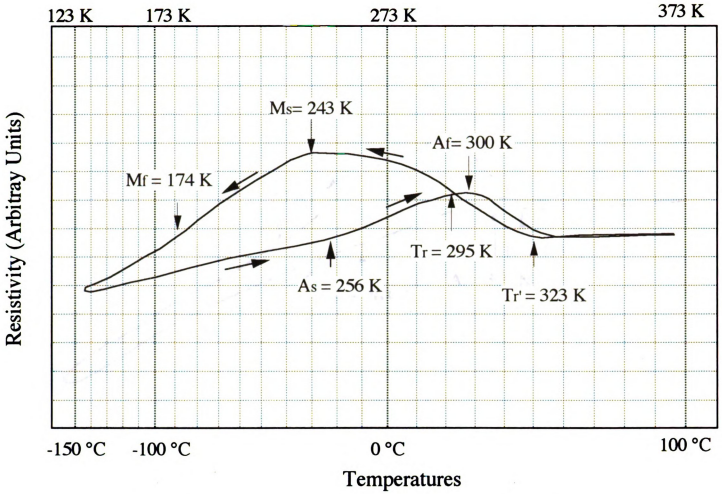

Figure A-10. Electrical Resistivity as a Function of Temperature for A/SIM3 tpye Film.

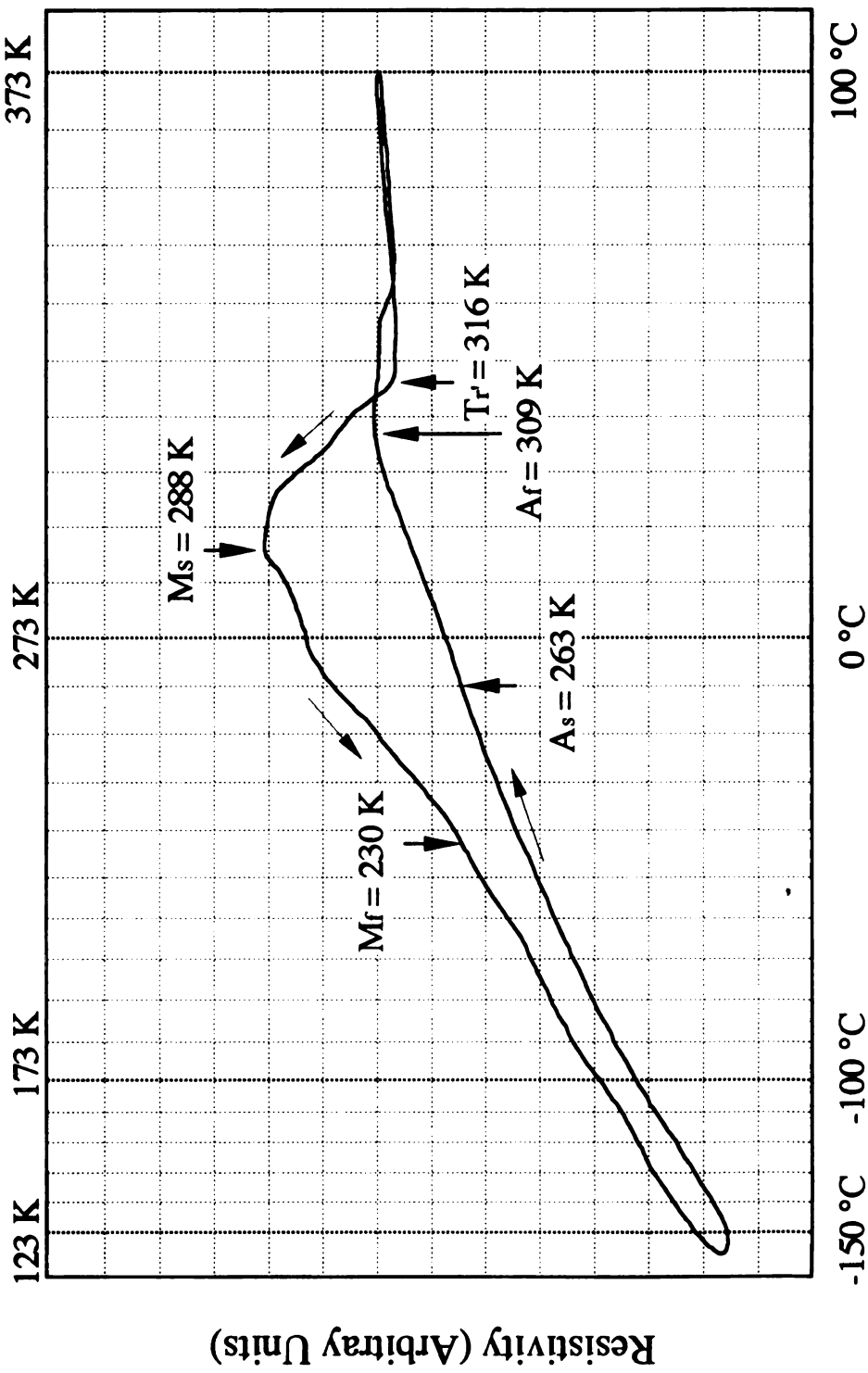

Figure A-11. Electrical Resistivity as a Function of Temperature for A/SIM4 tpye Film.

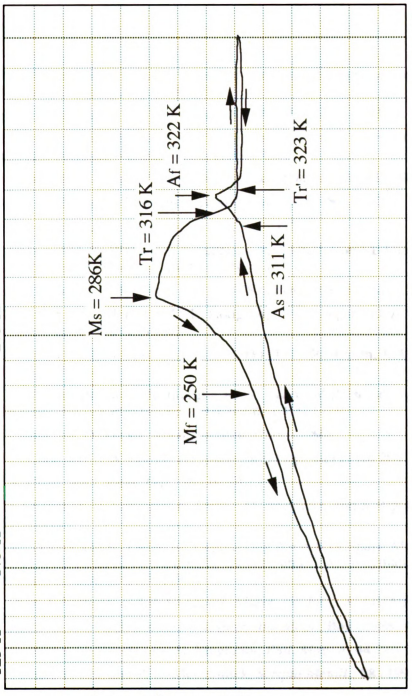

Figure A-12. Electrical Resistivity as a Function of Temperature for A/SIM5 tpye Film.

BIBLIOGRAPHY

1. J. O. Almen and P. H. Black, "Residual stresses and fatigue in metals", McGraw-Hill Book Company, Inc. (1963) 65.
2. T. Asaoka, H. Saito, and Y. Ishida, ICOMAT 92 (1992) 1003.
3. H.H. Anderson and H. L. Bay in "Sputtering by Particle Bombardment I", eds. R. Behrisch, Springer-Verlag, Berlin, (1981) 145.
4. Z. S.Basinski, R. Pascual, and S. J. Basinski, *Acta Metall.*, **31** (1983) 591.
5. Z. S.Basinski and S. J. Basinski, *Acta Metall.*, **37** (1989) 3263.
6. M.Bayerlein and H. Mughrabi, *Acta Metall.*, (1992).
7. G. Betz and G. K. Wehner in "Sputtering by Particle Bombardment II", eds. R. Behrisch, Springer-Verlag, Berlin (1983) 11.
8. I. E. Bolotov, V. Y. Kolosov, and A. V. Kozhyn, *Phys. Stat. Sol. A*, **72** (1982) 645.
9. J. D. Busch, A. D. Johnson, D. E. Hodgson, C. H. Lee, and D. A. Stevenson presented in ICOMAT (1989).
10. J. D. Busch, A. D. Johnson, C. H. Lee, and D. A. Stevenson, *J. Appl. Phys.*, **68** (1990) 6224.
11. R. W. Cahn, "Physical Metallurgy", R. W. Cahn and P. Haasen eds., North-Holland Physics Publishing, Amsterdam (1983) 1779.
12. L. Chang, Ph. D. Thesis, Michigan State Univ. (1993).
13. E. Y. Chen and E. A. Starke, Jr., *Mater. Sci. Eng.*, **24** (1976) 209.
14. H. S. Chen, *Appl. Phys. Lett.*, **29** (1976) 12.
15. J. P. Chevalier, V. Calvarac, A. Quivy, M. Harmelin, and J. Bigot, *Acta Metall*, **31** (1983) 465.
16. T. W. Duerig and R. Zadno in "Engineering Aspects of Shape Memory Alloys", eds. T. W. Duerig, K. N. Melton, D. Stockel, and C. M. Wayman, Butterworth-Heinemann, London (1990) 369.
17. L. Diaz, J. Victoria, and R. Gonzalez, *Mater. sic. Eng.*, **37** (1979) 103.
18. B. Emmoth and H. Bersaker, *Nucl. Instr. and Meth.*, **B33** (1988) 435.
19. U. Essmann, U. Gosele, and H. Mughrabi, *Phil. Mag. A*, **44**, No. 2 (1981) 405.
20. D. Favier, Y. Liu, and P. G. McCormick, *Scripta Metall.*, **28** (1993) 669.
21. C. E. Feltner, *Phil. Mag.*, **12** (1965) 1229.
22. C. E. Feltner and C. Laird, *Acta Metall.*, **15** (1967) 1621.
23. J. C. Figueroa and C. Laird, *Mater. Sci. Eng.*, **60** (1983) 45.

24. T. Fukuda, T. Saburi, K. Doi, and S. Nenno, *Mater. Trans. JIM*, **33** (1992) 271.
25. J. George, "Preparation of Thin Films", Marcel Dekker, Inc., New York, (1992) 41.
26. K. Giesser, J. D. Busch, A. D. Johnson, and A. B. Ellis, *Appl. Phys. Lett.*, **61** (1992) 1633.
27. I. Greenfiled and A. Purohit, *Mater, Sic. Eng.*, **46** (1980) 89.
28. D. S. Grummon, J. W. Jones, and G. S. Was, *Metall. Trans. A*, **19A** (1988) 2775.
29. D. S. Grummon, D. J. Morrison, J. W. Jones, and G. S. Was, *Mater. Sci. Eng.*, **A115** (1989) 331.
30. I. G. Greenfield and A. Purohit, *Mater. Sci. Eng.*, **46** (1980) 89.
31. L. Hou, unpublished data (1995).
32. K. Hohmuth, E, Richter, and B. Rauschenbach, *Mater. Sci. Eng.*, **69** (1985) 191.
33. A. Hunsche and P. Neumann, *Acta Metall.*, **34** (1986) 207.
34. C. M. Hwang, M. Meichle, M. B. Salamon, and C. M. Wayman, *Plil. Mag.A*, **47** (1983) 9.
35. C. M. Hwang, M. B. Salamon and C. M. Wayman, *Phil. Mag. A*, **47** (1983) 177.
36. C. M. Hwang, M. Meichle, M. B. Salamon, and C. M. Wayman, *Plil. Mag. A*, **47** (1983) 31.
37. A. Ishida, A. Takei and S. Miyazaki, *Thin Solid Films*, **228** (1993) 210.
38. K. Ikuta, H. Fujita, M. Ikeda, and S. Yamashita, *IEEE CH2832-4* (1990) 38.
39. C. M. Jackson, H. J. Wagner, and R. J. Wasilewski, NASA-SP 5110 (1972) 49.
40. A. D. Johnson, *J. Micromech. Microeng.*, **1** (1991) 34.
41. R. Kelly in "Ion Bombardment Modification of Surfaces", eds. O. Auciello and R. Kelly, Elsevier Science, Amsterdam, (1984) 101.
42. W. H. Kim and C. Laird, *Acta Metall.*, **26** (1978) 777.
43. J. J. Kim, P. Moine, and D. A. Stevenson, *Scripta Metall.*, **20** (1986) 243.
44. H. Kimura and T. Masumoto in "Amorphous Metallic Alloys", eds. F. E. Luborsky, Butterworth & Co. Ltd., Lodon, (1983) 187.
45. R. Kolodiziej and S. Soltys, *J. Mater. Sci. Lett.*, **11** (1992) 349.
46. U. Koster, *Z. Metallkd*, **75** (1984) 691.
47. D. Kuhlmann-Wilsdorf and C. Laird, *Mater. Sci. Eng.*, **46** (1980) 209.
48. V. T. Kuokkala and P. Kettunen, *Acta Metall.*, **33** (1985) 2041.
49. J. Lee, Master Thesis, Michigan State University, (1994).
50. J. M. Legresy , B. Prandi, and G. M. Raynaud, *J. De Phys. IV*, **1** (1991) C4-241.
51. H. C. Lin and S. K. Wu, *Scripta Metall.*, **26** (1992) 56.
52. H. C. Lin, S. K. Wu, T. S. Chou, and H. P. Kao, *Acta Metall.*, **39** (1991) 2006.
53. H. C. Ling and R. Kaplow, *Metall. Trans.*, **11A** (1980) 77.
54. W. Liu, M. Bayerlein, H. Mughrabi, A. Day, and N. Quested, *Acta Metall.*, **40** (1992) 1763.

55. B. -T. Ma and C. Laird, *Acta Metall.*, **37** (1989) 325.

56. A. F. Marshall, Y. S. Lee, and D. A. Stevenson, *Mater. Sci. Eng.*, **63** (1984) 215.

57. O. Matsumoto, S. Miyazaki, and H. Tamura, *Acta Metall.*, **35** (1987) 2137.

58. D. M. Mattox in "Handbbok of Deposition Technologies for Films annd Coatings", ed. R. F. Bunhsah, Noyes Publications, Park Ridge, New Jersey, (1994) 352.

59. K. N. Melton in "Engineering Aspects of Shape Memory Alloys", eds. T. W. Duerig, K. N. Melton, D. Stockel, and C. M. Wayman, Butterworth-Heinemann, London (1990) 21.

60. K. N. Melton and O. Mercier, *Metall. Trans.*, **9A** (1978) 1487.

61. J. Mendez, P. Violan and M. F. Denanot, *Nucl. Instr. and Meth.*, **B19/20** (1987) 232.

62. J. Mendez, P. Villechaise and P. Violan, "Strength of Metals and Alloys" (ICMSA 8) eds. P. O. Kettunen, T. K. Lepisto and M. E. Lehtonen, Pergamon Press, (1988) 737.

63. C. A. Meyers and D. S. Grummon, *Mater. Sci. Eng.*, **A130** (1990) 127.

64. S. Miyazaki, K Otsuka, and Y. Suzuki, *Scripta Metall.*, **15** (1981) 287.

65. S. Miyazaki, Y. Omni, K. Ostuka, and Y. Suzuki, *J. of De Phys.*, No.4 (ICOMAT 1982) (1982) C4-255.

66. S. Miyazaki and K Otsuka, *Phil. Mag. A*, **50** (1984) 393.

67. S. Miyazaki and K Otsuka, *Metall. Trans.*, **17A** (1986) 53.

68. S. Miyazaki and C. M. Wayman,*Acta Metall.*, **36** (1988) 181.

69. S. Miyazaki , Y Kohiyama, and K Otsuka, *J. Jpn. Inst. Met.* Int'l. Sysm. 6th. 1991, Sendai, Japan (1991) 691.

70. S. Miyazaki, Y. Sugaya, and K Otsuka, MRS Int'l. Mtg. on Avd. Mats., **9** (1989) 263.

71. S. Miyizaki, K. Otsuka, and C. M. Wayman, *Acta Metall.*, **37** (1989) 1873.

72. W. J. Moberly, J. D. Busch, A. D. Johnson, and H. Berkson in "Phase Transformation Kinetics in Thin Films", eds. M. Chen, M. Thompson, R. Schwarz,and M. Libera, MRS Int'l. Mtg. on Avd. Mats., **230**, (1991) 85.

73. D. J. Morrison, J. W. Jones, D. E. Alexander, C. Kovach, and G. S. Was, *Mater. Sci. Eng.*, **A115** (1989) 315.

74. Y. Motohashi, K. Ohsawa, T. Hoshiya, K. Okamoto, and M. Ohmori, *J. Jpn. Inst. Met.*, **55** (1991)132 [Japanese].

75. H. Mughrabi, *Mater. Sci. Eng.*, **33** (1978) 207.

76. H. Mughrabi, "Strength of Metals and Alloys", P. Hassen, V. Gerold and G. Kostorz eds., Pergamon Press, (1979) 1615.

77. H. Mughrabi, "Fatigue Mechanisms: Advances in Quantitative Measurement of Physical Demage" ASTM No.811 (1982) 5.

78. P. Neumann, "Physical Metallurgy", R. W. Cahn and P. Haasen eds., North-Holland Physics Publishing, Amsterdam (1983) 1553.

79. P. Neumann, *Mater. Sci, Eng.*, **81** (1986) 465.

80. P. Neumann and Tonnnessen, *Fatigue '87, Proc. 3rd Int. Conf. on Fatiguee and Fatigue Thresholds, Charlottesville, VA*, vol. I, eds. R. O. Ritchie and E. A. Starke, (1987) 3.

81. M. V. Nevitt, *Trans. AIME*, **218** (1960) 327.

82. M. Nishida and T. Honma, *Scripta Metall.*, **18** (1984) 1299.

83. M. Nishida, C. M. Wayman, and T. Honma, *Metall. Trans.*, **17A** (1986) 1505.

84. M. Nishida, C. M. Wayman, and A. Chiba, *Metallography*, **21** (1988) 275.

85. Z. Nishiyama, "Martensitic Transformation", Academic Press, New York (1978) 276.

86. I. C. Noyan and J. B. Cohen, "Residual Stress Measurement by Diffraction and Interpretation", Springer-Verlag New York Inc., (1986) 232.

87. H. Oechsner, *Appl. Phys.*,**8** (1975) 185.

88. M. Ohring, "The Materials Science of Thin Films", Academic Press, Inc., San Diego (1992) 197.

89. T. Okutani, M. Shikata, S. Ichimura, and R. Shimizu, *J. Appl. Phys.*, **51** (1980) 2884.

90. R. R. Olson, M.E. King, and G. K. Wehner, *J. Appl. Phys.*, **50** (1979) 3677

91. K. Otsuka, T. Sawamura, and K. Shimizu, *Phys. Stat. Soll. A*, **5** (1979) 457.

92. W. R. Patterson and I. G. Greenfield, *Acta Metall.*, **19** (1971) 123.

93. J. Polak and M. Klesnil, *Mater. Sci. Eng.*, **63** (1984) 189.

94. J. Polak and K. Obrtlik, M. Hajek, and A. Vasek, *Mater. Sci. Eng.*, **A151** (1992) 19.

95. A. K. Rai and R. S. Bhattacharya, *Mat. Sci. Eng.*, **85** (1987) 139.

96. K. V.Rasmussen and O. B. Pedersen, *Acta Metall.*, **28** (1980) 1467.

97. K. V.Rao, R. Malmall, S. M. Bhagat, G. Backstrom, and H. S. Chen, *IEEE Trans. on Mag.*, **MAG-16** (1980) 896.

98. T Saburi, M. Yoshida, and S. Nenno, *Scripta Metall.*, **18** (1984) 363.

99. Y. Shugo, S. Hanada, and T. Honma, *Bull. Res. Inst. Min. Met.*, Tohoku Univ., **41** (1985) 23.

100. P. Sigmund in "Sputtering by Particle Bombardment I", eds. R. Behrisch, Springer-Verlag, Berlin, (1981) 9.

101. A. W. Sleeswyk, H. J. G. Kok, and G. Boom, *Scripta Metall.*, **14** (1980) 919.

102. F. A. Smidt, *Inter. Mater. Rev.*, **35** (1990) 61.

103. S. Suresh, "Fatgue of Materials", Cambridge University Press, New York (1991) 40.

104. R. A. Swalin, "Thermodynamics of Solid", John Wiley & Sons, Inc, New York (1972) 33.

105. T. Tadaki and Wayman, *Scripta Metall.*, **14** (1980) 914.

106. D. Theirich and J. Engemann, *Nucl. Instr. and Meth.*, **B59/60** (1991) 336.

107. P. E. Thoma, M. Y Kao, S. Fariabi, and D. N. AbuJudom, ICOMAT 1992 (1992) 917.

108. C. V. Thompson, *Ann. Rev. Mater. Sci.*, **20** (1990) 245.

109. J. A. Thornton, *J. Vac. Sci. Tech.*, **11** (1974) 666.

110. J. A. Thornton, *Ann. Rev. Mater. Sci.*, **7** (1978) 239.

111. J. A. Thornton and D. W. Hoffman, *Thin Solid Films*, **171** (1989) 5.

112. H. Tobushi, H. Iwanaga, K. Tanaka T. Hori, and T. Sawada, *Continuum Mech. Thermodyn.*, **3** (1991) 79.

113. T. Todoroki and H. Tamura, *Trans. Japan Ins. Metals*, **28** (1987) 83.

114. N. Wade, Y. Adachi, and Y. Hosoi, *Scripta Metall.*, **24** (1990) 1051.

115. B. J. Walles, Master Thesis, Michigan State University, (1993).

116. R. Wang and H. Mughrabi, *Mater. Sci. Eng.*, **65** (1984) 235.

117. R. J. Wasileewski, S. R. Butler, J. E. Hanlon, and D. Worden, *Metall. Trans.*, **2** (1971) 229.

118. C. M. Wayman in "Engineering Aspects of Shape Memory Alloys", eds. T. W. Duerig, K. N. Melton, D. Stockel and C. M. Wayman, Butterworth-Heinemann, London (1990) 3.

119. A. T. Winter, *Phil. Mag.*, **30** (1974) 719.

120. A. T. Winter, O. B. Pedersen, and K. V. Ramussen, Acta Metall., **29** (1981) 735.

121. C. Y. Xie, L. C. Zhao, and T. C. Lei, *Scripta Metall.*, **24** (1990) 1753.

122. K. Zoltzer and R. Bormann, *J. Less-Comm. Metals*, **140** (1988) 335.

123. Metals Handbook, vol.2 (1979) 275.

124. Binary Alloy Phase Diagrams, vol.2, ed. T. B. Massalski, American Metal Society, Metal Park (1987) 1768.